ADVANCED STEEL CONSTRUCTION

An International Journal

Volume 11 Number 1

March 2015

CONTENTS

Technical Papers

Website: *http://www.hkisc.org*
ISSN 1816-112X
Science Citation Index Expanded, Materials Science Citation Index and ISI Alerting

Cover: Scene of London with aesthetic steel buildings
e-copy of IJASC is free to download at "www.ascjournal.com" in internet and mobile apps.

ADVANCED STEEL CONSTRUCTION

VOL.11, NO.1 (2015)

ADVANCED STEEL CONSTRUCTION

an International Journal

ISSN 1816-112X

Volume 11 Number 1 *March 2015*

ISSN 1816-112X

Science Citation Index Expanded, Materials Science Citation Index and ISI Alerting

Advanced Steel Construction
an international journal

Cover: Scene of London with aesthetic steel buildings

e-copy of IJASC is free to download at "www.ascjournal.com" in internet and mobile apps.

General Information
Advanced Steel Construction, an international journal

Aims and scope

The International Journal of Advanced Steel Construction provides a platform for the publication and rapid dissemination of original and up-to-date research and technological developments in steel construction, design and analysis. Scope of research papers published in this journal includes but is not limited to theoretical and experimental research on elements, assemblages, systems, material, design philosophy and codification, standards, fabrication, projects of innovative nature and computer techniques. The journal is specifically tailored to channel the exchange of technological know-how between researchers and practitioners. Contributions from all aspects related to the recent developments of advanced steel construction are welcome.

Instructions to authors

Submission of the manuscript. Authors may submit double-spaced manuscripts preferably in MS Word by emailing to one of the chief editors as follows for arrangement of review. Alternatively papers can be submitted on a diskette to one of the chief editors.

Asian Pacific , African and organizing editor : Professor S.L. Chan, Email: ceslchan@polyu.edu.hk
American editor : Professor W.F. Chen, Email: waifah@hawaii.edu
European editor : Professor R. Zandonini, Email: riccardo_zandonini@ing.unitn.it

All manuscripts submitted to the journal are recommended to accompany with a list of four potential reviewers suggested by the author(s). This list should include the complete name, address, telephone and fax numbers, email address, and at least five keywords that identify the expertise of each reviewer. This scheme will improve the process of review.

Style of manuscript

General. Author(s) should provide full postal and email addresses and fax number for correspondence. The manuscript including abstract, keywords, references, figures and tables should be in English with pages numbered and typed with double line spacing on single side of A4 or letter-sized paper. The front page of the article should contain:

a) a short title (reflecting the content of the paper);
b) all the name(s) and postal and email addresses of author(s) specifying the author to whom correspondence and proofs should be sent;
c) an abstract of 100-200 words; and
d) 5 to 8 keywords.

The paper must contain an introduction and a conclusion. The length of paper should not exceed 25 journal pages (approximately 15,000 words equivalents).

Tables and figures. Tables and figures including photographs should be typed, numbered consecutively in Arabic numerals and with short titles. They should be referred in the text as Figure 1, Table 2, etc. Originally drawn figures and photographs should be provided in a form suitable for photographic reproduction and reduction in the journal.

Mathematical expressions and units. The Systeme Internationale (SI) should be followed whenever possible. The numbers identifying the displayed mathematical expression should be referred to in the text as Eq. (1), Eq. (2).

References. References to published literature should be referred in the text, in the order of citation with Arabic numerals, by the last name(s) of the author(s) (e.g. Zandonini and Zanon [3]) or if more than three authors (e.g. Zandonini et al. [4]). References should be in English with occasional allowance of 1-2 exceptional references in local languages and reflect the current state-of-technology. Journal titles should be abbreviated in the style of the Word List of Scientific Periodicals. References should be cited in the following style [1, 2, 3].

Journal: [1] Chen, W.F. and Kishi, N., "Semi-rigid Steel Beam-to-column Connections, Data Base and Modelling", Journal of Structural Engineering, ASCE, 1989, Vol. 115, No. 1, pp. 105-119.
Book: [2] Chan, S.L. and Chui, P.P.T., "Non-linear Static and Cyclic Analysis of Semi-rigid Steel Frames", Elsevier Science, 2000.
Proceedings: [3] Zandonini, R. and Zanon, P., "Experimental Analysis of Steel Beams with Semi-rigid Joints", Proceedings of International Conference on Advances in Steel Structures, Hong Kong, 1996, Vol. 1, pp. 356-364.

Proofs. Proof will be sent to the corresponding author to correct any typesetting errors. Alternations to the original manuscript at this stage will not be accepted. Proofs should be returned within 48 hours of receipt by Express Mail, Fax or Email.

Copyright. Submission of an article to "Advanced Steel Construction" implies that it presents the original and unpublished work, and not under consideration for publication nor published elsewhere. On acceptance of a manuscript submitted, the copyright thereof is transferred to the publisher by the Transfer of Copyright Agreement and upon the acceptance of publication for the papers, the corresponding author must sign the form for Transfer of Copyright.

Permission. Quoting from this journal is granted provided that the customary acknowledgement is given to the source.

Page charge and Reprints. There will be no page charges if the length of paper is within the limit of 25 journal pages. A total of 30 free offprints will be supplied free of charge to the corresponding author. Purchasing orders for additional offprints can be made on order forms which will be sent to the authors. These instructions can be obtained at the Hong Kong Institute of Steel Construction, Journal website: http://www.hkisc.org

The International Journal of Advanced Steel Construction is published quarterly by learnt society, The Hong Kong Institute of Steel Construction, c/o Department of Civil & Environmental Engineering, The Hong Kong Polytechnic University, Hung Hom, Kowloon, Hong Kong.

Subscription inquiries and change of address. Address all subscription inquiries and correspondence to Member Records, IJASC. Notify an address change as soon as possible. All communications should include both old and new addresses with zip codes and be accompanied by a mailing label from a recent issue. Allow six weeks for all changes to become effective.

The Hong Kong Institute of Steel Construction
HKISC
c/o Department of Civil and Environmental Engineering,
The Hong Kong Polytechnic University,
Hunghom, Kowloon, Hong Kong, China.
Tel: 852- 2766 6047 Fax: 852- 2334 6389
Email: *ceslchan@polyu.edu.hk* Website: *http://www.hkisc.org/*
ISSN 1816-112X
Science Citation Index Expanded, Materials Science Citation Index and ISI Alerting

ISSN 1816-112X

Science Citation Index Expanded, Materials Science Citation Index and ISI Alerting

Advanced Steel Construction
an international journal

VOLUME 11 NUMBER 1 MARCH 2015

Technical Papers

PARAMETRIC ANALYSIS OF SHEAR PANEL DAMPERS UNDER HIGH AXIAL COMPRESSION

Zhiyi Chen[1, 2,*], Hui Fan[3] and Guoqiang Bian[3]

[1] *Associate Professor, Department of Geotechnical Engineering, Tongji University, Shanghai 200092, China*
[2] *Key Laboratory of Geotechnical and Underground Engineering of Ministry of Education, Shanghai 200092, China*
[3] *Department of Geotechnical Engineering, Tongji University, Shanghai 200092, China*
**(Corresponding author: E-mail: zhiyichen@tongji.edu.cn)*

Received: 21 December 2012; Revised: 18 March 2013; Accepted: 27 December 2013

ABSTRACT: To explore the hysteretic behaviors of shear panel dampers under axial compression, numerical analyses were carried out using the general-purpose finite element software *ABAQUS*. Two important parameters, namely the axial compression ratio and the web slenderness parameter, were selected as governing parameters. To trace the material nonlinearity, a modified two-surface model was adopted to simulate the constitutive relations of the steel material under cyclic shear loading. Discussions focused on the hysteretic behavior, maximum shear strength, and energy dissipation performance concerning the axial compression ratio. It was found that axial compression deteriorates the hysteretic behavior and energy dissipation performance of shear panel dampers. In addition, under high axial compression, a small web slenderness parameter leads to unexpected brittle failure.

Keywords: Shear panel damper, High axial compression ratio, Hysteretic energy dissipation, Underground structure, Numerical simulation

1. INTRODUCTION

Evidence from recent seismic disasters, especially the 1995 Kobe earthquake in Japan, indicates that underground structures are damaged seriously during a severe earthquake. Extensive studies and applications [1–4] have focused on shear panel dampers (SPDs) incorporated into ground buildings and bridges, which serve as a type of passive structural control device to dissipate seismic input energy. SPDs are able to dissipate a large amount of energy through plastic yielding and hysteretic deformation of the metal material. Characterized by simple configuration, and convenient replacement and maintenance, SPDs are used widely in ground structures and show outstanding energy dissipation performance and seismic control properties. However, both the application and research of SPDs in underground structures are still in their infancy [5].

In contrast with the design of ground structures, the seismic design of underground structures must consider fully the adverse effects of high axial compression on SPDs. This is because the columns of underground structures not only bear loading transferred from an upper structure [6], but they also suffer very strong dynamic axial forces due to the vertical vibration of overburdened soil under the effect of vertical ground motion [7]. Real failure modes and results of numerical analysis [8, 9] have shown that the collapse of columns at the Dakai subway station was caused primarily by the joint action of the horizontal seismic shear force and superior axial compression.

To date, research has concentrated on the hysteretic behavior of SPDs, such as the effects of initial deformation, buckling and post-buckling phenomena, ultimate shear bearing capacity, and energy dissipation capacity. In research on axial compression, Sasaki and Tanaka [10] explored the effect of static axial compression on the hysteresis curves of SPDs fabricated of low-yield-point steel. They also empirically obtained an allowable level of axial compression. Experiments on two-way stiffened SPDs made of low-yield-point steel were carried out by Nakashima et al. [11]. Results showed that when the axial compression ratio reached 0.3, hysteresis curves were pinched

conspicuously, but that the ability of the SPDs to dissipate energy was not reduced significantly because of the strain hardening of the steel material.

There has been relatively little research on the hysteretic behavior of SPDs under high axial compression loading. Chen et al. [5] conducted cyclic shear tests on five SPDs fabricated of Q235B mild steel. According to the code of *Steel Plates for Building Structure* [12], the yield stress and maximum stress of Q235B steel are about 235 MPa and 400–510 MPa, respectively. Elongation is equal to or more than 23%. These SPDs were designed to be capable of sustaining high axial compression induced in an underground structure by an earthquake. The experimental results revealed that shear capacity and ductility decrease with an increase of the axial compression ratio. When the axial compression ratio was 0.7, the cumulative energy consumption of the SPDs was almost half that for the case of a ratio of 0.3. In the present study, a comprehensive parametric study is carried out through numerical simulation to overcome the shortcomings of indoor tests, for which the number of specimens is rather limited and duplication is difficult and expensive. The validity of the numerical model and the accuracy of the simulation results are initially verified by indoor test results. Then, the axial compression ratio and the shear-web slenderness are taken as the two most significant control parameters. Hysteretic behavior, maximum shear strength, and energy dissipation performance are discussed concerning a high axial compression ratio.

2. NUMERICAL MODEL

2.1 Main Parameters of SPDs

Figure 1 is a schematic diagram of an SPD. Generally, the shear web, which comprises the primary energy dissipation components of SPDs, is made of mild steel or low-yield-point steel. Transverse and longitudinal units are reinforced all around to prevent the web from yielding too early. Web slenderness, R_w, is the key parameter affecting the hysteretic behavior and energy dissipation performance of an SPD and it can be defined and calculated according to Eq. 1, as proposed by Fukumoto [13]:

$$R_w = \frac{b_w}{t_w}\sqrt{\frac{12(1-\nu^2)\tau_y}{k_s \pi^2 E}} \tag{1}$$

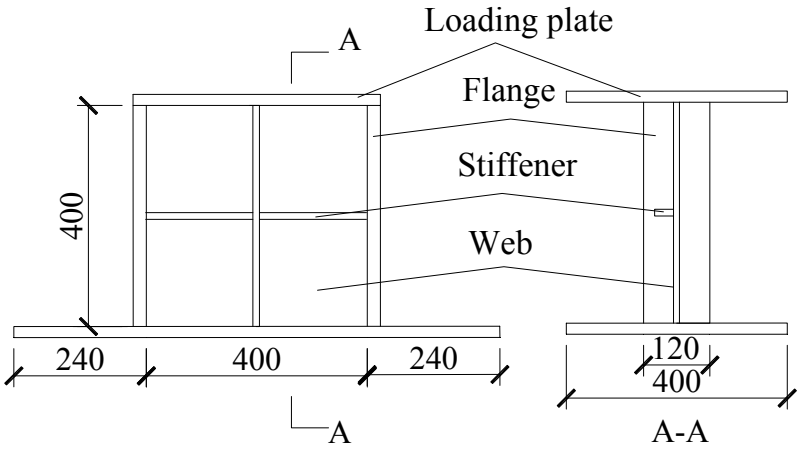

Figure 1. Schematic Diagram of Shear Panel Damper (Units: mm)

Here, b_w and t_w are the width and thickness of the web, respectively, ν is Poisson's ratio, τ_y is the shear yield strength of the web material, E is Young's modulus of elasticity, and k_s is the elastic buckling coefficient of a simply supported plate:

$$k_s = \begin{cases} (n_L+1)^2(5.35+1/\alpha_s^2), & \alpha_s \geq 1 \\ (n_L+1)^2(5.35/\alpha_s^2+4), & \alpha_s < 1 \end{cases} \tag{2}$$

where n_L is the number of longitudinal stiffeners and α_s is the aspect ratio of a subpanel.

Unstiffened SPDs have great ductility. However, they would yield in the early period of horizontal shear loading, leading to a reduction in shear strength and severe deterioration of their ability to dissipate energy. Therefore, a web plate is usually welded with a stiffener, effectively to prevent premature local buckling, to eliminate the pinch effect in the hysteresis loop, and to ensure a greater yielding range, thereby improving the energy dissipation capacity [14]. In this numerical analysis, the simulation model is stiffened in one-side and two-way (horizontal and vertical) modes. A two-way stiffener can efficiently prevent web buckling and degradation of the shear strength, allowing large deformation without conspicuous pinching of the hysteresis loop or reduction of the ultimate strength. Meanwhile, vertical stiffeners can resist part of the vertical axial compression force. Here, the width/thickness ratio is set at nine to avert premature local buckling. The stiffener rigidity is denoted as γ_s/γ_s* [15], where γ_s is the stiffness of the stiffener, which can be calculated using Eq. 3 and γ_s* is the optimal stiffness of the stiffener, which can calculated using Eq. 4.

$$\gamma_s = \frac{EI_s}{b_w D_w}, \tag{3}$$

$$\gamma_s^* = \left(\frac{23.1}{n_L^{2.5}} - \frac{1.35}{n_L^{0.5}}\right)\frac{(1+\alpha^{3/n_L-0.3})^{2n_L-1}}{1+\alpha^{5.3-0.6n_L-3/n_L}}, \tag{4}$$

where I_s is the inertia moment, D_w is the flexural rigidity per unit web width, and α is the aspect ratio of the full panel. It should be noted that the aspect ratio of the full panel is equal to that of the subpanel because the stiffeners are placed in equidistant pairs. The formulas are valid only when web parameters fall into the range of $n_L = n_T \leq 3$ and $0.5 \leq \alpha \leq 2.0$.

According to previous analysis results [16], R_w is set as 0.2, 0.3, and 0.4. In addition, an axial compression ratio, z, is defined as the ratio of the applied external axial force divided by the axial yielding force of the SPD. It is adopted to explore the effect of the axial compression force on the hysteretic behavior and energy dissipation performance of the SPDs. To clarify the effects of different magnitudes of the axial compression ratio, z is taken as 0.0 (without axial compression), 0.3 (low axial compression), 0.5 (medium axial compression), and 0.7 (high axial compression). As stated in a prior parametric study [16], when the stiffener rigidity γ_s/γ_s*, flange rigidity t_f/t_w, and web aspect ratio α satisfy: $\gamma_s/\gamma_s* \geq 3.0$, $t_f/t_w \geq 4.0$, and $0.5 \leq \alpha \leq 1.5$, the effects of these design parameters on the web shear strength can be neglected. Hence, the parameters in this paper are chosen as $\gamma_s/\gamma_s* = 3.0$, $t_f/t_w = 4.0$, and $\alpha = 1.0$. Numerical simulation parameters for SPDs are summarized in Table 1.

Table 1. Summary of simulation parameters for SPDs

z	R_w	b_w (mm)	t_w (mm)	t_f (mm)	b_f (mm)	t_s (mm)	b_s (mm)	P (kN)	τ_m/τ_y
0.7	0.4	400	4.42	17.67	120	5.4	48.6	1031.6	1.159
0.7	0.3	400	5.89	23.57	120	5.4	48.6	1361.3	1.303
0.7	0.2	400	8.84	35.35	120	5.4	48.6	2020.5	1.445
0.5	0.4	400	4.42	17.67	120	5.4	48.6	736.9	1.223
0.5	0.3	400	5.89	23.57	120	5.4	48.6	972.3	1.365
0.5	0.2	400	8.84	35.35	120	5.4	48.6	1443.2	1.654
0.3	0.4	400	4.42	17.67	120	5.4	48.6	442.1	1.275
0.3	0.3	400	5.89	23.57	120	5.4	48.6	583.4	1.448
0.3	0.2	400	8.84	35.35	120	5.4	48.6	865.9	1.684
0.0	0.4	400	4.42	17.67	120	5.4	48.6	0	1.395
0.0	0.3	400	5.89	23.57	120	5.4	48.6	0	1.517
0.0	0.2	400	8.84	35.35	120	5.4	48.6	0	1.666

Note: z: axial compression ratio; R_w: web slenderness parameter; b_w: width of web; t_w: thickness of web; b_f: width of flange; t_f: thickness of flange; b_s: width of stiffener; t_s: thickness of stiffener; P: axial force; τ_m/τ_y: dimensionless maximum shear strenth; τ_m: maximum shear stress; τ_y: yield shear stress.

2.2 Shear Angle Limit

As a device that dissipates seismic energy through metal yielding, the SPD has an energy dissipation capacity that depends mainly on its plastic deformation capacity and fatigue performance. That is, an SPD must have sufficient ductility to withstand the maximum shear deformation suffered during an earthquake [16]. Here, the allowable maximum shear deformation is usually measured using a dimensionless parameter, namely the shear angle limit. Research conducted by Takahashi and Shinabe [17] suggests that when R_w is less than 0.55, the maximum shear angles of low-yield-point SPDs under a cyclic loading condition and monotonic loading condition are 0.05 and 0.1, respectively. Experiments carried out by Chen and Kuo [3] demonstrated that despite the shear angle reaching 0.06, the shear bearing capacity remained stable. The *Code for Seismic Design of Subway Structures* in Shanghai [18] specifies that the inter-story elastic-plastic drift angle limit for concrete-framed underground structures is 1/250. Prior to the failure of SPDs, the vertical displacement of the flanges is relatively small. The shear deformation angle of the web, γ, can then be determined approximately according to the horizontal displacement divided by the height of the specimen (0.4 m). Considering that the two-yield-surface constitutive model used in numerical simulations is unable to simulate fatigue behavior [19], the maximum cyclic loading limit is set at 0.034 in the numerical analysis; i.e., the cyclic loading is terminated once the shear angle reaches 0.034. For ordinary mild steel, this value is equivalent to $20\gamma_y$ (where γ_y refers to the yield shear strain, = 0.002). Commonly, it is believed that within this range, the fatigue failure of steel under low-frequency cyclic action can be avoided; therefore, there is no necessity of modeling fracture in the numerical simulation. From the above discussion, it is safely concluded that the upper limit of an SPD shear angle is 0.034. This value provides a safety and security margin in engineering practice.

2.3 Model Construction

Figure 2 illustrates the numerical model of an SPD. It is clear that the shell elements S4 and S4R, which are provided by the *ABAQUS* element library, are available in this simulation. S4 is a four-node fully integrated, finite-membrane-strain shell element. The element's membrane response is treated with an assumed strain formulation that gives accurate solutions to in-plane bending problems. S4R is a four-node doubly curved, first-order, reduced integration shell element. S4 is compatible with S4R. However, S4 has four integration locations per element compared with one integration location for S4R, which makes S4 computationally more expensive. Considering that an SPD is subjected mainly to shear and axial forces, and that the two-yield-surface model used to simulate the material in the plastic phase is extremely computationally time-consuming, S4R is selected for the finite element modeling. The initial deformation and residual stress are considered. Depending on experimental inspections and the analytical study of plate assemblies [20], the distribution of the residual stresses in the web and the stiffeners is idealized in a rectangular pattern, as shown in Figure 3. Initial out-of-plane deflections have a sinusoidal distribution with the stiffener being the node of the curve and the amplitude being 1/150 of the height of the shear panel. To simulate accurately the large nonlinear deformation behavior of shear panels under cyclic loading, numerical simulations are based on a secondary-developed user subroutine platform provided by *ABAQUS*, using the modified two-yield-surface model exploited by a research group at Nagoya University in Japan [21]. This model comprises a yield surface (the inner surface) and boundary surface (the outside surface) to describe the constitutive law of steel under cyclic loading. The yield surface is embodied permanently by the boundary surface. Additionally, the dimensions and correlation of these two surfaces determine the plastic modulus of the SPD. The modified two-yield-surface model is validated by the works of Gao et al. [22] and Chusilp et al. [23, 24], in which experiments were conducted on box girders to validate the modeling of shear behavior of mild steel under cyclic loading. The results showed that the modified two-yield-surface model performs well in tracing the material's nonlinearity under cyclic loading.

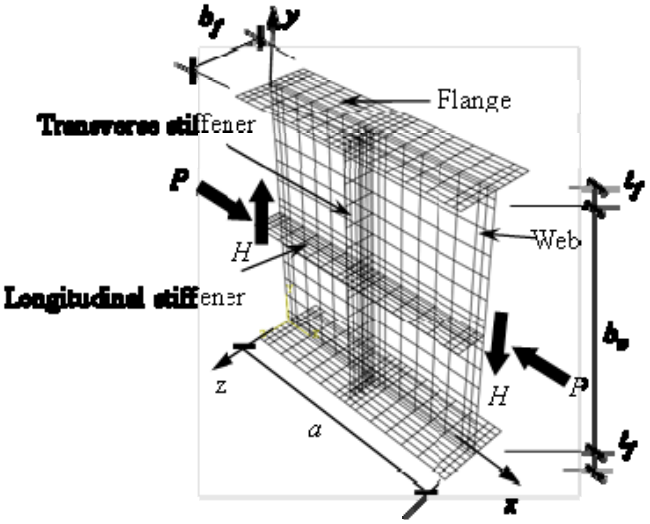

Figure 2. Finite Element Model

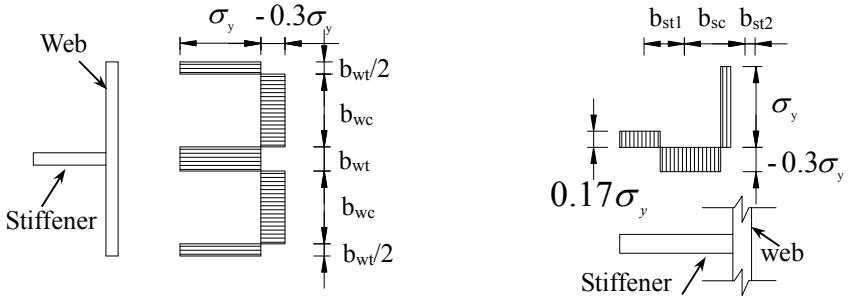

$b_{wt} : b_{wc} = 0.3:1$ $b_{st1} : b_{sc} : b_{st2} = 0.69 : 1 : 0.17$

(a) Web (b) Stiffener

Figure 3. Distribution of Residual Stresses

Taking into account the practical application, both ends of the panel are welded to a considerably stiff plate. Therefore, both ends of the model, at the planes $x = 0$ and $x = a$ in Figure 2, are assumed to be fixed, except for the displacement in the x and y directions of the loading edge. Cyclic transverse displacement is applied to the shear panels along the plane $x = a$, and the displacement in each cycle Δ is the multiple of the yield displacement of the web, Δ_y, in pure shear. The cyclic loading mode is illustrated in Figure 4. Then, the sum of the vertical reaction force in shear, H, is obtained along the plane $x = 0$ to calculate the average shear stress, τ_n, as shown in Eq. 5. In addition to the displacement loading, the SPD is also subjected to an axial compression P. As the axial compression is always translated to an SPD through a stiff loading plate, P is uniformly distributed along the plane $x = a$ in the numerical analyses. The main results obtained from the numerical analyses are the average shear stress, τ_n, and the average shear strain, γ, which are described by:

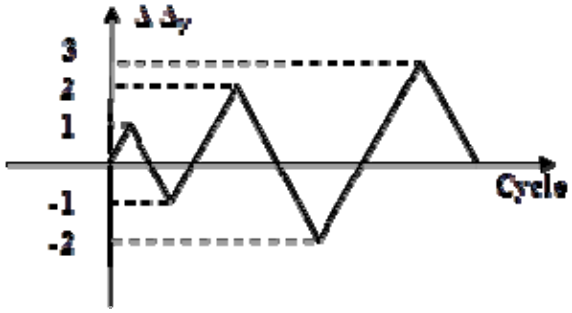

Figure 4. Loading Mode

$$\tau_n = \frac{H}{b_w t_w}, \quad \gamma = \frac{\Delta}{a} \tag{5}$$

where H is the sum of the vertical force in the plane $x = 0$, and Δ is the vertical load displacement.

3. VERIFICATION AND VALIDATION OF THE NUMERICAL ANALYSIS MODEL

This section aims to verify and validate the numerical model and simulation method using existing laboratory experimental results [5]. The specimen number is R_w03-z07. R_w03-z07 means that the tested specimen's web slenderness R_w is 0.3 and the axial compression ratio z is 0.7. That is, the axial load on the specimen is 0.7 times that of the axial yield strength of the cross-section. The dimensions of the shear-web specimen (see Figure 1) are 400 (width) × 400 (height) × 6 mm (thickness). The vertical flange thickness is 24 mm and the width is 120 mm. The areal dimensions of the loading plates are 450 × 400 mm (upper) and 880 × 400 mm (lower). The thicknesses of the loading plates are 20 mm. Stiffeners are 40-mm wide and 6-mm thick.

Figure 5 shows good agreement for (a) hysteretic curves and (b) cumulative dissipating energy between the laboratory test (R_w03-z07) and numerical simulation. The peak value of the dimensionless maximum shear strength, H/H_y, is 1.369 (γ = 0.0162) in the numerical simulation and 1.378 (γ = 0.0145) in the laboratory test, as shown in Figure 5(a). The error is within 0.65%. Additionally, the error in the normalized total cumulative dissipating energy is less than 0.82%, as shown in Figure 5(b); this error is extremely low. The above comparisons demonstrate that the presented SPD model and numerical simulation method are valid. The hysteretic behavior and energy dissipation performance of SPDs under high axial compression can be predicted reliably in this manner.

4. RESULTS AND DISCUSSION

4.1 Hysteretic Behavior

Figure 6 shows hysteresis curves of SPDs with various values of R_w and z. It can be seen that the strain-hardening phenomenon changes from isotropic hardening to a mix of kinematic and isotropic hardening with an increase in the axial compression ratio. Given a large value of z, the shear stress versus shear strain curves have obvious development stages, which include an elastic region, a yield region, a hardening zone, and a strength reduction stage. In the cases of z = 0.0 and 0.3, and R_w = 0.2 and 0.3, the hysteresis curves have a full shape and show the combined effects of kinematic and isotropic hardening. No web-buckling phenomenon is observed during the loading phase. Plastic deformation develops gradually throughout the entire steel web plate after yielding. Strain hardening occurs at 4γ_y and remains until the end of the loading process.

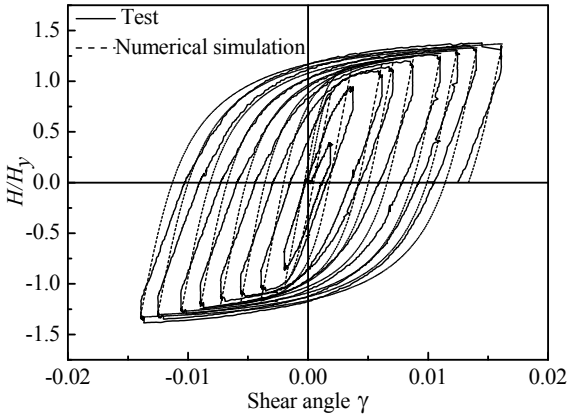

(a) Hysteretic Curves

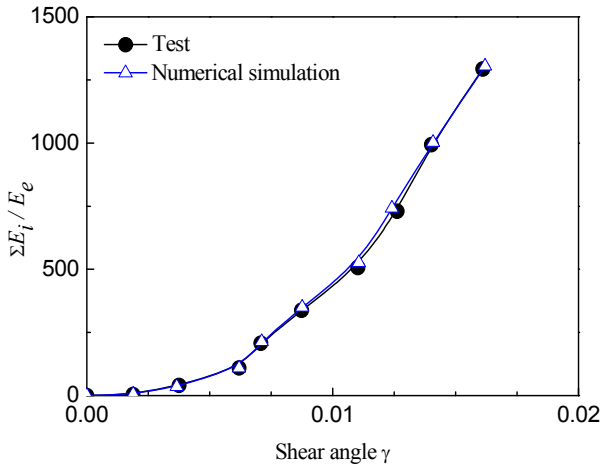

(b) Cumulative Energy Dissipation

Figure 5. Indoor Test versus Numerical Simulation of Specimen R_w03- z07

In the cases of z = 0.0, 0.3, and 0.5, and R_w = 0.4, the hysteresis curves are stable. Slight pinching, mainly due to web buckling, may be observed. However, pinching does not continue to develop under subsequent loading. Additionally, the average shear strength rises steadily until the end of loading.
In the cases of z = 0.5, and R_w = 0.2 and 0.3, hysteresis curves are well developed and no pinching phenomenon occurs. However, several unstable hysteretic loops can be seen clearly at the end of loading. This is because the axial compression ratio is relatively high, which leads to unstable numerical computation results.

Under high axial compression (z = 0.7), hysteresis curves show significant strength degradation and even abrupt failure. Herein, high axial compression has become the dominant factor controlling the hysteretic performance of SPDs. It is found that the maximum shear deformation angle is about 9γ_y; hereafter, apparent out-of-plane deflection reduces the shear strength rapidly, and consequently, the calculation did not converge and the loading system was terminated.

It is concluded from the prior loading process that when the axial load is relatively small (z = 0.0 or 0.3), its effect on the SPD under low cyclic loading action is rather limited. When the axial compression ratio is a mid-range value such as z = 0.5, the specimen (such as in the case of R_w = 0.2) has a hysteresis curve with evident fluctuations. This implies that relatively high axial compression has a certain effect on the shear bearing capacity of the SPD, which makes the SPD unstable. When the axial compression ratio is z = 0.7, the hysteresis curve changes from a full shape to a curve with an obvious pinch. The result is a deterioration of the shear strength and even termination of the loading process. Greatly reduced energy dissipation is strong evidence of the detrimental effect of high axial compression on the hysteretic behavior of SPDs. Therefore, in practical applications, the compression ratio should be limited within a rational range. In design and construction, a large axial force on the dampers should be avoided.

4.2 Maximum Shear Strength

The values of normalized maximum shear strength, τ_m/τ_y, are listed in Table 1. The table shows that, given the same axial compression ratio, the maximum shear strength increases with a decrease in the web slenderness (or an increase in the web thickness). This is because not only the web but also the flanges contribute to the total shear strength. The thicker the web, the larger the resisting areas of the flanges, and the larger the contribution to the total shear. However, τ_m is the average shear divided only by the area of the web. On the other hand, given the same web slenderness, peak values of shear strength decrease with an increasing axial compression ratio. This can be observed more directly from the envelope of the shear stress versus shear strain shown in Figure 7.

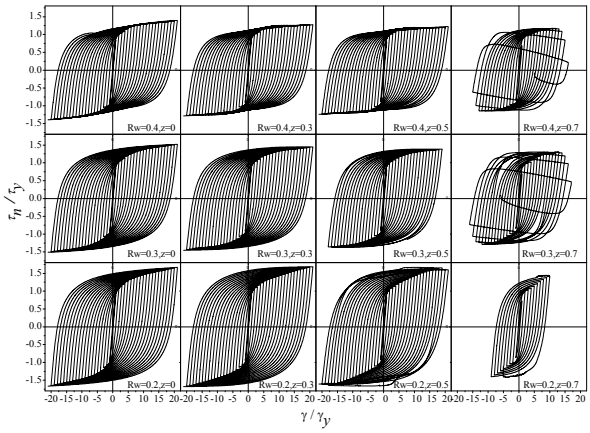

Figure 6. Shear Stress versus Shear Strain Hysteresis Curves

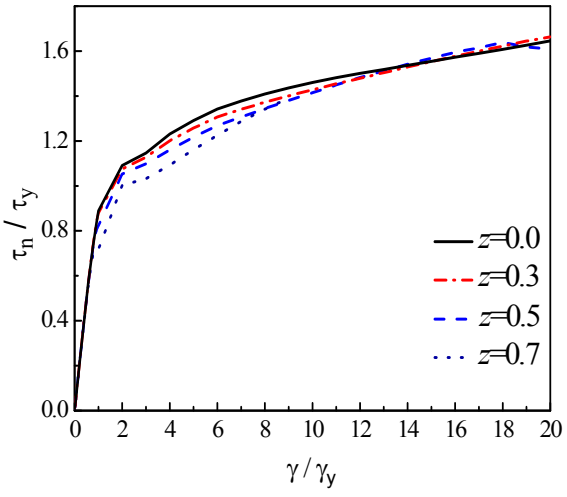

(a) R_w=0.2

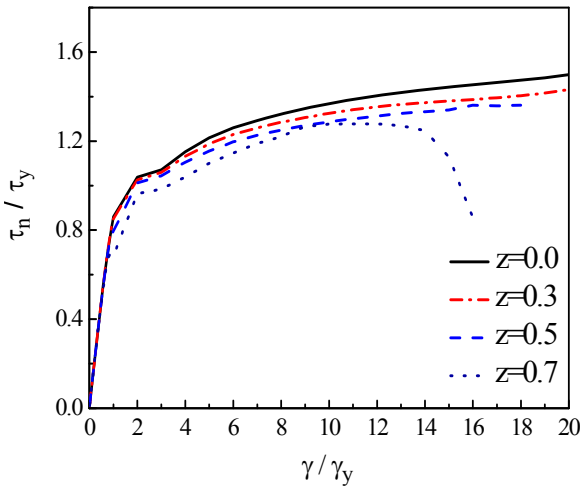

(b) R_w=0.3

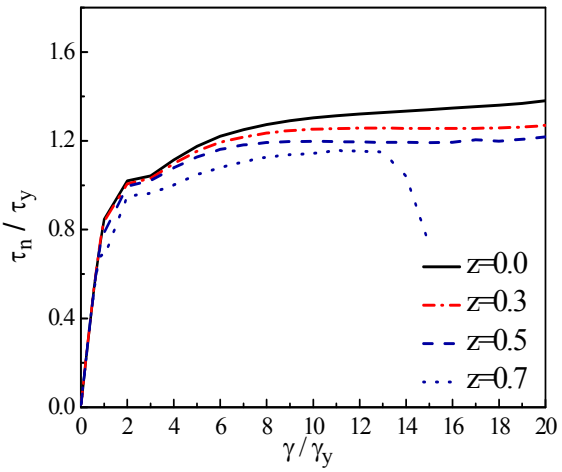

(c) R_w=0.4

Figure 7. Shear Stress versus Shear Strain Envelopes

Figure 7 shows skeletons of the hysteretic curves presented in Figure 6. The envelope curve is drawn by connecting the mean values of absolute values of shear stress that correspond to the maximum shear strain in each loading and unloading cycle. When the value of R_w falls within the range of 0.2–0.4, SPDs are prone to enter the plastic stage earlier with an increase in the axial compression ratio. In the case of R_w = 0.2, an increase in the axial compression ratio reduces the shear bearing capacity only in the initial stage of plastic deformation. In the subsequent large-deformation stage, the envelopes of the shear stress versus shear strain of the specimens are almost identical, except for the case of z = 0.7, in which the loading process is terminated suddenly. In the cases of R_w = 0.3 and 0.4, however, the increase of the axial compression ratio is accompanied by a gradual degradation of the shear bearing capacity.

When R_w varies in the range of 0.2–0.4 and the axial compression ratios are comparatively preferable (i.e., z = 0.0, 0.3, and 0.5), the skeleton curves ascend slowly as the shear deformation angle increases because of the strain hardening of mild steel. Shear bearing capacities of SPDs remain stable without deterioration. The shear bearing capacity at the moment loading ceases transpires as the maximum shear strength in the loading test. Meanwhile, under a high axial

compression ratio when z = 0.7 and R_w = 0.3 and 0.4, the maximum shear strength is $1.246\tau_y$ and $1.149\tau_y$, respectively, and the corresponding shear deformation angle is $14\gamma_y$ and $13\gamma_y$, respectively. There is a subsequent dramatic decrease in the shear bearing capacity and the situation continues until the specimens are destroyed. In the case of the specimen with a thicker web under the same high axial load (i.e., z = 0.7, R_w = 0.2), the envelope ceases unexpectedly at $9\gamma_y$ and the damper is damaged through brittle failure, similar to the case of concrete members. Previous laboratory experiments have revealed that the failure of the SPD specimens is primarily due to material fracture or large deformation of out-of-plain buckling. As stated before, fatigue failure (fracture) of steel material will not appear and may be ignored in simulations given the imposed shear deformation within $20\gamma_y$. Therefore, it could be concluded reasonably that the difficulty in convergence is due to out-of-plain buckling, which leads to the brittle failure of the specimen. Previous research has shown that under no axial compression and with the same web width condition, the lower the slenderness, the thicker the web and consequently, the larger the corresponding shear bearing capacity. However, under high axial compression, the hysteretic performances of SPDs deteriorate remarkably, as characterized by the brittle failure, apparently due to the combined hazards of the shear force and axial compression. Thus, low slenderness is not conducive to improving the bearing capacity and energy dissipation performance of SPDs when there is high axial compression.

4.3 Energy Dissipation Performance

Energy dissipation performance is one of the most important indicators for evaluating an SPD as an energy dissipation device. Dissipated energy for each hysteresis circle, E_i, is calculated in the manner illustrated in Figure 8. The cumulative dissipation energy $\sum E_i$ is then calculated and normalized by E_e (here $E_e = H_y\Delta_y/2$) to give the relationship versus cycle number, as shown in Figure 9.

When z = 0.0 and 0.3, $\sum E_i/E_e$ increases with a decrease in R_w. This is mainly because the area of metal, which goes into a plastic state, increases. When z = 0.5 or 0.7, there is no significant relation between the cumulative dissipation energy and the web slenderness. In fact, the high axial compression becomes the dominant factor controlling the energy dissipation performance of the SPDs.

On the other hand, from the aspect of the axial compression ratio, when R_w is comparatively large (i.e., R_w = 0.4 or 0.3), the cumulative dissipation energy drops slightly in the wake of an increasing axial compression ratio. When web slenderness R_w is relatively small (i.e., R_w = 0.2), the cumulative dissipation energy is amplified a little as the axial compression ratio increases from 0 to 0.5. This can be explained by the increasing web thickness, which makes it possible for a greater cross-section of metallic materials to enter the plastic energy dissipation stage. That is, enlarging the cross-section of an SPD to some extent benefits the resistance to the imposed axial compression. In general, SPDs have good shear bearing capacity and energy dissipation capacity when the axial compression ratio is less than or equal to 0.5. What should be noted, however, is that the hysteretic behavior degrades severely as the axial compression ratio reaches 0.7. Under this circumstance, the SPD goes into an unstable state and fails abruptly, even if the shear deformation is small. This leads to the dramatic deterioration of cumulative energy dissipation.

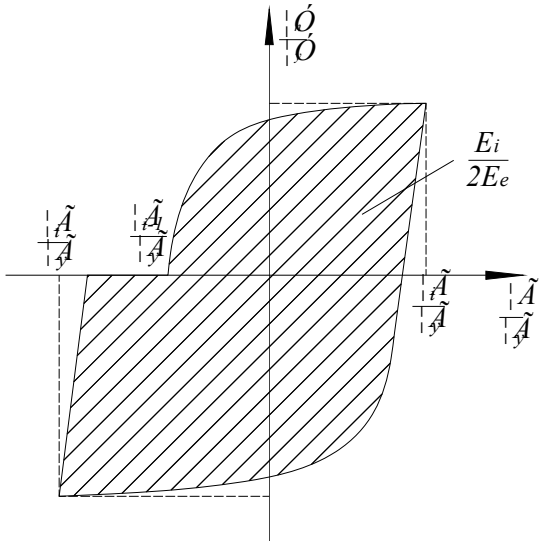

Figure 8. Schematic Diagram of Accumulated Energy

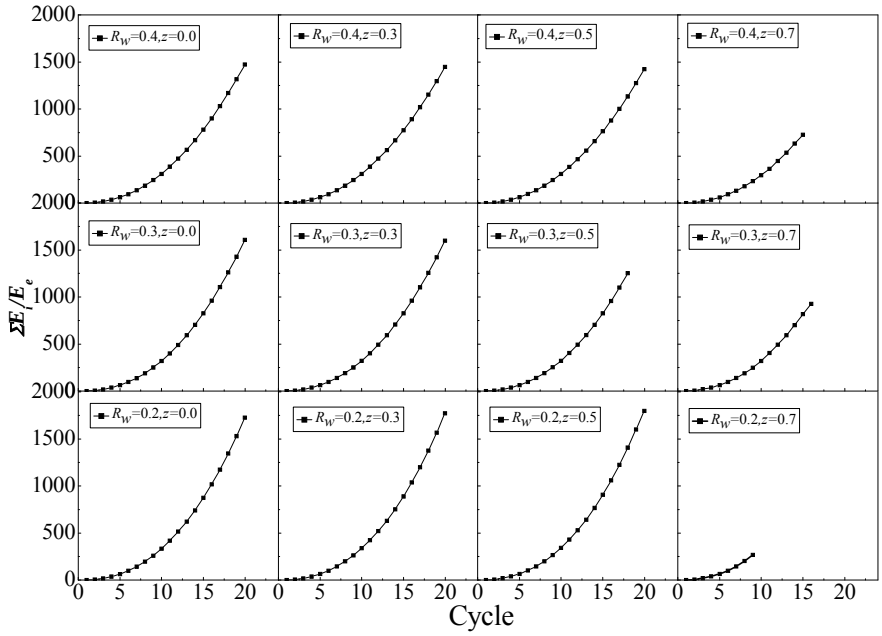

Figure 9. Cumulative Energy Dissipation

5. CONCLUSIONS

Extensive numerical analyses were conducted for stiffened SPDs under axial compression. The effects of the axial compression ratio and the web slenderness parameter on hysteretic behavior and energy dissipation performance were explored. The main findings were as follows:

1) Axial compression deteriorates the hysteretic behavior and energy dissipation performance of SPDs. Under relatively small axial compression ($z < 0.5$), negative impacts are negligible, whereas under high axial compression ($z = 0.7$), the ductility, shear bearing capacity, hysteresis, and energy dissipation of SPDs deteriorate remarkably.

2) The web slenderness parameter is a governing parameter for SPDs. Generally, a decrease in web slenderness benefits the shear strength and cumulative energy dissipation capacity under low and medium axial compression ratios, similar to cases without axial compression. However, in the case of high axial compression ratio, a small web slenderness parameter will lead to unexpected brittle failure (in the case of $z = 0.7$, $R_w = 0.2$). This is undesirable in the design of SPDs.

ACKNOWLEDGMENTS

This research was supported by the National Natural Science Foundation of China (Grant No. 51278524), the Program for Changjiang Scholars and Innovative Research Team in University (PCSIRT, IRT1029), and the State Key Laboratory of Disaster Reduction in Civil Engineering (SLDRCE12-MB-02). All supports are acknowledged gratefully.

REFERENCES

[1] Nakashima, M., "Strain-hardening Behavior of Shear Panels Made of Low-yield Steel.1: Test", Journal of Structural Engineering, 1995, Vol. 121, No. 12, pp. 1742-1749.

[2] Nakashima, M., Akazawa, T. and Tsuji, B., "Strain-hardening Behavior of Shear Panels Made of Low-yield Steel.2: Model", Journal of Structural Engineering, 1995, Vol. 121, No. 12, pp. 1750-1757.

[3] Chen, S.J. and Kuo, C.L., "Experimental Study of Vierendeel Frames With LYP Steel Shear Panels Steel Structures", Steel Structures, 2004, Vol. 4, pp. 179-186.

[4] Chen, Z.Y., Ge, H.B. and Usami T., "Study on Seismic Performance Upgrading for Steel Bridge Structures by Introducing Energy-dissipation Members", Journal of Structural Engineering, JSCE, 2007, Vol. 53, pp. 540-549.

[5] Chen, Z.Y., Bian, G.Q. and Huang, Y., "Hysteretic Behavior of Shear Panel Dampers under High Axial Compression Loading", Advanced Steel Construction, 2013, Vol. 9, No. 3, pp. 185-199.

[6] Ohta, Y., Kaneko, H., Kibayashi, M., Yamamoto, M., Muroya, T. and Nakane, K., "Study On Shear Panel Dampers Using Low Yield Strength Steel Applied To Reinforced Concrete Buildings", 13th World Conference on Earthquake Engineering, Vancouver, B.C., Canada, 2004, No. 2228.

[7] Galal, K.E. and Ghobarah, A., "Flexural and Shear Hysteretic Behavior of Reinforced Concrete Columns with Variable Axial Load", Engineering Structures, 2003, Vol. 25, No. 11, pp. 1353-1367.

[8] Gustavo, J.P.M., Bobet, A. and Ramirez, J., "Evaluation of Soil-structure Interaction and Structural Collapse in Daikai Subway Station during Kobe Earthquake", ACI Structural Journal, 2006, Vol. 103, No. 1, pp. 113-122.

[9] Huo, H., Bobet, A., Fernández, G. and Ramírez, J., "Load Transfer Mechanisms between Underground Structure and Surrounding Ground: Evaluation of the Failure of the Daikai Station", Journal of Geotechnical and Geoenvironmental Engineering, 2005, Vol. 131, No. 12, pp. 1522-1533.

[10] Sasaki, Y. and Tanaka, K., "Static Hysteretic Performance of Shear Panel Damper with Low Yield Strength Steel under Constant Axial loads", Journal of Fujita Technical Research Institute, 1999, No. 35, pp. 61-66.

[11] Nakashima, M., Iwai, S., Iwata, M., Takeuchi, T., Konomi, S., Akazawa, T. and Saburi, K., "Energy Dissipation Behavior of Shear Panels Made of Low Yield Steel", Earthquake Engineering and Structural Dynamics, 1994, Vol. 23, No. 12, pp. 1299-1313.

[12] GB/T 19879, “Steel Plates for Building Structure”, the People’s Republic of China State Administration of Quality Supervision, Inspection and Quarantine & China National Standardization Management Committee, Beijing: Standards Press of China, 2005.(in Chinese)
[13] Fukumoto, Y. ed., “Guidelines for Stability Design of Steel Structures”, Subcommittee on Stability Design, Committee on Steel Structures, Japan Society of Civil Engineers, Tokyo, Japan, 1987. (in Japanese)
[14] Alinia, M.M., Dastfan, M., “Cyclic Behavior, Deformability and Rigidity of Stiffened Steel Shear Panels”, Journal of Constructional Steel Research, 2007, Vol 63, No. 4, pp. 554-563.
[15] Chusilp, P. and Usami, T., “New Elastic Stability Formulas for Multiple-stiffened Shear Panels”, Journal of Structural Engineering, ASCE, 2002, Vol. 128, No. 6, pp. 833-836.
[16] Chen, Z.Y., Ge, H.B., Kasai, A. and Usami, T., “Numerical Study on Development of Hysteretic Model for Stiffened Steel Shear Panel Dampers”, Journal of Structural Engineering, JSCE, 2006, Vol. 52, pp. 573-582.
[17] Takahashi, Y. and Shinabe,Y., “Experimental Study on Restoring Force Characteristics of Shear Yielding Thin Steel Plate Elements”, Journal of Structural Engineering, AIJ, 1997, Vol. 494, pp. 107-114.
[18] DG/TJ08-2064-2009, “Code for Seismic Design of Subway Structures”, Shanghai Urban Constructions Communications, Shanghai, 2010. (in Chinese)
[19] Kasai, A., Watanabe, T., Amano, M. and Usami, T., “Strength and Ductility Evaluation of Stiffened Steel Plates Subjected to Cyclic Shear Loading”, Journal of Structural Engineering, 2001, Vol. 47, No.2, pp. 761-770.
[20] Usami T., Ge, H.B., “Strength Prediction of Thin-walled Plate Assemblies”, Journal of Structural Engineering, JSCE, 1996, Vol. 42, pp. 171-178.
[21] Shen, C., Mamaghani, I.H.P, Mizuno, E. and Usami, T., “Cyclic Behavior of Structural Steels. II: Theory”, Journal of Engineering Mechanics, 1995, Vol. 121, No. 11, pp. 1165-1172.
[22] Gao, S.B., Usami, T., and Ge, H.B., “Ductility evaluation of steel bridge piers with pipe sections”, Journal of Engineering Mechanics, ASCE, 1998, Vol. 124, No. 3, pp.260-267.
[23] Chusilp, P., Usami, T., Ge, H.B., Maeno, H., and Aoki, T., “Cyclic shear behavior of steel box girders: experiment and analysis”, Earthquake Engineering & Structural Dynamics, 2002, Vol. 31, No. 11, pp.1993-2014.
[24] Chusilp, P., “Seismic Design Methodology for Steel Bridge Structures with Shear-type Hysteric Dampers”, Thesis, presented to Nagoya University, Japan, in partial fulfillment of the requirements for the degree of Doctor of Engineering, 2002.

EXPERIMENTAL RESEARCHES OF A SUSPEN-DOME STRUCTURE WITH ROLLING CABLE-STRUT JOINTS

Chen Zhihua[1,2], Yan Renzhang[2], Wang Xiaodun[2], Liu Hongbo[1,2*] and Xiao Xiao[2]

[1] *State Key Laboratory of Hydraulic Engineering Simulation and Safety (Tianjin University), Tianjin 300072, China*
[2] *School of Civil Engineering, Tianjin University, Tianjin 300072, China*
**(Corresponding author: E-mail: hb_liu2008@163.com)*

Received: 28 April 2013; Revised: 13 October 2013; Accepted: 23 January 2014

ABSTRACT: Rolling cable-strut joints are applied in the suspen-dome structure to diminish the friction loss in the process of tensioning the cable and to guarantee the global stability of the structure. A 1:10 scaled-down model of the suspen-dome structure, which is adopted in Chiping Stadium, was built. Firstly, the prestressing optimization mathematical model of the suspen-dome structure was derived based on the principle of optimization of the finite element analysis software ANSYS, and the prestressing optimal design value of the 7 circles of cables were calculated using ANSYS. Secondly, tension test was conducted on the scaled-down model. Cable force values of each circle during the tension process were tested using the new cable force measurement device invented by the research group, namely the cable force measurement device based on clip anchorage connection. Then, full-span loading test and half-span loading test were conducted respectively on the suspen-dome structure exerting prestressing, and the displacement of the key nodes during the loading process were monitored using the new intelligent laser tracker, the measurement accuracy of which is 0.01mm. At last, A comparative analysis of the static performance of the suspen-dome structure and the single-layer reticulated shell without the tensegrity system was described in the paper. The static performance of the suspen-dome structure with rolling cable-strut joints was studied systematically. Experimental results indicate that the pretension of the outer circle of cable has the greatest influence on the suspen-dome structure, and pretensions of lower circles of cables influence each other, which, however, differs in terms of the influence degree according to relative locations of cables; the stress distribution of members in the upper part of the suspen-dome structure is similar to that of the single-layer reticulated shell under full span loads, which mainly shows compression in diagonal bars and circumferential bars near the inner ring and tension in bars near the outer ring. However, the maximum compressive stress and the maximum tensile stress of circumferential bars and the maximum defection of the suspen-dome structure were reduced by 15.0%, 43.7% and 51.5% respectively when compared with those of the single-layer reticulated shell. Therefore, due to the introduction of the tensegrity system in the supen-dome structure, the static performance of the suspen-dome structure is superior to that of the single-layer reticulated shell obviously.

Keywords: Rolling cable-strut joint, Suspen-dome, Tension test, Static test, Single-layer reticulated shell, Performance comparison

1. INTRODUCTION

The suspen-dome system is a new hybrid space structure, firstly proposed by Kawaguchi, et al. [1] of Hosei University in Japan in 1993, Kawaguchi. The suspen-dome structure is a self-balancing system that combines the single-layer reticulated shell and the tensegrity system together, thus solving problems of great horizontal thrust on supports and poor stability existing in the single-layer reticulated shell and difficulties in construction of the tensegrity system effectively. So far, experts and scholars have conducted a series of researches on several aspects of the suspen-dome system, including shape finding theory, optimization design, static and dynamic properties and construction control theory, Chen, et al. [2-3].

The advantage of the suspen-dome system is owing to the introduction of pretension in the lower part of the structure. Three methods are usually adopted in prestressing cables: stretching radial cables, jacking struts and stretching hoop cables. For the fact that there are much more radial cables and struts in the suspen-dome structure, more tensioning and jacking equipments would be needed when methods of stretching radial cables or jacking struts are adopted, and it is difficult to

synchronize all the equipments in the process of prestressing. Therefore, the method of stretching hoop cables is widely adopted in practice. Hoop cables are stretched circle by circle at tensioning points arranged symmetrically in each circle, and the pretension propagates through the cable-strut joints. Due to the friction between the cable and the joint, the cable force could not propagate in adjacent cable segments without loss, which results in unequal values of the pretension in different cable segments, known as the loss of prestress. The loss of prestress is common in engineering, and it affects the global stability of structures severely. Scholars and experts have conducted researches on the loss of prestress and feasible approaches in diminishing it, Liu, et al. [4-6].

Researchers from China Aeronautical Project & Design Institute and Beijing Building Construction Research Institute have conducted research on the loss of prestress of the suspen-dome for 2008 Beijing Olympic Badminton Stadium, Ge, et al. [7], and the approach of installing PTFE material in cable-strut joints was put forward in their studies. However, the approach was not effective to reduce the loss of prestress. The final measured results showed that the maximum prestress loss of each hoop cable was about 5% ~ 10%, and the total prestress loss reached to over 35%. Due to the relatively large prestress loss in the suspen-dome of the Badminton Stadium, internal forces of radial bars increase approximately 50%, and the axial force and the bending moment of bars in the single-layer shell increase approximately 50% and 20% respectively, and accordingly the global stability of the structure decreases approximately 15%. As a result, the prestress loss of the suspen-dome caused by cable-strut joints would lead to unevenly distributed internal forces and deformation of the single-layer shell, which affects the global stability of the suspen-dome structure greatly.

To solve the problem of great prestress loss of the suspen-dome structure in the process of stretching hoop cables, a new type of rolling cable-strut joint, as is shown in Figure 1, was proposed by Wu [8], in which a rolling wheel is installed in order to substitute rolling friction between the cable and the joint for sliding friction, and the simulation of the pre-stressing construction of suspen-dome when using this type of joint is putting forward, Chen, et al. [9-10]. Relevant researches on the rolling cable-strut joint show that the prestress loss could be reduced from 21.65% to 10.85% when new joints are adopted. The rolling cable-strut joint has been successfully applied in Chiping Stadium in Shandong Province of China.

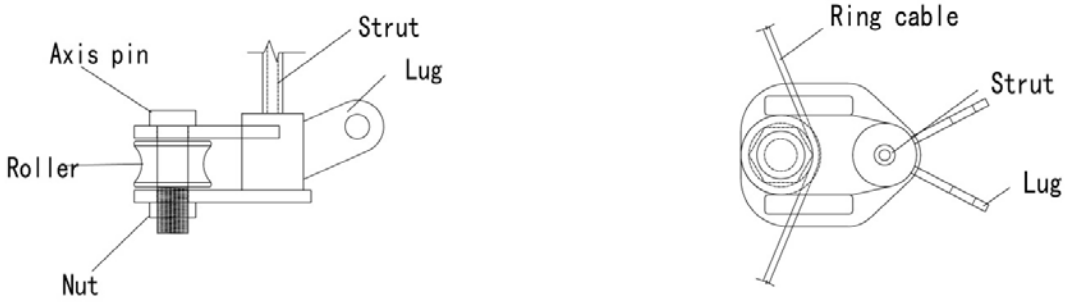

(a) Elevation drawing (b) Plan drawing

Figure 1. Model Drawing of the Sliding Cable-strut Joint

Researchers and scholars around the world have hitherto conducted several experimental researches on the suspen-dome system, including eight model tests and two full scale tests, Chen [2] and Nie, et al. [11]. However, most of the experiments are conducted to verify the designs or theoretical analysis of the suspen-dome structures. Few experiments focus on different mechanical properties of the suspen-dome and the single-layer reticulated shell. Only Kawaguchi carried out an experiment aiming at comparing mechanical properties of the suspen-dome structure with the corresponding single-layer reticulated shell in the suspen-dome system. In this paper, a 1:10

scaled-down model of the suspen-dome with rolling cable-strut joints applied in Chiping Stadium was used to study mechanical properties of the suspen-dome structure. A series of experiments, including the tension test, the full-span loading test and the half-span loading test, have conducted on the suspen-dome and the upper single-layer reticulated shell.

2. THE TEST MODEL

The suspen-dome system with an arch structure is adopted in the roof of Chiping Stadium, of which the span is 108m and the rise is 25.5m, as shown in Figure 2. The lamella single-layer reticulated shell is adopted in the upper part of the suspen-dome, and beneath the shell is the tensegrity system with seven circles of cables. Due to the fact that members of the suspen-dome are subjected to axial forces mainly, the test model was designed according to the consistency principle of axial stress, and the selected member specifications are listed in Table 1. Geometrical, physical and process similarities were taken into account in the design of the model, Yao and Liu [12]. The suspen-dome model was supported on two circles of platforms both consisting of an H-section ring beam and 12 columns, as shown in Figure 3. Columns of the inner ring and the outer ring are 1.45m and 2.3m high respectively. The rolling cable-strut joint adopted in the suspen-dome is shown in Figure 4.

Figure 2. Photo of Chiping Stadium

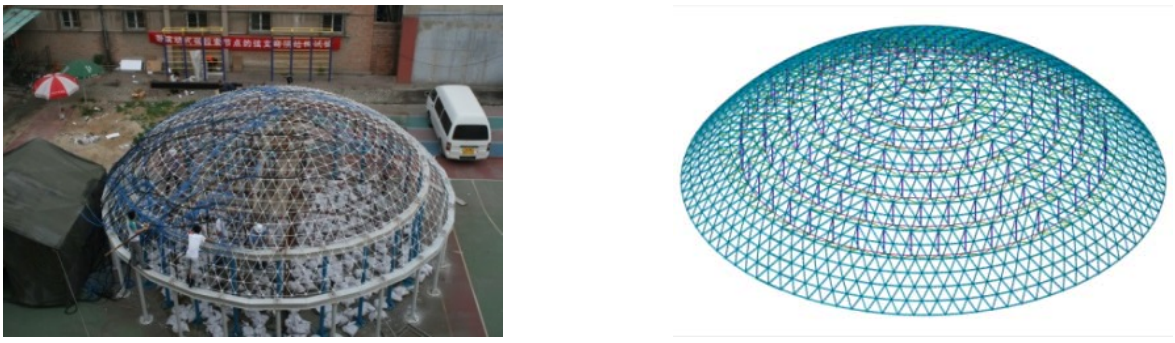

(a) Photo of the test model (b) 3D plot of the test model

Figure 3. Photo of the Experimental Model

Figure 4. Real Photo of the Sliding Cable-strut Joint

Table 1. Member Specifications of the 1:10 Scaled-down Model

Items	section of the prototype	section area (cm^2)	section of the model	section area (actual size/theoretical size) (cm^2)
single-layer reticulated shell	P203×6	37.130	P12×2.5	0.746 / 0.7426
	P219×7	46.620	P13×3	0.942 / 0.9324
	P245×7	52.340	P16×2.5	1.06 / 1.0468
	P273×8	66.600	P17×3	1.319 / 1.332
	P299×8	73.140	P19×3	1.508 / 1.463
the 6^{th} and 7^{th} hoop cables	Φ7×73	28.090	steel wire rope (Φ12)	0.5688 / 0.5618
1^{st} to 5^{th} hoop cables	Φ7×121	46.570	steel strand (1×7/Φ12.7)	0.987 / 0.9314
strut	P219×7	46.620	P13×3	0.942 / 0.9324
radial cable	Φ80	50.240	Φ11.5	1.039 / 1.0048

3. PRESTRESS OPTIMIZATION

An inappropriate value of prestress would not play a role in reducing the displacement of the upper shell or the thrust on supports and even have an adverse impact on the whole structure. Therefore, the designer should ensure a lower value of the prestress which satisfies all the requirements of the structure, Wang [13] and Zhang, et al. [14]. In this paper, the prestress optimization of the seven hoop cables in the tensegrity system is conducted by applying the OPT module of Ansys, with the optimization objective of minimizing the largest stress of bars in the upper shell. Three optimization variables namely design variable, state variable and objective function are used in the optimization module to describe the optimization process in ANSYS. The optimization method in ANSYS are mainly the zero-order method and the first-order method. The zero-order method is also called the direct method, the essence of which is to use the least square method to calculate the function sheets that fits the solution space and then calculate the extreme value of the function sheets. The first-order method is to use the state variable and the first-order partial derivative of the objective function to turn constraint problems into unconstraint problems through adding penalty functions to the objective function, and then searches the design space using objective function and the derivative of the optimization variable penalty function. In the optimization process, the cable force of the 7 circles of cables $[F_i](i=1,2,\ldots,7)$ at lower part are set to be the design variables, and the maximum vertical displacement of the structure $u_{z,max}$ is set to be the state variable, and the maximum stress of the bar on upper latticed shell σ_{max} is set to be the objective function. Since the objective function and state variable must be a function of the design variable, next, the Geometric

Nonlinear Theory of the suspen-dome structure will be introduced to derive the functional relations between the objective function and state variable or design variable.

Due to the introduction of the cable, which is a flexible member, the suspen-dome structure will have nonlinear problems. Thus, the effect on internal force caused by structural deformation should be considered in the finite element analysis of the structure, and the balance equation of the structure is established on the basis of subsequent deformation. Suspen-dome structure consists of upper single-layer reticulated shell and lower cable supported system. In the finite element analysis, beam elements are used to imitate the bars on the upper single-layer reticulated shell and truss elements are used to imitate the bars on the lower cable supported system. The element stiffness matrix of beam elements and truss elements are different from the traditional element elastic stiffness matrix because of the considering of geometric nonlinear effects. The following part will introduce the stiffness matrix of beam element and truss element in detail, and derived the relationship between design variable and state variable or objective function during the optimization of the prestressing.

3.1 Element Stiffness Matrix Considering the Geometric Nonlinearity

Define a local coordinate system, and the direction of its x axis is the same with the direction of the axis of the beam element. If a tiny displacement $u(x)$, $v(x)$, $w(x)$ occurs on any point of the element, then the length of the micro ds is expressed as Eq. 1, and the axial strain ε_x of the point on neutral axis of the beam element is expressed as Eq. 2.

$$ds = \sqrt{(dx+du)^2+(dv)^2+(dw)^2} = dx[1+\frac{du}{dx}+\frac{1}{2}(\frac{dv}{dx})^2+\frac{1}{2}(\frac{dw}{dx})^2] \tag{1}$$

$$\varepsilon_x = \frac{ds-dx}{dx} = \frac{ds}{dx}-1 = \frac{du}{dx}+\frac{1}{2}(\frac{dv}{dx})^2+\frac{1}{2}(\frac{dw}{dx})^2 \tag{2}$$

As Eq. 2 shows, the axial strain of the point on neutral axis consists of two parts, that is the strain along the x axis caused by axial deformation expressed as $\varepsilon_x^1 = \frac{du}{dx}$ and the additional strain on the neutral axis caused by the deflection of the beam element expressed as $\varepsilon_x^2 = \frac{1}{2}(\frac{dv}{dx})^2+\frac{1}{2}(\frac{dw}{dx})^2$. Additionally, bending strain will be caused on outer section of the neutral axis of the beam because of the lateral deflection of the beam along the y- direction and z-direction namely $v(x)$ and $w(x)$, and it can be expressed as $\varepsilon_x^3 = -z\frac{d^2w}{dx^2}-y\frac{d^2v}{dx^2}$ .Therefore, the strain of any point on the beam element consists of three parts, that are axial strain, additional strain and bending strain, and is expressed as Eq. 3. Without considering the effects of the beam torsion, the displacement vector composed by the displacements of both ends of the beam element node i and j can be expressed as $\delta^e = [u_i, u_j : v_i, \theta_{i,y}, w_i, \theta_{i,z}, v_j, \theta_{j,y}, w_j, \theta_{j,z}]^T$. Assume the axial displacement, deflexion and rotation are mutual independence at the same time, and then the shape function can be defined as Eq. 4

$$\varepsilon = \varepsilon_x^1+\varepsilon_x^2+\varepsilon_x^3 = \frac{du}{dx}+\left(\frac{1}{2}(\frac{dv}{dx})^2+\frac{1}{2}(\frac{dw}{dx})^2\right)+\left(-z\frac{d^2w}{dx^2}-y\frac{d^2v}{dx^2}\right) \tag{3}$$

$$\begin{bmatrix} u \\ v \\ w \end{bmatrix} = \begin{bmatrix} N_1 \\ N_2 \\ N_3 \end{bmatrix} \begin{bmatrix} u_i \\ u_j \\ v_i \\ \theta_{i,y} \\ w_i \\ \theta_{i,z} \\ v_j \\ \theta_{j,y} \\ w_j \\ \theta_{j,z} \end{bmatrix} = \begin{bmatrix} N_{11} & N_{12} & 0 & 0 & 0 & 0 & 0 & 0 & 0 & 0 \\ 0 & 0 & N_{21} & N_{22} & N_{23} & N_{24} & N_{25} & N_{26} & N_{27} & N_{28} \\ 0 & 0 & N_{31} & N_{32} & N_{33} & N_{34} & N_{35} & N_{36} & N_{37} & N_{38} \end{bmatrix} \begin{bmatrix} u_i \\ u_j \\ v_i \\ \theta_{i,y} \\ w_i \\ \theta_{i,z} \\ v_j \\ \theta_{j,y} \\ w_j \\ \theta_{j,z} \end{bmatrix} \tag{4}$$

And then,

$$\begin{cases} \dfrac{du}{dx} = [g_u]\{\delta^e\} & [g_u] = \left[\dfrac{dN_1}{dx}\right] = \left[\dfrac{dN_{11}}{dx} \quad \dfrac{dN_{12}}{dx} \quad 0 \quad \cdots \quad 0\right] \\ \dfrac{dv}{dx} = [g_v]\{\delta^e\} & [g_v] = \left[\dfrac{dN_2}{dx}\right] = \left[0 \quad 0 \quad \dfrac{dN_{21}}{dx} \quad \cdots \quad \dfrac{dN_{28}}{dx}\right] \\ \dfrac{dw}{dx} = [g_w]\{\delta^e\} & [g_w] = \left[\dfrac{dN_3}{dx}\right] = \left[0 \quad 0 \quad \dfrac{dN_{31}}{dx} \quad \cdots \quad \dfrac{dN_{38}}{dx}\right] \\ \dfrac{d^2v}{dx^2} = [B_v]\{\delta_2^e\} & [B_v] = \left[\dfrac{d^2N_2}{dx^2}\right] = \left[0 \quad 0 \quad \dfrac{d^2N_{21}}{dx^2} \quad \cdots \quad \dfrac{d^2N_{28}}{dx^2}\right] \\ \dfrac{d^2w}{dx^2} = [B_w]\{\delta_2^e\} & [B_w] = \left[\dfrac{d^2N_3}{dx^2}\right] = \left[0 \quad 0 \quad \dfrac{d^2N_{31}}{dx^2} \quad \cdots \quad \dfrac{d^2N_{38}}{dx^2}\right] \end{cases} \tag{5}$$

The strain of any point on the beam element only has the *x*- direction strain when the shear and torsional effects of the beam element are not considered, and so the strain energy of the beam element can be simplified as Eq. 6.

$$U = \frac{1}{2}\int \sigma\varepsilon d(Vol.) = \frac{1}{2}\int E\varepsilon^2 d(Vol.) \tag{6}$$

'*Vol.*' in Eq. 6 is the volume of the beam element.

Put Eq. 3 into Eq. 6, considering the section properties of the beam element ($\int_A dA = A$, $\int_A zdA = 0$, $\int_A ydA = 0$, $\int_A zydA = 0$, $\int_A z^2 dA = I_z$, $\int_A y^2 dA = I_y$, $F_x = E \cdot \dfrac{du}{dx}$), and ignore the fourth higher order terms, and then we can obtain Eq. 7 as follow.

$$U = \frac{1}{2}\int_l \{EA(\frac{du}{dx})^2 + EI_z(\frac{d^2w}{dx^2})^2 + EI_y(\frac{d^2v}{dx^2})^2 + F_x[(\frac{dw}{dx})^2 + (\frac{dv}{dx})^2]\}dx \tag{7}$$

Put Eq. 5 into Eq. 7, and we can obtain Eq. 8 as follow.

$$U = \{\delta^e\}^T \cdot \frac{1}{2}\int_A (EA[g_u]^T[g_u] + EI_z[B_w]^T[B_W] + EI_y[B_v]^T[B_v] + F_x[g_v + g_w]^T[g_v + g_w])dx \cdot \{\delta^e\} \tag{8}$$

The principle of virtual displacements can be expressed as follow.

$$U^* = \{(\delta^e)^*\}^T \{P\} \tag{9}$$

Where U^* is the virtual strain energy. Put Eq. 8 into Eq. 9, and we can obtain Eq. 10 as follow.

$$\{\delta^e\}^T \cdot \frac{1}{2}\int_A (EA[g_u]^T[g_u] + EI_z[B_w]^T[B_W] + EI_y[B_v]^T[B_v] + F_x[g_v + g_w]^T[g_v + g_w])dx \cdot \{\delta^e\} = \{(\delta^e)^*\}^T \{P\} \tag{10}$$

So the force P can be expressed as

$$P = \frac{1}{2}\int_A (EA[g_u]^T[g_u] + EI_z[B_w]^T[B_W] + EI_y[B_v]^T[B_v] + [g_v + g_w]^T F_x[g_v + g_w])dx \cdot \{\delta^e\} \tag{11}$$

Eq. 11 can be simplified as

$$P = (K_L + K_B + K_\sigma) \cdot \delta^e \tag{12}$$

Where K_L, K_B and K_σ are the axial stiffness, flexural stiffness and additional stress of the beam element, respectively, and they are defined as

$$\begin{cases} K_L = \frac{1}{2}\int_l [g_u]^T EA[g_u]dx \\ K_B = \frac{1}{2}\int_l ([B_w]^T EI_z[B_w] + [B_v]^T EI_y[B_v])dx \\ K_\sigma = \frac{1}{2}\int_l [g_v + g_w]^T F_x[g_v + g_w]dx \end{cases} \tag{13}$$

It can be seen from Eq. 13 that K_σ and F_x are related, that is to say, K_σ is a function of F_x as follow.

$$K_\sigma = f(F_x) \tag{14}$$

Where F_x is the initial axial internal force. Then the element stiffness matrix of the beam element can be described as

$$K^e = K_L + K_B + f(F_x) = g_B(F_x) \tag{15}$$

In a similar way, element stiffness of the spatial truss element considering geometric nonlinearity can be obtained when the bending stiffness of the beam element is ignored, and it can be described as

$$K^e = K_L + f(F_x) = g_L(F_x) \tag{16}$$

3.2 Structural Assembly Analysis

Suspen-dome structure is formed by a series of beam elements and truss elements. The global stiffness matrix of the structure is formed by element stiffness matrixs of each element. The spatial position of each elements and geometry and topology relations between them should be considered when assembling the global stiffness matrix. Deformation compatibility conditions and equilibrium conditions of the internal and external forces on the node should also be taken into consideration. It can be seen from Eq. 15 and Eq. 16 that an initial stress stiffness matrix K_σ that forming the element stiffness matrix is related to the initial internal force of the bars. So, the global stiffness matrix assembled by element stiffness matrixs is definitely the function of the internal force $\{F_{x,i}\}$ of each bar. And that is to say, when any of the internal forces of the bars in the structure change, the global stiffness matrix of the structure will change. For the overall structure, $\{P\}$ can be described as

$$\{P\} = [K]\{\delta\} = [K_L + K_\sigma(\{F_{x,i}\})] \cdot \{\delta\} \tag{17}$$

Where $[K_L]$ and $[K_\sigma]$ are elastic stiffness matrix of the structure and initial stress stiffness matrix (geometric stiffness matrix) of the structure, respectively, and $K_\sigma(\{F_{x,i}\})$ indicate that the initial stress stiffness matrix changes along with the change of axial force of each bar in the structure.

The overall displacement vector $\{\delta\}$ of each node in the structure can be derived based on Eq. 17, and it can be described as

$$\{\delta\} = [K_L + K_\sigma(\{F_{x,i}\})]^{-1} \cdot \{P\} \tag{18}$$

The stress vector of each bar can be derived based on the displacement vector of the structure, and it can be described as

$$\{\sigma\} = S\{\delta\} \tag{19}$$

Where S is the stress stiffness matrix of the structure. Put Eq. 18 into Eq. 19, and we can obtain Eq. 20 as follow

$$\{\sigma\} = S[K_L + K_\sigma(\{F_{x,i}\})]^{-1}\{P\} \tag{20}$$

3.3 Optimization Mathematical Model

(1) Design variable

In the process of tension test of the suspen-dome structure, prestressing was exerted by screwing the bolts at the tensioning device which can shorten the effective length of the cable. In the process of calculating by ANSYS, prestressing is exerted by imposing on the cables with initial strain. In order to ensure the cable not to be slack or destroyed in the tensioning process, the limit of the cables' internal forces are set for 7 circles of cables, that is $0 \le F_{c,x,i} \le 100kN$ （i=1，2，…，7）.

(2) State variable

According to the *Tianjin technical specification for spatial grid structures*, the maximum displacement of the single-layer latticed shell is span/400. Therefore, the maximum vertical nodal displacement of the upper shell is set as the state variable in this study. Pick up the vertical displacement component $\{u_z\}$ of each node from the nodal displacement vector of the structural computation. It can be seen that

$$\{\delta\} = \{\cdots \ \vdots \ u_{x,i} \quad \theta_{x,i} \quad u_{y,i} \quad \theta_{y,i} \quad u_{z,i} \quad \theta_{z,i} \ \vdots \ \cdots\}^T \tag{21}$$

And

$$\{u_z\} = [Z]\{\delta\} \tag{22}$$

Where

$$[Z] = \begin{bmatrix} z & 0 & \cdots & 0 \\ 0 & z & \cdots & 0 \\ & & \ddots & \\ 0 & 0 & \cdots & z \end{bmatrix} \tag{23}$$

Where $z = [0, 0, 0, 0, 1, 0]$

$$u_{z,\max} = \max\{u_z\} \tag{24}$$

Put Eq. 18, Eq. 22 and Eq. 23 into Eq. 24, and then state variable can be expressed as Eq. 25.

$$u_{z,\max} = \max([Z][K_L + K_\sigma(\{F_{x,i}\})]^{-1}\{P\}) \tag{25}$$

(3) Objective function

The minimum value of the maximum stress of the bars on upper shell is made as the objective function as follow

$$\sigma_{\max} = \max\{\sigma\} \tag{26}$$

Put Eq. 20 into Eq. 26, and we can obtain Eq. 27 as follow

$$\sigma_{\max} = \max(S[K_L + K_\sigma(\{F_{x,i}\})]^{-1}\{P\}) \tag{27}$$

It can be seen from Eq. 25 and Eq. 27 that state variable and objective function are both the function of internal force vector of each bar in the structure. In the suspen-dome structure, internal forces of some members are changed when prestressing is exerted on the 7 circles of cables, that is to say, internal force vector of the 7 circles of cables is the sub-array of the internal force vector of the bars in the structure and it can be expressed as

$$\{F_{c,x,i.i=1,2,\ldots,7}\} \subseteq \{F_{x,i}\} \tag{28}$$

And the optimization mathematical model of the suspen-dome structure can be expressed as follow.

$$\begin{cases} \min f(F_{c,x}) = \sigma_{\max} = \max(S[K_L + K_\sigma(\{F_{c,x}\})]^{-1}\{P\}) \\ F_{c,x} = \{F_{c,x,1} \quad F_{c,x,2} \quad \cdots \quad F_{c,x,7}\} \\ s.t. 0 \le F_{c,x,i} \le 100kN, i = 1,2,\cdots,7 \\ u_{z,\max} \le span/400 = 27mm \end{cases} \tag{29}$$

3.4 Optimization Results of the Cable Forces

The optimization methods in Ansys mainly include the zero-order method and the first-order method, which could be combined to obtain a reasonable solution for the prestress optimization, Huang [15] and Liu, et al [16]. In this paper, two groups of initial optimal prestress were obtained with the zero-method and the random search method respectively, and then the first-order method was applied further in estimating more optimal values of both the two groups of prestress. The final results turned out to be approximately the same, verifying the reliability of the optimal result. Detailed data obtained by the two methods is listed in Table 2.

Table 2. Optimal Results for the Test Model

method	Zero-order method	Zero-order + first-order	Random method	Radom + first-order
Load case	Gravity and Full-span loading (100kg/point)			
F_7（N）	532.35	212.65	1397	300
F_6（N）	1086.9	498.64	4129.3	1772.68
F_5（N）	1059.0	958.85	6672.3	1603.8
F_4（N）	2946.2	1723.2	7079.4	1998.2
F_3（N）	10109	2396.0	12763	2472.7
F_2（N）	5482.3	3434.9	10443	5041.4
F_1（N）	19750	14230	8832.1	11511
$U_{z,max}$（mm）	3.8617	2.0223	3.321	1.5215
σ_{max}（MPa）	80.795	43.630	93.482	44.778

The data in Table 2 shows that the result obtained by the zero-order method satisfies the requirements of the engineering well, which is not improved obviously by further optimization with the first-order method. In addition, there exists large difference between the result obtained by the random search method and the final optimal result, indicating that it is necessary to conduct a further optimization with the first-order method based on the result obtained by the random search method. The optimal prestress obtained by the random search method combined with the first-order method was adopted in the tests.

4. TEST MEASUREMENT

4.1 Stress Measurement

In order to make a contrast of the static properties of the suspen-dome and the corresponding single-layer reticulated shell, both the full-span loading and the half-span loading tests of the upper single-layer reticulated shell had been carried out before the tension test and the static test of the suspen-dome. A total number of 80 measuring points were arranged in the shell, as shown in Figure 5.

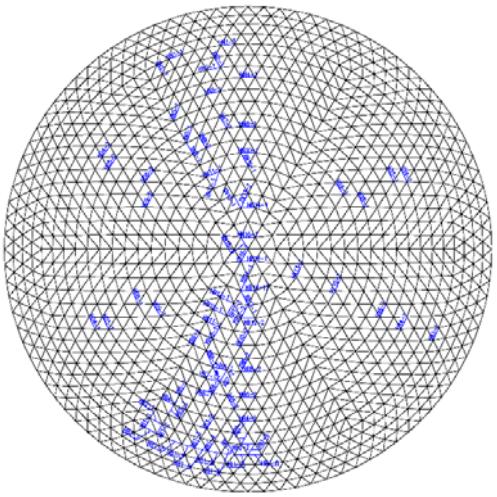

Figure 5. Arrangement of Measuring points on the upper shell

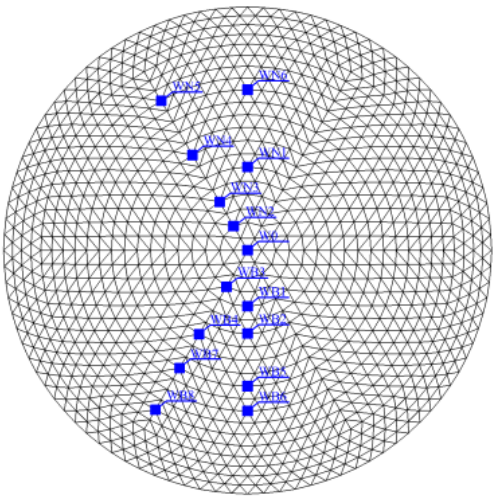

Figure 9. Arrangement of Displacement Measuring Points

4.2 Cable Force Measurement

Measuring points of the tensegrity system were arranged as is shown in Figure 6 and Figure 7, including 49 measuring points on radial tension bars, 22 on struts and 60 on hoop cables. The strain foils on radial tension bars and struts were arranged in the same way with those on the upper shell. Each radial bar or strut, where measuring points were arranged, had two strain foils which were arranged symmetrically along the axis of the member and connected to the strain gauge with the full-bridge method. Due to the fact that hoop cables were comprised of wire strands or wire ropes and hence strain foils could not attached on the surface of the cable directly, a new type of device connecting cables, firstly proposed by the author's group, was adopted in the test to measure the cable force, Chen, et al. [17], as shown in Figure 8. When the cable was stretched, the cable would be anchored by the two clamps in the device. The cable force could be obtained by calculation with the strain values measured by the strain foils arranged on the two sides of the device.

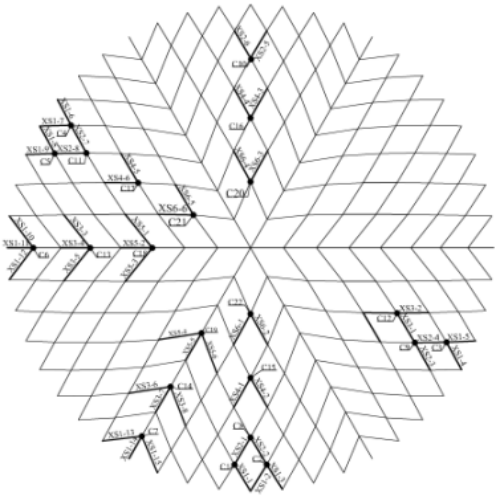

Figure 6. Arrangement of Measuring Points on the Radial Tension Bars

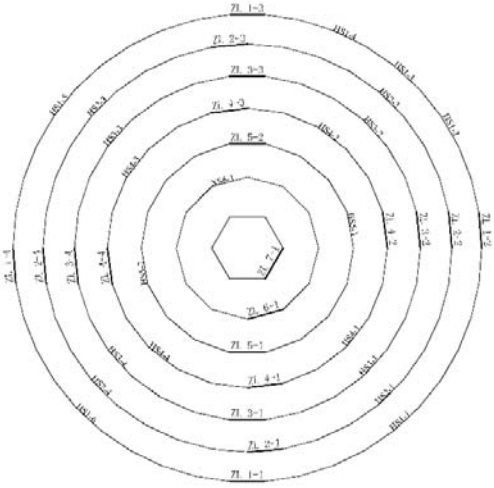

Figure 7. Arrangement of Measuring Points and Tension Points on the Hoop Cables

Figure 8. Device for Measuring Cable Force

4.3 Displacement Measurement

A total number of 15 displacement measuring points were arranged in the test, as shown in Figure 9. A laser tracker, comprised of a total station with a tracking detector, a computer and a target ball, was applied in tests to obtain the displacements of measuring points which were slight values. The laser beam emitted by the tracking detector together with the rotating mirror and the rotation axis formed the three axes in the spherical coordinate system. The displacements of measuring points at adjacent time point could be obtained by converting from space coordinates of each point measured by the laser tracker. The measurement precision of the laser tracker reaches to 0.01mm, satisfying the requirement of tests well. Figure 12 shows the scene of displacement measurement with the laser tracker.

Figure 10.
Tracking Detector

Figure 11. Target Ball

Figure 12. The Scene of Displacement Measurement with the Laser Tracker

5. TENSION TEST

5.1 Test Preparation

Hoop cables were stretched from the outer ring to the inner ring in two steps. From the 1st circle to the 4th circle of the cable, four tensioning points were arranged respectively, and two tensioning points for the 5th circle and one for the 6th and the 7th circle of the cable respectively. The arrangement of tensioning points is shown in Figure 7, and the control values of each circle are listed in Table 3. Tensioning devices, comprised of a pair of channels and bolt bars shown in Figure 13, were installed at tensioning points considering that the maximum designed prestress in the model was only 11.1 kN. The hoop cable was fixed with anchors in the device, and the prestress was applied by tightening the bolts on the two sides of the device. The value of prestress was

controlled by internal forces in the adjacent cable segments on the two sides of the device. The prestress of each tensioning point was applied at the same time, and the speed of screwing the bolts of each tensioning device should be as identical as possible to ensure the synchronization of applying the prestress. The cable force at each tensioning point was read and recorded by computer every five threads screwed with an interval of 2 minutes. Figure 14 shows the scene of the tension test, and control values of prestress in each step are listed in Table 3.

Table 3. Prestressing Level of Hoop Cables

level	1st circle	2nd circle	3rd circle	4th circle	5th circle	6th circle	7th circle
1st level (N)	4950	2220	1270	945	495	370	100
2nd level (N)	11500	5040	2470	2000	1600	1770	300

Figure 13. Tensioning Device

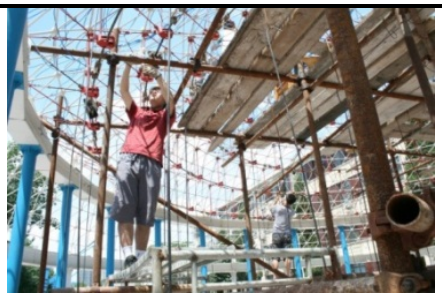

(a) Scene1

(b) Scene 2

Figure 14. The Scene of the Tension Test

5.2 Results of the Tension Test

(1) Internal forces of hoop cables

The mean of internal forces of cable segments on the two sides of the tensioning point was taken as the value of pretension at the point, considering the difference between the measured cable force at the tensioning point and the designed control value due to inevitable disturbance to cables during tensioning process. The actual value of each point is shown in Figure 15. The pretension in a circle of cable would have a great influence on the internal force of the next circle of cable. The curves in Figure 16 show the changes of internal forces of the 1st, 2nd, 3rd and 4th circle of the cable in the process of prestressing respectively. Though the internal forces at different tensioning points in the cable differ due to the friction existing between the cable and joints, the change trends of internal forces are the same, that is, internal forces of the cable would increase due to the pretension of subsequent circles of cables, and the pretension of the adjacent circles of cables would have the greatest influence on each other. For example, the internal forces of the 1st circle of cable would increase more when stretching the 2nd circle of cable, while the pretension of the 3rd ~ 7th circles of cables would have a slight influence on the internal forces of the 1st circle of cable. In the first step of pretension, the increase of internal forces of the 1st circle of cable ranges from 7.2% to 12.16% with the largest increase appearing at the point HS1-6 in the process of stretching the 2nd circle of cable; internal forces of the 2nd circle of cable increase approximately 10% with the maximum increase of 11.75% in the process of stretching the 3rd circle of cable. In the second step of pretension, the pretension of the 1st circle of cable would have a significant influence on internal forces of subsequence circles of cables. When the pretension of the 1st circle of cable reaches to the designed value, internal forces of the 2nd , 3rd and 4th circles of cables increase 44.51%~65.32%, 14.46%~22.02% and 2.86%~10.97% respectively, and a significant increase of internal forces also occurs in other circles of cables. Hence, the outmost circle (i.e. the 1st circle) of hoop cable would have the most significant influence on mechanical properties of the suspen-dome.

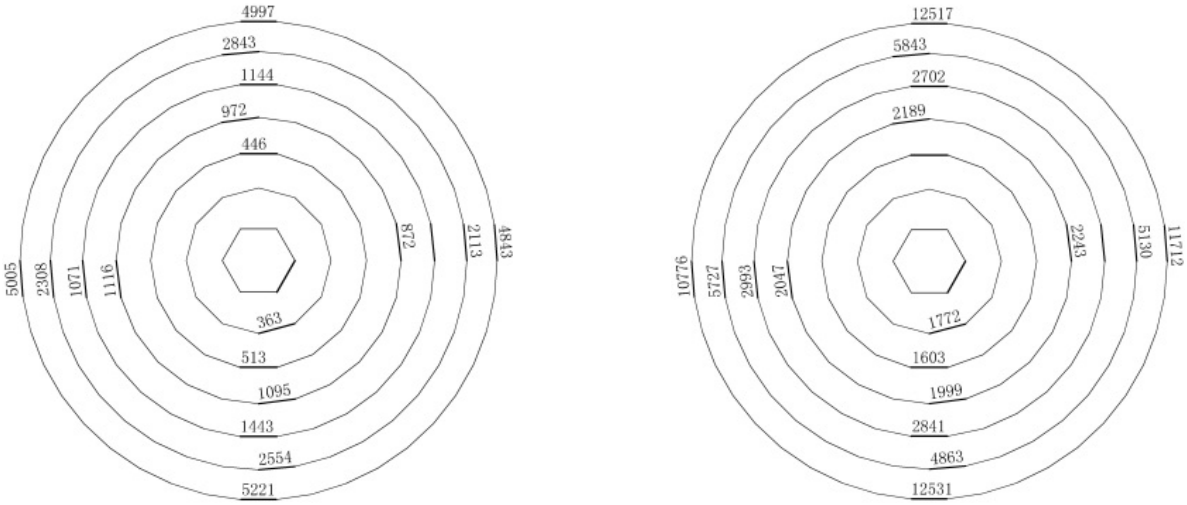

(a) Actual control values in the first step of pretension

(b) Actual control values in the second step of pretension

Figure 15. Actual Control Values of Cables (Unit: N)

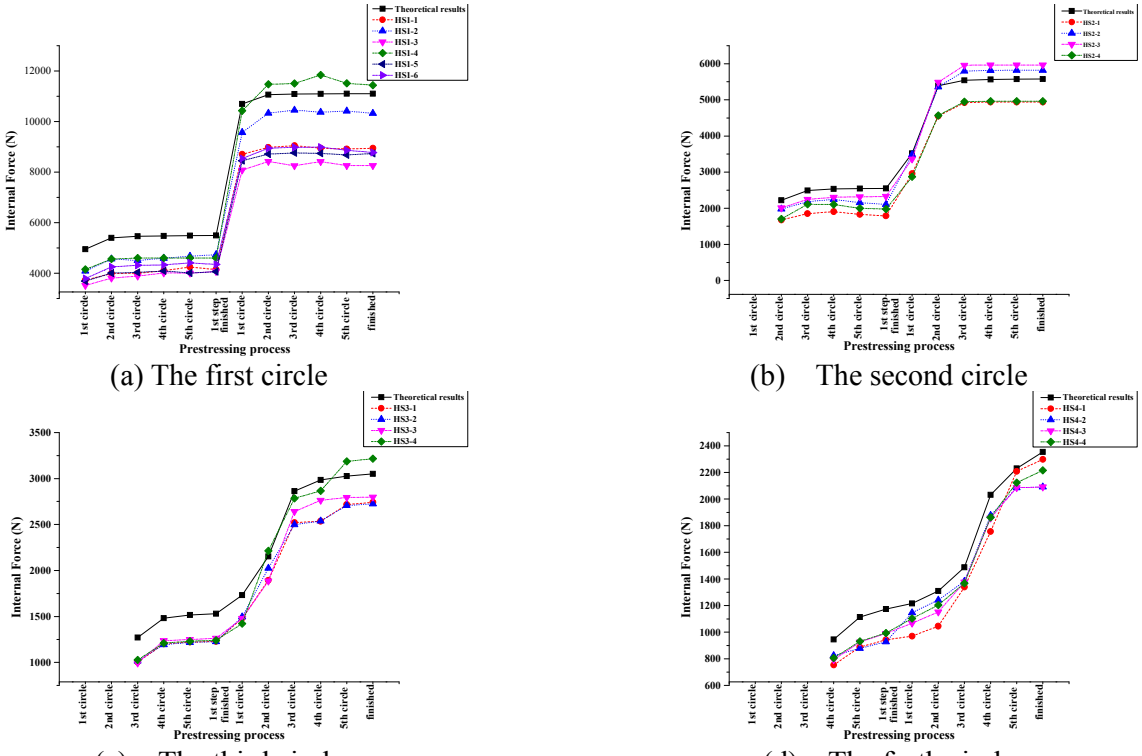

(a) The first circle

(b) The second circle

(c) The third circle

(d) The forth circle

Figure 16. Change Curves of the Cables' Internal Force in the Process of Prestressing

(2) Internal forces of radial tension members

The internal forces of radial tension members measured in the test, which are small values for all the circles except the 1st circle, fluctuate greatly due to the large disturbance to the members in the process of prestressing. In this paper, only the internal forces of the 1st circle of radial tension members are involved in the analysis owing to the space reasons. Curves in Figure 17 show the changes of internal forces of the 1st circle of cable in the process of prestressing. It is indicated that the change law of internal forces of radial tension members is similar to that of hoop cables. One reasonable interpretation for this is that the change of internal forces of hoop cables would affect

internal forces of radial members directly, because internal forces of radial tension members are generated due to the pretension in hoop cables. In addition, internal forces of radial tension members fluctuate in the process of prestressing due to the influence of pretension of subsequent circles of cables.

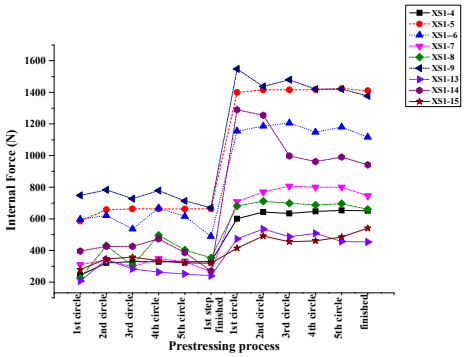

Figure 17. Change Curves of Internal Forces of Radial Tension Bars in the Process of Prestressing

(3) Stresses of bars in the upper shell

Axial stresses of bars in the upper shell are small in the process of prestressing, most of which are less than 10 MPa. Curves in Figure 18 show the changes of axial stresses of circumferential members HB1-1 and HB1-7 in the tensioning process. It is indicated in Figure 18 that the pretension of the 1st circle of hoop cable affects internal forces of bars in the upper shell significantly, while the pretension of the 2nd circle of cable results in a slight increase of internal forces of bars in the shell above the 1st circle of hoop cable and the influence of pretension of other circles of cables could be neglected.

In addition, internal forces of the bar HB1-1 and HB1-7 in the suspen-dome were compressive with the pretension of the 1st circle of hoop cable, which, however, turns out to be tensile in the corresponding single-layer reticulated shell when hoop cables were removed in the structure. It indicates that the structural responses of the suspendome under the loads on the shell could be counterbalanced by the pretension in cables.

(4) Mid-span vertical displacement

Curves in Figure 19 show the changes of the vertical displacement of the mid-span of the upper shell and the largest displacement in the tensioning process. It is obvious from Figure 19 that the mid-span vertical displacement remains relatively small in the tensioning process due to the arching effect caused by the pretension of cables.

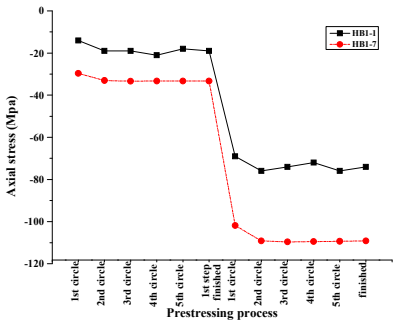

Figure 18. Change Curves of Stresses of Part of Members in the Tensioning Process

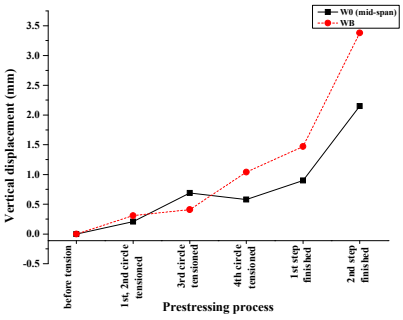

Figure 19. Change Curves of the Vertical Displacement in the Tensioning Process

6. STATIC LOADING TEST OF THE SUSPEN-DOME

Both the full-span loading test and the half-span loading test were carried out to investigate the static performance of the suspen-dome, Guo, et al. [18]. In order to avoid the cable sliding after the tensioning process, Liu, et al. [19], a pair of U-Shaped locks shown in Figure 20 was installed on the two sides of the rolling cable-strut joint to tighten up the cable with the bottom plate of the joint. With the purpose of making a contrast with the results of the single-layer shell, the loading scheme of the test was the same with that of the single-layer shell, Yan, et al. [20]: 80 loading points were selected in the upper shell; the loading process was divided into five steps with 0.2kN per point in each step; the unloading process was divided into three steps with 0.4kN per point in step 1 and 2 and 0.2kN per point in step3. The arrangements of loading points in the full-span loading test and the half-span loading test are shown in Figure 21. A pre-loading test was conducted in three steps before the loading test. Figure 22 shows the scene of the loading test.

Figure 20. U-shaped Locks to avoid Cable Sliding through the Joint

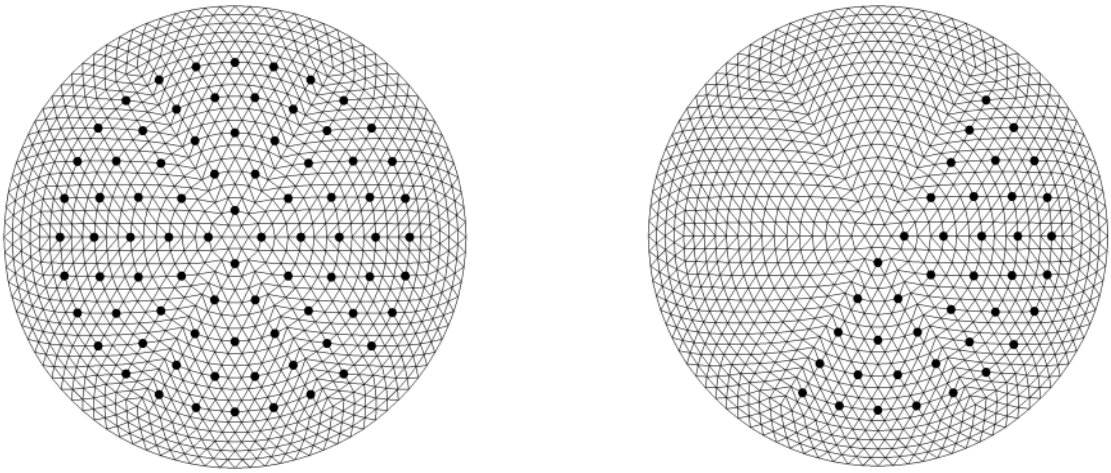

(a) Loading points in the full-span loading test (b) Loading Points in the Half-span Loading Test

Figure 21. Arrangement of Loading Points

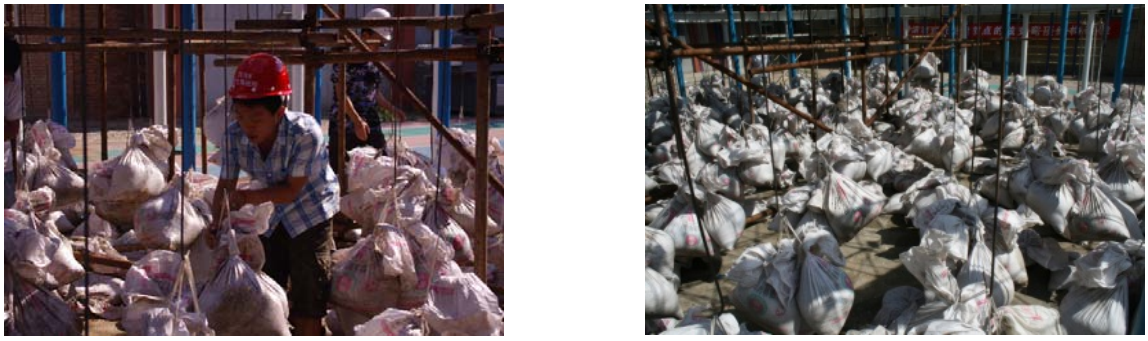

Figure 22. The Scene of Loading

6.1 The Full-span Loading Test

(1) Internal forces of hoop cables
Curves in Figure 23 show the changes of internal forces of hoop cables in the prestressing process. It is indicated in Figure 23 that internal forces of hoop cables increase linearly with the increase of loads; the internal force of the 1st circle of cable, which is 10023 N when the prestressing process is completed, increases 5103 N with an approximately increase of 50.9%; the internal force of the 5th circle of cable, which is 1591 N when the prestressing process is completed, decreases 784.5 N with an reduction of 49.3%; the changes of internal forces of the 2nd ~ 4th circles of cables are small. A reasonable interpretation for this result is that the force distribution ratio in hoop cables in outer rings would be greater due to the possible slackness of cables in inner rings caused by the deformation of the suspen-dome under the loading.

(2) Internal forces of radial tension bars
Internal forces of radial tension bars, which are generated directly due to the pretension of hoop cables, would be affected by the changes of internal forces of hoop cables. The change law of internal forces of radial members is the same with that of hoop cables. Internal forces of the outmost circle (i.e. the 1st circle) of radial members change largely, while the amplitude of variation of internal forces of those close to the inner ring decreases gradually. Curves in Figure 24 show the changes of internal forces of some typical radial tension bars. It is indicated from Figure 24 that the internal force of the 1st circle of radial tension bars, which is 1027 N when the prestressing process is completed, increases 865.3 N with an increase of 84%; while the internal force of radial tension bars close to the inner ring, which is 114 N when the prestressing process is completed, decreases 103.4 N.

The relationship of internal forces of radial tension bars and the applied loads is linear, similar to that of hoop cables. Internal forces of the tensegrity system close to the outer ring increase significantly, while internal forces of the system close to the inner ring turn out to be a reduction and even slackness of cables.

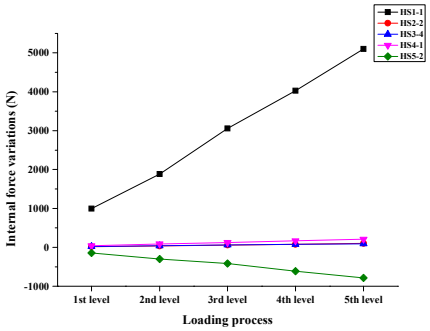

Figure 23. Change Curves of the Hoop Cables' Internal Force Variations in the Process of Loading

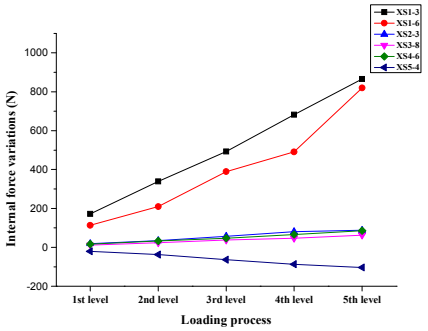

Figure 24. Change Curves of the Radial Bars' Internal Force Variations in the Process of Loading

(3) Stresses of bars in the upper shell
Diagonal bars in the upper shell are mainly subjected to compression under the full-span loading. The largest stress of diagonal bars occurs at XB14-1 near the mid-span, reaching to -61 MPa; relative large stresses of diagonal bars also occur in the 3rd ~ 5th and the 10th circle. For the reason that bars of the upper shell are in tension basically in the prestressing process, the actual stress values of diagonal bars in the upper shell would be less than the values obtained in the loading test. Change curves of stresses of diagonal bars are shown in Figure 25 (a) ~ (b), and the stress distribution of diagonal bars in the fifth step loading is shown in Figure 26.

Under the full-span loading, circumferential bars close to the inner ring are mainly subjected to compression, while those near the outer ring are mainly in tension. The stress distribution of circumferential bars is shown in Figure 27. It is indicated in Figure 27 that the tensile stresses of circumferential bars near the supports are relatively high, with the maximum stress of 40.3 MPa in the bar HB1-5; while circumferential bars near the 12th circle of cable are subjected to relatively high compression, with the maximum compressive stress of -38.4 MPa. Change curves of stresses of some circumferential bars in the loading process are shown in Figure 25 (e) ~ (f).

Though the change trend of stresses obtained in the test is similar to that obtained by FEM analysis, experimental values are greater than theoretical values. The main reason for this is that sectional areas of rusted bars are decreased due to the fact that the model was placed in outdoors and no corrosion protection was adopted previous. In addition, inevitable installation errors would result in greater experimental results.

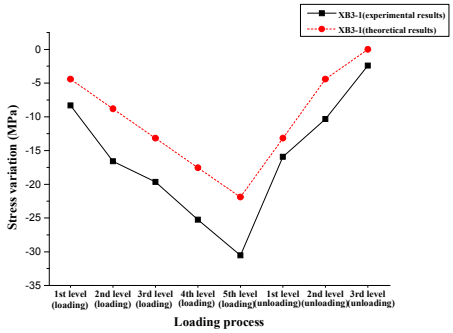

(a) diagonal bar XB3-1

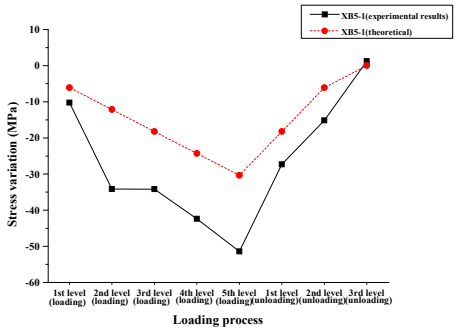

(b) diagonal bar XB5-1

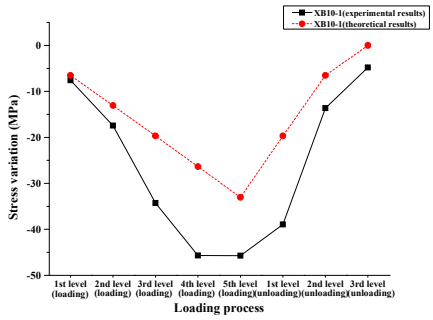

(c) diagonal bar XB10-1

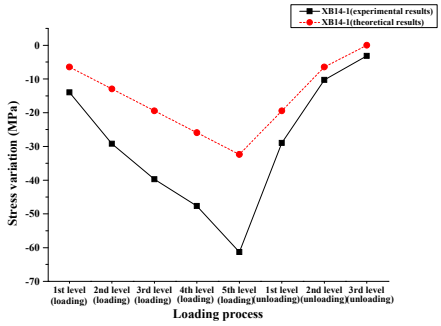

(d) diagonal bar XB14-1

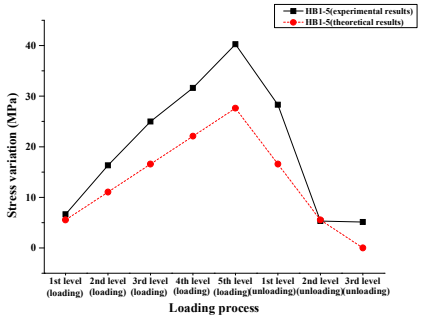

(e) circumferential bar HB1-5

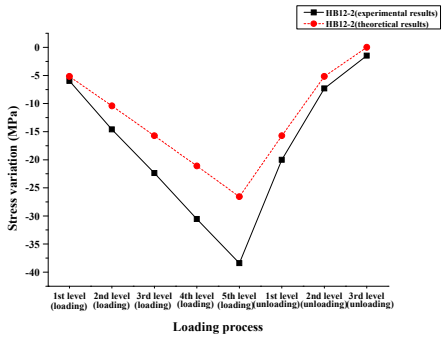

(f) circumferential bar HB12-2

Figure 25. Change Curves of Stresses of Some Typical Bars of the Upper Shell in the Prestressing Process

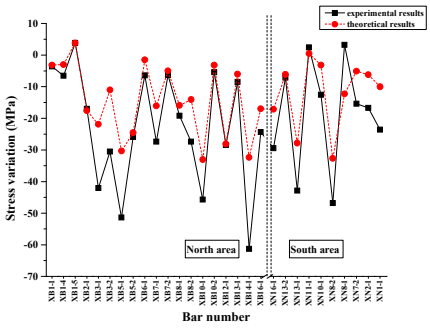

Figure 26. Stress Distribution of Diagonal Bars

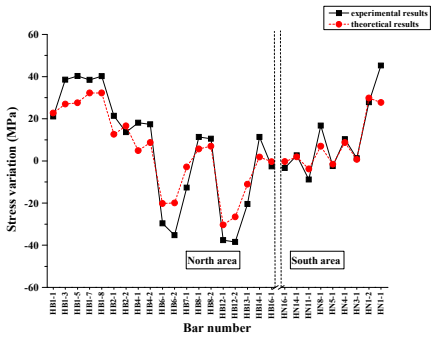

Figure 27. Stress Distribution of Circumferential Bars

(4) Vertical displacement of joints

The vertical deformation of the suspen-dome under the full-span loading is less than 2mm, with the maximum deflection at the point WN2 near the mid-span. Figure 28(a) shows the changes of vertical displacement of WN2 in the prestressing process. Vertical displacements of the point W0 at the mid-span and some other typical points are shown in Figure 28. Figure 29 shows the vertical displacement distribution of the upper shell in the fifth step of the loading. It can be seen in Figure 28 that the change trend obtained in the test is similar to that obtained by theoretical analysis. The displacement distribution of the suspen-dome in Figure 29 can be concluded that the vertical displacement near the mid-span is greater and the value decreases gradually outwards from the mid-span, which indicates the relatively large stiffness of the suspen-dome.

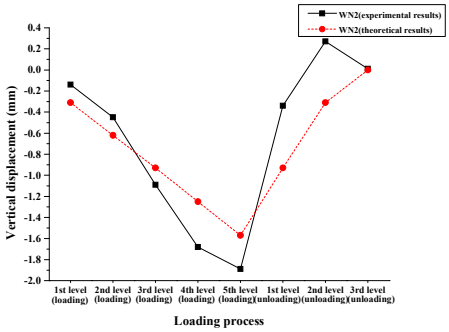

(a) measuring point WN2

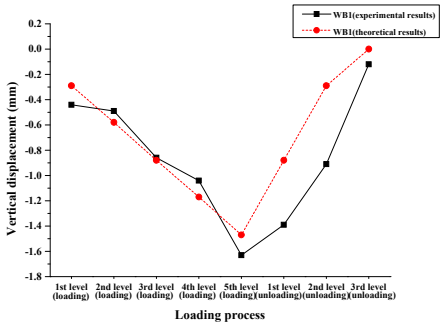

(b) measuring point WB1

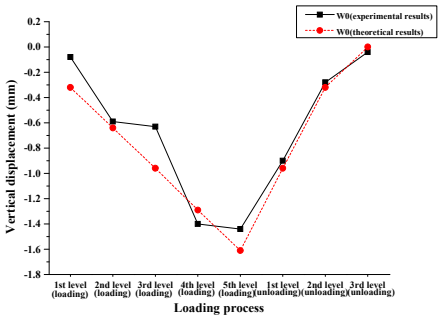

(c) point W0 in the mid-span

Figure 28. Change Curves of Vertical Displacement of Some Measuring Points in the Process of Loading

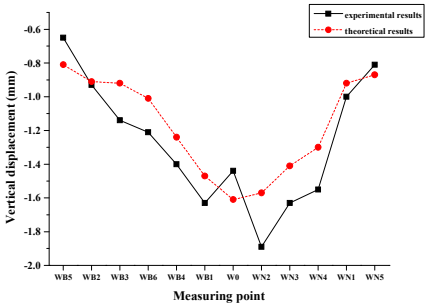

Figure 29. Structure's Deflection Distribution Map

6.2 The Half-span Loading Test

In this paper, the mechanical properties of the suspen-dome under the half-span loading were investigated in the test. Figure 30 shows the stress distribution of bars of the upper shell after the fifth step of the half-span loading. The stresses of bars of the upper shell, which are not subjected to the loading directly, are slight and almost 0 in value, while those subjected to the loading directly are mainly in compression with the maximum compressive stress reaches to -37.9 MPa at XB14-1 near the mid-span. However, the actual axial stress of the bar XB14-1 is less than -37.9 MPa, due to the fact that the bar is in tension when the prestressing process is completed. In Figure 30 (b), the axial stresses of circumferential bars are tensile near the outer ring and compressive near the inner ring. The maximum tensile stress is 30.4 MPa at the bar HB1-8, and the maximum compressive stress reaches to -21.9 MPa at the bar HB12-2. For the bar HB1-7, of which the stress increases 21.4 MPa, the axial stress is -109.1 MPa when the prestressing process is completed, hence the actual axial stress of the bar in the test is -87.7 MPa, which is different from the stress in the single-layer shell without the tensegrity system.

Under the half-span loading, the uneven stress distribution of the upper shell would result in the large difference of internal forces among cable segments of the same circle of cable in the tensegrity system. Experimental results and theoretical results of the 1st circle of the hoop cable are listed in Table 4. It is indicated that internal forces of the tensegrity system would be influenced significantly due to the uneven loading. Internal forces of hoop cables in the area where the loading is applied directly increase significantly, for example, the internal force of the cable HS1-1 increases 50.5% in the test when compared with the value of 8943 N after the prestressing process is completed. However, the increase of internal forces of those in the other area is slight, for example, the internal force of the cable HS1-5 increases only 1.2% when compared with the value of 8734 N after the prestressing process is completed. Hence, the stress distribution of cable segments in one circle of cable is related to the loading distribution. In addition, the stress distributions of hoop cables near the inner ring are similar to those in the full-span loading test, and the slackness of hoop cables near the inner ring may also occur due to negative increase of internal forces in those cables.

The deformation of the whole structure is slight under the half-span loading, with the maximum vertical displacement reaching to 1.31mm at W0 of the mid-span. The vertical displacement of the suspen-dome under the half-span loading is shown in Figure 31. In Figure 31, the vertical displacements of the area where the loading is applied directly are greater obviously than those in the other area.

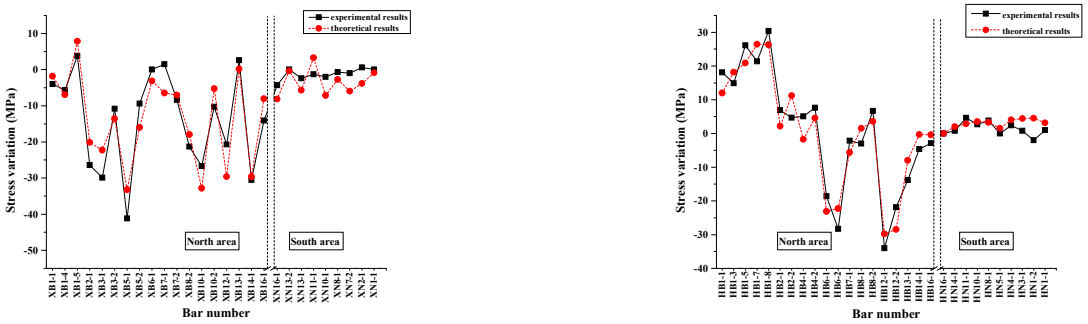

(a) Stress distribution of diagonal bars (b) Stress distribution of circumferential bars

Figure 30. Stress Distribution of Bars in the Upper Shell

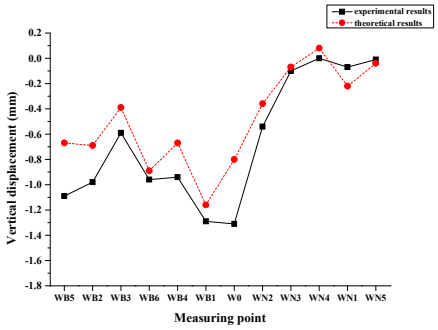

Figure 31. Vertical Displacement Distribution of the Suspen-dome

Table 4. Internal Forces of the 1st Circle of Hoop Cable in the Half-span Loading

Item		HS1-1	HS1-2	HS1-3	HS1-4	HS1-5	HS1-6
Increment of internal forces (N)	experimental results	4514	3923	3411	1867	108	2054
	theoretical results	4931	3672	3265	2202	475	2242
relative error (%)		-8.46	6.84	4.47	-15.21	-77.26	-8.39

7. COMPARISON OF STATIC PROPERTIES OF THE SUSPEN-DOME AND THE SINGLE-LAYER RETICULATED SHELL

The full-span loading test and the half-span loading test had been carried out on the upper single-layer reticulated shell without the tensegrity system below before the tests on the suspen-dome in order to study the static properties of the single-layer shell, and the corresponding test schemes are the same with those of the suspen-dome. The difference of static properties of the single-layer reticulated shell and the suspen-dome could be obtained by comparing experimental results of these two structures, owing to the fact that these two structures share the same single-layer shell structure.

1) Under the full-span loading, the stress distribution of diagonal bars of the single-layer shell is similar to that of the supen-dome and the bars of both structures are mainly subjected to compression, when initial stresses of bars in the suspen-dome caused by the pretension in the tensegrity system is not taken into account. In addition, the stress distribution of circumferential

bars of the single-layer shell is also similar to that of the suspen-dome, with bars close to the inner ring in compression and those close to the outer ring in tension. However, the stress values of circumferential bars of these two structures differ greatly. For the single-layer reticulated shell, the maximum compressive stress of circumferential bars of the inner ring is -45.2 MPa, and the maximum tensile stress of circumferential bars of the outer ring is 71.6 MPa; while the corresponding maximum compressive stress and maximum tensile stress of circumferential bars in the suspen-dome are -38.4 MPa and 40.3 MPa, which decrease 15% and 43.7% respectively when compared with the results of the single-layer reticulated shell. It is indicated that the stresses of bars in the upper shell decrease in the suspen-dome due to the pretension in the tensegrity system of the suspen-dome.

2) Under the half-span loading, the axial stress distribution of bars in the single-layer reticulated shell is similar to that in the suspen-dome, when initial stresses of bars in the suspen-dome caused by the pretension in the tensegrity system is not considered. For diagonal bars in the upper shell, though the maximum stress of bars in both structures occurs near the mid-span, the maximum stress value of the suspen-dome is less than -37.9 MPa, which decreases 52.9% when compared with the maximum value of -80.4 MPa in the single-layer shell. The stress distribution of circumferential bars shows that bars close to the outer ring mainly subjected to tension and the tensile stress decreases gradually outside in and finally turns into compression. However, circumferential bars close to the outer ring in the suspen-dome are actually subjected to compression due to the initial compressive stresses caused by the pretension of the tensegrity system in the suspen-dome.

3) The deformation of the two structures under the full-span loading is larger than that under the half-span loading. The maximum vertical displacement of the supen-dome is only 1.89 mm, which decreases 51.5% when compared with the maximum vertical displacement of the single-layer reticulated shell with a value of 3.90 mm.

The struts in the suspen-dome are supported on hoop cables which could be regarded as supports with elastic stiffness in the normal direction of the prestress caused by the pretension in cables. Due to the fact that the upper shell is supported on the struts and circumferential supports, the deflection of the upper shell is counterbalanced by the arching effect caused by the struts. Therefore, the global deformation of the suspen-dome decreases when compared with that of the single-layer reticulated shell. The vertical loading applied on the single-layer reticulated shell is transferred into in-plane forces in the shell, Yin et al. [21], which propagate in diagonal bars towards circumferential supports and are finally divided into the radial and the circumferential components. However, the stress distribution of the upper shell is changed due to the application of the tensegrity system in the suspen-dome. The in-plane forces in the shell would propagate in both diagonal bars of the shell and struts of the tensegrity system, which could achieve the same result of reducing the span of the upper shell. Hence, the stresses of the upper shell of the suspen-dome are decreased significantly when compared with that of the single-layer reticulated shell.

8. CONCLUSION

The rolling cable-strut joints are adopted in the suspen-dome of Chiping Stadium in Shandong Province to reduce the prestress loss in the prestressing process. A 1:10 scaled-down model of Chiping Stadium was used in the tension test and the loading tests to study the mechanical properties of the suspen-dome with rolling cable-strut joints installed. In addition, a comparative experiment on static properties of the suspen-dome and the single-layer reticulated shell is conducted for the first time in China, and some significant results are obtained in the paper. More detailed conclusions can be drawn in the following.

1) It is recommended to adopt the zero-order method combined with the first-order method in the prestress optimization design of the suspen-dome when the optimization objective is to minimize the largest stress of the upper shell. The prestress optimization result obtained with the first-order method only already satisfies the engineering in application well.

2) Test devices and surrounding environment should be taken into account in the design of the test model. For relatively large test models like the model used in paper, a laser tracker could be applied in the test when the deflection of the shell is difficult to measure with traditional measuring devices.

3) The pretension of the outmost circle (i.e. the 1st circle) of the hoop cable has the most significant influence on the suspen-dome. When the second step of stretching the 1st circle of the hoop cable is completed, internal forces of the 2nd, the 3rd and the 4th circles of hoop cables increase 44.51% ~ 65.32%, 14.46% ~ 22.02% and 2.86% ~ 10.97% respectively. In addition, internal forces of the hoop cables of which the prestressing process has already finished would increase due to the pretension of subsequent hoop cables, and the pretension of adjacent circles of cables would have the greatest influence on each other.

4) The trend of changes of internal forces of radial tension members is similar to that of hoop cables, due to the fact that internal forces of radial tension bars are generated due to the pretension of hoop cables. However, the stress distribution of radial tension bars is uneven due to the friction loss between hoop cables and joints

5) Stresses of bars in the upper shell are slight in the prestressing process. When compared with the structural response of the single-layer reticulated shell under the uniform loading, internal forces of some bars in the suspen-dome would be counterbalanced by the arching effect due to the pretension in the tensegrity system. The area over the 1st circle of hoop cables shows the most obvious arching effect.

6) The variation of structural responses of the suspen-dome under the full-span loading and the half-span loading obtained in tests is similar to that obtained by the FEM analysis.

7) Both the stresses of members and global deformation of the structure are slight under the full-span loading and the half-span loading, indicating that the strength and the stiffness of the suspen-dome are sufficient.

8) When compared with the single-layer reticulated shell, the stress distribution of the suspen-dome is optimized, and stresses of bars in the upper shell and the vertical displacement of the structure are decreased significantly under the loading, which verifies the advantages of the suspen-dome.

ACKNOWLEDGMENTS

The authors gratefully acknowledge the support of Independent Innovation Foundation of Tianjin University (Approval No.1304).The authors would also like to thank Shandong Zhongtong Steel Structure Engineering Co., Ltd and Tianjin Cable Space Structure Technology and Engineering Co., Ltd for providing the test model, thank Yu Jinghai who is of Tianjin University Research Institute of Architectural Design and Urban Planning for his constructive suggestions, thanks to the students in the steel research group of Tianjin University for their assistance with the laboratory work.

REFERENCES

[1] Kawaguchi, M., Abe, M. and Tatemichi, I., "Design, Test and Realization of Suspen-dome System", Journal of IASS, 1999, Vol. 40, No. 131, pp. 179-192.

[2] Chen, Z.H., "Research Progress and Engineering Practice on Suspen-dome Structure", Progress in Steel Building Structures, 2011, Vol. 13, No. 5, pp. 11-20.

[3] Kang, W.J., Chen, Z.H., Lam, H.F., et al., "Analysis and Design of the General and Outmost-ring Stiffened Suspen-domes Structures", 2003, Engineering Structures, Vol. 25, No. 13, pp. 1685-1695.

[4] Liu, H.B., Chen, Z.H. and Zhou, T., "Prestress Loss Induced by Friction in Suspendome Construction", Journal of Tianjin University, 2009, Vol. 42, No. 12, pp. 1055-1060.

[5] Liu, H.B., "Research on Prestress Loss Induced by Friction in Suspen-dome Structure", Proceedings, the 8th National Symposium on Modern Structural Engineering, 2008.

[6] Wang, S., Zhang, G.J. and Ge, J.Q., "Influence of Prestress Loss on Structural Behavior of the Badminton Gymnasium for 2008 Olympic Games", Journal of Building Structures, 2007, Vol. 28, No. 6, pp. 45-51.

[7] Ge, J.Q., Zhang, G.J. and Wang, S., "The Overall Stability Analysis of the Suspen-dome Structure System of the Badminton Gymnasium for 2008 Olympic Games", Journal of Building Structures, 2007, Vol. 28, No. 6, pp. 22-30.

[8] Wu, Y.J., "Analysis of Sliding Cable Element and Node", PhD Thesis, Tianjin University, Tianjin, China, 2010.

[9] Chen, Z.H., Wu, Y.J., Yin, Y. and Shan, C., "Formulation and Application of Multi-node Sliding Cable Element for the Analysis of Suspen-Dome Structures", Finite Elements In Analysis and Design, 2010, Vol. 46, No. 9, pp. 743-750.

[10] Liu, H.B., Chen, Z.H. and Wang, X.D., "Simulation of Pre-stressing Construction of Suspen-dome Considering Sliding Friction Based Little Curvature Assumption", Advanced Science Letters, 2011, Vol. 4, No. 8-10, pp. 2713-2718.

[11] Nie, G.B., Zhi, X.D. and Fan F., "Study of the Tension Formation and Static Test of a Suspendome for Dalian Gymnasium", China Civil Engineering Journal, 2012, Vol. 45, No. 2, pp. 1-10.

[12] Yao, Z.G. and Liu, Z.H., Building Structure Experiments, Tongji University Press, Shanghai, China, 2004.

[13] Wang, X.M., Building Structure Experiments, Tsinghua University Press, Beijing, China, 1998.

[14] Zhang, M.S., Bao, H.Z. and Zhang, Z.H., "Optimal Prestress Design of Suspen-domes", Spatial Structures, 2004, Vol. 10, No. 3, pp. 26-30.

[15] Huang, D.M., "Optimum Design and Experiment Study on the Construction Total Process of Suspendome", PhD Thesis, Beijing University of Technology, Beijing, China, 2007.

[16] Chen, Z.H., Liu, H.B. and Zhou, T., "APDL Parametric Calculation and Analysis of Space Steel Structures", China Water & Power Press, Beijing, China, 2009.

[17] Chen, Z.H., Yan R.Z., Liu H.B. and Bu Y.D., "Study of a Cable Force Determination Method in Prestressed Steel Structures", International Journal of Space Structures, 2013, Vol. 28, No. 2, pp. 59-73.

[18] Guo, J.M., Dong, S.L. and Yuan, X.F., "Model Designing and Experimental Research of Suspen-dome Structure", Engineering Mechanics, 2011, Vol. 28, No. 7, pp. 157-164.

[19] Liu, H.B. and Chen, Z.H., "Joint Design of Suspen-dome Structure", Proceedings, the 9th National Symposium on Modern Structural Engineering, 2009.

[20] Yan R.Z., Chen Z.H., Wang X.D., Xiao X. and Yang Y., "Calculation Theory and Experimental Study of the K6 Single-layer Reticulated Shell", International Journal of Steel Structures, 2014, Vol. 14, No. 2, pp. 195-212.

[21] Yin, D.Y., Liu, S.W. and Qian, R.J., "Design of Latticed Shell", China Architecture & Building Press, Beijing, China, 1996.

MODIFIED APPROACHES FOR CALCULATION OF EFFECTIVE LENGTH FACTOR OF FRAMES

Y.Y. Chen[1] and G.H. Chuan[2, *]

[1] *Professor, State Key Laboratory for Disaster Reduction in Civil Engineering, Tongji University, Shanghai, China*
[2] *M. D. Candidate, College of Civil Engineering, Tongji University, Shanghai, China.*
**(Corresponding author: E-mail: 1130335ChuanGH@tongji.edu.cn)*

Received: 10 August 2013; Revised: 2 March 2014; Accepted: 11 April 2014

ABSTRACT: As a crucial factor for stability calculation of frames, the effective length factor is generally determined by the traditional approaches in most current design codes, but some assumptions imposed do not reflect the real frame buckling behaviors. In this paper modified approaches are proposed based on the change of some unreasonable assumptions of the traditional approaches mainly in two aspects. Firstly, the premise that all frame columns buckle simultaneously is changed into an individual column buckling mode in braced frames, or story buckling mode in both braced and unbraced frames. Secondly, actual distribution of axial forces of columns is taken into account, so that the stability functions of columns may not be identical. Moreover, approximate formulas for calculation of the effective length factor are obtained based on the modified approaches, by which a series of numerical analysis is carried out. Numerical analysis results demonstrate that the modified approaches improve the accuracy well compared with the traditional ones.

Keywords: Steel structure, Frame, Buckle, Effective length factor, Critical load, Modified approaches

1. INTRODUCTION

The concept of effective length factor is instructive for buckling analysis of braced and unbraced axially loaded frames in design, especially for the regular frames because of the simplicity. The determination of effective length factor in codes of American, Australian and China is derived from buckling equations by traditional approaches (AISC [1], SAC [2], GB50017—2003 [3]). However, traditional approaches are based on assumptions of idealized conditions, which seldom exist in real structures. These assumptions are given as follows (AISC [1], Kuhn and Lundgren [4], Chen and Lui [5]):

1. Behavior is purely elastic.
2. All members have constant cross section.
3. All columns in the frame buckle simultaneously.
4. For columns in braced frames, the nodal rotations of columns in every other story are equal in magnitude and opposite in direction.
5. For columns in unbraced frames, the nodal rotations of columns in every other story are equal in magnitude and the same direction.
6. The stiffness parameter $l\sqrt{P/EI}$ of all columns is equal, indicating that stability functions for all columns are identical, where l, P and EI are the story height, column axial force and column flexural rigidity respectively.
7. No significant axial compression force exists in the girders.

Assumptions 3~5 show an important concept of traditional approaches that the global buckling of entire system is equal to the buckling of all columns in the frame. However, in the real situation, individual column buckling in the braced frame and single or several stories buckling in the braced or unbraced frame are more common. Assumption 6 comes to the conclusion that effective length factor is independent of axial load distribution, which is quite different from the reality (Bridge and Fraser [6]). In addition, when the column stiffness parameters are not identical, the errors caused by traditional approaches are significant (Kuhn and Lundgren [4]).

Much effort has been made to improve traditional approaches. Bridge and Fraser [6] modified the calculation of parameter *G* in traditional approaches. Essa [7] accounted for the effects of boundary conditions at the far ends of columns above and below the corresponding column. The boundary conditions may be rigid, hinged, or fixed. Chen et al. [8-9] considered semi-rigid beam-column joints, which expanded the scope of traditional approaches. Tong and Wang [10] abandoned assumptions 4 and 5 of traditional approaches. Their method is extended to multi-span with multi-story frames by using consolidation method. However, all the mentioned modifications were based on the premise that all columns in the whole frame buckle simultaneously.

This paper modifies traditional approaches in two aspects. First, the assumption that all columns of the entire frame system buckle together is not adopted and assumptions in traditional approaches about nodal rotations of columns are excluded. The second is that the different distribution of axial forces on columns is considered, which results in that effective length factor is not independent of load distribution. Based on the two modifications, the modified approaches are proposed.

Considering that the instability deformation of unbraced frame has the character of story buckling (Yura [11]), the story-buckling method is used. By the method, it is assumed that the buckling resistance of the story is approximately equal to the sum of the buckling resistance of all columns (Yura [11], White and Hajjar [12], Xu and Liu [13], Choi and Yoo [14]).

2. THEORETICAL ANALYSIS OF BUCKLING OF FRAMES

2.1 Slope-deflection Equations Considering the Effect of Axial Force

Figure 1 shows an axially compressed-bent member. The slope-deflection equations of the member are given as (Kuhn and Lundgren [4], Galambos and Surovek [15]):

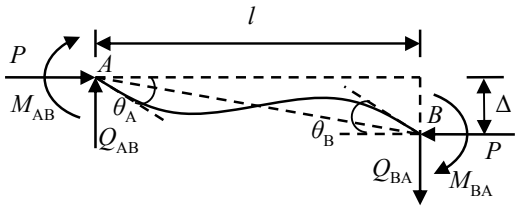

Figure 1. Axial Compression-bending Member

$$M_{AB} = si\theta_A + ci\theta_B - (s+c)i\rho \tag{1a}$$

$$M_{BA} = si\theta_B + ci\theta_A - (s+c)i\rho \tag{1b}$$

$$Q_{AB} = Q_{BA} = -(s+c)i(\theta_A + \theta_B)/l + [2(s+c) - \phi^2]i\rho/l \tag{1c}$$

where $i=EI/l$ is the span flexural rigidity, $\rho=\Delta/l$ is the relative drift of the member corresponding to the lateral displacement Δ, s and c are stability functions of the member. Noting the Euler critical load $P_E=\pi^2EI/l^2$, then

$$\phi = \pi\sqrt{P/P_E} \tag{2a}$$

$$s = \frac{\phi(\sin\phi - \phi\cos\phi)}{2 - 2\cos\phi - \phi\sin\phi} \tag{2b}$$

$$c = \frac{\phi(\phi - \sin\phi)}{2 - 2\cos\phi - \phi\sin\phi} \tag{2c}$$

2.2 Buckling Analysis of Braced Frames

The modified model is shown in Figure 2. The assumptions adopted for this model are:

1. The interaction of the story for buckling check and the upper and lower stories is considered, and the effect of other stories is incorporated equivalently with elastic rotational restraints k_1 and k_2.
2. At buckling, the end rotations of beams in the story are of equal magnitude but the opposite direction.
3. Axial forces in beams are neglected.
4. Actual forces of the upper and lower columns are considered, and the force of column in the story for buckling check is variable.

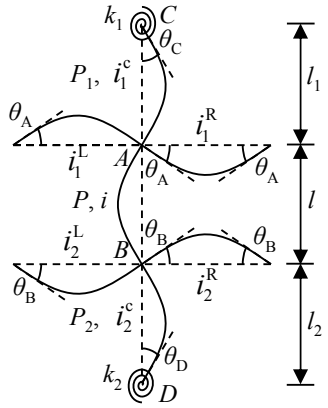

Figure 2. Model for the Braced Frame

Assumption 1 excludes the premise in traditional approaches that the nodal rotations of columns in every other story are equal, and as an alternative, elastic rotational restraints are considered for the effect of other stories. Assumption 4 excludes the previous premise that stability functions for all columns are identical, so that it is in more accordance with the buckling behavior of real structures.

By the slope-deflection equations of axially compressed-bent members, the equilibrium equation of moment for node C is

$$s_1 i_1^c \theta_C + c_1 i_1^c \theta_A + k_1 \theta_C = 0 \tag{3}$$

where s_1 and c_1 are stability functions of the upper column.

Then θ_C is given by

$$\theta_C = -\frac{c_1}{k_1 / i_1^c + s_1}\theta_A \tag{4}$$

Moments at the bottom end of the upper column and the top end of the corresponding column in the story for buckling check are

$$M_{\mathrm{AC}} = s_1 i_1^{\mathrm{c}} \theta_{\mathrm{A}} + c_1 i_1^{\mathrm{c}} \theta_{\mathrm{C}} \tag{5a}$$

$$M_{\mathrm{AB}} = si\theta_{\mathrm{A}} + ci\theta_{\mathrm{B}} \tag{5b}$$

where s and c are stability functions of the corresponding column.

The equilibrium equation of moment for node A is

$$M_{\mathrm{AC}} + M_{\mathrm{AB}} + 2(i_1^{\mathrm{L}} + i_1^{\mathrm{R}})\theta_{\mathrm{A}} = 0 \tag{6}$$

Substituting Eq. 4 and 5 into Eq. 6, the following equation is obtained

$$(s + 2W_1)\theta_{\mathrm{A}} + c\theta_{\mathrm{B}} = 0 \tag{7}$$

Analogously, for node B the following equation can be obtained

$$c\theta_{\mathrm{A}} + (s + 2W_2)\theta_{\mathrm{B}} = 0 \tag{8}$$

where $W_j = \dfrac{i_j^{\mathrm{L}} + i_j^{\mathrm{R}}}{i} + \dfrac{s_j^2 - c_j^2 + s_j k_j / i_j^{\mathrm{c}}}{2(k_j / i_j^{\mathrm{c}} + s_j)} \dfrac{i_j^{\mathrm{c}}}{i}, (j = 1, 2)$, (9)

and s_2 and c_2 are stability functions of the lower column.

At buckling, θ_{A} and θ_{B} are not all zeros. By Eq. 7 and 8, this condition can be written as

$$\begin{vmatrix} s + 2W_1 & c \\ c & s + 2W_2 \end{vmatrix} = 0 \tag{10}$$

By Eq. 2a, effective length factor of the column can be expressed as $K = \pi / \phi$.

So Eq. 10 can be expressed as

$$\frac{\pi}{K}[(\frac{\pi}{K})^2 + 2(W_1 + W_2) - 4W_1W_2]\sin\frac{\pi}{K} - 2[(W_1 + W_2)(\frac{\pi}{K})^2 + 4W_1W_2]\cos\frac{\pi}{K} + 8W_1W_2 = 0 \tag{11}$$

According to Assumption 4, W_1 and W_2 in Eq. 11 are known, and only effective length factor of the corresponding column is unknown. It is found that Eq. 11 is formally consistent with the buckling equation of braced frames obtained from traditional approaches, so effective length factor can be determined by alignment chart (AISC [1], SAC [2]), or by the following approximate analysis solution whose form is consistent with traditional approaches' (CM [16], Dumonteil [17-18])

$$K \approx \frac{0.64W_1W_2 + 1.4(W_1 + W_2) + 3}{1.28W_1W_2 + 2(W_1 + W_2) + 3} \tag{12}$$

In Eq. 12, when $W_1<0$ or $W_2<0$, setting $W_1=W_2=0$. It is a conservative solution either when the corresponding column unbuckles or buckles, where the former case is obvious. While the corresponding column buckles, the effective length factor is always smaller than 1 (Dumonteil [17-18]), hence setting $W_1=0$ and $W_2=0$ indicates $K=1$ and guarantees the conservatism of the result.

Effective length factor expressed in Eq. 12 is related to axial load distributions in columns according to Eq. 9. However effective length factor obtained from traditional approaches is independent of load distribution.

For different beam end conditions, adjustments are required. According to structural mechanics, when the far end of the beam is hinged or rigid, the span flexural rigidity should be multiplied by correction factor 1.5 or 2 respectively. When the near end of the beam is hinged, the span flexural rigidity of the beam is zero.

2.3 Buckling Analysis of Unbraced Frames

The modified model is shown in Figure 3. The assumptions 1, 3 and 4 adopted for the modified model are as the same as those specified for braced frames stated in above section, while assumption 2 is changed as follows: at buckling, the end rotations of beams in the same story are of equal magnitude and the same direction. And an extra assumption is supplemented as that: shear forces of columns in all stories are taken as zeros.

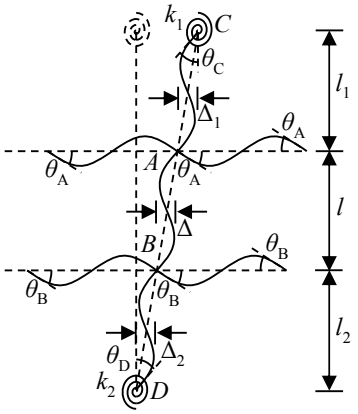

Figure 3. Model for the Unbraced Frame

The modified approaches exclude the premise in traditional approaches that all the story drifts are equal, so it is more rational in practice.

By the slope-deflection equations of axially compressed-bent members, the equilibrium equation of moment for node C is

$$s_1 i_1^c \theta_C + c_1 i_1^c \theta_A - (s_1 + c_1) i_1^c \rho_1 + k_1 \theta_C = 0 \tag{13}$$

where $\rho_1 = \Delta_1 / l_1$ is the relative drift of the upper story.

By the extra assumption, the shear force of the upper column is taken as zero, which can be expressed as

$$Q_1 = -(s_1 + c_1) i_1^c (\theta_C + \theta_A) / l_1 + [2(s_1 + c_1) - \phi_1^2] i_1^c \rho_1 / l_1 = 0 \tag{14}$$

By Eq. 13 and 14, solutions can be given by

$$\theta_C = \frac{(s_1 + c_1)^2 - [2(s_1 + c_1) - \phi_1^2] c_1}{(k_1 / i_1^c + s_1)[2(s_1 + c_1) - \phi_1^2] - (s_1 + c_1)^2} \theta_A \tag{15a}$$

$$\rho_1 = \frac{(s_1 + c_1)(k_1 / i_1^c + s_1 - c_1)}{(k_1 / i_1^c + s_1)[2(s_1 + c_1) - \phi_1^2] - (s_1 + c_1)^2} \theta_A \tag{15b}$$

Moments at the bottom end of the upper column and the top end of the corresponding column are

$$M_{AC} = s_1 i_1^c \theta_A + c_1 i_1^c \theta_C - (s_1 + c_1) i_1^c \rho_1 \tag{16a}$$

$$M_{AB} = si\theta_A + ci\theta_B - (s + c) i\rho \tag{16b}$$

where $\rho = \Delta / l$ is the relative drift of the story for buckling check.

The equilibrium equation of moment for node A is

$$M_{AC} + M_{AB} + 6(i_1^L + i_1^R)\theta_A = 0 \tag{17}$$

Substituting Eq. 15 and 16 into Eq. 17, the following equation is obtained

$$(s + 6T_1)\theta_A + c\theta_B - (s + c)\rho = 0 \tag{18}$$

Analogously, for node B the following equation can be obtained

$$c\theta_A + (s + 6T_2)\theta_B - (s + c)\rho = 0 \tag{19}$$

where $T_j = \frac{i_j^L + i_j^R}{i} + \frac{(s_j^2 - c_j^2 - s_j \phi_j^2) k_j / i_j^c - (s_j^2 - c_j^2)\phi_j^2}{6\{(k_j / i_j^c + s_j)[2(s_j + c_j) - \phi_j^2] - (s_j + c_j)^2\}} \frac{i_j^c}{i}, (j = 1, 2)$. (20)

The shear force of the corresponding column is taken as zero, that is

$$Q = -(s + c) i(\theta_A + \theta_B) / l + [2(s + c) - \phi^2] i\rho / l = 0 \tag{21}$$

At buckling, θ_A, θ_B and ρ are not all zeros, so Eq. 18, 19 and 21 can be written as

$$\begin{vmatrix} s + 6T_1 & c & -(s + c) \\ c & s + 6T_2 & -(s + c) \\ -(s + c) & -(s + c) & 2(s + c) - \phi^2 \end{vmatrix} = 0 \tag{22}$$

Eq. 22 can be expressed as

$$[36T_1T_2-(\frac{\pi}{K})^2]\sin\frac{\pi}{K}+6\frac{\pi}{K}(T_1+T_2)\cos\frac{\pi}{K}=0 \tag{23}$$

As stated earlier, effective length factor can be determined by alignment chart (AISC [1], SAC [2]), or by the following approximate analysis solution (CM [16], Dumonteil [17-18], Tong and Wang [10])

$$K\approx\sqrt{\frac{7.5T_1T_2+4(T_1+T_2)+1.52}{7.5T_1T_2+T_1+T_2}} \tag{24}$$

In Eq. 24, when T_1<0 or T_2<0, set T_1=T_2=0.0001, where 0.0001 is a very small number. When the corresponding column buckles, its effective length factor ranges from 1 to +∞ (Dumonteil [17-18]). Thus setting T_1=T_2=0.0001 indicates K=87, which can be regarded as an infinite number.

Effective length factor expressed in Eq. 24 is also related to axial load distributions in columns as the situation of Eq. 12.

According to structural mechanics, when the far end of the beam is hinged or rigid, the span flexural rigidity should be multiplied by correction factor 0.5 or 2/3 respectively. When the near end of the beam is hinged, the span flexural rigidity of the beam is zero.

2.4 Elastic Rotational Restraints k_1 and k_2

Elastic rotational restraints k_1 and k_2 represent the effect of boundary condition provided by other stories, however, it might be complex to solve these factors. Therefore, the following simple method is proposed.

Firstly to consider rotational restraint k_1 for braced frames. Figure 4 shows the column and beams connecting to node C. For beams, end rotations are assumed to be coincident with Assumption 2 stated in Section 2.3. For the column, the far end is considered to be hinged conservatively. To avoid over conservative concerning in derivation, the axial force is neglected when calculating the stiffness of the column. Based on those assumptions, k_1 can be written as

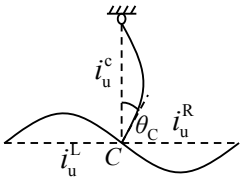

Figure 4. Model for Calculation of k_1

$$k_1=2(i_u^L+i_u^R)+3i_u^c \tag{25a}$$

For the rotational restraints k_2, the column and beams connecting to node D in Figure 2 can be similarly removed from the frame, and using index “d” in physical quantities. Analogously, k_2 is given by

$$k_2=2(i_d^L+i_d^R)+3i_d^c \tag{25b}$$

For unbraced frames, rotational restraints k_1 and k_2 can be also analogously written as

$$k_1 = 6(i_u^L + i_u^R) + 3i_u^c \quad (26a)$$

$$k_2 = 6(i_d^L + i_d^R) + 3i_d^c \quad (26b)$$

For different end conditions of beams, adjustments of span flexural rigidity of beams are required in Eq. 25 and 26. Correction factors are stated in Section 2.2 and Section 2.3.

Of cause, different calculating methods of rotational restraints k_1 and k_2 have effect on the accuracy of the model herein, but proposed method here is simple and practical without big error as shown by following demonstrations for validation.

3. MODEL VALIDATION

3.1 Frame Models

FEM solutions are considered as real solutions to assess the accuracy of the proposed effective length factors; meanwhile errors of the critical load proposed by this study and traditional approaches are compared. In order to provide a comprehensive comparison, four kinds of Frame Types are designed. For the computation of each model, both the buckling configuration in braced frame without side sway and the one in unbraced frame with side sway are supposed.

In the group of Frame Type 1, there are 16 frame models with the various spans and stories as shown in Table 1. All the span flexural rigidity of columns and beams is equal, set as $i_b=i_c=i$. All story heights and column spaces are equal l. Figure 5a shows the distribution of axial loads on columns. Load distributions in each story are the same, and the loads on external columns are half of those on other columns.

In the group of Frame Type 2, there are also 16 frame models generally same as Frame Type 1, except that the span flexural rigidity of columns and beams is equal respectively, set as $i_b=0.8i$ and $i_c=i$.

Table 1. Models of Frame Type 1 and 2

Number of spans	Number of stories							
3	1	3	5	10	15	20	25	30
8	1	3	5	10	15	20	25	30

Traditional approaches have a key assumption that stability functions for all columns are identical (Kuhn and Lundgren [4], Chen and Lui [5]). In order to compare the two kinds of approaches when this assumption is satisfied, Frame Type 3 is designed. This type contains 3-span and 8-span with 10-story frames. Loads at the top of every column including the external column are set equal as shown in Figure 5b, and the column span flexural rigidity reduces from the 1st floor to the 10th floor to make stability functions of all columns identical, and the span flexural rigidity of columns and beams in the same story is supposed to be the same. The column span flexural rigidity of the first story is noted i.

In contrast to Frame Type 1~3 in which all column-beam joints are fixed and all column spaces are identical, other 6 frame models classified as Frame Type 4 are designed as shown in Figure 6. In those frame models, unequal spans and hinged end conditions of columns and beams are supposed, so that the validity of the modified approaches can be further checked. Each frame model has 3

spans and 5 stories. Frame model 1 and 2 are with unequal spans. In Frame model 3 and 4, a part of beams are with hinged connection to columns. Frame model 5 and 6 contain leaning columns. All frames in Type 4 have the same story height l and the same section of beams and columns. Load distributions are the same as Frame Type 1~2 as shown in Figure 5a. Braced and unbraced buckling modes are considered for each frame model.

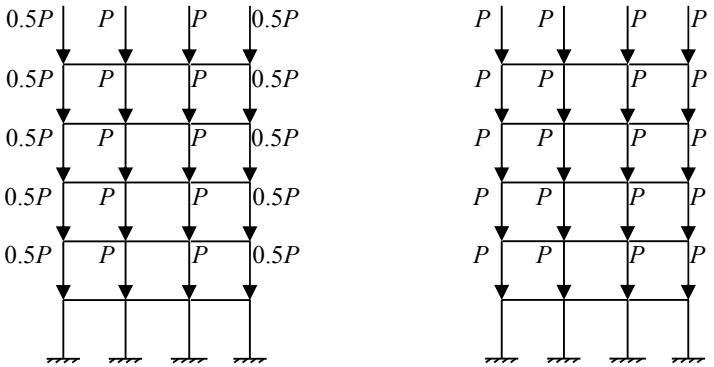

(a) Frame Type 1, 2 and 4 (b) Frame Type 3

Figure 5. Load Distribution for Frame Type 1~4

3.2 The Determination of Critical Load

3.2.1 Calculation of critical load using modified approaches

In order to solve the critical load of the frame, the following iteration is adopted:

1. Setting an initial load P_0, and calculating critical forces of all columns.

2. Determining and correcting critical story loads by utilizing critical forces of columns. For braced frames, critical force of each story is the minimum one of critical forces of columns in the story. For unbraced frames, story critical forces can be obtained by story-buckling method (Yura [11], White and Hajjar [12], Xu and Liu [13], Choi and Yoo [14]). For the load distribution in Frame Type 1, 2 and 4, the story critical force is given by

$$P_{\mathrm{s\_cr}}^{j}=\frac{1}{N}\sum_{m=1}^{N+1}P_{\mathrm{c\_cr},m}^{j}\,, \tag{27a}$$

and for the load distribution pattern in Frame Type 3

$$P_{\mathrm{s\_cr}}^{j}=\frac{1}{N+1}\sum_{m=1}^{N+1}P_{\mathrm{c\_cr},m}^{j} \tag{27b}$$

where N is the number of spans, $P_{\mathrm{s\_cr}}^{j}$ is the critical force of the j-th story, and $P_{\mathrm{c\_cr},m}^{j}$ is the critical force of the m-th column in the j-th story.

3. Determining critical load of the frame. Every story critical force corresponds to a critical load P_{cr}' of the frame. It is clear that the minimum one noted as P_{cr} is the critical load of the frame under the distribution of P_0.

4. If $P_0=P_{\mathrm{cr}}$, that is the critical load of the frame; if $P_0>P_{\mathrm{cr}}$ or $P_0<P_{\mathrm{cr}}$, reducing or increasing P_0 to calculate P_{cr} again by step 1to 4 until $P_0=P_{\mathrm{cr}}$.

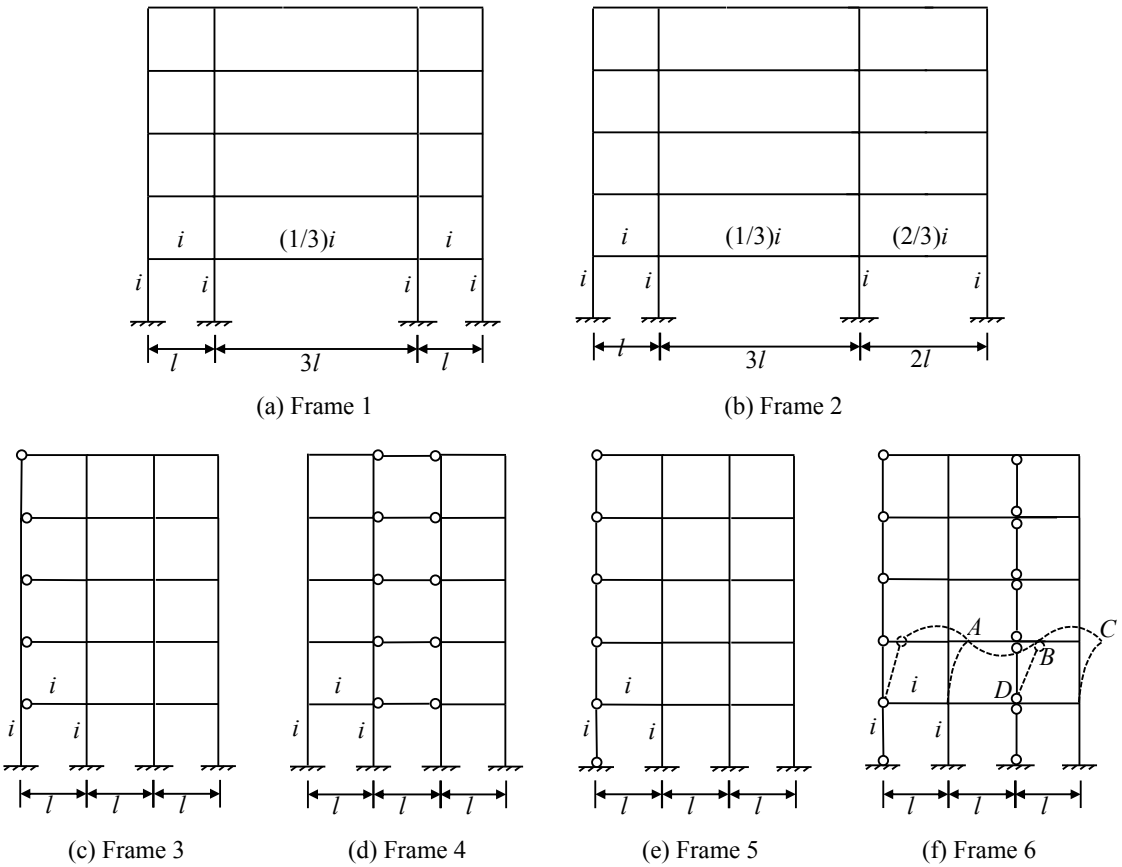

Figure 6. Frame Type 4

A special consideration should be paid for side sway buckling of Frame model 6 in Frame Type 4. For examples, the span flexural rigidity of beams like *AB* and *BC* as shown in Figure 6f should be modified. Due to the existence of leaning column *BD*, the rotations at the ends of beam *AB* and *BC* do not coincide with the Assumption 2 for unbraced frames stated in Section 2.3, but are analogous to the features of braced frame. This observation leads to a correction factor 1/3 for span flexural rigidity of beams *AB* and *BC*.

3.2.2 Calculation of critical load using traditional approaches

1. Calculating critical forces of all columns.
2. Obtaining critical story loads by using Eq. 27a or 27b.
3. The minimum of story critical forces is the critical load of the frame.

3.2.3 Calculation of critical load by FEM software

FEM solutions are obtained by the buckling analysis of ABAQUS software.

3.2.4 The definition of errors

Setting P_{cr}^{FEM}, P_{cr}^{M} and P_{cr}^{T} are critical load of the frame calculated by FEM, proposed effective length factor in modified approaches, and traditional approaches respectively. Errors of modified approaches and traditional approaches are defined as

$$\varepsilon^{\mathrm{M}}=\frac{P_{\mathrm{cr}}^{\mathrm{FEM}}-P_{\mathrm{cr}}^{\mathrm{M}}}{P_{\mathrm{cr}}^{\mathrm{FEM}}}\times 100\% \tag{28a}$$

$$\varepsilon^{\mathrm{T}}=\frac{P_{\mathrm{cr}}^{\mathrm{FEM}}-P_{\mathrm{cr}}^{\mathrm{T}}}{P_{\mathrm{cr}}^{\mathrm{FEM}}}\times 100\% \tag{28b}$$

3.3 Numerical Results

Comparison for Frame Type 1~4 can be seen from Table 2~5. The data in brackets in Table 2~4 are those corresponding to 8-span frame models, and non-bracket data are those of 3-span frame models.

Shown in Table 2, errors of modified approaches are significantly smaller than that of traditional approaches. For braced buckling, the maximal error of modified approaches is 7.4%, however errors of traditional approaches hover around 21% (for 3-span frames) and 15% (for 8-span frames). For unbraced buckling, except for the results of 3-span with 3-story frame, the maximal error of modified approaches is 7.9%, however errors of traditional approaches hover around 11%. Besides, when the number of story is bigger than 3~5, the absolute values of errors of modified approaches are within 5%.

From Table 2, it is found that the prediction by modified approaches is not conservative when the number of stories is bigger than 15~20, but the absolute values of these errors are within 5% which is acceptable.

Table 3 also shows that errors of modified approaches are obviously smaller than that of traditional approaches. Errors shown in Table 3 are mostly consistent with that in Table 2, which demonstrates the decrease of span flexural rigidity of beams has no significant effect on the accuracy of the two kinds of approaches. From Table 3, though modified approaches are not conservative when the number of story is bigger than 15~20, the absolute values of these errors are within 5%.

Results of the two kinds of approaches are the same for the single story frames. It is because for the single story frame, inter-story interaction dose not exit, and modified approaches is consistent with traditional approaches.

From Table 4, although the two kinds of frames satisfied the key assumption of traditional approaches that stability functions of all columns are equal, errors of modified approaches are much smaller than that of traditional approaches. All the absolute values of errors of modified approaches in Table 4 are within 5%.

By the results from Frame Type 4, it also exhibits the good accuracy of modified approaches compared with traditional approaches as shown in Table 5. The average error of modified approaches is 4.7%, while the error of traditional approaches is 19%. Modified approaches are not conservative for unbraced buckling of Frame model 5 and 6, while absolute values of the errors are within 5% which is acceptable in practice.

Table 2. Comparison of Critical Loads for Frames of Type 1

Buckling mode	Number of spans	Number of stories	Critical load of the frame ($\times i/l$)			Error of critical load (%)	
			FEM	Modified approaches	Traditional approaches	Modified approaches	Traditional approaches
Braced buckling	3 (8)	1	29.837 (28.687)	28.573	28.573	4.2 (0.4)	4.2 (0.4)
		3	9.5757 (9.1404)	8.9466	8.1575	6.6 (2.1)	15 (11)
		5	5.2370 (4.9584)	4.8474	4.0788	7.4 (2.2)	22 (18)
		10	2.3323 (2.1914)	2.1806	1.8128	6.5 (0.5)	22 (17)
		15	1.4774 (1.3809)	1.3984	1.1654	5.3 (-1.3)	21 (16)
		20	1.0780 (1.0021)	1.0282	0.8587	4.6 (-2.6)	20 (14)
		25	0.8487 (0.7843)	0.8076	0.6798	4.8 (-3.0)	20 (13)
		30	0.7007 (0.6434)	0.6639	0.5626	5.3 (-3.2)	20 (13)
Unbraced buckling	3	1	10.395	7.9725	7.9725	23	23
		3	3.2137	2.7909	2.9653	13	7.7
		5	1.7735	1.6336	1.5577	7.9	12
		10	0.7972	0.7777	0.6923	2.4	13
		15	0.5059	0.5034	0.4450	0.5	12
		20	0.3685	0.3709	0.3279	-0.6	11
		25	0.2891	0.2932	0.2596	-1.4	10
		30	0.2376	0.2415	0.2148	-1.7	9.6
	8	1	9.1651	8.1842	8.1842	11	11
		3	2.8838	2.7219	2.6318	5.6	8.7
		5	1.6162	1.5586	1.4449	3.6	11
		10	0.7353	0.7250	0.6422	1.4	13
		15	0.4686	0.4678	0.4128	0.2	12
		20	0.3421	0.3446	0.3042	-0.7	11
		25	0.2688	0.2726	0.2408	-1.4	10
		30	0.2210	0.2255	0.1993	-2.0	9.8

Table 3. Comparison of Critical Loads for Frames of Type 2

Buckling mode	Number of spans	Number of stories	Critical load of the frame ($\times i/l$)			Error of critical load (%)	
			FEM	Modified approaches	Traditional approaches	Modified approaches	Traditional approaches
Braced buckling	3 (8)	1	28.716 (27.553)	27.524	27.524	4.2 (0.1)	4.2 (0.1)
		3	9.1750 (8.7529)	8.5694	7.6174	6.6 (2.1)	17 (13)
		5	4.9759 (4.7113)	4.6166	3.8087	7.2 (2.0)	23 (19)
		10	2.1983 (2.0659)	2.0694	1.6928	5.9 (-0.2)	23 (18)
		15	1.3879 (1.2979)	1.3261	1.0882	4.5 (-1.4)	22 (16)
		20	1.0105 (0.9402)	0.9722	0.8018	3.8 (-3.4)	21 (15)
		25	0.7943 (0.7350)	0.7619	0.6348	4.1 (-3.7)	20 (14)
		30	0.6549 (0.6025)	0.6263	0.5253	4.4 (-4.0)	20 (13)
Unbraced buckling	3	1	9.9414	7.6489	7.6489	23	23
		3	2.9887	2.6699	2.7667	11	7.4
		5	1.6221	1.5364	1.3834	5.3	15
		10	0.7197	0.7163	0.6148	0.5	15
		15	0.4545	0.4616	0.3952	-1.6	13
		20	0.3303	0.3398	0.2912	-2.9	12
		25	0.2587	0.2686	0.2306	-3.8	11
		30	0.2123	0.2212	0.1908	-4.2	10
	8	1	8.8111	7.8803	7.8803	11	11
		3	2.7053	2.5801	2.4850	4.6	8.1
		5	1.4907	1.4506	1.2947	2.7	13
		10	0.6692	0.6663	0.5754	0.4	14
		15	0.4245	0.4290	0.3699	-1.1	13
		20	0.3091	0.3159	0.2726	-2.2	12
		25	0.2425	0.2498	0.2158	-3.0	11
		30	0.1992	0.2066	0.1786	-3.7	10

Table 4. Comparison of Critical Loads for Frames of Type 3

Buckling mode	Number of spans	Critical load of the frame (×i/l)			Error of critical load (%)	
		FEM	Modified approaches	Traditional approaches	Modified approaches	Traditional approaches
Braced buckling	3 (8)	1.5499 (1.5864)	1.5961	1.3434	-3.0 (-0.6)	13 (15)
Unbraced buckling	3	0.5574	0.5670	0.5137	-1.7	7.8
	8	0.5061	0.5232	0.4673	-3.4	7.7

Table 5. Comparison of Critical Loads for Frames of Type 4

Buckling mode	Number of frame	Feature of frame	Critical load of the frame (×i/l)			Error of critical load (%)	
			FEM	Modified approaches	Traditional approaches	Modified approaches	Traditional approaches
Braced buckling	1	Unequal spans	4.8911	4.5579	3.6157	6.8	26
	2		4.5352	4.2382	3.2227	6.5	29
	3	Hinged conditions	5.1982	4.9298	4.0788	5.2	22
	4		4.6960	4.3490	3.3584	7.4	28
	5	Leaning columns	3.9548	3.9478	3.9478	0.2	0.2
	6		1.9809	1.9739	1.9739	0.4	0.4
Unbraced buckling	1	Unequal spans	1.6402	1.5282	1.3931	8.4	15
	2		1.4385	1.3562	1.1816	5.7	22
	3	Hinged conditions	1.4321	1.4082	1.1795	1.7	18
	4		1.5361	1.4012	1.2790	8.8	17
	5	Leaning columns	1.3644	1.4082	1.1795	-3.2	14
	6		0.6725	0.6846	0.4308	-1.8	36

4. CONCLUSIONS

Referring to the traditional approaches, this paper proposed modified approaches to calculate effective length factor of frame columns. Computing results show that the modified approaches guarantee significantly higher accuracy than traditional approaches in general, and the absolute values of errors of modified approaches are within 5% in most computed frame models. Modified approaches are more rational than traditional approaches. Besides, approximate formulas for effective length factor based on modified approaches are explicit analysis expressions which are easy to apply.

It also should be pointed out that iteration is needless in engineering application for modified approaches. Based on actual loads of the frame, critical story loads can be obtained by using Eqs. 12 or 24. By comparing critical and actual story loads, the stability of the frame could be estimated.

Though effective length method is easily used in design process, it mainly applies to the determination of elastic critical loads of the frame structures. For complex and irregular structures like domes whose second order effects are significant, advanced analysis is required.

REFERENCES

[1] American Institute of Steel Construction (AISC), "Specification for Structural Steel Buildings", ANSI/AISC 360-10, Chicago, 2010.

[2] Standards Australia Committee (SAC) BD/1, Steel Structures, "AS4100—1998, Australian Standard—Steel Structures", Standards Australia, New South Wales, 1998.

[3] GB50017—2003, "Code for Design of Steel Structures", Ministry of Construction, Architecture and Building Press, Beijing, 2003. (in Chinese)

[4] Kuhn, G. and Lundgren, H. R., "An Appraisal of the Effective Length Alignment Charts", International Colloquium on Stability of Structures under Static and Dynamic Loads, ASCE, New York, 1977, pp. 212-242.

[5] Chen, W.F. and Lui, E.M., "Structural Stability—Theory and Implementation", Elsevier, New York, 1987.

[6] Bridge, R.Q. and Fraser, D.J., "Improved G-factor Method for Evaluating Effective Lengths of Columns", Journal of Structural Engineering, 1987, Vol. 113, No. 6, pp. 1341-1356.

[7] Essa, H.S., "Stability of Columns in Unbraced Frames", Journal of Structural Engineering, 1997, Vol. 123, No. 7, pp. 952-957.

[8] Kishi, N., Chen, W.F. and Goto, Y., "Effective Length Factor of Columns in Semirigid and Unbraced Frames", Journal of Structural Engineering, 1997, Vol. 123, No. 3, pp. 313-320.

[9] Kishi, N., Chen, W.F., Goto, Y. and Komuro, M., "Effective Length Factor of Columns in Flexibly Jointed and Unbraced Frames", Journal of Constructional Steel Research, 1998, Vol. 47, No. 1-2, pp. 93-118.

[10] Tong, G.S. and Wang, J.P., "Column Effective Lengths Considering Inter-story and Inter-column Interactions in Sway-permitted Frames", Journal of Constructional Steel Research, 2006, Vol. 62, No. 5, pp. 413-423.

[11] Yura, J.A., "The Effective Length of Columns in Unbraced Frames", Engineering Journal, 1971, Vol. 8, No. 2, pp. 37-42.

[12] White, D.W. and Hajjar, J.F., "Buckling Models and Stability Design of Steel Frames: A Unified Approach", Journal of Constructional Steel Research, 1997, Vol. 42, No. 3, pp. 171-207.

[13] Xu, L. and Liu, Y., "Story Stability of Semi-braced Steel Frames", Journal of Constructional Steel Research, 2002, Vol. 58, No. 4, pp. 467-491.

[14] Choi, D.H. and Yoo, H., "Iterative System Buckling Analysis, Considering A Fictitious Axial Force to Determine Effective Length Factor for Multi-story Frames", Engineering Structures, 2009, Vol. 31, No. 2, pp. 560-570.

[15] Galambos, T.V. and Surovek, A.E., "Structural Stability of Steel: Concepts and Applications for Structural Engineers", John Wiley & Sons, Inc., Hoboken, New Jersey, 2008.

[16] Commission des Regles C. M. 66, "Regles de calcul des constructions en acier", Eyrolles, Paris, 1966. (in French)

[17] Dumonteil, P., "Simple Equations for Effective Length Factors", Engineering Journal, 1992, Vol. 29, No. 3, pp. 111-115.

[18] Dumonteil, P., "Historical Note on K-factor Equations", Engineering Journal, 1999, Vol. 36, No. 2, pp. 102-103.

CYCLIC BEHAVIOR OF REBAR-PENETRATED CONNECTION BETWEEN GANGUE CONCRETE FILLED STEEL TUBULAR COLUMN AND REINFORCED GANGUE CONCRETE BEAM

Guochang Li[1], Chen Fang[2,*], Xing Zhao[1], Yuwei An[1] and Yu Liu[1]

[1] *School of civil engineering, Shenyang Jianzhu University, Shenyang, 110168, China*
[2] *Department of Civil Engineering, University of Texas at El Paso, El Paso, TX 79968, USA*
**(Corresponding author: E-mail: cfang@miners.utep.edu)*

Received: 31 July 2013; Revised: 22 April 2014; Accepted: 23 October 2014

ABSTRACT: Gangue concrete filled steel tube is a new composite system which has advantages of remarkable earthquake-resistant property and economical efficiency. However, few researches have been done with respect to the behavior of the composite system. Therefore, based on proper material constitutive models and reasonable contact models among different materials, the paper has developed finite element analysis models of rebar-penetrated connection between gangue concrete filled steel tubular column and reinforced gangue concrete beam using software ABAQUS 6.10. Furthermore, finite element analysis results are verified by experiments, demonstrating that the load-displacement curves computed by ABAQUS agree with experimental curves very well and finite element analysis models are reliable to analyze the behavior of the rebar-penetrated connection. Then, these models are used to conduct stress analysis on the composite connection to investigate the failure modes and the force-transferring mechanism. The analysis results show that the rebar-penetrated connection, with full and spindle-shaped load-displacement hysteretic curve, has the reasonable force-transferring route and good energy-dissipation capacity. Finally, the effects of axial load level, stiffness ratio of beam and column, steel ratio and compressive strength of gangue concrete on the behavior of the connection are investigated on the basis of the different models by changing the parameters.

Keywords: Gangue concrete filled steel tubular, Connection, Finite element analysis, Cyclic behavior, Failure mode, Parametric analysis

1. INTRODUCTION

Gangue concrete filled steel tubular (GCFST) column is a new and promising structure in the whole concrete filled steel tubes (CFST) families [1]. The normal concrete is replaced by the gangue concrete to fill in the steel tube. The GCFST column not only keeps advantages of high earthquake-resistant performance of the CFST column, but also possesses prominent merits of less weight and economic efficiency [2]. Owing to less apparent density of the gangue concrete than the normal concrete, the weight of gangue concrete is reduced by as much as 20 percent. More important is that the lateral deformation characteristic of gangue concrete is superior to the normal concrete. It is more helpful to give full play to the confinement effect of the steel tube on the core gangue concrete and improve the bearing capacity of the column [3]. Moreover, the connection between column and beam is the most essential component of the composite column-beam structure. The performance of the connection is key to the accuracy of the force-transferring route and the safety of the whole building [4]. And numerous severe damages of the connections have been occurred around the world, especially in the severe earthquake [5-6]. These damages of the connection resulted in large-loss collapse of the structure. Therefore, it is vital and worthy to investigate the behavior of the connection between GCFST column and reinforced gangue concrete (RGC) beam under the cyclic loading.

In the past years, many designers and scholars proposed different kinds of the connections between CFST column and reinforced concrete (RC) beam and made various researches on these connections. J. Beutel and D. Thambiratnam [7] made an experimental research on the connection

between CFST column and compound beam. Based on the analysis of the failure mode and stress distribution under low cyclic reversed loading, the connection was proved to have high strength and good ductility. Kawaguchi Jun and Morino Shosuke [8] conducted the experiment and finite element analysis on the CFST frame under the vertical reversed loading to analyze the force-transferring mechanism and strength deterioration of the frame. Jian Cai and Chun Yang [9] made an experimental study on the CFST column-beam connection with piercing reinforcing bar to analyze bearing capacity and failure mode. The study showed that the connection has the good and reliable mechanical performance. Guohuang Yao and Yiyan Chen [10-11] proposed a new type of connection between CFST column and RC beam and also made the analysis on the failure process, failure mode and energy dissipation capacity according to experimental research and finite element analysis. However, there is little research on the behavior of the connection between GCFST column and RGC beam. To conduct the study of the connection between GCFST column and RGC beam is an excellent method to fill in the blank of the field.

The paper presents a new type of connection between GCFST column and RGC beam, which can be regarded as a typical rebar-penetrated connection [12]. Based on experimental conditions, the paper creates finite element analysis models of the rebar-penetrated connection between GCFST column and RGC beam. In addition, finite element analysis results are verified by experiments to determine the accuracy of the models. Then, stress analysis on the rebar-penetrated connection is conducted under the low cyclic reversed loading to study the failure modes and force-transferring mechanism. The load-displacement hysteretic curves of the rebar-penetrated connection are calculated and drawn. Finally, the effects of some typical parameters on the behavior of the connection are investigated with different finite element models. The parameters include axial load level, steel ratio, compressive strength of gangue concrete and so forth.

2. FINITE ELEMENT MODEL

2.1 Material Constitutive Model

2.1.1 Gangue concrete

In order to simulate reasonably stiffness deterioration of the concrete, the concrete plastic damage model provided by ABAQUS 6.10 is used to simulate the concrete material [13]. For the compressive zone of the gangue concrete filled in the tube, owing to the constraint effect of tube on the gangue concrete, the gangue concrete is subjected to three-dimensional compressive stress. So the stress-strain relationship curve of the light aggregate concrete filled in steel tube proposed by Bohai Ji [14] is applied to simulation on the property of the gangue concrete filled in tube. For the compressive zone of the unrestrained gangue concrete, the stress-strain relationship curve of light aggregate concrete provided by Southeast University [15] is used, shown in the Figure 1. Because this relationship curve can make the computation easy to converge and also finite element analysis results computed by using the model conform well to the experimental results. The energy fracture criterion [16] can define the softening property of the concrete and enhance the convergence of computation. Hence, the fracture energy (G_f)-crack displacement relation curve is chosen to simulate the property of the gangue concrete in the tensile zone, shown in the Figure 2.

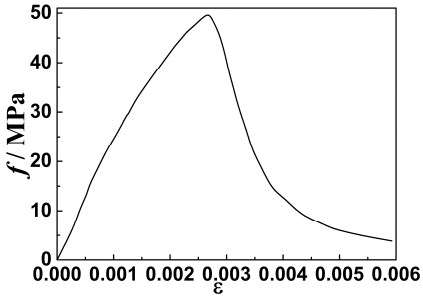

Figure 1. Constitutive Model of Unrestrained concrete

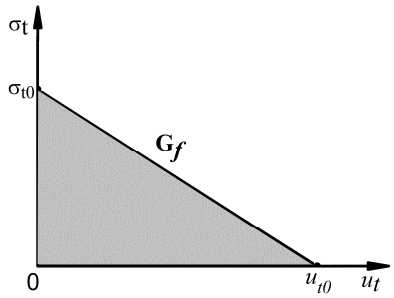

Figure 2. Fracture Energy-crack Displacement Relation Curve

2.1.2 Steel

For the steel of tube and strengthening ring, the stress-strain relationship curve of steel under cyclic loading [17] is applied, shown in the Figure 3. In addition, as Bauschinger effect [18] has an important influence on the bearing capacity of the connection, the Kinematic Hardening model with a von Mises yield surface [19] is applied in the constitutive model of steel. On the basis of many trials and previous researches, the double linear model with bearing capacity deterioration (USTEEL02) in the hysteretic constitutive model collection (PQ-Fiber) proposed by Tsinghua University [20] is used to simulate on the property of the rebar embedded in the gangue concrete beam. The model (USTEEL02) can present the hysteretic behavior of the rebar under cyclic loading and simulate the bond slip between rebar and gangue concrete. In the meanwhile, this model is easy to ensure the convergence of the computation and the accuracy of the finite element analysis results.

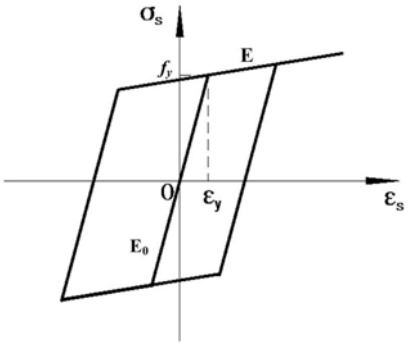

Figure 3. Stress-strain Relation of Steel

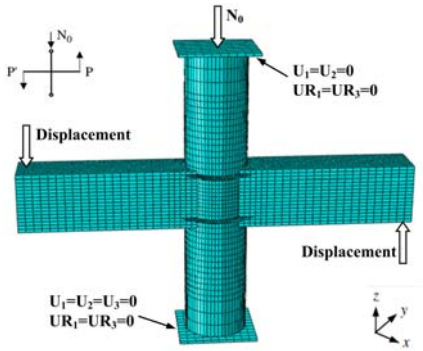

Figure 4. Analysis Model of Rebar-penetrated Connection

2.2 Element and Mesh

The 8-node brick element with reduced integration (C3D8R) is used as the element model to create the gangue concrete. The mapping self-customized meshing is chosen to mesh the gangue concrete. The continuous shell element is used for the steel and the type of element is the four-node conventional shell element with reduced integration (S4R). Truss element is applied to emulation of the rebar embedded in the beam. Figure 4 shows the finite element analysis model of the rebar-penetrated connection. In order to be same as boundary conditions in the experiment, all degrees of freedom except the rotation around y axis in the bottom of the column are constrained. The displacements in x, y direction and the rotations around x, z axes in the top of column are constrained to simulate the pinned connection. During the process of computation, the concentrated force is applied in the top of the column and two displacements with the same magnitude but the opposite direction are applied on both beam ends.

2.3 Contact Model

The contact model between tube and core gangue concrete is composed of the contact in both the normal direction and the tangential direction. Hard contact is adopted to simulate the contact in the normal direction so as to transfer fully the compressive stress between the contact surfaces. Coulomb friction model [21] is applied to simulation of the tangential force. In the model, the penalty friction formula with the elastic slip is used to compute the tangential force. The friction coefficient between the steel and gangue concrete column is taken as 0.6 [22]. As the plate in the top and bottom of the column only transfers the compressive stress in the normal direction, the plate is assumed as elastic plate with large stiffness to simulate the bases. The elastic modulus is defined as 1×10^{12}MPa and Possion's ratio is 0.0001 [23]. The shell-to-solid coupling is used to simulate the contact model between the plate and tube, while the hard contact is applied to contact model between the plate and gangue concrete filled in the tube [24].

3. VERIFICATIONS

3.1 Failure Modes

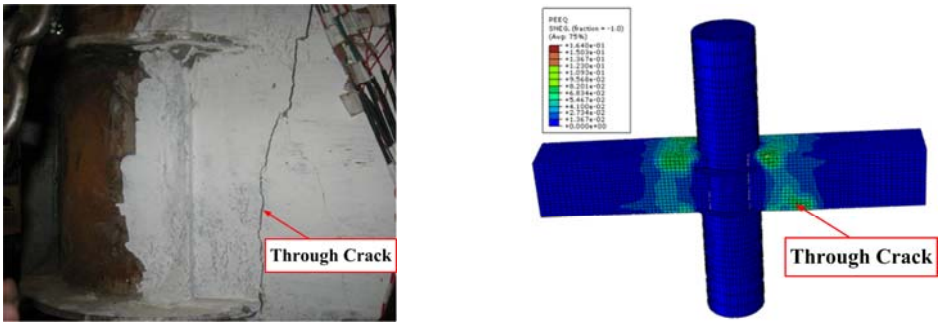

(a) Experiment (b) Finite Element Analysis

Figure 5. Failure Modes of the Rebar-penetrated Connection

Figure 5 shows failure modes of the rebar-penetrated connection in the finite element analysis and the experiment under low cyclic reversed loading. It is clear that, the failure mode received in the finite element analysis achieves a good agreement with those in the experiment. The collapse of the composite structure is due to the shear fracture of the reinforced gangue concrete beam, but the core region of the connection is not out of work and the collapse is not appeared in the GCFST column. This demonstrates that the rebar-penetrated connection between GCFST column and RGC beam has large stiffness and high strength to maintain the safety and stability of the whole building under the severe earthquake. Owing to the plastic hinge in the RC beam, the composite structure is collapsed with the shear fracture. These meet the design ideas of code for seismic design of buildings (GB50011-2010) that "strong column and week beam, strong connection and week members" [25].

3.2 Load-Displacement Hysteretic Curve

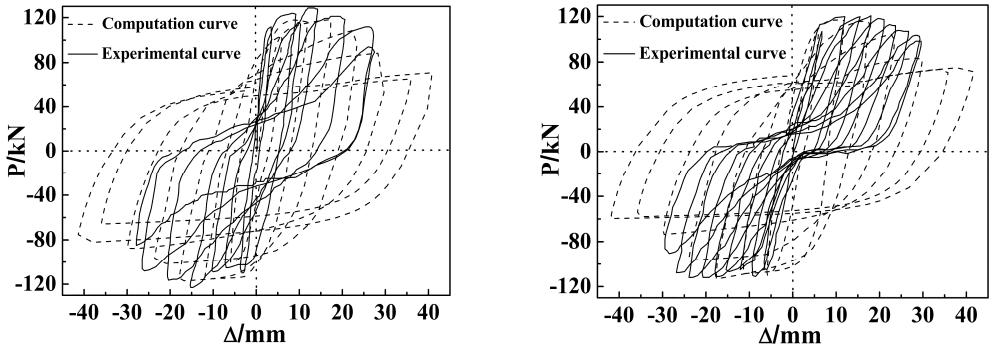

(a)Exterior Connection (b) Interior Connection

Figure 6. Comparison between Experimental Curve and Computation Curve

In order to verify the feasibility of finite element analysis models created using ABAQUS and the accuracy of finite element analysis results, finite element analysis results under low cyclic reversed loading are compared and analyzed with experimental results. Figure 6 shows the comparison of load (P)-displacement (Δ) hysteretic curves of exterior connection with one beam and interior connection with two beams between finite element analysis results and experimental results.

From Figure 6, it is clear that the stiffness and bearing capacity of the connection in the finite element analysis are consistent with the experimental values. However, the experimental curves have the obvious pinch effect phenomenon, while the computation curves are relatively fuller than the experimental curves. So, the shapes of the finite element analysis curves are a little different from experimental curves. But the whole changing trends of finite element analysis curves are accurate and reasonable, which are the same as the experimental curves.

The reasons to result in the difference between finite element analysis curves and experimental curves include: (1) the constitutive model of the gangue concrete used in the paper has some problems in simulating the large bond-slip between rebar and gangue concrete and the crack contact effect of the gangue concrete. At present, few research and analysis are investigated on the constitutive model of gangue concrete. Especially, no studies on the constitutive model of gangue concrete under cyclic loading have been done. However, the crack contact effect of the concrete generated by cyclic load makes a significant influence on the mechanical property of the concrete. Therefore, without the relatively reasonable constitutive model of gangue concrete, it is difficult to make finite element analysis results identical with experimental results. (2) To remedy the defeat of the constitutive model of gangue concrete, the spring model can be used to simulate the bond-slip between rebar and gangue concrete. However, the spring model provided by ABAQUS 6.10 only reflect well the bond-slip under the static loading. Also, the computation convergence is hard to realize with the spring model. As a whole, finite element analysis curves conform well to experimental curves and therefore finite element analysis models are able to complete the research content and purpose.

3.3 Skeleton Curve

Figure 7 shows the comparison of skeleton curves of exterior connection with one beam and interior connection with two beams between finite element analysis results and experimental results.

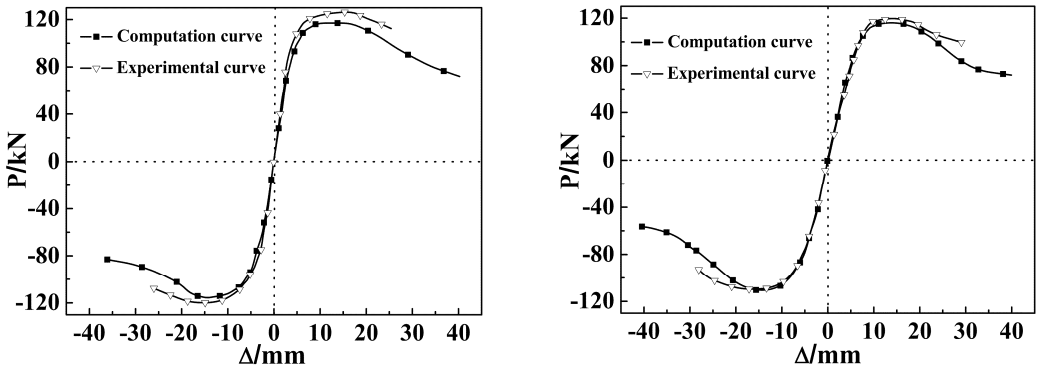

(a)Exterior Connection (b) Interior Connection

Figure 7. Comparison of Skeleton Curves between Experimental Curves and Computation Curves

Figure 7 shows that skeleton curves in finite element analysis are consistent with those in the experiment. The changing trends of finite element analysis curves are the same as experimental curves. Before the peak value of the curve, the curves in finite element analysis are identical with experimental curves. But the values in the finite element analysis are less than experimental values after the ultimate bearing capacity. It is due to the constitutive model of gangue concrete and tie model used to connect the different steel components. Tie model provided by ABAQUS 6.10 has some flaws in simulating the performance of the connection under cyclic loading.

Table 1. Comparison of Characteristic Loads between Experimental Results and Calculation Results

Number		P_0 (kN)	Δ_y (mm)	P_y (kN)	Δ_{max} (mm)	P_{max} (kN)	P_u (mm)
Exterior Connection	Experiment	47.65	5.92	107.4	17.31	122.53	104.5
	Computation	46.58	5.88	103.11	16.88	116.46	98.99
Interior Connection	Experiment	45.2	5.81	108.3	17.27	119.83	99.6
	Computation	44.40	5.85	107.15	17.15	117.53	99.05

NOTE: P_0 represents the cracking load; Δ_y represents the yield displacement; P_y represents the yield load; Δ_{max} represents the maximum displacement; P_{max} represents the maximum load; P_u represents the failure load.

Table 1 shows the comparison of characteristic loads between finite element analysis results and experimental results of the rebar-penetrated connection. The comparative analysis demonstrates that the difference of the bearing capacity between finite element analysis and the experiment is less than 10%. Based on Figure 6 and Figure 7, it is clear that finite element analysis results agree well with experimental results in the elastic stage. After ultimate bearing capacity, finite element analysis results are less than experimental results, but the difference is small. The changing trends of experimental curves and finite element analysis curves are reasonable and accurate. As a result, the models of the rebar-penetrated connection between GCFST column and RGC beam created by ABAQUS 6.10 are accurate and reliable to analyze the cyclic behavior of the rebar-penetrated connection.

4. STRESS DISTRIBUTION

In order to compare stress state of each component in different stages and analyze properly the force-transferring mechanism of the rebar-penetrated connection under cyclic loading, four characteristic points are marked in the hysteretic curve to describe the development of the crack in the gangue concrete [26]. Figure 8 shows the typical P-Δ curve of the connection between CFST column and RC beam. In the curve, A is defined as the point in which has the first crack in the RGC beam. B corresponds to the yield point of the rebar-penetrated connection. C indicates the ultimate bearing capacity (P_{max}) which corresponds to the peak point of the curve. D is the point of failure load (P_u) which is defined as the stage when the load reaches 85% of P_{max}.

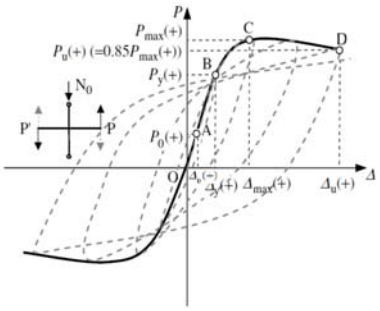

Figure 8. Typical P-Δ Curve

4.1 Gangue Concrete Filled Steel Tubular Column

Figure 9 shows the stress distribution (S33) of the gangue concrete filled in the tube corresponding to characteristic points A, B, C and D. Before the ultimate bearing capacity is reached, with the increase of the cyclic load, the compressive zone of the core gangue concrete filled in the tube develops along the length of the column and the compressive stress increases. In addition, when the constant load is exerted in the top of the column, the lateral deformation of the gangue concrete filled in the tube increases. The increase of lateral deformation results in the increasing confinement effect of the tube on gangue concrete filled in the tube. When the cyclic load arrives at the point C, the maximum compressive stress of the gangue concrete is 44.22MPa which amounts to about 1.86 f_c' and f_c' is the cylinder compressive strength of the gangue concrete. This demonstrates that the tube has an obvious confinement effect on the core gangue concrete and improves the bearing capacity of the gangue concrete to bear the external force. After the ultimate bearing capacity of the connection (point C), the compressive stress of the gangue concrete filled in the tube decreases gradually and then reaches at the failure load (point D).

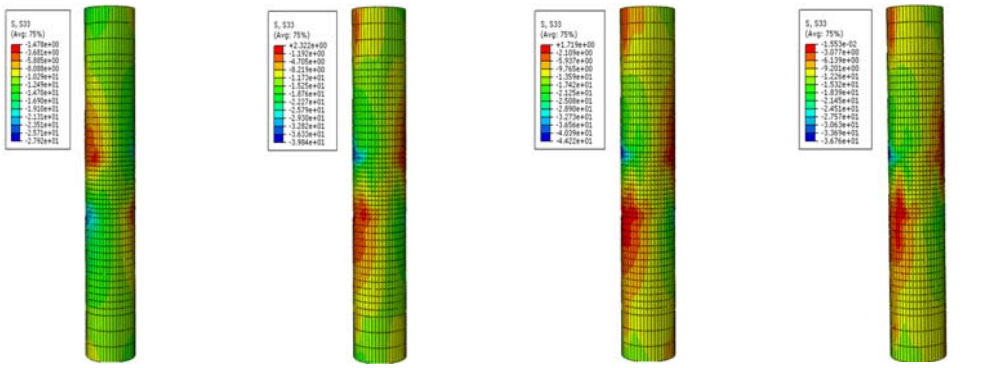

A B C D

Figure 9. Stress Distribution of the Core Gangue Concrete in the Tube (S33)

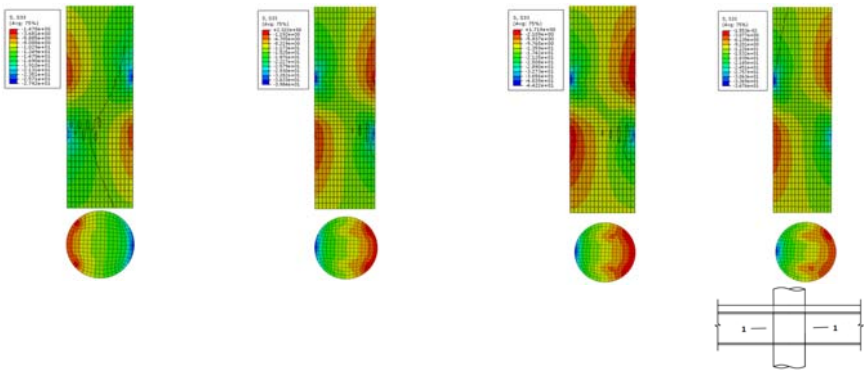

A B C D

Figure 10. Stress Distribution of the Transverse Section of the Core Gangue Concrete (S33)

Figure 10 shows the cut views of the gangue concrete filled in the tube corresponding to each characteristic point. As the cyclic load increases, the neutral axis gradually shifts from the tensile zone to the compressive zone. In the transverse section along the length of the column, the stress distribution with the shape of the diagonal compressive strut is formed obviously in the core area of the rebar-penetrated connection. This demonstrates that the shear stress produced by the cyclic load is undertaken by the core gangue concrete. The compressive strut develops and extends with the increase of the cyclic load before the ultimate bearing capacity, and the average stress of the compressive strut also increases. Owing to the confinement effect of the tube on the gangue concrete, the core gangue concrete is subjected to the tri-axial compressive stress so that the compressive stress of the core concrete reaches the maximum value at the point C. After the point C, the diagonal compressive strut continues developing with the increase of the cyclic load, but the compressive stress of the core concrete decreases due to the damage of the gangue concrete.

Figure 11 shows the vector diagram of the principle stress between column and beam. It is obvious that the diagonal compressive strut with 45 degree is formed to transfer the stress between GCFST column and RGC beam. This demonstrates that the GCFST column undertakes the shear stress produced by the cyclic load and the stress transferring route of the rebar-penetrated connection is clear and reasonable. Figure 12 shows the shear stress distribution (S12) in the core zone of the connection corresponding to each characteristic point. From the Figure 12, the shear stress with the shape of diagonal compressive strut is shown along the diagonal direction in the initial stage of loading. With the increase of the cyclic load, the shear stress gradually increases and the maximum area of the diagonal compressive strut is shown clearly at the point B. After the point B, the shear stress continues increasing and the area of the diagonal compressive strut develops and extends. Finally, a short column with the shape of the diagonal compressive strut is formed in the core zone of the rebar-penetrated connection.

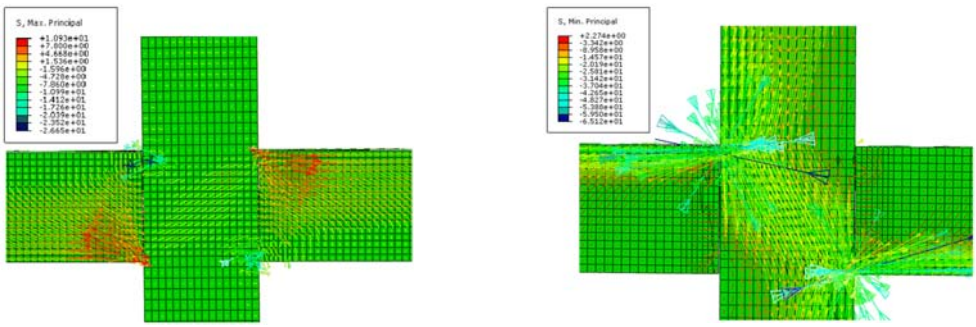

(a) Maximum principal stress (b) Minimum principal stress

Figure 11. Principle Stress of the Rebar-penetrated connection (S. Principle)

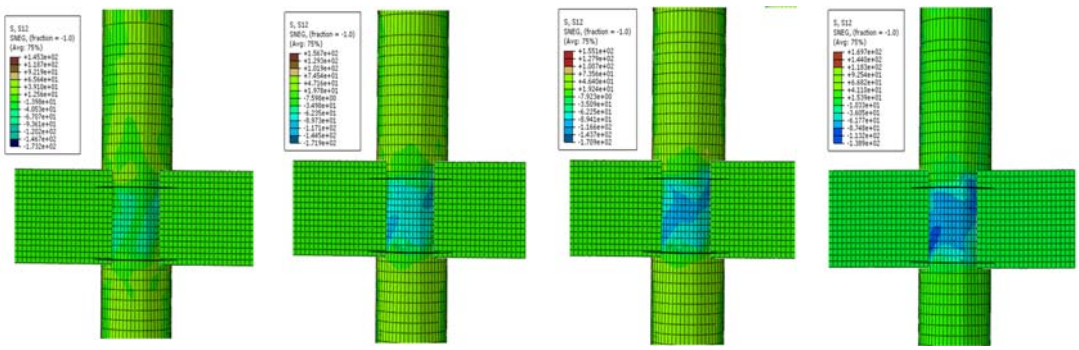

A B C D

Figure 12. Shear Stress Distribution in the Core Zone

Figure 13 shows Mises stress distribution of the steel tube and the strengthening ring. From the Figure 13, in the process of loading, the stress in most parts of the tube is relatively small. It is clear that the stress of the tube is positive. This means the tube has an effective confinement effect on the gangue concrete. The compressive stress and the tensile stress in the tube do not reach the yield strength of the steel. In the process of loading, no obvious buckling is appeared in the tube. The stress of the tube computed in the finite element analysis is consistent with the experimental results.

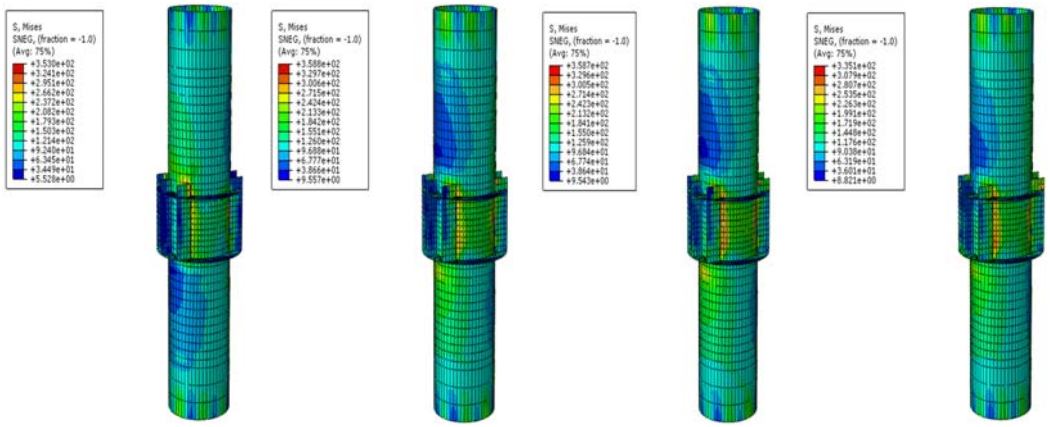

A B C D

Figure 13. Mises Stress Distribution of Tube and Strengthening Ring

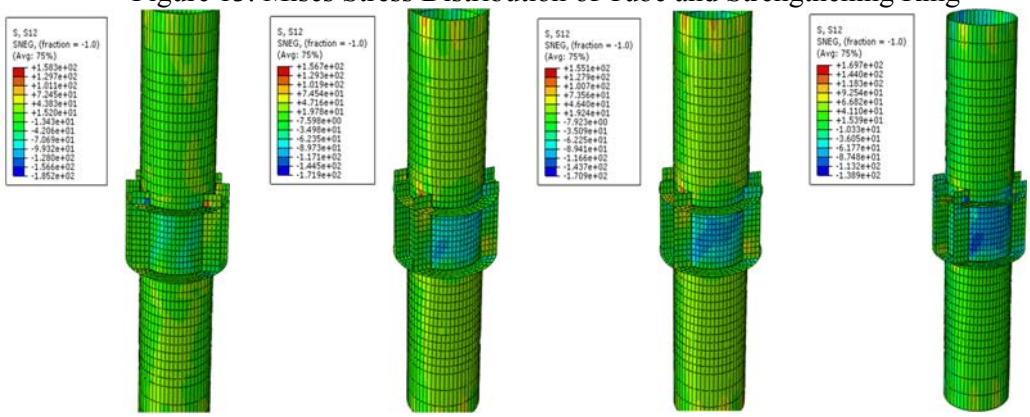

A B C D

Figure 14. Shear Stress Distribution of Tube and Strengthening Ring (S12)

From Figure 13, in the initial stage, the stress in the strengthening ring is small. With the increase of the cyclic load, the stress in the strengthening ring increases gradually and the shear stress in the core zone of the connection also increases. Figure 14 shows the shear stress distribution (S12) of the tube and strengthening ring corresponding to each characteristic point. Based on Figure 12, Figure 13 and Figure 14, when the rebar embedded in the RGC beam is yielded at the point B, the stiffening ring starts to undertake some shear stress under the axial load in the top of column and the bending moment produced by cyclic load. The stress in the strengthening ring is less than the yield strength of the steel and the strengthening ring is working in the elastic stage. It is obvious that the shear stress in the tube is larger than that in the stiffening rib. Therefore, while the stiffening rib is subjected to some bending moments, its primary function is to transfer the bending moment to the GCFST column and the majorities of bending moments produced by cyclic load are undertaken by the GCFST column.

4.2 Reinforced Gangue Concrete Beam

Figure 15 shows the stress distribution (S22) of the GC beam corresponding to each characteristic point. In the initial stage, the tensile zone of the GC beam is very small and the compressive zone develops along the length of the beam with the increase of the cyclic load. In the meantime, the tensile zone develops from the top surface to the middle part in the beam. The maximum stress of the GC beam concentrates on the part in which it is connected to the strengthening ring, and the beam finally collapses in the part. This meets the requirements of the seismic design principle that "strong connection and weak construction members, strong column and weak beam". The development process of the equivalent plastic strain of the GC beam corresponding to each characteristic point is shown in Figure 16. From Figure 15 and Figure 16, it is clear that the initial crack appears in the part of the beam in which it is connected to the strengthening ring. This phenomenon agrees well with the experimental results. With the increase of the cyclic load, the crack is developed along the length of the beam and the width of the crack increases. At the point B, a visible crack is shown in the part of the beam in which it is connected to the strengthening ring. After the point C, owing to the fracture of the gangue concrete, the bearing capacity of the rebar-penetrated connection decreases and the damage is gradually aggravated with the width of the crack increases. At the failure point D, a wide crack, which is penetrated through the depth of the beam, is formed in the same part of the beam. It is clear that the gangue concrete beam collapses, which means the composite structure fails. The development of the crack in the finite element analysis is the same as the experiment phenomenon.

Figure 17 shows stress distribution (S11) of rebar embedded in the GC beam corresponding to each characteristic point. With the increase of the cyclic load, the stress of the longitudinal rebar increases gradually and the shear stress undertaken by stirrup also increases. Under the axial load and the bending moment, the longitudinal rebar is yielded at the point B. This demonstrates that the rebar-penetrated connection is yielded and then enters into the elastic-plastic stage. When point C is reached, the stirrup is yielded under the shear stress and the majority of shear stress is transferred to GCFST column by stiffening ribs. After the point C, the stress of the longitudinal rebar increases, but it does not exceed the ultimate strength of the steel. This illustrates that the bending moment is endured by the longitudinal rebar. Figure 18 shows stress value curve of the longitudinal rebar along the length of beam at point C. It is clear that the maximum stress of the rebar concentrates on the connection part between the beam and the strengthening ring. The maximum value of the stress 415.45 MPa exceeds the yield strength of steel (f_y), but other parts of the rebar still work in the elastic stage. The stress of the longitudinal rebar are identical in the region below the strengthening ring. This demonstrates that the strengthening ring endures some bending moment produced by the cyclic load and therefore the strengthening ring plays an important role in undertaking the bending moment.

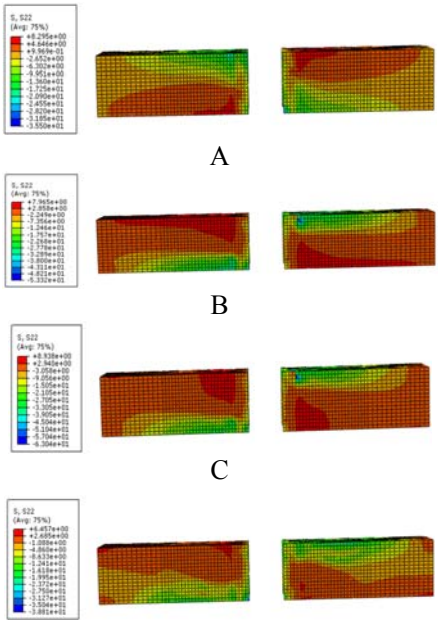

A

B

C

D

Figure 15. Stress Distribution of GC beam

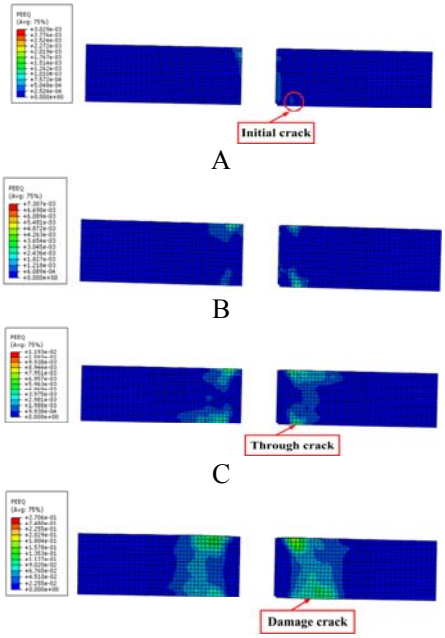

A

B

C

D

Figure 16. Equivalent Plastic Strain of GC beam

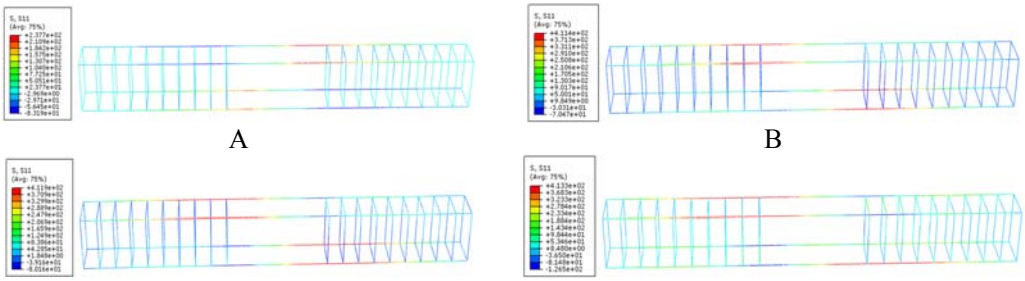

A

B

C

D

Figure 17. Stress Distribution of Rebar (S11)

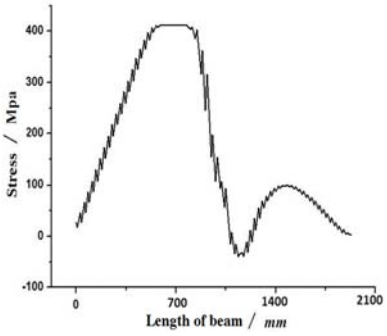

Figure 18. Stress Variation Curve along the Length of Beam

5. PARAMETRIC ANALYSIS

Table 2. Dimensions of the Connection Model

Number	D×t/ mm	*l*/ mm	L/ mm	*d*/ mm	α	*k*	λ	$f_{cu,c}$/ MPa	$f_{cu,b}$ / MPa	N_0/ kN	*n*
J6	325×6	1000	1500	60	0.078	0.853	36	30	30	1800	0.6
J6-*n*-0.2	325×6	1000	1500	60	0.078	0.853	36	30	30	600	0.2
J6-*n*-0.8	325×6	1000	1500	60	0.078	0.853	36	30	30	2250	0.8
J5-α-0.056	325×5	1000	1500	60	0.056	0.853	36	30	30	1800	0.6
J8-α-0.106	325×8	1000	1500	60	0.106	0.853	36	30	30	1800	0.6
J6-*d*-40	325×6	1000	1500	40	0.078	0.853	36	30	30	1800	0.6
J6-*d*-80	325×6	1000	1500	80	0.078	0.853	36	30	30	1800	0.6
J6-$f_{cu,c}$-20	325×6	1000	1500	60	0.078	0.853	36	20	30	1800	0.6
J6-$f_{cu,c}$-40	325×6	1000	1500	60	0.078	0.853	36	40	30	1800	0.6
J6-$f_{cu,b}$-20	325×6	1000	1500	60	0.078	0.853	36	30	20	1800	0.6
J6-$f_{cu,b}$-40	325×6	1000	1500	60	0.078	0.853	36	30	40	1800	0.6
J6-λ-25	325×6	1000	1000	60	0.078	0.853	25	30	30	1800	0.6
J6-λ-49	325×6	1000	2000	60	0.078	0.853	49	30	30	1800	0.6
J6-*k*-1.066	325×6	800	1500	60	0.078	1.066	36	30	30	1800	0.6
J6-*k*-0.711	325×6	1200	1500	60	0.078	0.711	36	30	30	1800	0.6

NOTE: D and t are external diameter and wall thickness of tube; *l* is the length of beam; L is length of column; *d* is the width of strengthening ring; α is steel ratio; k is stiffness of column and beam ratio; $f_{cu,c}$ is cubic compressive strength of gangue concrete in the tube; $f_{cu,b}$ is cubic compressive strength of unrestrained gangue concrete; *n* is axial load level; λ is the slenderness ratio of column.

Based on the stress distribution of the rebar-penetrated connection under low cyclic reversed loading, different finite element analysis models are created by changing the primary parameters to further analyze the behavior of the rebar-penetrated connection and remedy the experimental defects. The primary parameters include the axial load level, compressive strength of gangue concrete, steel ratio, and the width of the strengthening ring. The paper creates 15 finite element analysis models of the rebar-penetrated connection between GCFST column and RGC beam. The material parameters and geometrical parameters are shown in the table 2. Figure 19 shows the bending moment (M)-rotation (θ) hysteretic curves of 15 connections computed by ABAQUS 6.10.

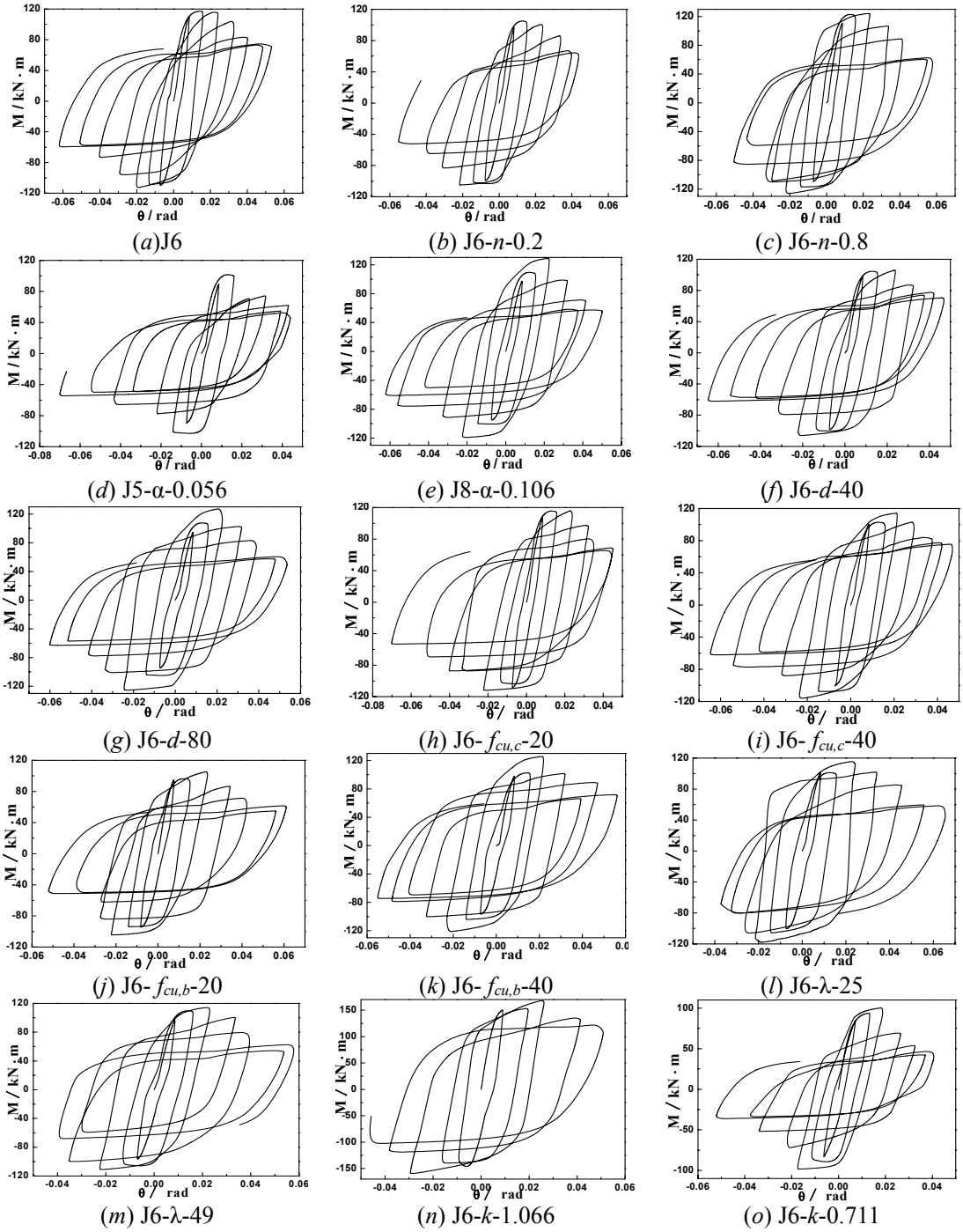

Figure 19. Bending Moment-rotation Hysteretic Curve of Rebar-penetrated Connection

5.1 Axial Load Level (*n*)

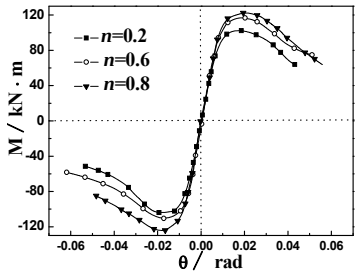

Figure 20. Effect of *n* on *M-θ* Curve

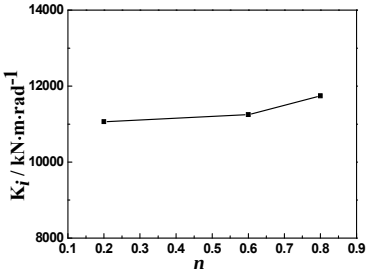

Figure 21. Effect of *n* on Initial Rigidity

Figure 20 shows the effect of the axial load level on skeleton curves of the M-θ curve under the condition to keep other basic parameters unchanged. Figure 21 shows the effect of axial load level on the initial rigidity. Based on Figure 20 and Figure 21, (1) under the cyclic loading, the axial load level has a clear influence on the flexural capacity of the rebar-penetrated connection. As the axial load level increases, the whole curve shifts up and the ultimate flexural bearing capacity increases gradually. (2) In the initial stage, the skeleton curve is almost linear and the length of the elastic stage increases with the increase of the axial load level. The initial rigidity of the connection increases gradually and almost presents the linear increase. (3)With the increase of the axial load level, the rigidity of the connection in the hardening stage increases.

5.2 GCFST Column Steel Ratio (α)

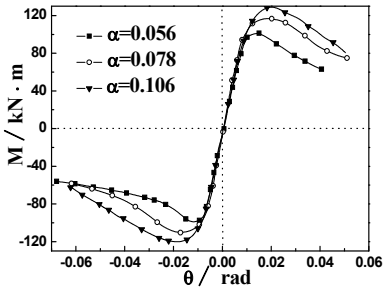

Figure 22. Effect of α on *M-θ* Curve

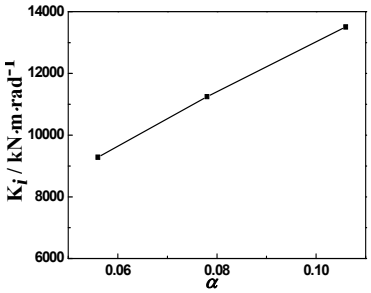

Figure 23. Effect of α on Initial Rigidity

In the paper, the wall thickness of tube is altered to change the steel ratio under the condition to keep other parameters unchanged. Figure 22 shows the effect of different steel ratio on skeleton curve of M-θ curve. Figure 23 shows the effect of steel ratio on initial rigidity. Based on Figure 22 and Figure 23, (1) under the cyclic loading, the connection with larger steel ratio has longer elastic stage and the initial rigidity of the connection with steel ratio of 0.106 is bigger 26% than that of connection with steel ratio of 0.056. Therefore, the steel ratio has a significant influence on the elastic stage of curve. (2)With the increase of the steel ratio, the flexural bearing capacity of the connection increases gradually and the whole curve shifts up without the change of curve shape. As a result, steel ratio has little effect on the shape and variation trend of the curve, but has an obvious influence on the bearing capacity of the rebar-penetrated connection.

5.3 Width of Strengthening Ring (*d*)

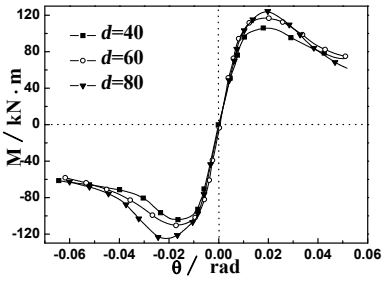

Figure 24. Effect of *d* on *M-θ* Curve

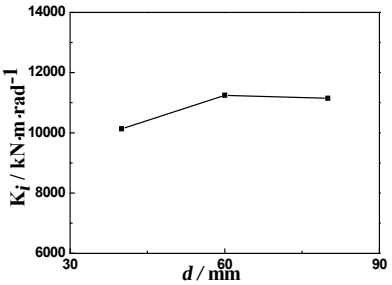

Figure 25. Effect of *d* on Initial Rigidity

Figure 24 shows the effect of the width of the strengthening ring on skeleton curve of the M-θ curve under the condition to keep other basic parameters unchanged. Figure 25 shows the effect of width of the strengthening ring on the initial rigidity. Based on Figure 24 and Figure 25, (1) As the width of strengthening ring increases, the flexural bearing capacity of the rebar-penetrated connection increases, but the shape and variation trend of the curves are barely changed. (2) In the initial stage, the initial rigidity of the connection maintains about 10000kN·m·rad^{-1} and does not change markedly with the increase of the width of strengthening ring. So, the width of strengthening ring has no obvious effect on the elastic stage of the curve. The ultimate flexural bearing capacity increases gradually with the increase of the width of strengthening ring. The ultimate flexural bearing capacity of the connection with the width of strengthening ring of 80 mm increases by 17% more than the connection with the width of strengthening ring of 40 mm, but the initial rigidity of the connection changes barely. As a result, the width of strengthening ring has an obvious effect on the behavior of the rebar-penetrated connection.

5.4 Compressive Strength of Gangue Concrete Filled in the Tube ($f_{cu,c}$)

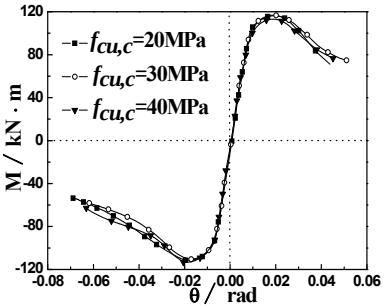

Figure 26. Effect of $f_{cu,c}$ on *M-θ* Curve

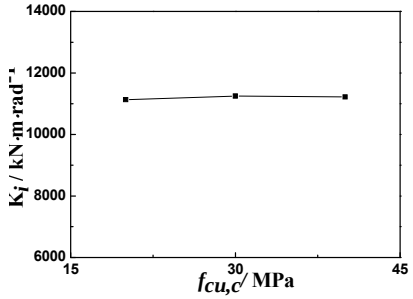

Figure 27. Effect of $f_{cu,c}$ on Initial Rigidity

Figure 26 shows the effect of the compressive strength of the gangue concrete filled in the tube on skeleton curve of the M-θ curve under the condition to keep other basic parameters unchanged. Figure 27 shows the effect of the compressive strength of the gangue concrete filled in the tube on the initial rigidity. Based on Figure 26 and Figure 27, the compressive strength of the gangue concrete filled in the tube has no effect on the mechanical performance of the connection. The shape and changing trend of the curves are not changed with the increase of the compressive strength of the gangue concrete filled in the tube. The initial rigidity of the connection remains unchanged with the change of the compressive strength. The paper focuses on the performance of the connection with the basic design theory "Strong column and weak beam", so the gangue concrete strength has no influence on the bearing capacity of the connection.

5.5 Compressive Strength of Gangue Concrete in the Beam ($f_{cu,b}$)

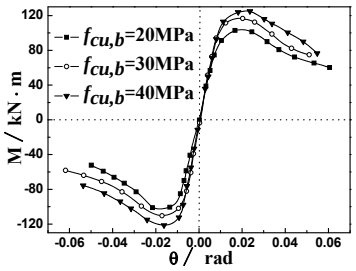

Figure 28. Effect of $f_{cu,b}$ on *M-θ* Curve

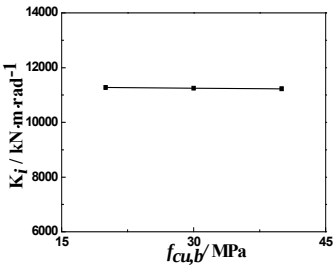

Figure 29. Effect of $f_{cu,b}$ on Initial Rigidity

Figure 28 shows the effect of the compressive strength of gangue concrete in the beam on skeleton curve of the M-θ curve under the condition to keep other basic parameters unchanged. Figure 29 shows the effect of compressive strength of gangue concrete in the beam on the initial rigidity. Based on Figure 28 and Figure 29, (1) As the compressive strength of the gangue concrete increases, the flexural bearing capacity of the rebar-penetrated connection increases, but the shape and changing trend of the curves are barely changed. (2) In the initial stage, the initial rigidity of the connection maintains about 11000kN·m·rad^{-1} and does not change markedly with the increase of the gangue concrete strength in the beam. So, the strength of the gangue concrete in the beam has no obvious effect on the elastic stage of the curve. With the increase of the gangue concrete strength in the beam, the length of the elastic stage increases. The ultimate flexural bearing capacity of the connection increases gradually. Therefore, the compressive strength of gangue concrete has a significant effect on the behavior of the rebar-penetrated connection.

5.6 Slenderness Ratio of GCFST Column (λ)

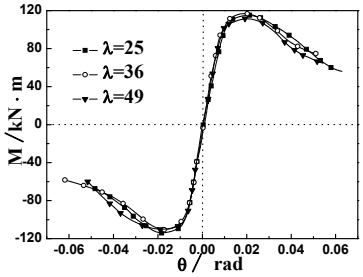

Figure 30. Effect of λ on *M-θ* Curve

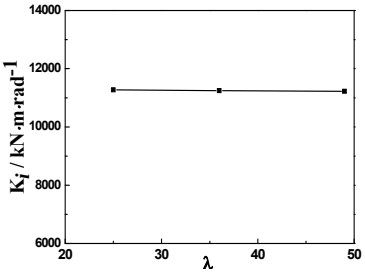

Figure 31. Effect of λ on Initial Rigidity

In the paper, the length of column is altered to change the slenderness ratio of the GCFST column under the condition to keep other basic parameters unchanged. Figure 30 shows the effect of different slenderness ratio on skeleton curve of M-θ curve. Figure 31 shows the effect of slenderness ratio on initial rigidity of the connection. Based on Figure 30 and Figure 31, the slenderness ratio has no effect on the mechanical performance of the rebar-penetrated connection. The shape and changing trend of the curves are not changed with the increase of the slenderness ratio. The initial rigidity of the connection remains identical with the change of the slenderness ratio.

5.7 Stiffness Ratio of Column and Beam (*k*)

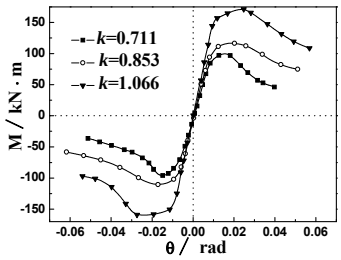

Figure 32. Effect of *k* on *M-θ* Curve

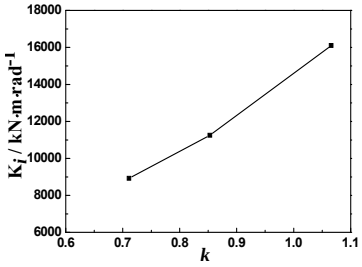

Figure 33. Effect of *k* on Initial Rigidity

In the paper, the length of beam is altered to change the stiffness ratio of column and beam under the condition to keep other basic parameters unchanged. Figure 32 shows the effect of different stiffness ratio on skeleton curve of M-θ curve. Figure 33 shows the effect of stiffness ratio on initial rigidity. Based on Figure 32 and Figure 33, (1) under the cyclic loading, as the stiffness ratio of column and beam increases, the flexural bearing capacity of the rebar-penetrated connection increases and the whole curves shifts up. At the same time, the initial rigidity increases gradually, but the shape and changing trend of the curves are not changed. (2) In the initial stage, the connection works in the elastic stage. With the increase of the stiffness ratio of column and beam, the length of the elastic stage increases and the initial rigidity of the connection increases gradually. The initial rigidity of the rebar-penetrated connection with the stiffness ratio of 1.066 is improved by 70% more than that of the connection with the stiffness ratio of 0.711. (3) As the stiffness ratio of column and beam increases, the ultimate flexural bearing capacity increases and the ultimate flexural bearing capacity of the connection with stiffness ratio of 1.066 is 1.71 times as large as that of the connection with the stiffness ratio of 0.711. As a result, changing the stiffness ratio of column and beam can affect the behavior of the rebar-penetrated connection.

6. CONCLUSIONS

The paper makes finite element analysis on the rebar-penetrated connection between GCFST column and RGC beam to investigate the behavior of the connection under low cyclic reversed loading. The following conclusions are drawn: (1) Based on the comparative analysis on finite element analysis results and experimental results, finite element analysis results are accurate and reasonable so that the finite element analysis models of the rebar-penetrated connection created in the paper can be used to further analyze the behavior of the rebar-penetrated connection. (2) The load-displacement hysteretic curve of the rebar-penetrated connection is full and spindle-shaped. The stiffness degeneration of the rebar-penetrated connection is reasonable. These demonstrate that the rebar-penetrated connection has excellent seismic performance. (3) The strengthening ring is subjected to some bending moments produced by cyclic load and plays an essential function on transferring the bending moment to the GCFST column. The majorities of the bending moment are undertaken by the GCFST column. (4) The maximum stress in the RGC beam concentrates on the part of the beam in which it is connected to the strengthening ring. The beam is collapsed in this part, which fits to the basic seismic design principle “Strong connection and weak members, strong column and weak beam”. (5) In the parametric analysis, axial load level, steel ratio, the compressive strength of the gangue concrete in the beam and the stiffness ratio of column and beam have obvious influences on the bearing capacity of the rebar-penetrated connection, but the shape and changing trend of the curves are not affected. The compressive strength of the gangue concrete filled in the tube and the slenderness ratio of the column has no effects on the behavior of the rebar-penetrated connection.

ACKNOWLEDGEMENT

This project was supported by Liaoning Science Fund (201102177), Technology Program of Ministry of Housing and Urban-Rural Development (2011-k3-23), Liaoning Talents Program (LR2011014).

REFERENCES

[1] Li, G.C. and Zhong, S.T., "Strength and Transverse Deformation Coefficient of Gangue Concrete Filled in the Steel Tube", Journal of Harbin University of Civil Engineering and Architecture, 2002, Vol. 35, No. 3, pp. 20-23.

[2] Li,G.C., Gao, C.F., and Xing, Y.J., "Development on Composite Structure of Steel and Gangue Concrete", Journal of Harbin Institute of Technology, 2003, Vol. 35, pp. 60-62.

[3] Li,G.C., Long, H.B. and Wang, Z.Q., "Inelastic Buckling Load of Gangue Concrete Filled Steel Tubular Middle Long Column under Axial Load", Journal of Shenyang Architectural and Civil Engineering Institute, 2004, Vol. 20, No. 4, pp. 291-293.

[4] Han, L.H., "Concrete Filled Steel Tubular Structure: Theory and Practice", Beijing: Science Press, 2000.

[5] Miller, D.K., "Lessons Learned from the Northridge Earthquake", Engineering Structure, 1998, Vol. 20, No. 4-6, pp. 249-260.

[6] Popov, E.P., Yang, T.S. and Chang, S.P., "Design of Steel MRF Connections before and after 1994 Northridge Earthquake", Engineering Structure, 1988, Vol. 20, No. 12, pp. 1030-1038.

[7] Beutel, A.J., Thambirathnama, D., Pererab, N., "Cyclic Behavior of Concrete Filled Steel Tubular Column to Steel Beam Connections", Engineering Structures, 2002, Vol. 28, No. 24, pp. 29-38.

[8] Kawaguchi, J., Shosuke, M., Hiroshi, A. and Shinya, Y., "Strength Deterioration Behavior of Concrete-filled Steel Tubular Beam-column", Composite Construction in Steel and Concrete II, Proceedings of an Engineering Foundation Conference, 1997, Vol. 1, pp. 825-839.

[9] Cai, J., Yang, C. and Su, H.Q., "Experimental Study of Joints of CFST Column Piercing Reinforcing Bar Hidden Bracket", Industrial Construction, 2003, Vol. 16, No. 3, pp. 61-64.

[10] Yao, G.H., Chen, Y.Y. and Lin, S., "Study on Seismic Performance of a New-type of Concrete-filled Steel Tube Column-RC Beam Joint", Industrial Construction, 2011, Vol. 41, No. 2, pp. 97-102.

[11] Yao, G.H., Chen, Y.Y. and Lin, S., "Finite Element Analysis on a New-type of Concrete-filled Steel Tube Column-RC Beam Joint", Special Structure, 2010, Vol. 27, No. 6, pp. 34-38.

[12] Zhong, S.T., "High-rise Concrete-filled Steel Tubular Construction", Harbin: Heilongjiang Science and Technology Press, 1999.

[13] Yu, T., Teng, J.G., Wong, Y.L. and Dong, S.L., "Finite Element Modeling of Confined Concrete-II: Plastic-damage Model", Engineering Structure, 2010, Vol. 32, No. 3, pp. 680-691.

[14] Ji, B.H. and Yang, M., "Confinement Effect and Strength Criterion of Lightweight Aggregate Concrete Confined by Steel Tube", Bridge Construction, 2006, Vol. 11, No. 4, pp. 11-14.

[15] Zhang, J.W., and Cao, S.Y., "Research on the Stress-strain Curves of Structural Lightweight Aggregate Concrete", Building Science, 2008, Vol. 24, No. 11, pp. 83-85.

[16] 3D Dassault Systems, "ABAQUS Version 6.4: Theory Manual, Users' Manual, Verification Manual and Example Problems Manual", The 3DEXPERIENCE Company, 2003.

[17] Han, L.H., "Concrete Filled Steel Tubular Structures: Theory and Practice (Second Edition)", Beijing: Science Press, 2007.
[18] Li,G.C. and Zhao, B.D., "Analysis of Deflection Process of Gangue Concrete-filled Steel Tubular Member under Bending Moment", Steel Construction, 2003, Vol. 18, No. 1, pp. 19-21.
[19] Boger, R.K., "Non-Monotonic Strain Hardening and its Constitutive Representation", Ph.D. disseration, The Ohio State University, 2006.
[20] Lu, X.Z., Ye, L.P. and Miao, Z.W., "Static-plastic Analysis on Seismic Performance of Construction", Beijing: China Building Industry Press, 2009.
[21] Hu, H.T., Huang, C.S. and Chen, Z.L., "Finite Element Analysis of CFT Columns Subjected to an Axial Compressive Force and Bending Moment in Combination", Journal of Constructional Steel Research, 2005, Vol. 61, No. 12, pp. 1692-1712.
[22] Liu, W., "The Study of Working Mechanism of Concrete Filled Steel Tube under Partial Compression", Journal of Harbin Institute of Technology, 2003, Vol. 35, No. 5, pp. 63-66.
[23] Li, G.C., Fang, C. and Yu, H.P., "Finite Analysis on Performance of Joint between Gangue Concrete Filled Steel Tubular Column with through Rebar and Gangue Concrete Beam under the Monotonic Loading", Applied Mechanics and Materials, 2012, Vol. 204-208, pp. 3724-3730.
[24] Tao, Z., Uy, B., Han, L.H. and Wang, Z.B., "Analysis and Design of Concrete-filled Stiffened Thin-walled Steel Tubular Columns under Axial Compression", Thin-Walled Structures, 2009, Vol. 47, No. 12, pp. 1544-1556.
[25] GB50011-2010, P.R.C. National Standard, "Code for Seismic Design of Buildings", Beijing: China Building Industry Press, 2010.
[26] Qu, H., Tao, Z. and Han, L.H., "Experimental Investigation on Cyclic Performance of CFST Column-RC Beam Joints Enclosed by Rebars", Industrial Construction, 2006, Vol. 36, No. 11, pp. 27-31.

SHEAR-TENSION INTERACTION STRENGTH OF J-HOOK CONNECTORS IN STEEL-CONCRETE-STEEL SANDWICH STRUCTURE

Jia-Bao Yan[1], J.Y. Richard Liew[2,*] and Min-Hong Zhang[3]

[1]*Research Fellow,* [2,3] *Professor, Department of Civil & Environmental Engineering, National University of Singapore, E1A-07-03, One Engineering Drive 2, Singapore 117576*
**(Corresponding author: E-mail: ceeljy@nus.edu.sg)*

Received: 7 December 2013; Revised: 15 January 2014; Accepted: 23 January 2014

ABSTRACT: Steel-concrete-steel (SCS) sandwich structure with ultra-lightweight cement composite core has been developed and proposed for applications in offshore, bridge and building constructions. A new form of J-hook connector is introduced to bond the steel face plates and cement composite core to form an integrated unit which is capable of resisting extreme loads. Design formulae were proposed to predict the shear, tension, and their interaction resistances of J-hook connectors. Thirty push-out tests and eighteen tensile tests were carried out on steel-concrete-steel sandwich plates with J-hook connectors embedded in different kinds of concrete to determine their shear and tension resistance, respectively. Nonlinear finite element (FE) model was also developed to predict the load-slip and ultimate behavior of J-hook connectors under combined shear and tensile loads. Finally, the design formulae were validated by comparing the predicted results with those obtained from tests and FE analyses. The formulae may be used to evaluate the tension, shear, and shear-tension interaction resistances of the J-hook connectors in steel-concrete-steel sandwich composite structures.

Keywords: Shear resistance, Tension resistance, Shear-tension interaction, Push-out test, Tensile test, J-hook connector, Steel-Concrete-Steel sandwich

1. INTRODUCTION

Steel-Concrete-Steel (SCS) sandwich structure, consisting of two steel face plates and an internal sandwiched concrete core, has been developed and used in civil and offshore constructions due to its excellent strength to cost performance. Mechanical connectors or adhesive materials are commonly used to bond the steel face plates and the concrete core to resist interfacial slip and thus enhance the bending moment and transverse shear resistance. However, the cohesive material was found to be less effective due to the presence of imperfections on the bonding surface that often resulted in crack initiation on the steel and concrete interface at the service stage [1]. Different types of mechanical shear connectors have been developed for SCS sandwich structures to overcome this disadvantage. Angle shear connectors were developed and used in the SCS sandwich structures as the bonding measures in Japan (See Figure 1a) [2]. Due to the shallow embedment of the angle connectors, bond failure tended to occur under transverse shear loads unless additional stiffening plates or transverse reinforcements were provided. Double skin structure with overlapped headed shear studs (as shown in Figure 1b) was developed and it was initially proposed as the alternative form of submerged tunnels [3]. The disadvantage of double skin structure with overlapping connectors is that the tension separation behavior greatly depends on the strength of the concrete core and the overlapping length of the connector. Therefore its use is restricted to sandwich structure with very thick core. If the overlapping length is not adequate as in the case of thin core, lack of tensile bond may cause uplifting of the face plates which would compromise the integrity of the structure. Another representative type of connector was the friction welded bar connectors in 'bi-steel' structure as shown in Figure 1(c) [4]. The friction welded connectors were proved to be effective in providing longitudinal shear and transverse shear resistance [5]. However, the equipment for the friction welding limited the thickness of the sandwich plate within 200-700 mm. To overcome this disadvantage and develop slim deck for offshore constructions, J-hook connectors were developed by Liew et al. [6] as shown in Figure 1(d). From the previous studies,

sandwich structure with J-hook connectors exhibited excellent performances under impact, blast, and fatigue loadings [7, 8]. This type of structure has great potential for applications in hulls of cargo tank, bridge decks, offshore decks, shear walls, and protective structures as shown in Figure 2.

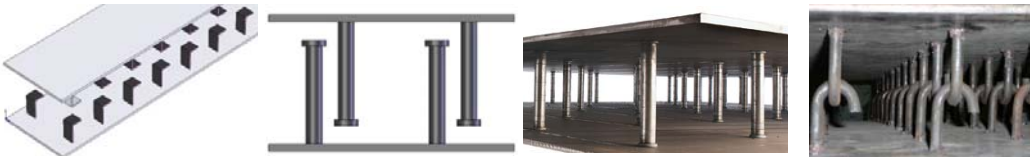

(a) SCS with angle connector (b) SCS with headed shear studs (c) Bi-steel structure (d) SCS with J-hook connectors

Figure 1. SCS with Different Shear Connectors

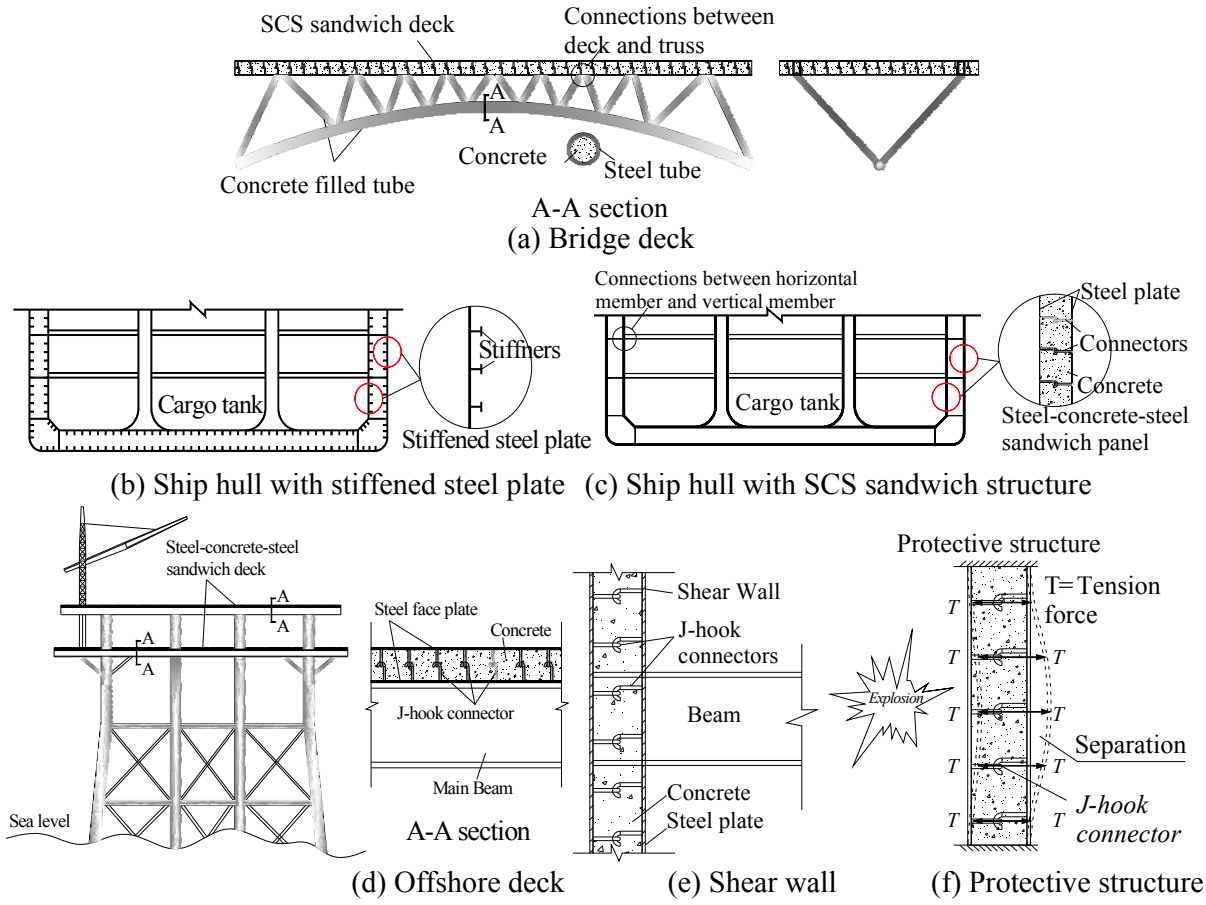

Figure 2. Potential Applications of the SCS Sandwich Structure with J-hook Connectors

The shear connectors have to resist shear force due to the relative slip between the concrete core and steel when the SCS sandwich composite deck is subjected to lateral loads. The most critical scenario is that they are subjected to combined shear and tension as in the case of connections between the tension members and sandwich deck as shown in Figure 2a; connections between the horizontal beams and shear walls as shown in Figure 2c and 2d; high shear region of the beam and slab, and sandwich structures subjected to impact and blast as shown in Figure 2e and 2f. The shear resistance of the headed shear stud connectors in the steel-concrete composite structures has been extensively studied by Viest [9], Driscoll and Slutter [10], Chinn [11], Steele [12], Davies [13], Mainstone and Menzies [14], Goble [15], Topkaya et al.[16], Ollgaard et al.[17], Oehlers and

Bradford [18], An and Cederwall [19], and Pallarés and Hajjar [20]. Research works on tensile resistance of the headed shear studs connectors has been also carried out by Cook et al. [21, 22], Zamora et al. [23], Shirvani et al. [24], Eligehausen and Balogh [25], Eligehausen et al. [26], Fuchs et al. [27], Bode and Roik [28], Balogh et al. [29], Klinger and Mendonca [30], and Pallarés and Hajjar [31]. The resistance of the anchorage under combined shear and tensile load was studied by Pallarés and Hajjar [31], McMakin et al. [32], Sari et al. [33], and Mirza and Uy [34]. From these literatures, it can be found that most of these experimental and numerical studies were carried out on headed studs to investigate their resistances against tension and shear forces as well as combined shear and tensile forces. There is little information for the J-hook connectors [35]. Meanwhile, design formulae for headed studs are also available in PCI [36] and ACI 318 [37]. However, the design guides have not been developed and validated for J-hook connectors to be used for sandwich structures with different concretes grades.

The innovations of the new concrete materials also challenge the application of SCS sandwich structure with the novel J-hook connectors. The use of lightweight concrete (LWC) or ultra-lightweight cement composite (ULCC) in Steel-Concrete-Steel (SCS) sandwich composite structure may lead to significant reduction in weight which is critical for offshore and floating structures. LWC with compressive strength 30 MPa and density 1450 kg/m^3 was used to produce slim deck for offshore structure [38]. More recently, ULCC with compressive strength 60 MPa and density of 1450 kg/m^3 has been developed by the authors for producing SCS sandwich composite structures [39].

Since J-hook connectors are used together with ultra-lightweight cement composite material (ULCC), the resistances of J-hook connectors acting on ULCC need to be carefully determined. However, most of the studies or design guidelines were mainly developed for headed shear studs rather than J-hook connectors. Hence, these design guidelines need to be examined whether they are applicable to the design of J-hook connectors. In this research, design formulae were firstly developed to predict the shear resistance, tension resistance, and shear-tension interaction resistance of the J-hook connectors. Thirty push-out tests and eighteen tensile tests were carried out to obtain the shear and tension resistances of the J-hook connectors embedded in normal weight concrete (NWC), LWC, and ULCC, respectively. These push-out tests and tensile tests were also used to validate the finite element (FE) model. With the validated FE model, shear-tension interaction resistances of the J-hook connectors were obtained through the FE analysis (FEA). The test data and FEA results were used to validate the design formulae to predict shear-tension interaction resistance of the J-hook connectors in sandwich structures.

2. RESISTANCES OF J-HOOK CONNECTORS

A pair of interlocking J-hook connectors may be subject to longitudinal shear force, tensile force, and most likely combined shear and tension forces. The formulae for calculating the resistances against such forces are given in the following subsections.

2.1 Shear Resistance

Design codes such as ACI 318 [37] and Eurocode 4 [40] may be used to predict the shear resistance of headed shear studs. In Eurocode 4 [40], the design shear resistance of the J-hook connectors may be determined as

$$V_u = \frac{0.29\alpha d^2\sqrt{f_{ck}E_c}}{\gamma_V} \le \frac{0.8 f_u \pi d^2/4}{\gamma_V} \quad (1)$$

where f_u = ultimate strength of the steel; d= diameter of the connector, mm; $\alpha = 0.2(h_{ef}/d+1)$ for $3 \le h_{ef}/d \le 4$, or $\alpha = 1$ for $h_{ef}/d > 4$; h_{ef}= overall nominal height of headed stud connector, mm; f_{ck} = compressive strength of concrete cylinder; E_c = elastic modulus of concrete; γ_V = the partial factor for connector and may be taken as 1.25 [40].

A semi-empirical formula to predict the design shear resistance was proposed for J-hook connectors by Yan et al. [35] based on calibration with results from push out tests:

$$V_J = \frac{0.855 f_{ck}^{0.265} E_c^{0.469} A_s \left(h_{ef}/d\right)^{0.154}}{\gamma_V} \le \frac{0.8 f_u \pi d^2}{4\gamma_V} \quad (2)$$

where h_{ef}= nominal height of J-hook connector, mm; f_{ck} in MPa; E_c in MPa;; A_s=cross sectional area of connector, mm^2; f_u = ultimate tensile strength of the connector; A_s=cross sectional area of connector.

2.2 Tension Resistance

Four possible failure modes may take place when a pair of interlocked J-hook connectors is subjected to axial tension, which are concrete breakout failure, pullout failure, J-hook tensile failure, and punching shear failure of the steel plate to which the connector is welded (See Figure **3**). The formulae used to predict the resistances corresponding to these four failure modes are developed below.

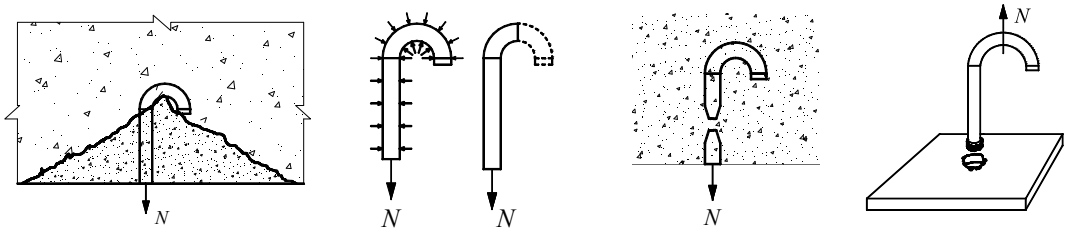

(a) Concrete breakout failure (b) Pullout failure (c) Tensile fracture (d) Punching shear failure of steel plate

Figure 3. Failure Modes of the J-hook Subject to Direct Tension

2.2.1 Concrete breakout failure

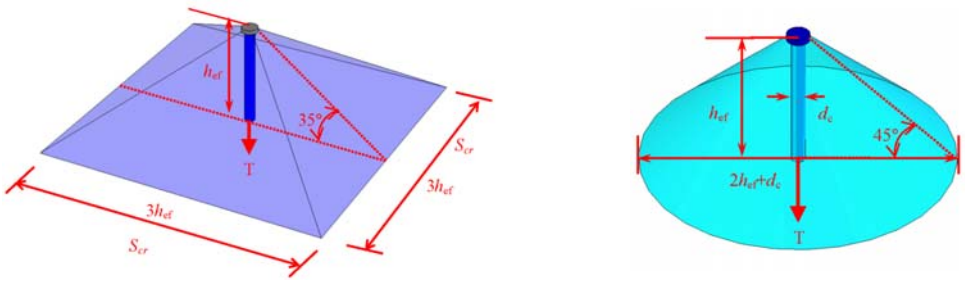

(a) Concrete capacity design method (b) 45-degree cone method

Figure 4. Illustration on Methods of Calculating Concrete Breakout Resistance

The concrete breakout resistance may be calculated by the 45-degree concrete cone model, which is obtained by modifying CEB-FIP [41] and ACI 349 [42] as

$$N_{CB} = \frac{0.333\sqrt{f_{ck}}A_N}{\gamma_c} \tag{3}$$

where $A_N = \pi h_{ef}^2 \left(1 + d / h_{ef}\right)$ is the projected area of the cone failure surface as shown in Figure **4**; d = diameter of the connector. γ_c = partial factor for concrete and may be taken as 1.5 in accordance to with Ref. [43].

2.2.2 Pullout failure

The pullout failure of the connector is due to compression failure of the concrete surrounding the connector as shown in Figure 3b. The design pullout resistance of the connector $N_{pl}^{'}$ can be calculated by modifying design formulae in ACI [37] as

$$N_{pl}^{'} = \psi_{c,p} N_P / \gamma_c \tag{4a}$$

where $\psi_{c,p}$ =1.4 for connectors in uncracked concrete and 1.0 for connectors in cracked concrete under service load. N_P = pullout resistance of connector. For hook shaped connectors, the pullout resistance N_p can be calculated by [37]:

$$N_P = 0.9 f_{ck} e_h d \tag{4b}$$

where e_h = distance from the inner surface of the shaft of a J-hook connector to the outer tip of the J-hook as shown in Figure 6, and $3d \le e_h \le 4.5d$.

However, for a pair of J-hook connectors, the influence of interlocked J-hook should be considered. The tensile force acting on one connector will be partially transmitted directly to the other connector and partially to the surrounding concrete. Therefore, the tension resistance of a pair of J-hook connectors consists of two parts i.e. pullout resistance of a single J-hook and hook straightening resistance of the bare J-hook. This can be expressed as the following

$$N_{Pl} = N_{pl}^{'} + N_{hs} \tag{5}$$

where N_{hs} = bare hook straightening resistance, and equal to $0.116 f_y d^2 / \gamma_{M0}$; f_y= yield strength of the steel; $N_{pl}^{'}$ can be obtained from Eq. 4a. γ_{M0} = partial factor and may be taken as 1.00 for connector design in accordance to Ref. [44].

2.2.3 J-hook tension failure

Tensile fracture of the J-hook connector may occur as shown in Figure **3**c. The tension resistance of the steel shank N_S may be estimated as

$$N_S = \frac{\left(\pi d^2 / 4\right) f_{us}}{\gamma_{M2}} \tag{6}$$

where f_{us} = ultimate tensile strength of the steel connector; γ_{M2} = partial factor and may be taken as 1.25 for connector design in accordance to Ref. [45].

2.2.4 Punching shear failure of the steel face plate

The punching shear failure of the steel face plate is shown in
Figure **3**d. In Eurocode 3 [44], the punching shear resistance N_{ps} of the steel face plate that the connectors were welded to is calculated by

$$N_{ps} = \frac{\pi dt\left(f_y / \sqrt{3}\right)}{\gamma_s} \tag{7}$$

where *d*= diameter of the connector; *t* = thickness of the steel plate; f_y = characteristic yield strength of the steel plate; γ_s = 1.0 is the partial factor for steel plate [44].

2.2.5 Design tension resistance of J-hook connectors

In summary, the tension resistance of the J-hook connectors may be determined by the smallest value of the resistances calculated by Eqs. (3), (5), (6), and (7). Hence, the tension resistance of the J-hook connector in the ULCC can be determined by

$$N_u = \min\left(N_{CB}, N_{pl}, N_s, N_{ps}\right) \tag{8}$$

2.3 Interaction of Shear and Tension

The design resistance of the connector under combined shear and tensile loads may be calculated as follow [36, 37]:

1) If applied shear force $V \le 0.2V_u$, full resistance in tension shall be permitted:

$$N \le N_u \tag{9a}$$

2) If applied tensile force $N \le 0.2\phi N_u$, full resistance in shear shall be permitted:

$$V \le V_u \tag{9b}$$

3) If $V > 0.2\phi V_u$ and $N > 0.2\phi N_u$, then

$$\frac{V}{V_u} + \frac{N}{N_u} \le 1.2 \tag{9c}$$

Another expression of the shear-tension interaction relationship is given as

$$\left(\frac{V}{V_u}\right)^{5/3} + \left(\frac{N}{N_u}\right)^{5/3} \leq 1.0 \tag{10}$$

where, V= design shear force; V_u= design shear resistance of the connector calculated by Eq. 1 or 2; N= design tension force, N_u = design tension resistance of the connector calculated by Eq. 8.

Eqs. 9(a-c) and Eq. 10 may be used to estimate the resistance of J-hook connectors subjected to combined shear and tension forces. Their accuracies will be evaluated based on calibration with test data and results from finite element analysis which will be reported in Section 5. Based on experimental and numerical calibration, suitable formulae will be recommended for design purpose. These recommendations will be used for the evaluation of SCS sandwich section subjected to moment and transverse shear resistance.

In Eqns. 1-10, partial factors in Eurocodes [40, 43-44] were used to calculate the corresponding design resistances of J-hook connectors. However, for comparision with test results, these factor should be taken as 1,0 (i.e., $\gamma_C = \gamma_s = \gamma_{M2} = 1.0$) for the calculation of the resistance of J-hook connector.

3. PUSH-OUT AND TENSILE TESTS ON J-HOOK CONNECTORS

The shear and tension resistances of the J-hook connectors were studied through push-out tests and tensile tests, respectively. These push-out and tensile tests were used to validate the design formulae to calculate the shear and tension resistance of J-hook connector.

3.1 Concrete Materials used in Push-out and Tensile Tests

A type of fibre-reinforced ultra-lightweight cement composite (ULCC) was developed with 28-day compressive strength about 60 MPa and a low density of 1450 kg/m^3 [39]. Compared with typical normal weight concrete with similar strength (60 MPa) and density of 2400 kg/m^3, the ULCC has higher specific strength (strength-to-density ratio). Besides a 40% weight reduction from normal weight concrete, the ULCC exhibits comparable tensile strengths to the normal weight concrete of similar compressive strength. Due to its porous structure, the ULCC has lower modulus of elasticity approximately 50% that of normal weight concrete.

Table 1 shows mechanical properties of different concrete mixtures at 28 days. The stress-strain curve of the ULCC under compression was compared with the NWC of similar compressive strength as shown in Figure 5. The ULCC was made of ordinary Portland cement, cenospheres, 6 mm polyvinyl alcohol (PVA) fibres, silica fume, and chemical admixtures. The PVA fibres (0.5% by volume) were used to reduce the brittleness of the ULCC.

Table 1. Basic Material Properties of Various Types of Concretes at Age 28-day

Concrete	w (kg/m^3)	f_{cu} (MPa)	f_{ck} (MPa)	f_{ck} / f_{cu} Ratio	f_{sp} (MPa)	f_t (MPa)	E_c (GPa)	u
ULCC C60	1450	64.0	64.6	1.01	4.4	6.7	16.0	0.25
LWC C25$^+$	1602	-	26.7	-	2.2	-	17.5	0.22
LWC C45$^+$	1852	51.7	47.9	0.93	3.3	-	18.0	0.22
LWC C60$^+$	1883	-	60.6	-	4.6	-	20.8	0.24
LWC C30	1450	24.0	24.0	1.00	-	1.8	11.7	0.24
LWFC C30	1450	30.0	28	0.93	-	4.5	12.3	0.22
NWC C30	2337	46.1	33.1	0.72	3.9	4.0	20.2	0.24
NWC C45	2400	62.4	48.7	0.78	4.4	-	24.0	0.25
NWC C80	2365	-	70.0	-	4.8	-	39.0	0.25
HPC	2750	-	180	-	11.8	-	60.0	0.25

$^+$ Natural sand was used to replace fine expanded clay lightweight aggregate; LWFC= lightweight fiber reinforced concrete; w = density; f_{cu}= compressive strength of cube; f_{ck} = compressive strength of cylinder; f_{sp} = splitting strength of cylinder; f_t = flexural tensile strength of prism; E_c = elastic modulus; u=Poisson's ratio.

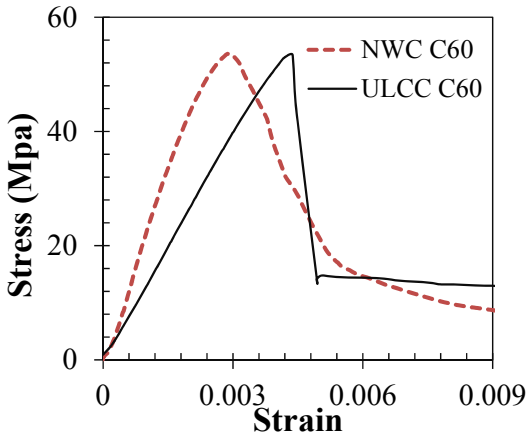

Figure 5. Comparison of Stress-strain Curves between NWC and ULCC

The LWC was also used in the tests. Ordinary Portland cement and expanded clay type of lightweight coarse and fine aggregate with an average particle density of 1000 kg/m^3 and maximum particle size of 8 mm, and water were used to produce the lightweight concrete. In some mixtures the natural sand was used to replace the fine aggregate. In order to improve the tensile strength of the LWC, steel fibres were used in several specimens. The properties of the LWC are shown in Table 1.

The NWC was made of Portland cement, granite coarse aggregates (Max size = 20 mm), natural sand, and water. Densities for the natural sand and granite aggregate were 2560 and 2610 kg/m^3, respectively.

Normal weight high performance concrete (HPC) with a compressive strength of 180 MPa was used in one specimen to investigate the effects of high compressive strength and elastic modulus on the confinement.

3.2 Push-out Test on J-hook Connectors

The shear resistance of connectors embedded in concrete is traditionally obtained from the push-out test. In Eurocode 4 [40], a recommended test standard for headed shear studs is given. However, this proposed method is not suitable for a pair of directly interacted connectors. A test method recommended by Xie et al. was used for the push-out test on the J-hook connectors that was originally developed for the friction welded connectors in Bi-steel structures [45].

3.2.1 Test setup

The geometry of the sandwich specimens and load apparatus for push-out tests are shown in Figure 6. A pair of J-hook connectors was welded separately on two steel plates as shown in Figure 6. Three types of concretes NWC (C30, C45, and C60), LWC (C25, C30, and C45) and ULCC were used in this test. The diameters of the J-hook connectors were 10, 12, 16 and 20 mm. Four different thicknesses of concrete cores 80, 100, 150, and 200 mm were investigated. Dimensions and properties of the materials for thirty specimens are given in Table 2.

All the specimens were cured and tested at 28 days after the casting. A steel plate spreader was used to averagely distribute the load from the actuator to the concrete core. The interfacial slips between the concrete core and steel face plates were recorded by the Linear Varying Displacement Transducers (LVDTs).

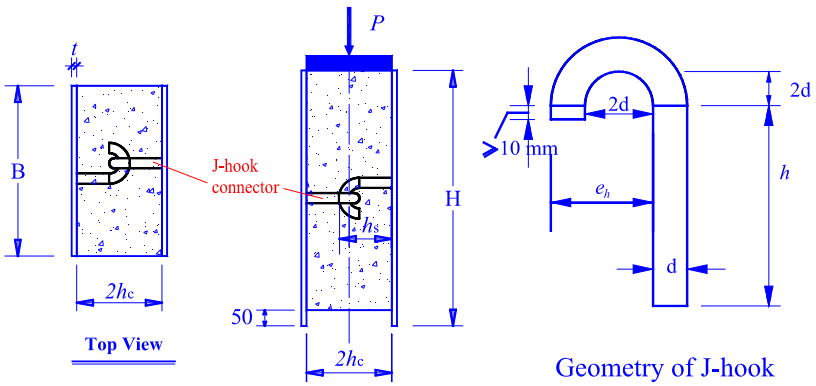

Figure 6. Push-out Test Setup and Geometry of Specimen

3.2.2 Test results and validation of design equation

The shear resistance of one J-hook connectors and the failure modes of the specimens were listed in Table 2. Three types of failure modes were observed from the test i.e. shear failure across the connector's shank, concrete failure, and shear failure across the welding toe. The detailed information of the failure modes and shear-slip behaviour of the J-hook connectors was reported by Yan et al. [35].

The shear resistances predicted by Eurocode 4 [40] and Eq. 2 are compared with the test results in Figure 7 and Table 2. It can be observed that both equations underestimate the shear resistance of J-hook connectors. There are no significant differences in terms of average test-to-prediction ratios (mean) and coefficient of variance (COV) between the proposed model (Eq. 2) (mean=1.26, COV=0.16) and the Eurocode 4 [40] (mean=1.22, COV=0.18). However, the proposed model (Eq. 2) offers safer predictions with test-to-prediction ratio is larger than 1.0 compared with the Eurocode 4 method [40].

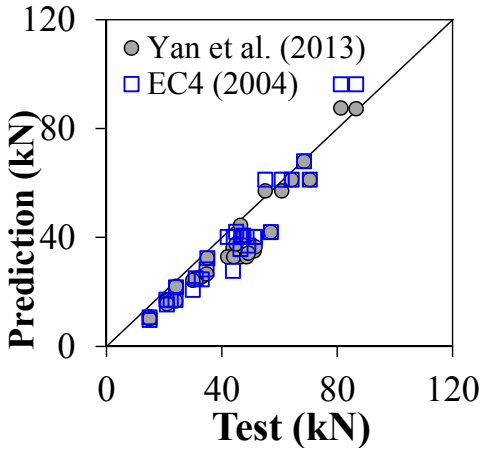

Figure 7. Comparisons of Shear Resistance between Predictions and Test Results

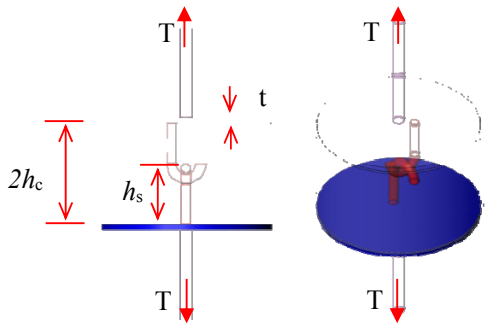

Figure 8. Tensile Tests on J-hook Connector

Table 2. Details of Push-out Test Specimens

Specimen	t mm	d mm	h_c mm	h_s mm	B mm	f_u MPa	f_{ck} MPa	E_c GPa	w kg/m^3	$\frac{h_c}{d}$	V_t (kN)	Failure Mode	V_{J2} (kN)	V_t/V_{J2}	V_{J1} (kN)	V_t/V_{J1}
PN1	6	9.9	40	49.9	300	405	48.3	32.5	2400	4.04	31.0	SS	24.9	1.24	24.9	1.24
PN2	6	15.5	40	55.5	300	450	65.0	30.0	2400	2.58	68.5	SS	67.9	1.01	67.9	1.01
PN3	6	11.8	50	61.8	250	464	45.0	37.0	2355	4.24	47.5	SS	40.6	1.17	40.6	1.17
PN4	6	12.0	50	62.0	250	464	70.0	39.0	2365	4.17	57.0	SS	42.0	1.36	42.0	1.36
PN5	6	15.5	75	90.5	250	405	45.0	37.0	2355	4.84	64.2	SS	61.1	1.05	61.1	1.05
PN6	6	15.5	75	90.5	250	405	70.0	39.0	2365	4.84	70.5	SS	61.1	1.15	61.1	1.15
PN7	6	11.8	75	90.5	250	480	47.7	24.0	2343	6.36	47.2	SS	39.2	1.20	42.0	1.12
PN8	6	11.7	75	90.5	250	450	34.1	19.5	2329	6.41	36.4	CC	32.1	1.14	32.4	1.12
PL1	6	9.9	40	49.9	300	405	28.5	12.7	1450	4.04	20.8	CC	16.7	1.25	17.1	1.22
PL2	6	15.5	40	55.5	300	450	26.4	11.7	1440	2.58	43.9	CC	36.0	1.22	27.7	1.58
PL3	6	15.5	40	55.5	300	450	30.2	17.0	1700	2.58	46.5	CC	44.4	1.05	35.8	1.30
PL4	6	11.5	40	51.5	300	450	30.2	17.0	1700	3.48	33.1	CC	25.6	1.29	24.6	1.34
PL5	6	10.0	40	50.0	200	610	24.0	11.7	1440	4.00	21.0	CC	15.6	1.34	15.4	1.37
PL6	6	7.9	40	47.9	200	610	24.0	11.7	1440	5.06	15.0	CC	10.1	1.48	9.6	1.56
PL7	6	11.8	50	61.8	250	464	25.0	11.5	1345	4.24	24.2	CC	22.0	1.10	21.7	1.12
PL8$^+$	6	10.0	75	90.5	250	450	51.0	19.0	1874	7.50	34.8	SS	26.4	1.32	28.3	1.23
PL9$^+$	6	11.7	75	90.5	250	450	48.1	18.0	1852	6.41	49.2	SS	33.8	1.45	36.9	1.33
PL10$^+$	6	11.7	75	90.5	250	450	18.1	15.0	1596	6.41	30.0	CC	24.0	1.25	20.7	1.45
PLF1	6	9.9	40	49.9	300	405	28.1	12.6	1460	4.04	22.6	CC	16.5	1.37	16.9	1.34
PLF2	6	10.0	40	50.0	200	610	28.0	12.3	1460	4.00	24.0	CC	16.7	1.44	17.0	1.41
PLF3	6	7.9	40	47.9	200	610	28.0	12.3	1460	5.06	15.0	CC	10.8	1.39	10.6	1.41
PU1	4	11.8	50	61.8	250	464	60.0	16.5	1490	4.24	46.8	CC	32.9	1.42	40.2	1.16
PU2	6	11.8	50	61.8	250	464	60.0	16.5	1440	4.24	42.1	CC	32.9	1.28	40.2	1.05
PU3	8	11.8	50	61.8	250	464	60.0	16.5	1440	4.24	44.2	CC	32.9	1.35	40.2	1.10
PU4	12	11.8	50	61.8	250	464	60.0	16.5	1440	4.24	48.6	CC	32.9	1.48	40.2	1.21
PU5	6	11.8	75	86.8	250	464	60.0	16.5	1440	6.36	51.2	SS	35.0	1.46	40.2	1.27
PU6	6	11.8	100	111.8	250	464	60.0	16.5	1440	8.47	51.6	SS	36.6	1.41	40.2	1.28
PU7	6	15.5	75	90.5	250	405	57.0	16.5	1440	4.84	55.1	SW	57.1	0.97	61.1	0.90
PU8	6	19.5	75	94.5	250	403	57.0	16.5	1440	3.85	86.6	SW	87.2	0.99	96.3	0.90
PU9	6	15.5	75	90.5	200	405	57.0	16.5	1440	4.84	60.8	SS	57.1	1.07	61.1	0.99
Mean														1.26		1.22
COV														0.16		0.18

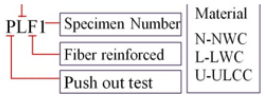

$^+$ Presents lightweight concrete with natural sand; NWC= normal weight concrete; LWC= light weight concrete; ULCC= ultra-light weight cement composite; f_u= ultimate tensile strength of connector; f_{ck} = compressive strength of cylinder; B, d, h_c, h_s, and t are as shown in Fig. 6; E_c = elastic modulus; w= density of concrete; CC=concrete crack failure; SF=shear failure cross the shank; SW=shear failure cross the welding; V_t=shear resistance by test; V_{J1}=shear prediction by Eq. 1; V_{J2}=shear prediction by Eq. 2; COV=coefficient of variance; Mean= average test-to-prediction ratio.

3.3 Tensile Test of J-hook Connectors

The tension resistance of a pair of interlocked J-hook connectors in SCS sandwich structure is obtained from the direct tensile test [46].

3.3.1 Test setup

The test setup is shown in Figure 8. Details of the specimens are summarized in Table 3. Steel moulds were used in the specimens to simulate confinement of surrounding concrete in the SCS sandwich structures. The diameter of the cylindrical specimen was 200 mm. The height of the

specimens was about 100 mm, which is the typical thickness of the SCS sandwich structure. Four diameters of the J-hooks i.e. 10, 12, 16, 19 mm and four types of concrete, i.e. NWC (C30, C50, C60), LWC (C25, C30, C60), ULCC and HPC were used in the specimens. LVDTs were installed to record the axial elongation of the connectors.

3.3.2 Test results and comparisons with predictions by design equations

The ultimate tension resistance N_t and failure modes of the specimens are presented in Table 3. Two types of failure modes were observed from the tension tests i.e. J-hook straightening and concrete breakout failure (shown in Table 3). Details of the failure modes were reported by Yan [46], and herein only the ultimate tension resistance and failure modes were reported.

Table 3. Details of Tensile Test Specimens, Test Results and Predictions

Specimen	t mm	h_s mm	h_c mm	d mm	σ_y MPa	σ_u MPa	f_{ck} MPa	N_t kN	Failure mode	N_P (kN)	Ratio of N_t/N_p
TN1	6	57.0	100	10.0	353	405	48.3	22.0	HS	17.1	1.28
TN2+	6	57.0	100	10.0	353	405	59.0	23.0	HS	20.0	1.15
TN3+	6	59.0	100	12.0	353	450	59.0	40.0	CB	22.9	1.75
TN4	6	58.8	100	11.8	310	480	47.7	26.2	CB	20.5	1.28
TN5	6	58.8	100	11.8	310	450	33.0	21.0	HS	17.1	1.23
TL1	6	57.0	100	10.0	353	405	27.4	16.0	HS	11.5	1.39
TL2+	6	57.0	100	10.0	353	405	28.5	18.0	HS	11.8	1.53
TL3+	6	59.0	100	12.0	353	450	28.5	25.0	HS	15.9	1.57
TL4	6	56.3	95	11.8	310	465	30.0	23.7	HS	14.8	1.60
TL5	6	58.8	100	11.8	310	450	21.8	15.3	HS	13.2	1.16
TL6	6	56.5	100	9.5	310	450	48.1	17.6	HS	15.0	1.18
TL7	6	56.5	100	9.5	310	450	61.0	23.6	HS	18.1	1.30
TU1!	6	56.3	95	11.8	310	465	65.2	26.8	CB	21.9	1.22
TU2!	6	71.3	125	11.8	310	465	65.2	29.8	HS	29.5	1.01
TU3!	4	57.3	95	11.8	310	465	65.2	28.4	CB	21.9	1.30
TU4!	8	55.3	95	11.8	310	465	65.2	30.5	CB	21.9	1.39
TU5!	12	53.3	95	11.8	310	465	65.2	27.1	CB	21.9	1.24
TU6!	6	60.5	95	16.0	280	405	65.2	37.8	CB	23.4	1.61
TH1	6	56.3	95	11.8	310	465	180.0	53.9	CB	36.3	1.48
Mean											1.34
COV											0.14

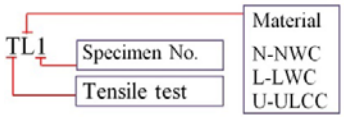

+ Presents 1% steel fiber was added to the specimen; ! Presents 0.5% PVA fiber was added to the specimen NWC= normal weight concrete; LWC denotes light weight concrete; ULCC denotes ultra-lightweight cement composite; CB=concrete breakout failure; HS=hook straightening failure.

The tension resistance predicted by Eqs. 3-8 were compared with the test data in Figure 9 and Table 3. It is observed that the average test-to-prediction ratio is 1.34 with a COV of 0.14. Specimens TN3, TL2, and TL3 with 1% steel fibers added in the concrete exhibit larger test-to-prediction ratios compared with the rest. This is because that influence of the fibers on the concrete strength was ignored in the design equations. Addition of the steel fibers or PVA fibers to the concrete increases the tensile strength of the concrete and delay the propagation and formation of the shear cracks in the concrete. This beneficial effect has not been captured in the design equations method which give conservative predictions (with average 34 % underestimation) on tension resistance of the J-hook connectors in embedded in different types of concrete.

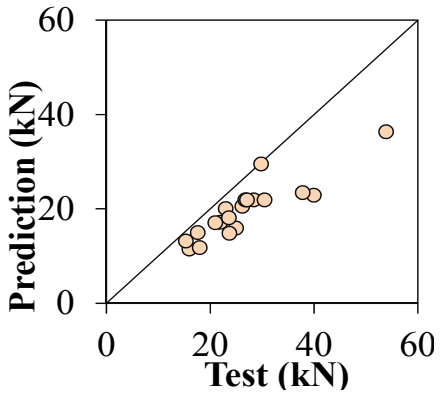

Figure 9. Comparisons of Tension Resistance between Predictions and Test Results

4. FINITE ELEMENT ANALYSIS ON SHEAR-TENSION INTERACTION OF J-HOOK CONNECTORS

Finite element (FE) software package ABAQUS was used for the analysis of the shear-tension interaction resistance of the J-hook connectors. ABAQUS/Standard implicit type of solver was used for the solution.

4.1 Material Models of the Finite Element Analysis

4.1.1 Material models for concretes

Concrete damage plasticity model in ABAQUS was chosen for NWC, LWC, and ULCC. In this model, the uniaxial compressive and tensile behaviors need to be defined. The stress-strain characteristics of ULCC were obtained from compressive and tensile tests as shown in Figure 10a. It can be observed that stress of ULCC firstly increases almost linearly to the peak 60 MPa and then suddenly drops to about 20 MPa that is one third of the peak stress 60 MPa due to the cracking of the concrete. The residual strength is due to the addition of 0.5% per volume PVA fibers (6mm long). Based on the material tests, elastic modulus of ULCC is 17.5 GPa and Poisson's ratio is 0.25. The same methods were applied to the NWC and LWC that were involved in this study. Other parameters including flow potential eccentricity of 0.6, dilation angle of 36°, and ratio of the biaxial/uniaxial compressive strength ratio of 1.16 were set for this plastic damage model.

4.1.2 Material models for steel face plates and connectors

Typical elastic and plastic isotropic material model in ABAQUS material menu was chosen for steel material. A bi-linear stress-strain behavior was used for FE simulation as shown in Figure 10b. The stress-strain relationship behaves linearly up to the yield point followed by a stress hardening behaviour. The mechanical properties of the steel plates and connectors obtained from tensile tests were tabulated in Table 2 and Table 3, respectively.

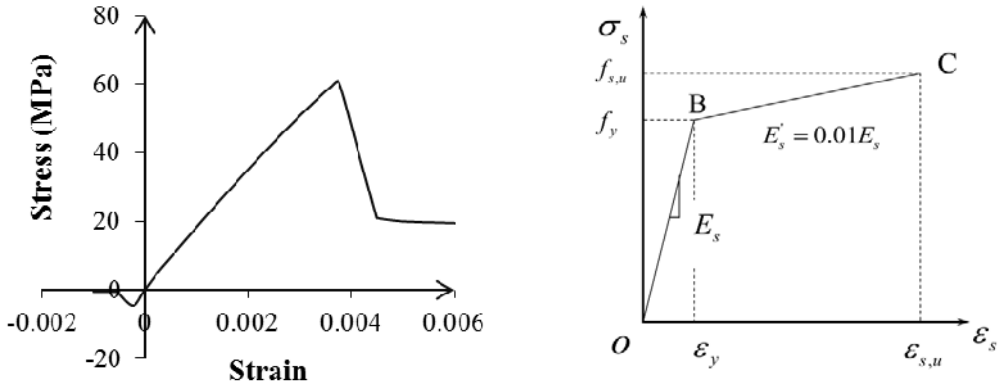

(a) Stress-strain curves of ULCC (b) Stress-strain mode for steel

Figure 10. Stress-strain Models for ULCC and Steel

4.3 Geometry, Element Type and Mesh Size Study

4.3.1 Geometry

A pair of J-hook connectors was simplified to two rods linked at the center by nonlinear spring element as shown in Figure 11.

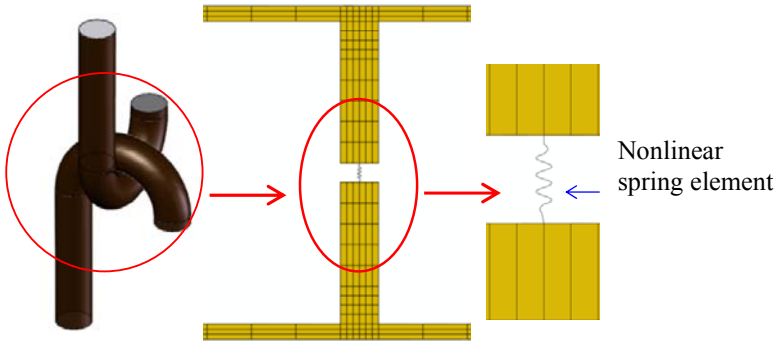

Figure 11. Simplification of J-hook Connector

The tension-elongation behaviors of the spring element were obtained from the tensile tests on the J-hook connectors as presented in section 3.3. Considering symmetry of the loading and geometry of the specimen, only half of the specimen was modeled as shown in Figure 12. From this figure, it can be seen that different components of specimens in the FE model such as steel face plates, concrete, connector and loading plate are simulated. Symmetrical constraints were applied to the surfaces as shown Figure 12.

Contact pairs were defined between steel plate and concrete and between connectors and concrete.

4.3.2 Element type and mesh size study

Three dimensional eight node continuum element (C3D8R) was chosen to simulate the concrete core, connectors, and steel face plates. At different locations, different mesh sizes were used to make a balance between the FE analysis accuracy and computing processing time. A mesh sensitivity study of FE analysis was also carried out. Three cases with different mesh sizes were studied and they are coarse mesh, medium mesh and fine mesh are shown in Figure 13 (a)-(c), respectively. For coarse meshes, concrete mesh size in the vicinity of connector is 8x8x8 mm^3 and

other regions are 25x25x12.5 mm^3 and mesh size for connector is 2x2x4 mm^3. For medium mesh size, the concrete in vicinity of connector is 6x6x3 mm^3 and connector is 1.5x2x3 mm^3. Finally, for fine mesh size, the concrete mesh in the vicinity of connector is 2x4x2 mm^3 and for connector is 1x1x1 mm^3.

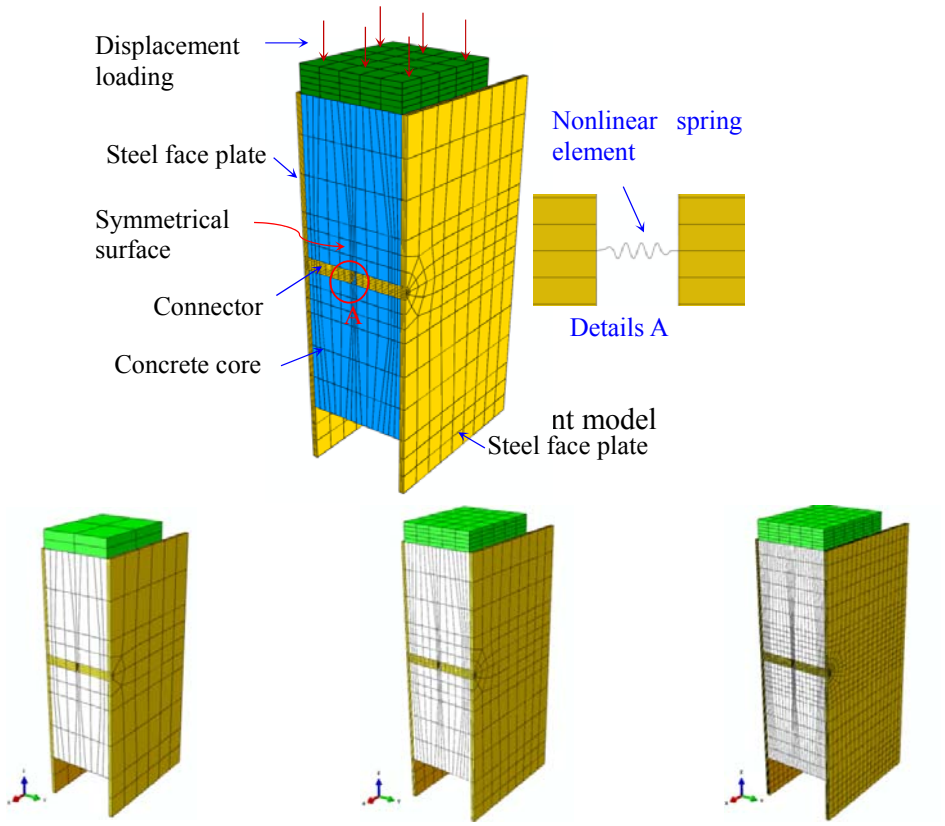

(a) Coarse mesh size (b) Medium mesh size (c) Fine mesh size

Figure 13. FE Model with Different Mesh Size

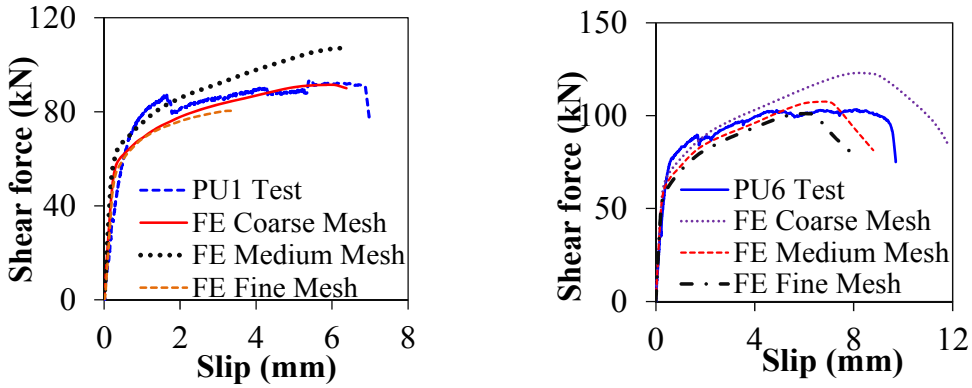

Figure 14. Effect of the Mesh Size on the FE Simulation

The load-slip curves by the FE analysis with different mesh sizes are compared with the experimental curves of specimens PU1 and PU6 in Figure 14. It can be observed that FE model with fine or medium mesh size offers better agreements than model with coarse mesh, but fine mesh will lead to more elements and restraining nodes for the contact and thus it increase the computation time. The medium mesh size is adopted for further analyses for computational efficiency and result accuracy.

4.3.3 Contact definition and study of contact friction coefficient

Contact pairs were defined between steel plates and concrete, and between connectors and concrete. Hard contact and penalty friction properties were specified for the interaction at the steel and concrete interface in the normal direction and the in-plane direction, respectively. Hard contact property is defined that the pressure is transferred once two interacting surfaces touch whereas no pressure is transferred once separated. For penalty friction contact, friction interaction was specified when the two interacting surfaces were in contact. In the penalty friction property, the friction coefficient is an empirical value less than one that needs to be determined further. Two cases of push-out tests on PU1and PU5 with varying friction coefficients from 0 to 0.5 were studied to determine the proper friction coefficient for further FE analysis. The influence of the different friction coefficients on the FE simulation is shown in Figure 15. It can be observed that larger friction coefficient leads to higher shear resistance. The ultimate shear resistance of the connector increases about 10 % when the friction coefficient increases from 0 to 0.5. The FE simulation using friction coefficient $\mu = 0.4$ was found to best fit the load slip curves obtained from the push out tests.

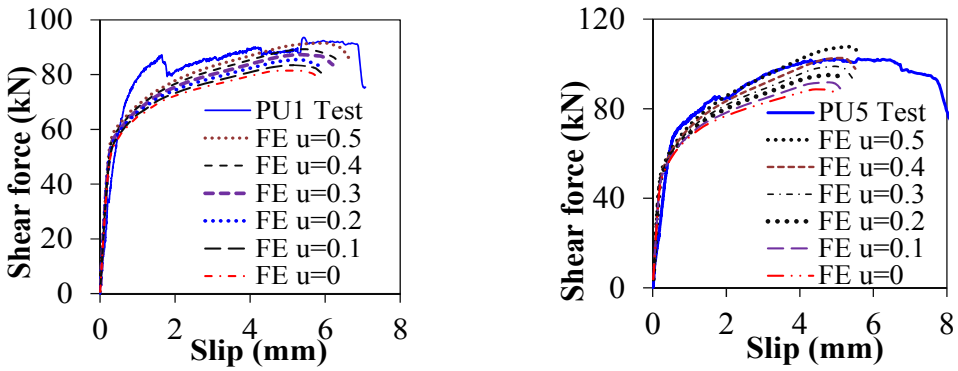

Figure 15. Effect of the Friction Coefficient on the FE Simulation

4.4 Validations of the FE Model

The validations of the FE analysis against push-out tests and tensile tests were carried out to evaluate the accuracy of the FE analysis.

Thirteen push-out tests carried out in Section 3 were chosen for the validation of the FE model, and the same specimens were then used in further analysis on shear-tension interaction resistance of J-hook (as listed in Table 4). The shear force versus slip curves obtained from the push-out tests were compared with the curves by FE analysis in Figure 16(a)-(f). It can be seen that the load-slip curves obtained from the FE analysis resembles well the experimental load-slip curves. The experimental ultimate shear resistances of one J-hook connector are compared with the FE analysis in Table 2. From this table, it can be found that the average test-to-FE prediction ratio is 0.99 with a COV of 0.05. From these comparisons of shear-slip behaviors and ultimate shear resistance, it can be concluded that the developed FE model is capable of predicting the structural behaviors of the J-hook connectors under shear loads.

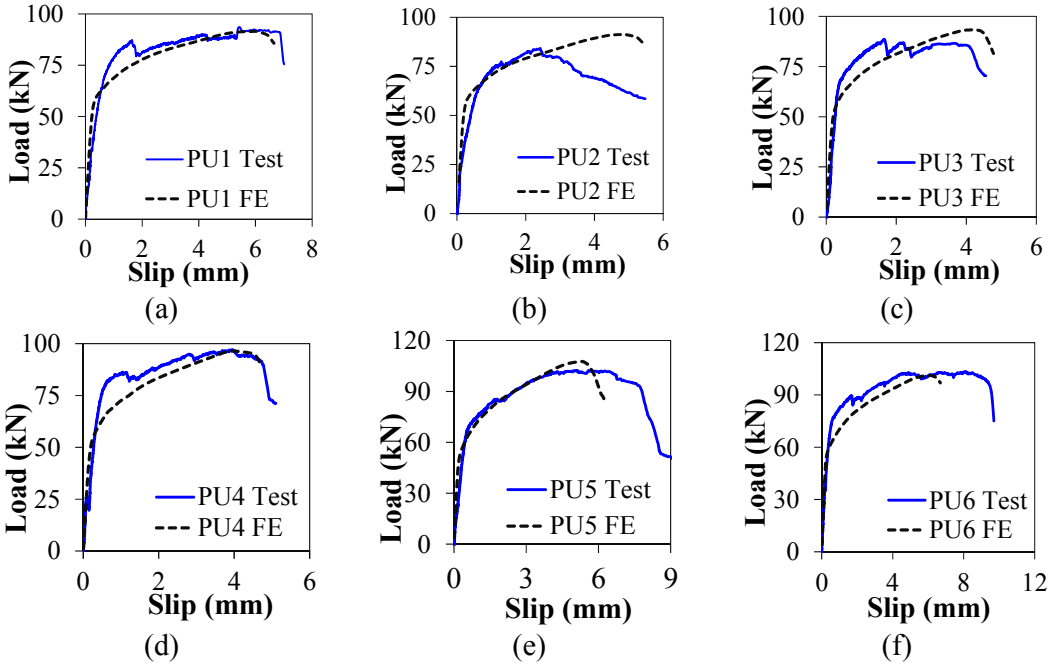

Figure 16. Comparisons of Load-slip Curves between Test and FE Simulation

Table 2. Comparisons between FE Predictions and Test Results

No	Item	P_{Test} (kN)	P_{FE} (kN)	P_{Test}/P_{FE}	No	Item	P_{Test} (kN)	P_{FE} (kN)	P_{Test}/P_{FE}
1	PN1	31.0	31.6	0.98	8	PU1	46.8	45.7	0.98
2	PN7	47.2	50.4	0.94	9	PU2	42.1	45.6	1.09
3	PN8	36.4	37.5	0.97	10	PU3	44.2	46.7	1.06
4	PL1	20.9	21.1	0.99	11	PU4	48.6	48.2	0.99
5	PL8	34.0	38.4	0.89	12	PU5	51.2	53.8	1.05
6	PL10	30.0	31.4	0.96	13	PU6	51.7	50.6	0.98
7	PLF1	22.6	23.0	0.98					
								Mean	0.99
								COV	0.05

The tension-elongation behaviors of the FE model were compared with the tensile tests in Figure 17. From this figure, it can be seen that the FE model resembles well with the experimental tension-elongation curves. This implies the FE model is capable of describing the tension-elongation behavior of J-hook connectors.

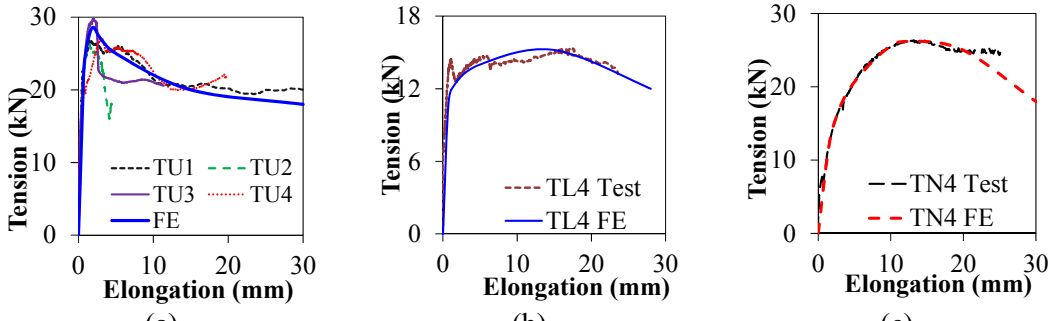

Figure 17. Comparsions of Tension-elongation Behaviors between Test and FE Simulation

From the above verifications, it can be concluded that the developed FE model is capable of simulating the shear-slip behavior and tension-elongation behavior of the J-hook connectors. The ultimate shear and tension resistances from the FE analysis show good correlation with the test results. This developed FE model is recommended for the further analysis on shear-tension interactions of J-hook.

4.5 Shear-tension Interaction Resistance by FE Analysis

Table 3. Details of Specimens for Shear-tension Interaction Analysis of J-hook Connectors

Specimen	Push-out Test	Tensile Test	f_{ck} (MPa)	E_C (GPa)	σ_y (MPa)	σ_u (MPa)	d (mm)	t (mm)
VTN1	PN1	TN1	48.3	32.5	353	405	9.9	6
VTN2	PN7	TN4	47.7	24	310	480	11.8	6
VTN3	PN8	TN5	33.6	19.5	310	450	11.7	6
VTL1	PL1	TL1	28.0	12.7	353	405	10.0	6
VTL2	PLF1	TL2	28.3	12.6	353	405	9.9	6
VTL3	PL10	TL5	19.9	15.0	310	450	11.7	6
VTL4	PL8	TL6	49.6	19.0	310	450	10.0	6
VTU1	PU1	TU3	62.6	16.5	310	465	11.8	4
VTU2	PU2	TU1	62.6	16.5	310	465	11.8	6
VTU3	PU3	TU3	62.6	16.5	310	465	11.8	8
VTU4	PU4	TU5	62.6	16.5	310	465	11.8	12
VTU5	PU5	TU2	62.6	16.5	310	465	11.8	6
VTU6	PU6	TU2	62.6	16.5	310	465	11.8	6

*VTN1-V denotes shear, T denotes tension, N denotes normal weight concrete, 1 denotes number; f_{ck}=compressive strength of concrete; E_c= elastic modulus; σ_y= yield strength of connector; σ_u= ultimate strength of connector; d= diameter of connector; t= thickness of steel plate in the specimen.

Experimental study on resistance under combination of shear and tension is limited by the test apparatus and proved to be very costly. The proposed FE model provides an alternative method to investigate the shear-tension interaction of J-hook connectors as shown in Figure 18. Two loading steps, tension step and followed shear step, were successively applied to the specimens to obtain different shear-tension resistance couples by the FE analysis.

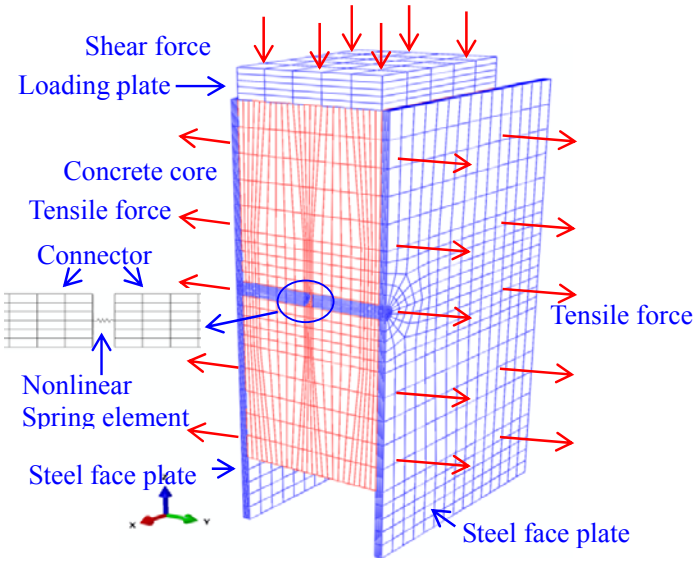

Figure 18. FE Model for Shear-tension Interaction Analysis of J-hook

In this paper, FE analyses on shear-tension interaction of thirteen specimens were carried out. Details of these thirteen specimens are tabulated in Table 3.

For each analysis case, the push-out tests and tension resistances obtained from the tests reported in Section 3.2 and 3.3 were given in this table. The shear-tension interaction resistances of J-hook connectors obtained from the FE analysis are tabulated in Table 4. From this table, it can be seen that the tension and shear resistance interact each other. As the tension resistance increases from zero to the ultimate tension capacity, the shear resistance of the J-hook decreases from the ultimate resistance to zero in a parabolic relationship. The shear especially decreases dramatically when the tension resistance nearly achieves the ultimate tension capacity.

5. COMPARISON OF RESULTS FROM FE ANALYSIS AND DESIGN EQUATIONS

The generalized shear-tension diagrams obtained from the FE analysis and tests were compared with the predictions by the design formulae in Figures. 19-21.

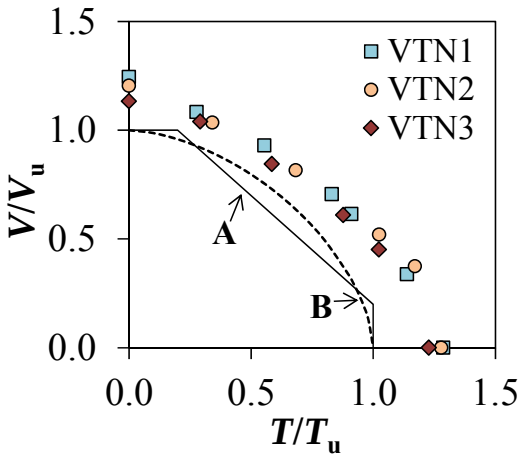

Figure 19. Shear-tension Interaction Resistance of J-hook Connectors in NWC
(Prediction curves A and B were predicted by Eqs. 9 and 10, respectively)

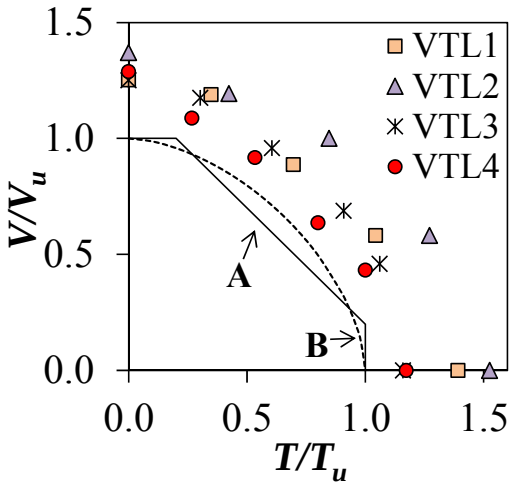

Figure 20. Shear-tension Interaction Resistance of J-hook Connectors in LWC

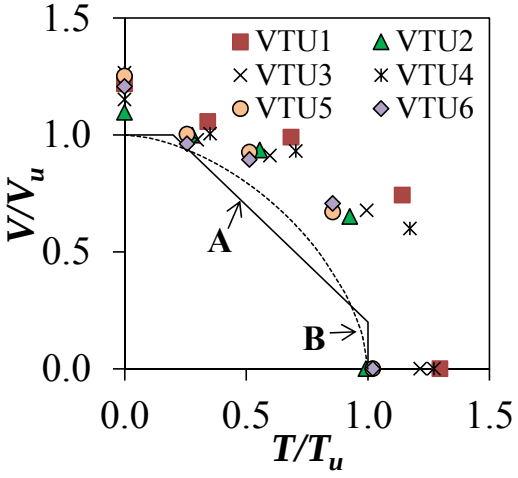

Figure 21. Shear-tension Interaction Resistance of J-hook Connectors in ULCC

From these figures and Table 4, it can be found that (1) both Eq. 9 and 10 were capable of evaluating the shear-tension interaction resistance of the J-hook connectors in NWC, LWC, and ULCC; (2) Eqs. 9 and 10 offer more conservative predictions to NWC compared with predictions with specimens with LWC and ULCC; (3) the conservative predictions for specimens with LWC and ULCC were caused by the addition of fibers in the LWC and ULCC that was not considered in the design equations; (4) compared with specimens with LWC and ULCC, the variance of the predictions for specimens with NWC was smaller. This larger variance of the predictions for specimens with LWC and ULCC was also caused by the addition of the fiber and variance of their strengths.

Table 4. Shear-tension Resistances of J-hook Connectors by FE Analysis and Tests

Specimen	T (kN)	V (kN)	T/T_u	V/V_u	Specimen	T (kN)	V (kN)	T/T_u	V/V_u
VTN1	0.0	31.0[t]	0.00	1.24	VTL1	0.0	20.9[t]	0.00	1.25
	4.7	27.0	0.28	1.08		4.0	19.9	0.35	1.19
V_u=24.9	9.5	23.1	0.55	0.93	V_u =16.7	8.0	14.8	0.70	0.89
T_u=17.1	14.2	17.6	0.83	0.71	T_u =11.5	12.0	9.7	1.04	0.58
	15.6	15.3	0.91	0.61		16.0[t]	0.0	1.39	0.00
	19.5	8.4	1.14	0.34	VTL2	0.0	22.6[t]	0.00	1.37
	22.0[t]	0.0	1.29	0.00		5.0	19.7	0.42	1.19
Unit: kN					V_u =16.5	10.0	16.5	0.85	1.00
					T_u =11.8	15.0	9.6	1.27	0.58
						18.0[t]	0.0	1.53	0.00
VTN2	0.0	47.2[t]	0.00	1.20	VTL3	0.0	30.0[t]	0.00	1.25
	7.0	40.6	0.34	1.04		4.0	28.2	0.30	1.18
V_u=39.2	14.0	32.0	0.68	0.82	V_u =24.0	8.0	23.0	0.61	0.96
T_u =20.5	21.0	20.4	1.02	0.52	T_u =13.2	12.0	16.5	0.91	0.69
	24.0	14.7	1.17	0.38		14.0	11.0	1.06	0.46
	26.2[t]	0.0	1.28	0.00		15.3[t]	0.0	1.16	0.00
VTN3	0.0	36.4[t]	0.00	1.13	VTL4	0.0	34.0[t]	0.00	1.29
	5.0	33.4	0.29	1.04		4.0	28.7	0.27	1.09
V_u=32.1	10.0	27.1	0.58	0.84	V_u =26.4	8.0	24.2	0.53	0.92
T_u =17.1	15.0	19.6	0.88	0.61	T_u =15.0	12.0	16.8	0.80	0.64
	17.5	14.5	1.02	0.45		15.0	11.4	1.00	0.43
	21.0[t]	0.0	1.23	0.00		17.6[t]	0.0	1.17	0.00
VTU1	0.0	46.8[t]	0.00	1.42	VTU4	0.0	48.6[t]	0.00	1.48
	7.5	40.6	0.34	1.23		7.5	38.6	0.34	1.17
V_u=32.9	15.0	38.0	0.68	1.16	V_u =32.9	15.0	35.8	0.68	1.09
T_u =21.9	25.0	26.4	1.14	0.80	T_u =21.9	25.0	23.0	1.14	0.70
	28.4[t]	0.0	1.30	0.00		27.1[t]	0.0	1.24	0.00
VTU2	0.0	42.1[t]	0.00	1.28	VTU5	0.0	51.2[t]	0.00	1.46
	7.5	38.3	0.34	1.17		7.5	41.0	0.25	1.17
V_u=32.9	15.0	35.9	0.68	1.09	V_u =35.0	15.0	37.9	0.51	1.08
T_u =21.9	25.0	25.0	1.14	0.76	T_u =29.5	25.0	27.4	0.85	0.78
	26.8[t]	0.0	1.22	0.00		29.8[t]	0.0	1.01	0.00
VTU3	0.0	44.2[t]	0.00	1.34	VTU6	0.0	51.6[t]	0.00	1.41
	7.5	37.6	0.34	1.14		7.5	41.2	0.25	1.13
V_u=32.9	15.0	35.0	0.68	1.06	V_u =36.6	15.0	38.3	0.51	1.05
T_u =21.9	25.0	26.0	1.14	0.79	T_u =29.5	25.0	30.2	0.85	0.83
	30.5[t]	0.0	1.39	0.00		29.8[t]	0.0	1.01	0.00

[t]Data from tests; V_u= predicted ultimate shear resistance; T_u= predicted ultimate tension resistance.

From the above observation, it can be concluded that the proposed design formulae are capable of describing the shear-tension interaction behaviors of J-hook connectors in SCS sandwich structure with NWC, LWC, and ULCC.

6. CONCLUSIONS

This paper investigates the ultimate resistance behaviors of new type of J-hook connectors subjected to pure shear, pure axial tension, and combined shear and tensile forces occurred at the steel and concrete interfaces of sandwich structure.

Thirty push-out tests were carried out to determine the longitudinal shear resistance of J-hook connectors embedded in different grades of concretes. The push-out test results were used to validate the design equations in order to predict the maximum shear resistance of J-hook connectors. Equation 2 offers reasonably accurate and conservative prediction of the shear resistance of the J-hook connector compared to the results obtained from the Eurocode method, which was developed mainly for headed stud connectors.

Eighteen tensile tests were carried out to investigate the tension resistance of J-hook connectors embedded in various types of concrete. The proposed design equations were found to be capable of predicting the tension resistance of J-hook connectors with acceptable accuracy (test-to-prediction ratio: mean value=1.34; COV=0.14). The equations neglect the beneficial effects of fibers in the core material and therefore the prediction is on the conservative side.

Three-dimensional nonlinear finite element model was developed to obtain the shear-tension interaction resistance of J-hook connectors. The FE model was validated by push-out tests and tensile tests. The FE model may be used to simulate the shear-slip behavior and tension-elongation behavior of the J-hook connectors with reasonably good accuracy compared to the test results. Shear-tension interaction resistance couples of J-hook connectors were obtained from FE analyses. Design equations on shear-tension interaction of J-hook connectors were proposed based on calibration with FE analysis and test results. Finally, Equations 9 and 10 were recommended to evaluate the combined shear-tension resistance of the J-hook connectors for steel concrete steel sandwich structures.

ACKNOWLEDGMENTS

The research described herein was funded by the Maritime and Port Authority of Singapore, and supported by the American Bureau of Shipping (ABS) and National University of Singapore under research project titled “Curved steel-concrete-steel sandwich composite for Arctic region″ (Project No. R-302-501-002-490).

REFERENCES

[1] Solomon, S.K., Smith, D.W. and Cusens, A.R., “Flexural Tests of Steel-concrete-steel Sandwiches”, Magazine of Concrete Research, 1976, Vol. 28, No. 94, pp. 13-20.

[2] Malek, N., Machida, A., Mutsuyoshi, H. and Makabe, T., “Steel-concrete Sandwich Members without Shear Reinforcement”, Transactions of Japan Concrete Institute, 1993, Vol. 15, No.2, pp. 1279-1284.

[3] Narayanan, R., Wright, H.D., Francis, R.W. and Enans, H.R., “Double Skin Composite Construction for Submerged Tube Tunnels”, Steel Construction Today, 1987, Vol. 1, pp. 185-189.

[4] Xie, M. and Chapman, J.C., “Development in Sandwich Construction”, Journal of Constructional Steel Research, 2006, Vol. 62**,** No**.** 11, pp. 1123-1133.

[5] Xie, M., Foundoukos, N. and Chapman, J.C., "Static Tests on Steel–Concrete–Steel Sandwich Beams", Journal of Constructional Steel Research, 2007, Vol. 63**,** No. 6, pp. 735-750.

[6] Liew, J.Y.R., Sohel, K.M.A. and Koh, C.G., "Impact Tests on Steel–Concrete–Steel Sandwich Beams with Lightweight Concrete Core", Engineering Structures, 2009, Vol. 31**,** No. 9, pp.2045-2059.

[7] Liew, J.Y.R. and Wang, T.Y., "Novel Steel-Concrete-Steel Sandwich Composite Plates Subject to Impact and Blast Load", Advances in Structural Engineering, 2011, Vol. 14, No. 4, pp. 673-687.

[8] Dai, X.X. and Liew, J.Y.R., "Fatigue Performance of Lightweight Steel–Concrete–Steel Sandwich Systems", Journal of Constructional Steel Research, 2010, Vol. 66, No. 2, pp. 256-276.

[9] Viest, I.M., "Investigation of Stud Shear Connectors for Composite Concrete and Steel T-beams", Journal of the American Concrete Institute, 1956, Vol. 27, No. 8, pp.875-91.

[10] Driscoll, G.G. and Slutter, R.G. "Research on Composite Design at Lehigh University", In: Proceedings of the National Engineering Conference, Chicago (IL): American Institute of Steel Construction, 1961, pp. 18-24.

[11] Chinn, J., "Pushout Tests on Lightweight Composite Slabs", Engineering Journal, AISC, 1965, Vol. 2, No. 4, pp.129-34.

[12] Steele, D.H., "The Use of Nelson Studs with Lightweight Aggregate Concrete in Composite Construction", M.S. Thesis, Boulder (CO): University of Colorado; 1967.

[13] Davies, C., "Small-scale Push-out Tests on Welded Stud Shear Connectors", Concrete, 1967, Vol. 1, No. 9, pp. 311-6.

[14] Mainstone, R.J. and Menzies, J.B., "Shear Connectors in Steel Concrete Composite Beams for Bridges", Concrete, 1967, Vol. 1, No. 9, pp. 291-302.

[15] Goble, G.G., "Shear Strength of Thin Flange Composite Specimen", Engineering Journal, AISC, 1968, Vol. 5, No. 2, pp. 62-5. 2nd Quarter.

[16] Topkaya, C., Yura, J.A. and Williamson, E.B., "Composite Shear Stud Strength at Early Concrete Ages", Journal of Structural Division, ASCE, 2004, Vol. 130, No. 6, pp. 952-60.

[17] Ollgaard, J.G., Slutter, R.G. and Fisher, J.W., "Shear Strength of Stud Connectors in Lightweight and Normal-weight Concrete", Engineering Journal, AISC, 1971, Vol. 8, No.2, pp. 55-64.

[18] Oehlers, D.J. and Bradford, M.A., "Composite Steel and Concrete Structural Members: Fundamental Behavior", Oxford U.K: Pergamon; 1995.

[19] An, L. and Cederwall, K., "Push-out Tests on Studs in High Strength and Normal Strength Concrete", Journal of Constructional Steel Research, 1996, Vol. 36, No. 1, pp. 15-29.

[20] Pallarés, L. and Hajjar, J.F., "Headed Steel Stud Anchors in Composite Structures, Part I: Shear", Journal of Constructional Steel Research, 2010, Vol. 66, No.2, pp.198-212.

[21] Cook, R.A., Collins, D.M., Klingner, R.E. and Polyzois, D., "Load-deflection Behavior of Cast-in-place and Retrofit Concrete Anchors", ACI Structural Journal, 1992, Vol. 89, No. 6, pp. 639-49.

[22] Cook, R.A., Kunz, J., Fuchs, W. and Konz, C.D., "Behavior and Design of Single Adhesive Anchors under Tensile Load in Uncracked Concrete", ACI Structural Journal, 1996, Vol. 95, No. 1, pp. 9-26.

[23] Zamora, N.A., Cook, R.A., Konz, R.C. and Consolazio, G.R., "Behavior and Design of Single, Headed and Unheaded, Grouted Anchors under Tensile Load", ACI Structural Journal, 2003, Vol. 100, No. 2, pp. 222-30.

[24] Shirvani, M., Klingner, R.E. and Graves III, H.L., "Breakout Capacity of Anchors in Concrete, Part 1: Tension", ACI Structural Journal, 2004, Vol. 101, No.6, pp.812-20.

[25] Eligehausen, R. and Balogh, T., "Behavior of Fasteners Loaded in Tension in Cracked Reinforced Concrete", ACI Structural Journal, 1995, Vol. 92, No. 3, pp. 365-79.

[26] Eligehausen, R., Cook, R.A. and Appl, J., "Behavior and Design of Adhesive Bonded Anchors", ACI Structural Journal, 2006, Vo. 103, No. 6, pp. 822-31.
[27] Fuchs, W., Eligehausen, R. and Breen, J.E., "Concrete Capacity Design Approach for Fastening to Concrete", ACI Structural Journal, 1995, Vol. 92, No. 1, pp.73-94.
[28] Bode, H. and Roik, K., "Headed Studs- Embedded in Concrete and Loaded in Tension", American Concrete Institute SP 103-4. Farmington Hills (MI): American Concrete Institute; 1987, pp. 61-88.
[29] Balogh T., Kovácsházy G. and Frigy A., "Pull-out Tests on Steel Embedment in Concrete", In: Anchors in concrete -Design and behavior, ACI SP130-9. Farmington Hills (MI): American Concrete Institute; 1991, pp. 221-33.
[30] Klingner R.E. and Mendonca J.A., "Tensile Capacity of Short Anchor Bolts and Welded Studs: A Literature Review", ACI Structural Journal, 1982, Vol. 79, No.4, pp.270-9.
[31] Pallares, L. and Hajjar, J.F., "Headed Steel Stud Anchors in Composite Structures, Part II: Tension and Interaction", Journal of Constructional Steel Research, 2010, Vol. 66, No. 2, pp. 213-228.
[32] McMakin, P.J., Slutter, R.G. and Fisher, J.W., "Headed Steel Anchor under Combined Loading", Engineering Journal, AISC 1973; (Second Quarter):43-52.
[33] Saari, W.K., Hajjar, J.F., Schultz, A.E. and Shield, C.K., "Behaviour of Shear Studs in Steel Frames with Reinforced Concrete Infill Walls", Journal of Constructional Steel Research, 2004, Vol. 60, No. 10, pp. 1453-1480.
[34] Mirza, O. and Uy, B., "Effects of the Combination of Axial and Shear Loading on the Behavior of Headed Stud Steel Anchors", Engineering Structures, 2006, Vol. 32, No. 1, pp. 93-105.
[35] Yan, J.B., Liew, J.Y.R., Sohel, M.A. and Zhang, M.H., "Push-out Tests on J-hook Connectors in Steel-Concrete-Steel Sandwich Structure", Materials and Structures, 2014, Vol. 47, No. 10, pp. 1693-1714.
[36] PCI, "PCI design handbook, 6th edition", Prestressed Concrete Institute, 2004, Chicago.
[37] American Concrete Institute (ACI) Committee 318, "Building Code Requirements for Structural Concrete (ACI318-02) and Commentary (ACI 318R-02)", American Concrete Institute, 2002, Detroit, MI.
[38] Liew, J.Y.R. and Sohel, K.M.A., "Lightweight Steel–Concrete–Steel Sandwich System with J-hook Connectors", Engineering Structures, 2009, Vol. 31, No. 5, pp. 1166-1178.
[39] Wang, J.Y., Zhang, M.H., Li, W., Chia, K.S. and Liew, J.Y.R., "Stability of Cenospheres in Lightweight Cement Composites in Terms of Alkali–silica Reaction", Cement and Concrete Research, 2012, Vol. 42, No. 5, pp. 721-727.
[40] British Standards Institution BS EN 1994: Design of Composite Steel and Concrete Structures-Part 1-1 General Rules and Rules for Buildings, 2004, London, UK.
[41] CEB-FIP. CEB-FIP Model Code for Concrete Structures, 3rd Edition, Comité Euro-International du Béton/FédérationInternationale de la Précontrainte, 1978, Paris.
[42] ACI Committee 349, Code Requirements for Nuclear Safety Related Concrete Structures (ACI 349-01) and Commentary (ACI 349R-01). ACI, 2001, Farmington Hills.
[43] British Standards Institution BS EN 1992:. Design of Concrete Structures, Part 1-2:General Rules and Rules for Buildings, 2004, BSI, London.
[44] British Standards Institution BS EN 1993: Design of Steel Structures. Part 1-1: General Rules and Rules for Buildings. 2005, BSI, London.
[45] Xie, M., Foundoukos, N. and Chapman, J.C., "Experimental and Numerical Investigation on the Shear Behaviour of Friction-welded Bar–plate Connections Embedded in Concrete", Journal of Constructional Steel Research, 2005, Vol. 61, No. 5, pp. 625-649.
[46] Yan, J.B., Liew, J.Y.R., Zhang, M.H., "Tensile resistance of J-hook connectors in Steel-Concrete-Steel sandwich composite structure. Journal of Constructional Steel Research, 2014, Vol. 100, pp. 146-162.

PRACTICAL ADVANCED ANALYSIS FOR ECCENTRICALLY BRACED FRAMES

Shujun Hu [1] and Zhan Wang [2,*]

[1] *School of Civil Engineering and Architecture, Nanchang University, Nanchang 330031, China*
[2] *State Key Laboratory of Subtropical Building Science, South China University of Technology, Guangzhou 510640, China)*
**(Corresponding author: E-mail: wangzhan@scut.edu.cn)*

Received: 19 March 2014; Revised: 23 April 2014; Accepted: 5 May 2014

ABSTRACT: Under severe earthquakes, flexural or shear yielding of the inelastic links in eccentrically braced frames (EBFs) was often observed. The behavior of links could not be well predicted by the traditional advanced analysis method when they experienced shear yielding and strain hardening. In this paper, the analytical model of links is obtained by using three rotational subsprings and three translational subsprings with zero-length, respectively, at each element end to simulate the flexural and shear yielding behavior with strain hardening effect. For the other elements in EBFs, a spring with zero-length is provided at each end to consider yielding on the cross-sectional level. The yield functions for the links and other elements are derived based on the section assemblage concept, and a practical advanced analysis method for EBFs is proposed. The proposed elements have the same nodal degree of freedom as conventional element by condensing the non-nodal degree of freedom that introduced in the derivation. Numerical analysis shows that the proposed method has a high efficiency and accuracy as well as easy determination of the element yielding sequence.

Keywords: Eccentrically braced frames (EBFs), Advanced analysis, Shear link, Section assemblage concept, Yield function, Strain hardening

1. INTRODUCTION

Eccentrically braced frames (EBFs), which combine the advantages of moment resisting frame (MRF) and concentrically braced frame (CBF), are one type of hybrid structural system with good ductility and lateral stiffness. The links in EBFs are generally designed to yield prior to frame structures, acting as the "structural fuse" member. The ductility of EBFs depends on links, which is determined by the plastic rotational capacity [1]-3]. Under severe earthquake, the main structures are generally designed to be elastic with yielding of links only so that damage on the structures can be minimized.

From previous studies, the links had three types, which were shear links, flexural links and shear-flexural links. It is also known that the behavior of links had a significance effect on the seismic behavior of EBFs and the links might experience shear or/and flexural yielding [4-5]. Detailed researches on the static and dynamic behavior of links were conducted by Ricles et al. [6], Ramadan et al. [7] and Richards et al. [8], in which the analytical model of links considering the flexural yielding, shear yielding and strain hardening were obtained. These models were regarded as the "complete element", in which a plastic hinge with zero-length was assumed at each end of link while the middle of link remained elastic without yielding. For each plastic hinge, moment hinge and shear hinge were used to simulate the rotational and horizontal deformations. Multiple subsprings with elastic-perfectly plastic model were provided at each link end to simulate the strain hardening effect. However, there were no easy methods to determine whether the design requirements and expected goals were met even though the performances of all the members were known.

The advanced analysis methods of steel frames, which included the plastic-zone method and the plastic-hinge method, have been a subject of extensive research for decades. The plastic-hinge method has been the commonly used method because of its simplicity and efficiency, which was further modified by using the refined plastic hinge analysis model proposed by Liew et al.[9], Kim et al. [10] and Chen [11]. Chan et al. [12] also proposed a new analytical model based on section assemblage concept and section spring stiffness. However, these methods could only be used to simulate flexural yielding of elements with elastic perfectly-plastic since two plastic hinges were provided at element ends. Obviously, the shear yielding behavior and strain hardening effect of elements such as links in EBFs could no longer be well predicted by the traditional advanced analysis methods.

In this paper, the advanced analytical model of links is proposed by using three rotational subsprings and three translational subsprings elements with zero-length, respectively, at each element end to simulate the flexural and shear yielding behavior and strain hardening effect. For the conventional elements in EBFs, a spring with zero-length is provided at each end to consider gradually yielding of elements. The yield functions for all the elements are derived based on the section assemblage concept, in which strain hardening effect is only considered in links. A practical advanced analysis method for EBFs is proposed by only using one element per member. The efficiency and accuracy of the proposed method is validated and the yielding sequence of all the members is obtained. The proposed method is also used to evaluate the expected design goals for the structures.

2. ADVANCED ANALYSIS METHOD OF CONVENTIONAL ELEMENT

2.1 Stability Functions Accounting for Second-order Effect

Assuming small strains and large displacement, and considering the boundary conditions, the element moment-rotation relationship that considers the second-order effects can be written as:

$$\begin{cases} M_1 = \dfrac{EI}{L}(S_1\theta_1 + S_2\theta_2) \\ M_2 = \dfrac{EI}{L}(S_2\theta_1 + S_1\theta_2) \end{cases} \tag{1}$$

in which M_1, M_2 are the element end moments; E, I, L=elastic modulus, moment of inertia, and length of element; θ_1, θ_2=joint rotations; S_1, S_2=stability function.

The simplified stability functions reported by Chen [13] are used here, and can be written as:

$$S_1 = \begin{cases} \dfrac{\alpha\sin\alpha - \eta\alpha^2\cos\alpha}{2 - 2\cos\alpha - \eta\alpha\sin\alpha} ; & P < 0 \\ \dfrac{4+\beta}{1+\beta} ; & P = 0 \\ \dfrac{\eta\alpha^2\cosh\alpha - \alpha\sinh\alpha}{2 - 2\cosh\alpha + \eta\alpha\sinh\alpha} ; & P > 0 \end{cases} \qquad S_2 = \begin{cases} \dfrac{\eta\alpha^2 - \alpha\sin\alpha}{2 - 2\cos\alpha - \eta\alpha\sin\alpha} ; & P < 0 \\ \dfrac{2-\beta}{1+\beta} ; & P = 0 \\ \dfrac{\alpha\sinh\alpha - \eta\alpha^2}{2 - 2\cosh\alpha + \eta\alpha\sinh\alpha} ; & P > 0 \end{cases} \tag{2}$$

in which $\eta = 1 + \mu P / GA$, $\beta = 12\mu EI / GAl^2$, $\alpha = l\sqrt{|P|/(\eta EI)}$. μ=section coefficient for shear deformation; P=axial force (positive in tension and negative in compression); G=shear modulus.

2.2 Initial and Full Yield Functions

Section assemblage concept [14] is derived on the basis of plate assemblage of a H or I section. It is assumed that web takes axial loads and the remaining unyielded part resists moments. For analysis of I or H sections, the section is idealized as composed of several rectangular strips. Section parameters such as breadth, depth, flange and web thickness are used to calculate section capacity.

Initial yield function. Section stiffness will reduce gradually after the axial load and moment exceed first yield value. In the presence of residual stress and axial force, initial yield function can be written as

$$M_{er} = \left(f_y - f_r - P/A\right)W_{ey} \tag{3}$$

in which M_{er} = first yield moment, W_{ey}= elastic modulus, f_r = maximum residual stress.

Residual stress is based on the recommendation by ECCS [15], and the maximum residual stress is assumed to be dependent on the ratio of depth/breadth. The distribution is shown in Figure 1.

Full yield function. Section stiffness will be reduced to zero after the axial loads and moments exceed full yield value, and residual stress is ignored.

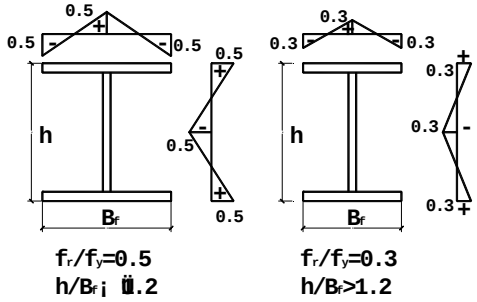

Figure 1. ECCS Residual Stress Distribution for I-section

The half depth of plastic zone for axial load can be written as:

$$\begin{cases} \lambda = \dfrac{P}{2f_y t_w} & \text{for} \quad \lambda \le \dfrac{h_w}{2} \\ \lambda = \dfrac{P - f_y t_w h_w}{2f_y B_f} + \dfrac{h_w}{2} & \text{for} \quad \dfrac{h_w}{2} \le \lambda \le \dfrac{h_w}{2} + h_f \end{cases} \tag{4}$$

Upon determination of plastic zone in the section, moment resisted by the remaining unyielded zones can be written as

$$\begin{cases} M_{pc} = [W_{py} - \lambda^2 t_w] f_y & \text{for} \quad \lambda \le \dfrac{h_w}{2} \\ M_{pc} = \left[\dfrac{h^2}{4} - \lambda^2\right] B_f f_y & \text{for} \quad \dfrac{h_w}{2} \le \lambda \le \dfrac{h_w}{2} + h_f \end{cases} \tag{5}$$

in which M_{pc}=the reduced plastic moment in the presence of axial force, W_{py}= plastic modulus, f_y= yield stress, h_w, t_w=web depth and thickness, B_f, h_f=flange breadth and thickness, h = section depth.

The curves of first and full yield surface are determined by Eq.3 and Eq.5, as shown in Figure 2. From Eq. 3 and Eq. 5, the M_{er} and M_{pc} are controlled by axial loads and residual stress, and section spring stiffness S_c [14] can be written as

$$\begin{cases} S_c = \infty & \text{for } M < M_{er} \\ S_c = \dfrac{6EI}{L}\dfrac{\left|M_{pc} - M\right|}{\left|M - M_{er}\right|} & \text{for } M_{er} \le M < M_{pc} \\ S_c = 0 & \text{for } M \ge M_{pc} \end{cases} \tag{6}$$

So from Eq. 6, the magnitude of S_c is determined by first yield moment and full yield moment.

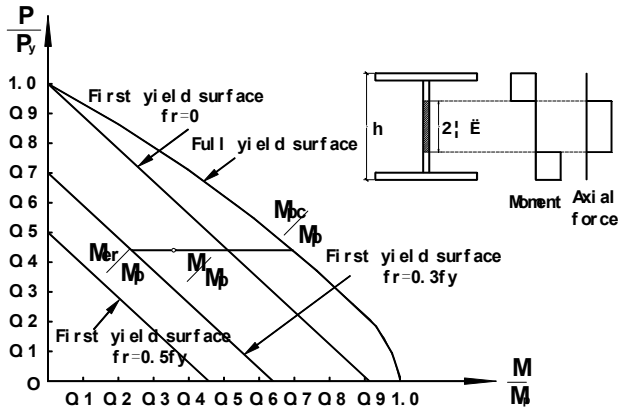

Figure 2. First Yield and Full Yield Surfaces of Section

2.3 Element Stiffness Formulation Accounting for Plasticity Effect

Advanced analysis of steel frames assumes plastic hinges occur only at both ends, and a spring with zero-length at each end is assumed to account for the section yielding. The deformed element with end-section pseudo-spring is shown in Figure 3. Owing to the gradual yielding of the end springs, the rotational stiffness and displacement on the both sides of each spring are generally unequal.

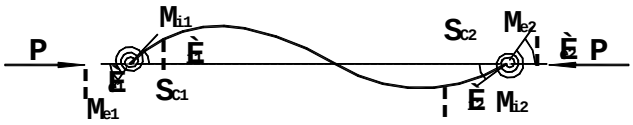

Figure 3. Internal Forces of an Element with End-section Pseudo-spring

Considering the moment equilibrium condition at each spring, the incremental equation can be written as

$$\begin{Bmatrix} \Delta M_e \\ \Delta M_i \end{Bmatrix} = \begin{bmatrix} S_c & -S_c \\ -S_c & S_c \end{bmatrix} \begin{Bmatrix} \Delta\theta_e \\ \Delta\theta_i \end{Bmatrix} \tag{7}$$

in which ΔM_e, $\Delta\theta_e$= the incremental moment and rotation between the global node and the spring; ΔM_i, $\Delta\theta_i$ = the incremental moment and rotation between the spring and the beam at each end.

Combining the section spring stiffness and stability function, the element incremental moment-rotation relationship can be written as

$$\begin{Bmatrix} \Delta M_{e1} \\ \Delta M_{i1} \\ \Delta M_{i2} \\ \Delta M_{e2} \end{Bmatrix} = \begin{bmatrix} S_{c1} & -S_{c1} & 0 & 0 \\ -S_{c1} & S_{c1}+K_{11} & K_{12} & 0 \\ 0 & K_{21} & S_{c2}+K_{22} & -S_{c2} \\ 0 & 0 & -S_{c2} & S_{c2} \end{bmatrix} \begin{Bmatrix} \Delta\theta_{e1} \\ \Delta\theta_{i1} \\ \Delta\theta_{i2} \\ \Delta\theta_{e2} \end{Bmatrix} \tag{8}$$

in which $K_{11}= K_{22}= S_1EI/L$, $K_{12}= K_{21}= S_2EI/L$, S_1, S_2 as shown in Eq. 2.

Eliminate non-nodal degrees of freedom. With $\Delta\theta_{i1}$ and $\Delta\theta_{i2}$ condensed, Eq. 8 becomes

$$\left(K_{ee} - K_{ei}K_{ii}^{-1}K_{ei}^{T}\right)\{\Delta\theta_{ee}\} = \{\Delta M_{ee}\} - K_{ei}K_{ii}^{-1}\{\Delta M_{ii}\} \tag{9}$$

in which $\{\Delta M_{ee}\}$ and $\{\Delta M_{ii}\}$ are the incremental nodal moments vectors at both ends; $\{\Delta\theta_{ee}\}$ and $\{\Delta\theta_{ii}\}$ are the incremental nodal rotation vectors corresponding to these moments.

$$\begin{aligned} &\{\Delta M_{ee}\} = \left[\Delta M_{e1}, \Delta M_{e2}\right]^T, \{\Delta M_{ii}\} = \left[\Delta M_{i1}, \Delta M_{i2}\right]^T \\ &\{\Delta\theta_{ee}\} = \left[\Delta\theta_{e1}, \Delta\theta_{e2}\right]^T, \{\Delta\theta_{ii}\} = \left[\Delta\theta_{i1}, \Delta\theta_{i2}\right]^T \\ &K_{ee} = \begin{bmatrix} S_{c1} & 0 \\ 0 & S_{c2} \end{bmatrix}, K_{ei} = \begin{bmatrix} -S_{c1} & 0 \\ 0 & -S_{c2} \end{bmatrix} \\ &K_{ii} = \begin{bmatrix} S_{c1}+K_{11} & K_{12} \\ K_{21} & S_{c2}+K_{22} \end{bmatrix} \end{aligned} \tag{10}$$

Whilst loads are only applied at the nodes, the internal incremental moments $\{\Delta M_{ii}\}=\{0\}$, and Eq.9 can be written as

$$\{\Delta M_{ee}\} = \left(K_{ee} - K_{ei}K_{ii}^{-1}K_{ei}^{T}\right)\{\Delta\theta_{ee}\} \tag{11}$$

From Eq. 8 to 11, the incremental stiffness relationship accounting for section yielding becomes

$$\begin{Bmatrix} \Delta P_1 \\ \Delta M_{e1} \\ \Delta M_{e2} \end{Bmatrix} = \begin{bmatrix} EA/L & 0 & 0 \\ 0 & S_{c1} - S_{c1}^2(S_{c2}+K_{22})/\beta & S_{c1}S_{c2}K_{12}/\beta \\ 0 & S_{c1}S_{c2}K_{21}/\beta & S_{c2} - S_{c2}^2(S_{c1}+K_{11})/\beta \end{bmatrix} \begin{Bmatrix} \Delta u \\ \Delta\theta_{e1} \\ \Delta\theta_{e2} \end{Bmatrix} \tag{12}$$

in which ΔP_1 is the increment axial force, $\beta=(S_{c1}+K_{11})\ (S_{c2}+K_{22}) - K_{12}K_{21}$.

3. IMPROVED ADVANCED ANALYSIS ACCOUNTING FOR LINKS

Under severe earthquake, the links are designed to yield firstly by the high moments or shears. The analytical model of links considering the static and dynamic behavior have been proposed by many researches [6]~[8]. The accuracy of link analytical model is of crucial importance to the overall performance of EBFs.

3.1 Link Element Model and Yield Surfaces

The advanced analytical model of links that can be accurately modeled is attempted in this paper, as shown in Figure 4. The following three assumptions are made: (1) The out-of-plane degrees of freedom is neglected; (2) As link is yielding and subsequent strain hardening, there is no interaction between the shear and moment; (3) There is also no interaction between the shear and axial force [16].

A plastic hinge includes shear hinge and moment hinge with zero-length is assumed at each end of link, and the inner element between two plastic hinges should be constrained to remain elastically under any condition, so the deformation is only confined to occur at the ends. The load-displacement relationship of link is multilinear hardening modeling accounting for strain hardening effect. As the interaction between shear and moment is neglected, the shear hinge and moment hinge are independent. Each shear hinge and moment hinge have been divided into three translational subsprings and rotational subsprings, and each subspring has specific deformation mode and load-displacement relationship, as shown in Figure 4.

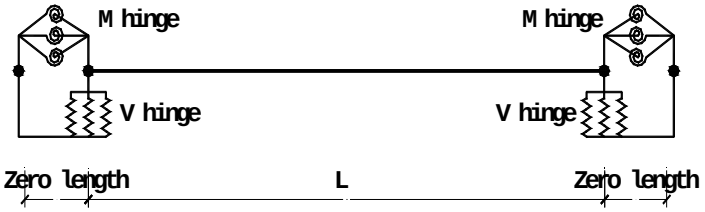

Figure 4. Link Model

Yield surfaces of links. The effect of residual stress in initial yield function, in which considers the interaction between axial forces and moment for flexural links, cannot be ignored. The effect of strain hardening is also significant to the yield surface. Section stiffness will be gradually reduced to zero when the shear and moment increase and exceed the full yield surface 3. The yield surfaces for all kinds of links can be shown in Figure 5.

3.2 Link Strain Hardening

In the EBFs, shear yielding, flexural yielding and shear-flexural yielding may be experienced depending on different kinds of links. The load-displacement curves are multilinear hardening modeling with the behavior of links for reasonable design. When the shear or moment exceeds V_3 or M_3, as shown in Figure 6, the shear hinge or moment hinge is formed.

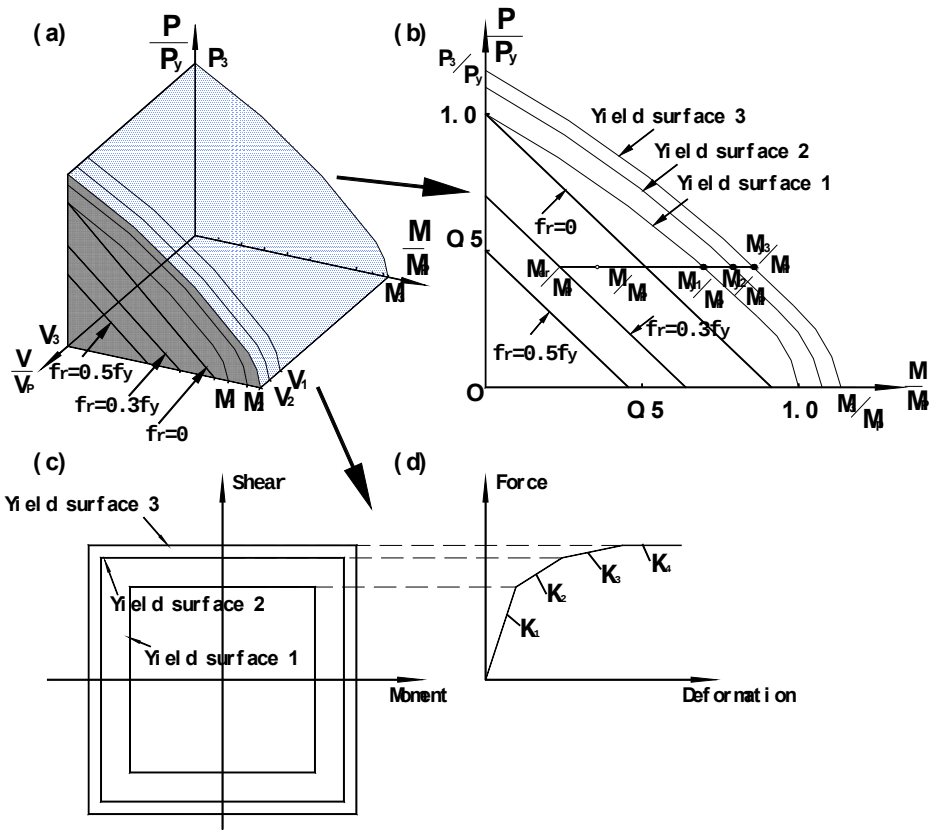

(a) Yield surface of links; (b) Yield surface of flexural links
(c) Uncoupled yield surface for shear and moment; (d) Load-displacement curve for link model

Figure 5. Yield Surfaces of Links

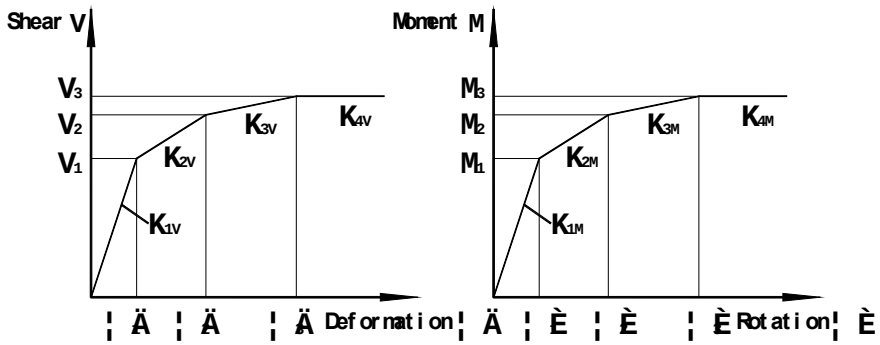

Figure 6. Shear Force and Moment for Multilinear Link Model

In Figure 6, the *K* values reported by Ricles and Popov [8] are used here, and can be written as:

$$\begin{cases} K_{2V} = 0.03K_{1V}; & K_{2M} = 0.03K_{1M} \\ K_{3V} = 0.015K_{1V}; & K_{3M} = 0.015K_{1M} \\ K_{4V} = 0; & K_{4M} = 0 \end{cases} \tag{13}$$

in which $K_{1V}= GA_{web}/e$; $K_{1M}=6EI/e$; E, I, e=elastic modulus, moment of inertia, and length of link; A_{web}= area of the web of link.

$$M_y = M_p; \quad V_y = 0.9V_p \tag{14}$$

The plastic moment capacity M_p and plastic shear capacity V_p can be expressed as:

$$M_p = Z\sigma_y; \quad V_p = \tau_y(d - t_f)t_w; \quad \tau_y = \sigma_y/\sqrt{3} \tag{15}$$

in which Z=section plastic modulus of link; d=section depth of link; t_f, t_w=section flange and web thickness of link; σ_y, τ_y= yield stress in tension and shear.

The V values and M values, as shown in Figure 6, are obtained in many test for links. All the values reported by Ricles and Popov [8] are also used here, and can be expressed in Table 1.

Table 1. Yielding Values of the Shear Forces and Moments for the Multilinear Inelastic Link Element

	First yielding		Second yielding		Third yielding	
	Shear V_1	Moment M_1	Shear V_2	Moment M_2	Shear V_3	Moment M_3
Ricles and Popov (1994)	$1.0V_p$	$1.0M_p$	$1.26V_p$	$1.13M_p$	$1.40V_p$	$1.20M_p$

The link multilinear hardening modeling at each end is divided into three zero-length translational subsprings and three zero-length rotational subsprings, and each subspring has an elastic perfectly-plastic load-displacement relationship, as shown in Figure 7. The force and stiffness of each subspring can be obtained in Table 1 and Eq.13, so the behavior of links in EBFs can be well predicted.

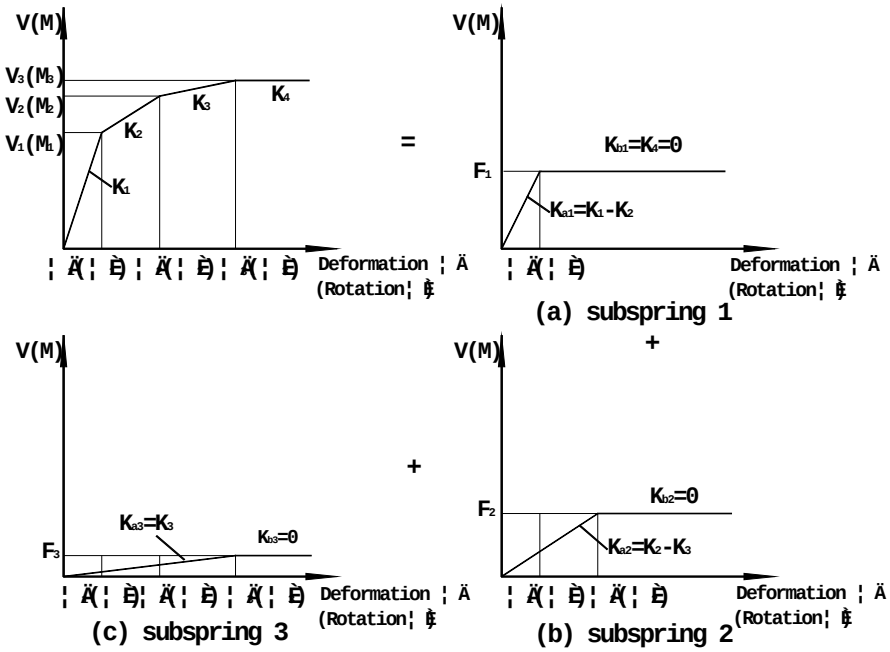

Figure 7. Load-displacement Relationship of Subsprings

3.3 Advanced Analytical Model of Flexural Links

The element stiffness accounting for strain hardening will be influenced by changing in moment at each end of flexural link. Based on section assemblage concept and section spring stiffness, the yield function and stiffness of flexural links are proposed by considering the interaction between axial force and moment.

Initial yield function. The initial yield function is the same as conventional element, as shown in Eq.3.

Other yield functions. After the strain hardening of flexural links is considered, the half depth of plastic zone for axial load becomes

$$\begin{cases} \lambda = \dfrac{P}{2\beta_i f_y t_w} & \text{for} \quad \lambda \le \dfrac{h_w}{2} \\ \lambda = \dfrac{P - \beta_i f_y t_w h_w}{2\beta_i f_y B_f} + \dfrac{h_w}{2} & \text{for} \quad \dfrac{h_w}{2} \le \lambda \le \dfrac{h_w}{2} + h_f \end{cases} \tag{16}$$

Upon determination of plastic zone in the section, yielding moment M_{py} that resisted by the remaining unyielded zones can be written as:

$$\begin{cases} M_{py} = [W_{py} - \lambda^2 t_w]\beta_i f_y & \text{for} \quad \lambda \le \dfrac{h_w}{2} \\ M_{py} = \left[\dfrac{h^2}{4} - \lambda^2\right] B_f \beta_i f_y & \text{for} \quad \dfrac{h_w}{2} \le \lambda \le \dfrac{h_w}{2} + h_f \end{cases} \tag{17}$$

in which β_i=material enhancement factor for moment strain hardening, corresponding to the first, second and third yielding values, as shown in Figure 7. As the β_i equals β_1, β_2 or β_3, the M_{py} corresponds to M_{y1}, M_{y2} or M_{y3}, and β_1=1, β_2=M_2/M_1, β_3=M_3/M_1.

Based on the yielding values accounting for moment strain hardening, section spring stiffness S_c can be written as

$$\begin{cases} S_c = \infty & \text{for} \quad M < M_{er} \\ S_c = S_p = \dfrac{6EI}{L}\dfrac{|M_{y1} - M|}{|M - M_{er}|} & \text{for} \quad M_{er} \le M < M_{y1} \\ S_c = 0 & \text{for} \quad M \ge M_{y1} \end{cases} \tag{18}$$

Assuming the right of link is elastic under any condition, and moment at left is changed, the section subspring stiffness and subelement stiffness in extreme conditions can be written as

(a) subspring is full elastic
The section subspring stiffness S_{ca}= ∞, subelement stiffness K_{Ma} can be written as:

$$K_{Ma} = \begin{bmatrix} EA/L & 0 & 0 \\ 0 & K_{11} & K_{12} \\ 0 & K_{21} & K_{22} \end{bmatrix} \tag{19}$$

(b) subspring is partially yielded
The section subspring stiffness $S_{ca}= S_p$, subelement stiffness K_{Mb} can be written as:

$$K_{Mb}=\begin{bmatrix} EA/L & 0 & 0 \\ 0 & K_{11}/(1+K_{11}/S_{c1}) & K_{12}/(1+K_{11}/S_{c1}) \\ 0 & K_{12}/(1+K_{11}/S_{c1}) & K_{22}-K_{12}K_{21}/(K_{11}+S_{c1}) \end{bmatrix} \tag{20}$$

(c) subspring is fully yielded
The section subspring stiffness S_{ca}=0, subelement stiffness K_{Mc} can be written as:

$$K_{Mc}=\begin{bmatrix} EA/L & 0 & 0 \\ 0 & 0 & 0 \\ 0 & 0 & K_{22}-K_{12}K_{21}/K_{11} \end{bmatrix} \tag{21}$$

in which $K_{11}= K_{22}= S_1EI/L$, $K_{12}= K_{21}= S_2EI/L$. S_1, S_2=stability function accounting for shear deformation.

When the link moment exceeds first yielding moment M_{y1}, only full elastic or full yield can occur in all the subsprings. As changes in moment at left end of flexural links, section spring stiffness of each subspring may be equal to S_{ca1}, S_{ca2} or S_{ca3}. The element stiffness is equal to the sum of subelements stiffness. Several conditions of element stiffness K can be expressed in Table 2:

Table 2. Section Subspring Stiffness and Element Stiffness K for Flexural Links

	$M<M_{er}$	$M_{er}\le M<M_{y1}$	$M_{y1}\le M<M_{y2}$	$M_{y2}\le M<M_{y3}$	$M>M_{y3}$
S_{ca1}	∞	S_p	0	0	0
S_{ca2}	∞	∞	∞	0	0
S_{ca3}	∞	∞	∞	∞	0
K	K_{Ma}	$\beta_{1M} K_{Mb}+(\beta_{2M}+\beta_{3M}) K_{Ma}$	$\beta_{1M} K_{Mc}+(\beta_{2M}+\beta_{3M}) K_{Ma}$	$(\beta_{1M}+\beta_{2M}) K_{Mc}+\beta_{3M} K_{Ma}$	K_{Mc}

in which $\beta_{1M}=(K_{1M}-K_{2M})/K_{1M}$; $\beta_{2M}=(K_{2M}-K_{3M})/K_{1M}$; $\beta_{3M}=K_{3M}/K_{1M}$. K_{1M}, K_{2M} and K_{3M} are as shown in Eq.13. When $M>M_{y3}$, all the subsprings at the left of link are in plastic stage.

If the moment at the right of link is changed as the left, the element stiffness K can be formed by only changing the K_{Ma}, K_{Mb} and K_{Mc} in Table 2.

3.4 Advanced Analytical Model of Shear Links

When the link is designed as shear link in EBFs, shear failure will precede flexural failure. The conventional advanced analytical model cannot predict the behavior of shear yielding.

As the interaction between the shear and axial force is neglected, the stability function S_1 and S_2 that consider the shear deformation and ignore the effect of axial force can be written as

$$S_1=\frac{4+\beta}{1+\beta},\quad S_2=\frac{2-\beta}{1+\beta} \tag{22}$$

in which $\beta=12\mu EI/(GAl^2)$.

Considering the effect of shear strain hardening, element stiffness of shear links will reduce gradually with the shear increasing. Assume $\alpha=GA/l$, then $\alpha_1=\lambda\alpha=\lambda GA/l$, in which λ=material enhancement factor for shear strain hardening. So β becomes

$$\beta=\frac{12\mu EI}{\lambda GAl^2}=\frac{12\mu EI}{\lambda\alpha l^3} \quad (23)$$

in which $r=12\mu EI/(\alpha l^3)$. Combined with the Eq. 22 and Eq.23, S_1 and S_2 can become

$$\begin{cases} S_1=\dfrac{4\lambda+r}{\lambda+r}=\dfrac{3\lambda}{\lambda+r}+1 \\ S_2=\dfrac{2\lambda-r}{\lambda+r}=\dfrac{3\lambda}{\lambda+r}-1 \end{cases} \quad (24)$$

The element stiffness K accounting for shear strain hardening can be written as:

$$K_V=\frac{EI}{L}\frac{3\lambda}{\lambda+r}\begin{bmatrix}0&0&0\\0&1&1\\0&1&1\end{bmatrix}+\frac{EI}{L}\begin{bmatrix}A/I&0&0\\0&1&-1\\0&-1&1\end{bmatrix} \quad (25)$$

From Eq. 25, different λ corresponds to different element stiffness K. When λ=1, the K is identical to the elastic stiffness that considers the shear deformation effect; when λ=0, the incremental shear equals zero, and the K is only related to moment.

Whilst loads are only applied at the nodes in EBFs, the shear V is constant along the link. According to the shear yielding values in Table 1, several conditions of element material enhancement factor λ can be expressed in Table 3.

Table 3. Shear Yielding Values and Element Material Enhancement Factor λ for Shear Links

	$V<V_1$	$V_1\leq V<V_2$	$V_2\leq V<V_3$	$V>V_3$
λ_1	β_{1V}	0	0	0
λ_2	β_{2V}	β_{2V}	0	0
λ_3	β_{3V}	β_{3V}	β_{3V}	0
λ	1	$\lambda_2+\lambda_3$	λ_3	0

in which $\beta_{1V}=(K_{1V}-K_{2V})/K_{1V}$, $\beta_{2V}=(K_{2V}-K_{3V})/K_{1V}$, $\beta_{3V}=K_{3V}/K_{1V}$. The K_{1V}, K_{2V} and K_{3V} are as shown in Eq.13. The zero in Table 3 represents the subspring has yielded. When $V>V_3$, all the subsprings are in plastic stage. The element stiffness of shear links K can be formed by only changing the λ in Eq.25.

4. NUMERICAL EXAMPLES

4.1 EBF with Flexural Link

An experimental study of EBF K2 with flexural link has been reported by Shi et al.[17], it is used for the case study in this paper. The load-displacement curve of K2 is obtained by the experimental results. All the beams are H120x70x6x6, columns are H150x120x6x8, and braces are □60x6. The loads and dimensions are shown in Figure 8. E=210kN/mm^2, f_y= 306 N/mm^2 for all the members.

In the advanced analysis of the EBF, flexural yielding, strain hardening, geometric and material nonlinearity, shear deformation and residual stress are explicated. Two kinds of analysis are carried out: (1) NC-EBF: the effect of strain hardening is ignored in EBF; (2) C-EBF: the effect of strain hardening is considered in EBF. The ultimate loads and displacements of all the analyses are compared in Table 4. In the elastic stage, the experimental value is somewhat larger than the results of analysis (1) and (2), it may be influenced by the panel zone. In the elastic-plastic stage, the ultimate load and displacement of analysis (2) are in close agreement with experimental value, but the results obtained from analysis (1) are different from others. The first plastic hinge of analysis (2) is formed at column base, and subsequent plastic hinge is formed at beam segment outside of the link, it is the same as the experimental result for the element yielding sequence. However, the first plastic hinge of analysis (1) is formed at both ends of link, and subsequent plastic hinge is at the column base. So it is important to consider the effect of moment strain hardening. The proposed practical advanced analysis method is suitable for the analysis of EBFs with flexural link, and has a high accuracy. The load-displacement curves obtained by the analyses are shown in Figure 9.

Table 4. Comparison of Ultimate Load and Displacement

	Ultimate Load (kN)	Ultimate displacement(mm)
Experimental	220	11.0
C-EBF	215	12.4
NC-EBF	201	9.0

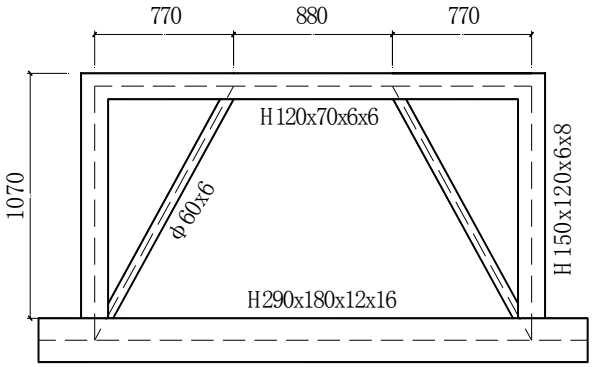

Figure 8. Eccentrically Braced Frame K2: Flexural-link

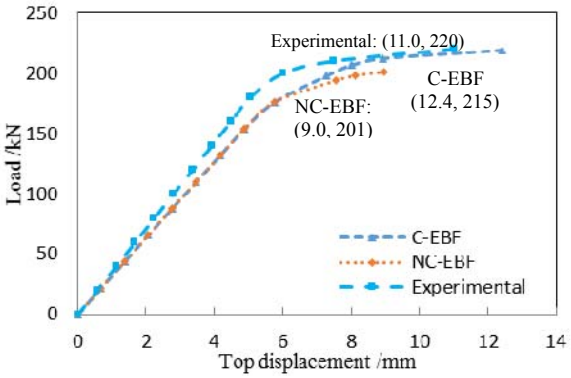

Figure 9. Load-displacement Curve of K2

4.2 EBF with Shear Link

A one-storey EBF with shear link, based on the provision of Code for Seismic Design of Buildings [18], has been designed for the case study in this paper. All the beams are H300x150x6.5x9, columns are H350x350x10x16, and braces are □150x8. The dimensions and loads are shown in Figure 10. E=206kN/mm^2, f_y= 235 N/mm^2 for all the members.

In the advanced analysis of this EBF, shear yielding, strain hardening, geometric and material nonlinearity, shear deformation and residual stress are explicated. Three kinds of analyses are also carried out: (1) NC-EBF: the effect of shear yielding and strain hardening is ignored in EBF; (2) C-EBF: the effect of shear yielding and strain hardening is considered in EBF; (3) Finite Element Analysis: ANSYS is used to analyze in EBF. The ultimate loads and displacements of all the analyses are compared in Figure 11. In the elastic stage, the result of analysis (3) is different from analyses (1) and (2), it may also be influenced by the panel zone. In the elastic-plastic stage, the ultimate load and displacement obtained from analysis (3) are in close agreement with analysis (2), but it is much different from analysis (1). As to the element yielding sequence, first of the analysis (2) occurs at link with shear yielding, and subsequent plastic hinge is formed at the column base. It is the same as the analysis (3), and the stress contour is shown in Figure 12. However, the yielding sequence of analysis (1) is at both ends of link with moment yielding, and subsequent is at the column base. So the effect of shear links and strain hardening are of crucial importance in EBFs. The proposed practical advanced analysis method is also suitable for the analysis of EBFs with shear link, and has a high accuracy. The load-displacement curves obtained by the analyses are shown in Figure 11.

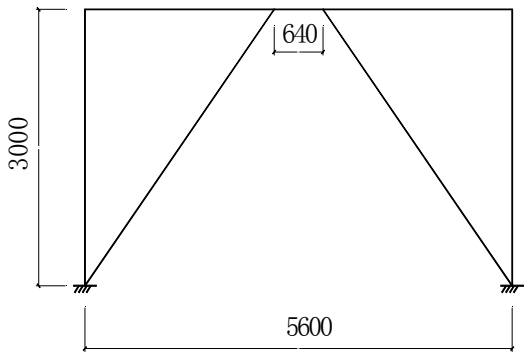

Figure 10. EBF with Shear Link

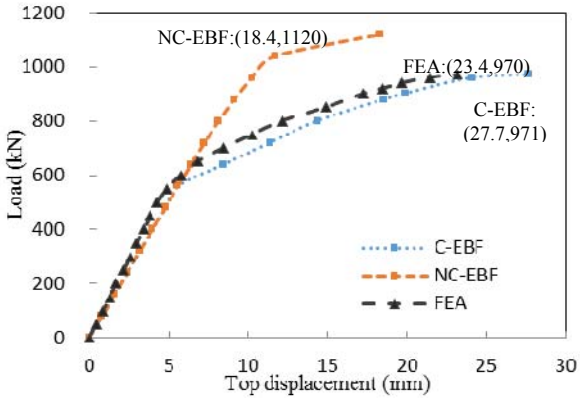

Figure 11. Load-displacement Curve of EBF with Shear Link

4.3 Three-storey EBFs with Shear Links

A global seismic response of two EBFs with shear links is investigated in this paper, as show in Figure 13. It is reported by Rozon et al.[19]. The sizes of beams, columns and braces in every storey are different because of the different seismic intensity, as shown in Table 5. As the seismic intensity of structure A is lower than structure B, all the section dimensions of structure A are smaller than structure B. The shear load at each layer is based on static equivalent force method using inverse triangle. E=205kN/mm^2, f_y= 235 N/mm^2 for all the members.

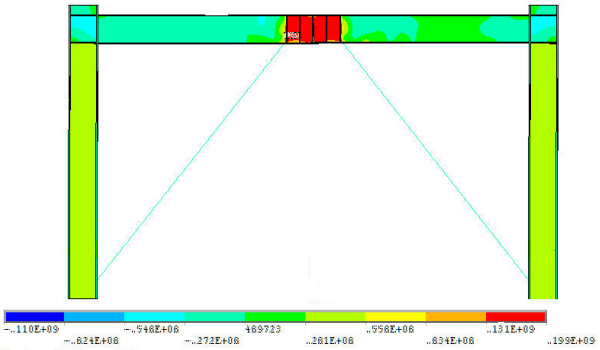

(a) Shear stress contour

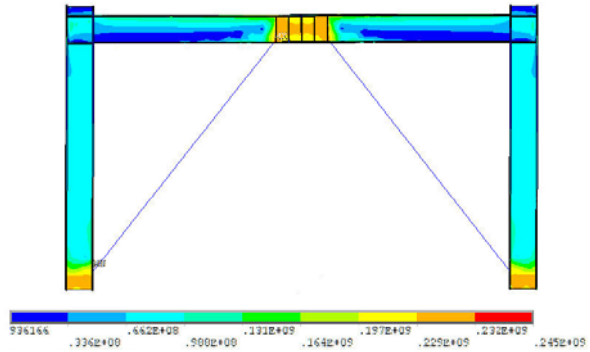

(b) Mises stress contour

Figure 12. Stress Contour of EBF with Shear Link

Shear yielding, strain hardening effect, geometric and material nonlinearity, shear deformation and residual stress are explicated in the advanced analyses of two EBFs. Two kinds of analyses are carried out: (1) NC-EBF: the effect of shear yielding and strain hardening is ignored in two EBFs; (2) C-EBF: the effect of shear yielding and strain hardening is considered in two EBFs. In the elastic stage, the loads and displacements of analyses (1) and (2) are the same because all the members are elastic. In the elastic-plastic stage, whether the effect of shear links is considered will influence the ultimate loads and displacements significantly. All the shear links in two EBFs are yielding from the analysis (2), and the yielding sequence is 2, 3 and 1, as shown in Figure 13. At last yielding occurs at column base, and all the other members are elastic. It is demonstrated that the two structures are designed rationally. The design requirements and expected goals of EBFs can be easily judged by using the proposed practical advanced analysis method. Numerical analysis also shows that the proposed method has a high efficiency as well as easy determination of the element yielding sequence. It can also make a conclusion that shear links should be yielded firstly and the other members are generally elastic for rational design of EBFs under severe earthquake. The load-displacement curves obtained by the analyses are shown in Figure 14.

Table 5. Summary of Selected Shapes and Sizes

	Structure A			Structure B		
Storey	Braces	Columns	Beams	Braces	Columns	Beams
1	HSS203x203x8	W310x79	W250x45	HSS254x254x8	W310x86	W460x60
2	HSS178x178x8	W310x79	W200x31	HSS203x203x9.5	W310x86	W360x39
3	HSS152x152x8	W250x33	W130x28	HSS152x152x9.5	W250x33	W200x27

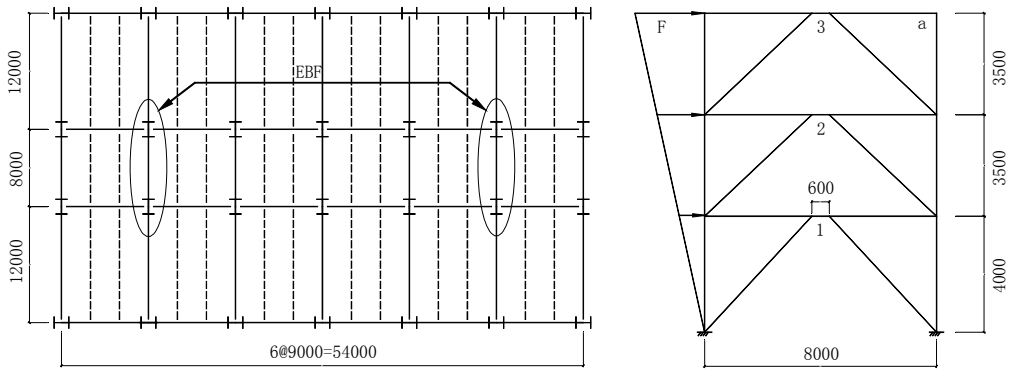

Figure 13. Layout and Elevation of Three-storey EBF

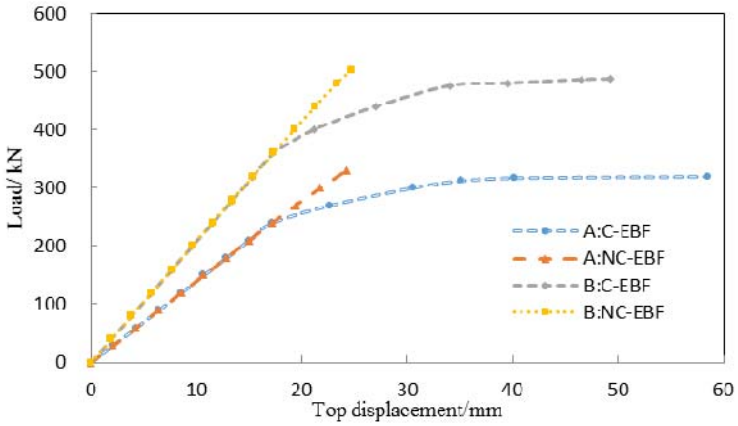

Figure 14. Load-displacement Curves of Two EBFs

5. CONCLUSIONS

A simple and effective model for practical advanced analysis of EBFs, which considers shear and flexural yielding behavior, geometric nonlinearity, material nonlinearity, shear deformation, residual stress, and strain hardening effect, is proposed in this paper. Based on the assumed multiple springs with zero-length at each end to simulate the yielding and the strain hardening effect, the element stiffness of shear and flexural links can be well predicted at different load level. The yield functions for links that derived by using the section assemblage method can be used to evaluate the loading bearing capacity of elements in elastic and inelastic range. Comparison analysis is conducted on the EBFs with flexural-yielding type and shear-yielding type links, and it shows that the strain hardening effect and stiffness variation effect are of crucial importance. Also, the proposed method has a high efficiency and accuracy by using one element or member only.

ACKNOWLEDGEMENT

The authors gratefully acknowledge the research grant provided by the National Nature Science Foundation of China (No. 51178192; 51378219; 51378009), State Key Laboratory of Subtropical Building Science Foundation, South China University of Technology (No. 2012ZA05).

REFERENCES

[1] Kasai, K. and Popov, E.P., "General Behavior of WF Steel Shear Link Beams", Journal of Structural Engineering, ASCE, 1986, Vol.112, No.2, pp. 362-382.

[2] Kasai, K. and Popov, E.P., "Cyclic Web Buckling Control of Shear Link Beams", Journal of Structural Engineering, ASCE, 1986, Vol. 112, No. 3, pp. 505-523.

[3] Prpov, E.P. and Engelhardt, M.D., "Seismic Eccentrically Braced Frames", Journal of Constructional Steel Research, 1988, Vol. 10, pp. 321-354.

[4] Okazaki, T. and Engelhardt, M.D., "Cyclic Loading Behavior of EBF Links Constructed of ASTM A992 Steel", Journal of Constructional Steel Research, 2007, Vol. 63, No. 6, pp. 751-765.

[5] Daneshmand, A. and Hosseini, B., "Performance of Intermediate and Long Links in Eccentrically Braced Frames". Journal of Constructional Steel Research, 2012, Vol. 70, pp. 167-176.

[6] Ricles, J.M. and Popov, E.P., "Inelastic Link Element for EBF Seismic Analysis", Journal of Structural Engineering, ASCE, 1994, Vol. 120, No. 2, pp. 441-463.

[7] Ramadan, T. and Ghobarah, A., "Analytical Model for Shear-link Behavior", Journal of Structural Engineering, ASCE, 1995, Vol. 121, No.11, pp. 1574-1580.

[8] Richards, P.W. and Uang, C.M., "Testing Protocol for Short Links in Eccentrically Braced Frames", Journal of Structural Engineering, ASCE, 2006, Vol. 132, No. 8, pp. 1183-1191.

[9] Liew, J.Y.R., White, D.W. and Chen, W. F., "Second-order Refined Plastic Hinge Analysis of Frame Design, Part 1", Journal of Structural Engineering, ASCE, 1993, Vol. 119, No. 11, pp. 3196-3216.

[10] Kim, S.E. and Chen, W.F., "Practical Advanced Analysis for Braced Steel Frames Design", Journal of Structural Engineering, ASCE, 1996, Vol.122, No.11, pp. 1266-1274.

[11] Chen, W.F., "Structural Stability: from Theory to Practice", Engineering Structures, 2000, Vol. 22, No. 2, pp. 116-122.

[12] Chan, S.L. and Chui, P.P.T., "A Generalized Design-based Elastoplastic Analysis of Steel Frames by Section Assemblage Concept", Engineering Structures, 1997, Vol. 19, No. 8, pp. 628-636.

[13] Chen, W.F. and Lui, E.M., "Stability Design of Steel Frames", CRC Press, 1992.

[14] Chan, S.L. and Chui, P.P.T., "Non-linear Static and Cyclic Analysis of Semi-rigid Steel Frames", Elsevier Science, 2000.

[15] European Convention for Constructional Steelwork, "Ultimate Limit State Calculation of Sway Frames with Rigid Joints, ECCS", Technical Working Group 8.2, Systems, Publication No. 33, 1983.

[16] Ghobarah, A. and Ramadan, T., "Effect of Axial Forces on the Performance of Links in Eccentrically Braced Frames", Engineering Structures, 1990, Vol. 12, No. 2, pp. 106-113.

[17] Shi, Y.J., Xiong, J. and Wang, Y.Q., "Experimental Studies on Seismic Performance of Multi-storey Steel Frame with Eccentric Brace", Journal of Building Structures, 2010, Vol. 31, No. 2, pp. 29-34.

[18] Code for Seismic Design of Buildings, GB50010-2010, Beijing, China Architecture & Building Press, 2010.

[19] Rozon, J., Koboevic, S. and Tremblay, R., "Study of Global Behavior of Eccentrically Braced Frames in Response to Seismic Loads", The 14th World Conference on Earthquake Engineering, Beijing, 2008.

SUB-FRAMES WITH REVERSE CHANNEL CONNECTIONS TO CFT COMPOSITE COLUMNS –EXPERIMENTAL EVALUATION

Fernanda Lopes[1], Aldina Santiago[1,*], Luís Simões da Silva[1], Naveed Iqbal[2], Milan Veljkovic[2] and José Guilherme S. da Silva[3]

[1] *ISISE - Department of Civil Engineering, University of Coimbra, Pólo II, 3030 Coimbra, Portugal*
[2] *Division of Structural and Construction Engineering of the Luleå University of Technology, Luleå, Sweden*
[3] *Department of Structural Engineering of the State University of Rio de Janeiro, Rio de Janeiro, Brazil*
**(Corresponding author: E-mail: aldina@dec.uc.pt)*

Received: 19 March 2014; Revised: 23 April 2014; Accepted: 5 May 2014

ABSTRACT: This paper presents the experimental results of the investigation on the coupled joint-structure behaviour of the composite sub-frame, using the reverse channel connections between an I-beam and the concrete filled tube (CFT) columns. This experimental programme includes seven full-scale tests: three tests at ambient temperature and four tests under heating-cooling curves. The parametric study was dedicated to: temperature-time curve and channel wall thickness (8, 10 and 12 mm).

The main objective of these tests is to provide experimental information on the behaviour of the reverse channel joints and its influence on the structure under a heating-cooling fire. The restraining effects from the unaffected part of surrounding structure induce highly variable loading histories on the joints during fire; therefore the investigation on coupled joint-structure behaviour should lead to a realistic prediction of progressive collapse of the structure.

Keywords: Full-scale tests, Heating-cooling curves, Reverse channel connection, Concrete filled tubes, Robustness.

1. INTRODUCTION

Fire safety requirements have caused a significant cost increase of steel construction by implying a systematic need for fire protection, resulting from severe traditional prescriptive regulations [1], which can impose an extra 20% to 30% onto the cost of the steelwork [2]. Over the past few years, one of the main achievements of structural steel research has been the development of the new engineering methods of analysis and design that take into account the real conditions of fire and the real fire resistance of steel structures ([3], [4], [5]). Such methods allow safer and more economical design and construction of steel structures.

Composite structures are widely used to optimize fire resistance. Concrete-filled hollow sections combine the advantages of steel and concrete and they are often assumed to possess inherently high fire resistance without the use of steel rebars and provide continuous confinement of concrete. In addition, the use of concrete-filled hollow sections also improves the productivity by eliminating the need for formwork. However, connecting to hollow sections is complicated and expensive because there is no access to the inside of the sections. The most common arrangements for beam-to-column joints make use of bolted connections by means of attachments welded to the walls of the steel profile of the composite column; a typical example is the fin plate connection, using a flat plate welded to the column wall. An alternative joint configuration is the web cleat connection, using single- or double-angle sections, or T-sections, welded to the column wall. Additionally, the reverse channel connection has gradually become an alternative option for bolted connections to hollow sections.

Several experimental and analytical studies have been performed to characterize the moment-rotation behaviour of joints between concrete filled tubular columns and I-beams ([6], [7]) at ambient temperature. However, there is a paucity of knowledge on their behaviour in fire.

The demand for connection performance to prevent fracture is very high in fire design for structural robustness, and a way to prevent fracture is to enhance the connection's ductility rather than its strength. The use of connections that deform and accommodate the large axial deformations that arise from thermally induced changes in beam length reduces the internal forces that are developed if these changes are resisted.

Different types of connections between concrete filled tubular columns and steel beams have been studied in fire to improve structural fire resistance enhancing of the deformational capacity of the joints to develop catenary action in the connected beam at high temperatures. In previous experimental studies on structural fire behaviour of different type of steel beam to concrete filled tubular column assemblies [8], the reverse channel connection appears to have the best combination of desirable features: moderate construction cost, ability to develop catenary action and extremely high ductility through deformation of the web channel. In a series of component and joint tests conducted during the European RFCS COMPFIRE project ([9], [10], [11]), the results showed that the reverse channel improved the rotational capacity of the connection and had an ultimate strength similar to an endplate connection tested at the same temperature. Within the same project, the effect of the surrounding structure was also evaluated and small-scale sub-frame tests under a standard fire curve ISO 834 were performed. It was observed that the reverse channel cut form hot-rolled tubes can give considerable deformation capacity to the connection, to enable the structure to survive to higher temperatures than the beam's conventional limiting temperature ([9], [12]).

The experimental tests presented in this paper investigated the behaviour of the reverse channel connections between a steel beam and two composite columns, during the entire fire and considering the development of bending, compression, local yielding and buckling and catenary action within the joint and its components.

2. EXPERIMENTAL TESTS

2.1 Sub-frame and Testing Arrangement

The experimental tests were performed at the Department of Civil Engineering of the University of Coimbra. Seven full-scale tests were performed: three tests at ambient temperature and four tests under two different heating curves, including cooling phase, as presented in Table 1.

Table 1. Experimental Programme

Test nº	Temperature	Column section	Reverse channel connection
1	Ambient	CHS 244.5x10	C1 - U 200x135x8
2	Ambient	SHS 250x10	S1 - U 200x90x8
3	Ambient	SHS 250x10	S2 - U 200x90x10
4	Heating 1 + cooling	SHS 250x10	S2 - U 200x90x10
5	Heating 2 + cooling	SHS 250x10	S2 - U 200x90x10
6	Heating 1 + cooling	SHS 250x10	S1 - U 200x90x8
7	Heating 1 + cooling	SHS 250x10	S3 - U 200x90x12

The basic configuration of the test sub-frames consisted of an I-beam IPE300 and two concrete filled tube columns (square or circular hollow sections). The beam was connected to the columns using reverse channel connections. The columns were 3525 mm tall and the beam span was 5000 mm (Figure 1). The beam was restrained against lateral movements at three points: at the beam mid-span and at 1000 mm on both side of the beam mid-span. The top and bottom restraints of the columns prevented horizontal movements at these points, but allowed the expansion of the columns at the top.

The columns and beam, as well as the reverse channel section were of steel grade S355. The steel grade of endplate at the ends of the beam was S275. Concrete filling of the hollow section columns were grade C30/37 (more details are presented in Section §2.4).

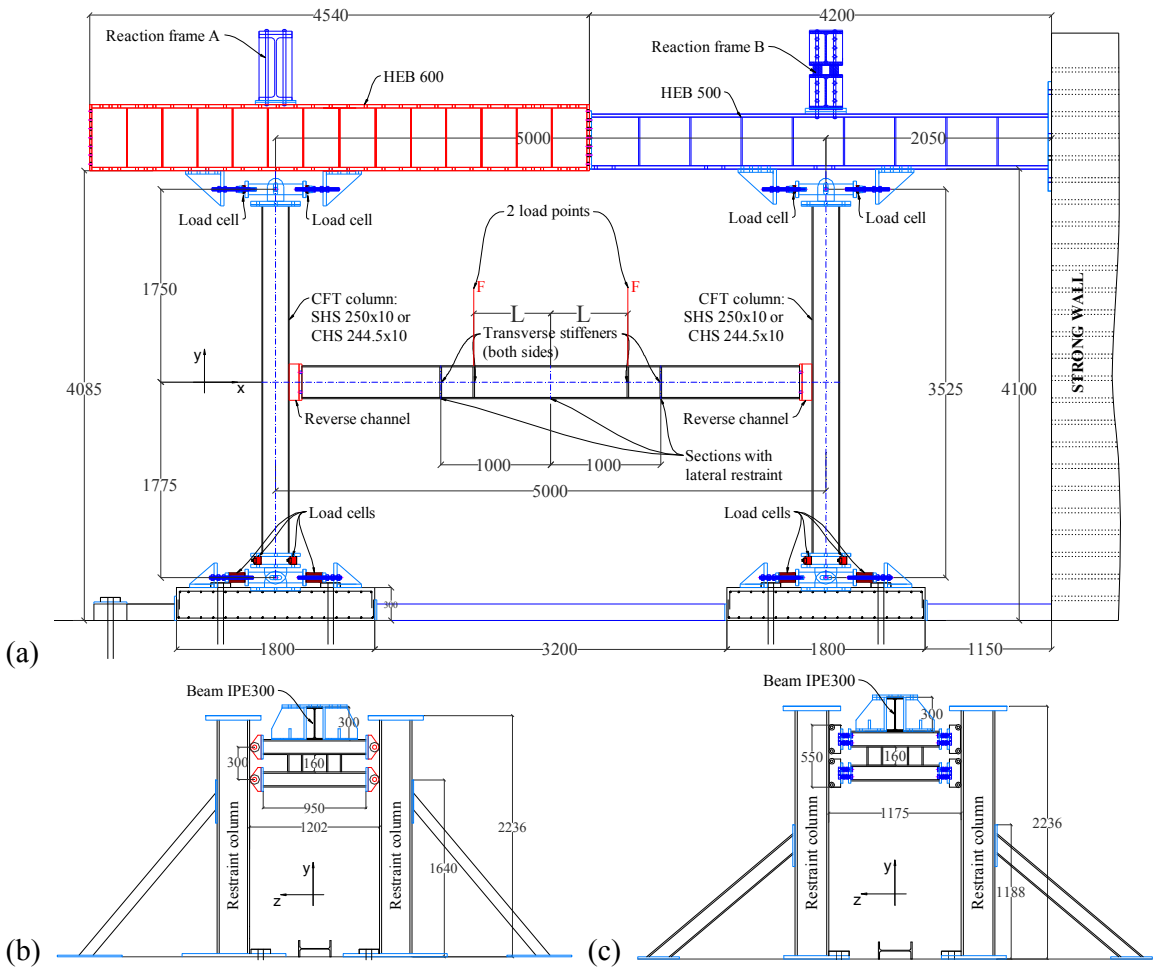

Figure 1. Outline of the Experimental Tests: (a) Elevation View; (b) Lateral Restraint at the Beam Mid-span; (c) Lateral Restraint at the Left and Right Sides of the Beam Mid-span

The reverse channel connections were built through a bolted endplate to web of a channel section with its flanges welded to the column face. Figure 2 illustrates the reverse channel connections to SHS and CHS columns. The bolts (M24) and the nuts were black grade 10.9. The reverse channel sections were fabricated from square hollow sections that were cut lengthwise. To reach these geometric dimensions, three different wall thicknesses of SHS200x200 were used: 8, 10 and 12 mm.

The connections in the tests should presented high ductility to accommodate the large deflection of the beam. The connections were designed at ambient temperature according to the component method defined in EN 1993-1-8 [13] and in CIDECT Report 5BP-4/05 [14]. A detailed description of the design method and the identified components of the reverse channel joints have been found in [10]. The deformation of the loaded face of the reverse channel determined the resistance of the tested connections and the weakest component was the reverse channel in bending, except for those with wall thickness equal to 12 mm, which presented the beam web in tension as the weakest component. Material properties from uniaxial tensile tests (section § 2.4) were used in the

analytical calculation without safety factor. The design moment resistance ($M_{j,Rd}$) of the joints S1 and C1 was 0.17 times the design plastic moment resistance of a beam ($M_{b,pl,Rd}$). They were classified as nominally pinned at ambient temperature. The joints S2 and S3 presented the design moment resistance greater than 0.25 times the design plastic moment resistance of the beam. They were classified as partial-strength. Regarding the initial stiffness ($S_{j,ini}$), all connections were semi-rigid (Table 2).

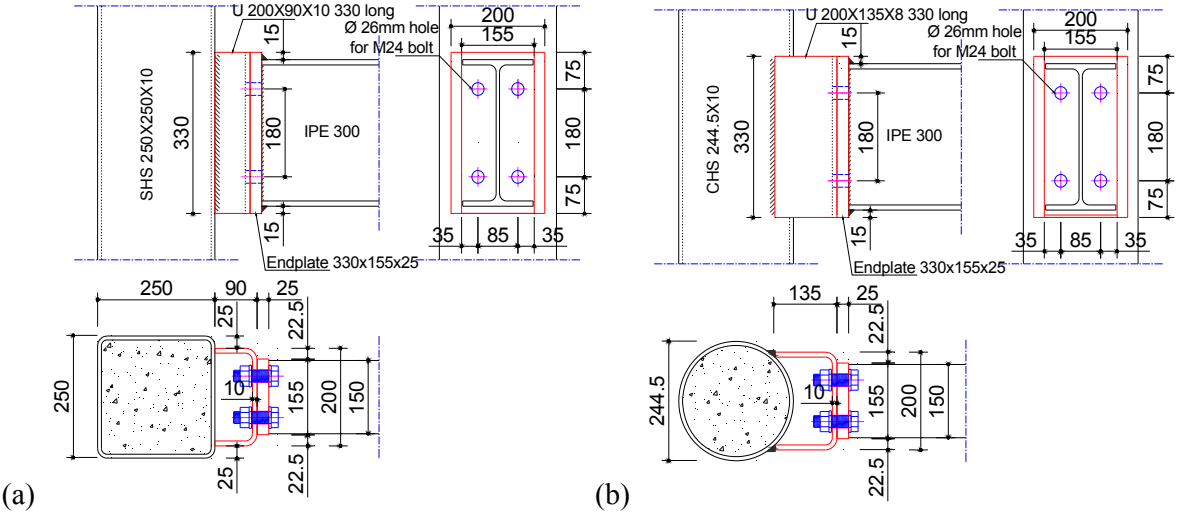

Figure 2. Reverse Channel Joints: (a) Square Column SHS 250x10 and Reverse Channel Connection S2; (b) Circular Column CHS 244.5x10 and Reverse Channel Connection C1

Table 2. Analytical Results of Stiffness and Strength of the Reverse Channel Connections

Reverse channel connection	Stiffness		Strength		
	$S_{j,ini}^{*}$ (kNm/rad)	Class.	$M_{j,Rd}$ (kNm)	$M_{j,Rd}/M_{b,pl,Rd}$	Class.
S1/C1 (t_w=8mm)	8560.12	Semi-rigid	37.96	0.17	Nominally pinned
S2 (t_w=10mm)	12970.40	Semi-rigid	94.62	0.42	Partial-strength
S3 (t_w=12mm)	19699.26	Semi-rigid	101.98	0.46	Partial-strength

2.2 Mechanical and Thermal Loadings

During the ambient temperature tests (Tests 1 to 3), the mechanical loading was continually increased by a hydraulic actuator (maximum test load 1000 kN, maximum piston stroke ±150 mm) at two points symmetrically located at 800 mm to either side of the beam mid-span. A reinforced HEB240, S355, was connected under the actuator to apply the load-increasing test with the aid of two cylinders (Ø 80mm), as illustrated in Figure 3(a). The load was gradually applied under displacement control with a speed of 0.02mm/s until failure.

For all heating-cooling tests (Tests 4 to 7), two pairs of reinforced concrete blocks (700 mm x 700 mm x 900 mm) were used to apply the constant mechanical loading. Each pair of concrete blocks was positioned at ambient temperature hanging from a HEA100, transversely positioned and welded to the beam top flange (Figure 3(b)). Due to geometric limitations in the experimental layout, especially due to the dimensions of the concrete blocks and the positions of the lateral restraints, load points at 800 mm from the mid-span were no longer possible; so, they were symmetrically located 600 mm away from the beam mid-span. Two pairs of concrete blocks, two beams HEA100 and the lateral restraint devices contributed to the total amount of the applied load: 47 kN. The nominal load ratio was 0.20, which is defined as the ratio of the applied load during the

heating-cooling tests ($M_{fi,Ed}$ = 45 kNm) to the nominal loading-carrying capacity of the simply-supported beam at ambient temperature (M_{Rd} = 223 kNm).

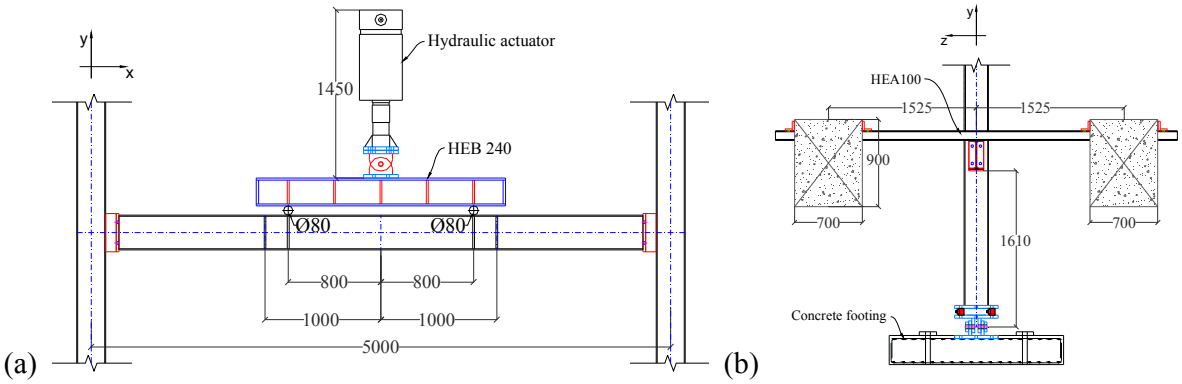

Figure 3. Mechanical Loading: (a) at Ambient Temperature; (b) under Heating-cooling Curves

Flexible Ceramic Pad (FCP) heaters applied the thermal loading of the heating-cooling tests. Reverse channel, endplates, bolts, and beam (web and bottom flange) were heated, as shown in Figure 4. In order to simulate the heat sink of a concrete slab, flexible ceramic pads were not attached to the top flange of the beam. The columns were not directly heated.

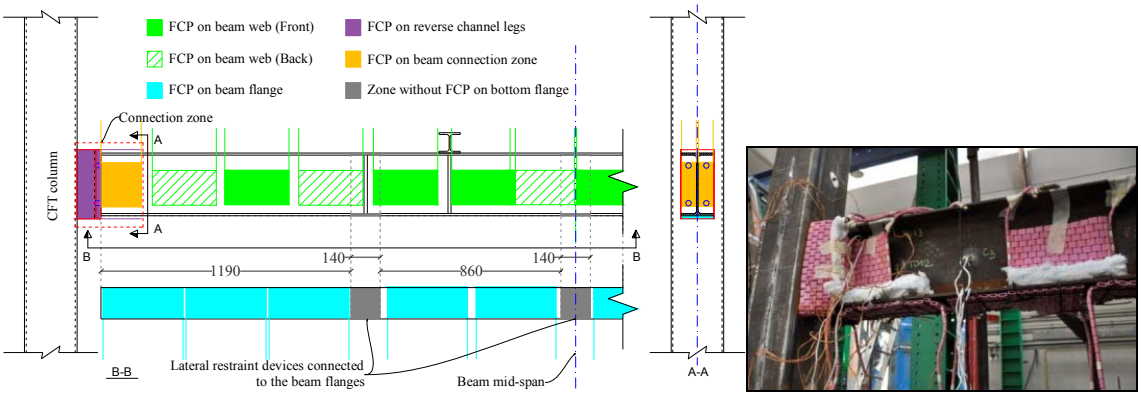

Figure 4. Heating Elements on the Beam and Connection

The steel temperatures were controlled in different zones: reverse channel, beam web, beam bottom flange, endplates and bolts. The heating rate and target temperature were previously defined a priori. To evaluate the effect of heating temperatures, two different heating profiles were used in the tests. A high heating rate was used for all tests: 800ºC/h (Tests 4, 6 and 7) or 700ºC/h (Test 5) for the temperature control of the beam bottom flange and reverse channel, and 600ºC/h (Tests 4, 6 and 7) or 500ºC/h (Test 5) for the temperature control of the beam web. The lower heating rates increases the duration of the heating phase in Test 5, allowing a more uniform distribution of temperature along the beam length. The heating rate for the endplates and bolts was around 400ºC/h for all tests. Figure 5 illustrates the heating profiles. When the temperature reached the target (*Target temp*. in Figure 5), i.e., 900ºC (Tests 4, 6 and 7) or 800ºC (Test 5) in the beam bottom flange and 800ºC (Tests 4, 6 and 7) or 700ºC (Test 5) in the beam web, the increase of the temperature was stopped and temperatures remained constant for about 15 minutes (*End temp*. in Figure 5). After that, the power units were turned off. The cooling phase developed without removing the thermal insulation.

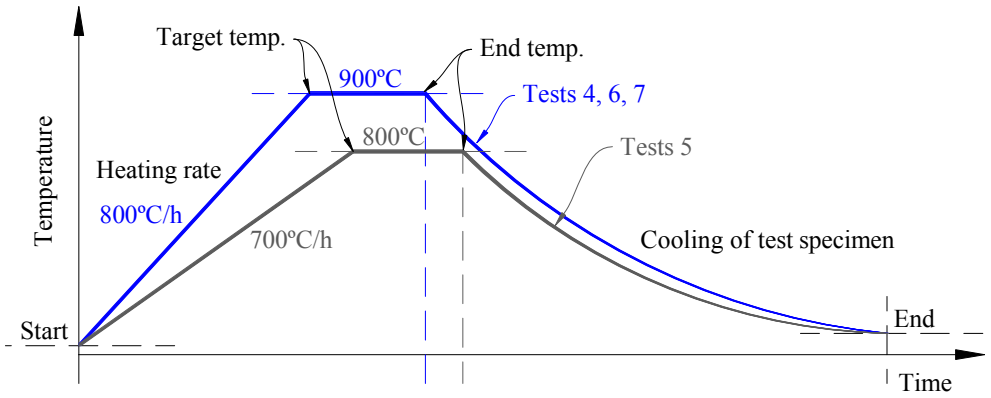

Figure 5. Control Temperature of the Heating Elements at the Beam Bottom Flange

2.3 Instrumentation of Test Specimens

The main requirements of the instrumentation were to measure the temperature, the distribution of internal/reaction forces and the deformed shape of the structural elements. Figure 6 illustrates the location of the load cells and displacement transducers in the experimental test set-up. A total of 72 thermocouples were employed to monitor the temperature evolution of the structure during the heating-cooling tests (Figure 7). The beam was divided into six sections of temperature control: sections 1, 2, and 3a were located at the left side of the beam, while sections 3b, 4, and 5 monitored the temperatures in the right side.

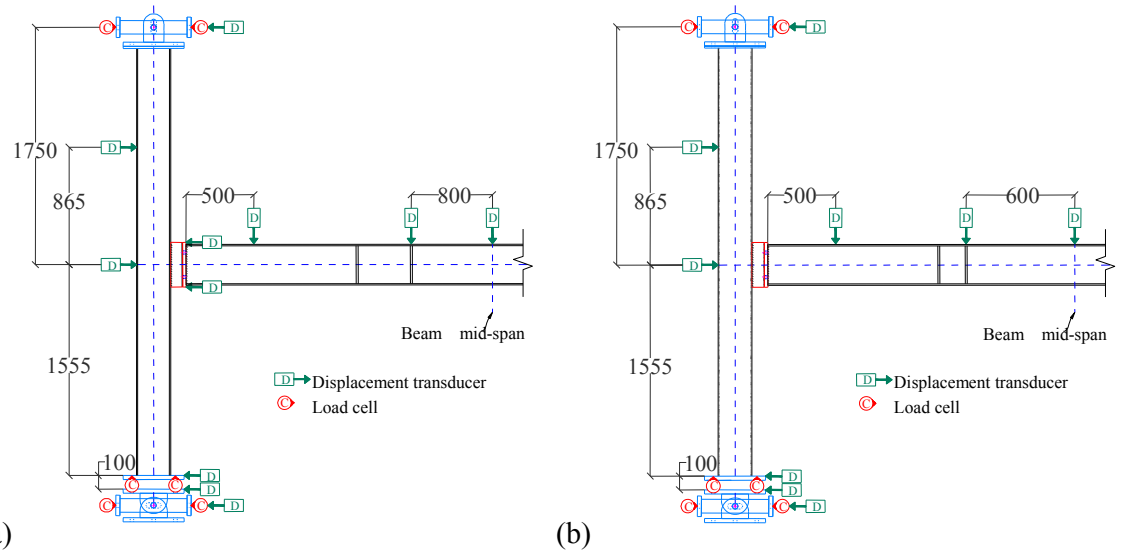

Figure 6. Location of the Load Cells and Displacement Transducers:
(a) Ambient Temperature Tests; (b) Heating-cooling Tests

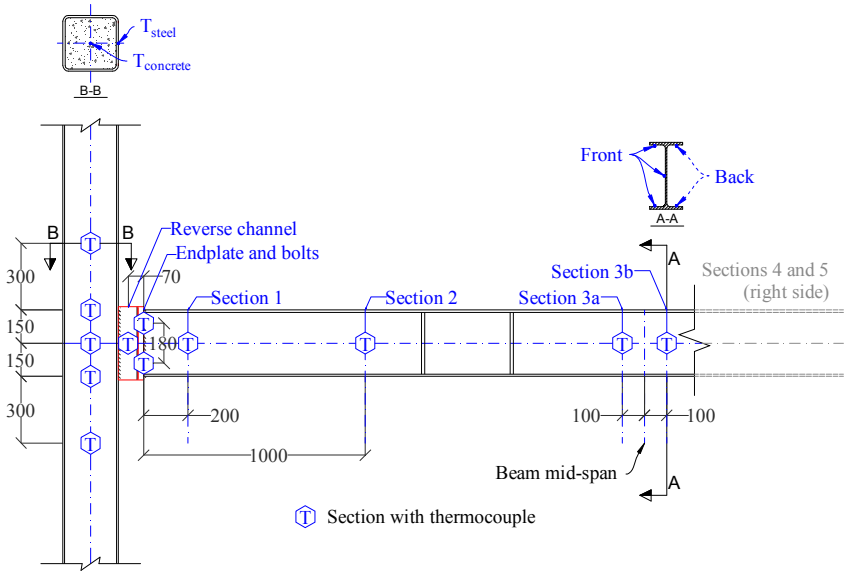

Figure 7. Location of the Thermocouples

2.4 Control Tests and Material Properties

Tensile tests of the main steel elements and compressive strength tests of the concrete infill of the columns were performed to obtain the mechanical properties to be considered for the validation of further numerical and analytical models. The steel test specimens were extracted from the beam web and flanges, the column walls, the endplate, and the reverse channel sections. A total of 24 test specimens were used for tensile tests at ambient temperature. The material of the reverse channel sections (8, 10 and 12 mm thicknesses) was also tested at elevated temperatures, totalling 36 test specimens: 12 specimens were extracted from each reverse channel section and 3 tensile tests were performed for each constant elevated temperature: 200ºC, 400ºC, 600ºC and 800ºC. The testing machine and some test specimens are shown in Figure 8. The tensile tests were performed according to ISO 6892-1 [15] and EN 10002-5 [16].

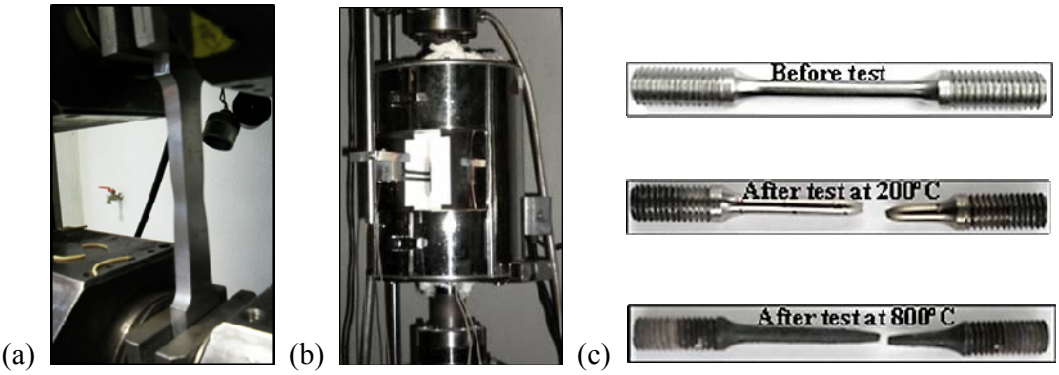

Figure 8. Tensile Tests of the Steel Materials: (a) Tensile Testing Machine; (b) Testing Furnace; (c) Test Specimens for Tensile Tests at Elevated Temperatures

The tensile nominal stress-engineering strain curves of steel at the ambient and elevated temperatures are illustrated in Figure 9. At ambient temperature (Figure 9(a)), the four typical regions of the stress–strain curve of a low carbon structural steel are very clear in the hot rolled specimens: linear elastic region, yield plateau, strain hardening region and strain softening or necking portion, after the maximum load has been reached; however, in the curves from the cold

work specimens, the yielding plateau is not evidenced. Additionally, it is noted that for the same steel grade (S355), the yield strength and ultimate stress of the hollow sections (cold work specimen) were higher than the steel coupons cut from the beam (hot rolled specimen). The cold-formed steel sections also presented a decrease in ductility when compared with the steel of the beam and endplate; furthermore, the stress-strain curves obtained from hot-tension testing exhibit a much smaller spread between yield strength and ultimate, as shown in Figure 9(b). The increased strength caused by cold forming was drastically reduced at temperature above 600ºC and the stress-strain curves exhibit a softening response after yielding. The stress-strain curves in Figure 9(b) show that the ductility of the cold form steel section was reduced when subjected to elevated temperature until 600ºC.

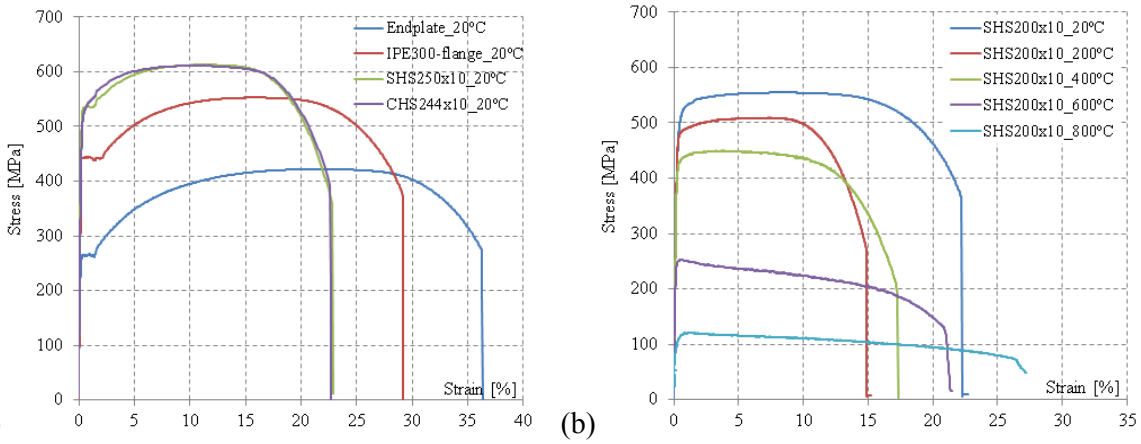

Figure 9. Strain-stress Curves of the Steel Materials: a) Ambient Temperature Tensile Tests; b) Comparison of the Ambient and Elevated Temperature Tensile Tests of the Reverse Channel Sections

Table 3 summarizes the mechanical properties from tensile tests of the main steel elements.

Table 3. Mechanical properties of steels S275 and S355

		EN 10025-5 EN 1993-1-2	Tests results		
Steel	Temp. (ºC)	Yield strength f_y (MPa)	Yield strength f_y (MPa)	Tensile strength f_u (MPa)	Elongation after fracture A (%)
S275, End-plate	20	275	236.7	424.7	40.1
S355, IPE 300 (flange)	20	355	446.0	562.0	31.0
S355, SHS 250x10	20	355	554.7	621.3	27.0
S355, CHS 244.5x10	20	355	579.3	627.7	28.0
S355, SHS 200x10	20	355	513.3	558.7	27.3
	200	355	489.3	515.7	20.1
	400	355	447.3	473.0	24.5
	600	166.9	249.7	252.3	35.6
	800	39.1	119.7	124.0	36.9

All columns were filled with the same concrete mix. A total of 27 cubes were prepared and tested: three compression tests were performed after 7 days, 28 days, and also at the day of each sub-frame test. The tests at 28 days confirmed the concrete properties C30/37 according to EN 206-1 [17]. The strength average of the tests was 41.9 MPa ($f_{ck,cube}$ at 28 days).

3. EXPERIMENTAL TEST RESULTS

3.1 Summary of the Test Results

A summary of the ambient temperature and heating-cooling test results is presented in Table 4. The deflection of the beam at the mid-span ($\Delta_{y,max}$) indicates the maximum deformation that was imposed at the mid-span of the beam. The axial force in the beam (F_x) resulted from the thermal expansion and contraction of the beam during the heating-cooling tests. In the tests at ambient temperature, in which there were not horizontal forces previously applied in the sub-frame, the horizontal reactions at the ends of the columns were very small.

Table 4. Summary of the Test Results

Test	Temperature	$F_{y,max}$[1] (kN)	$\Delta_{y,max}$[2] (mm)	$F_{x,comp,max}$[3] (kN)	$F_{x,tens,max}$[4] (kN)
1	Ambient	356.3	-127.1		
2	Ambient	379.5	-138.6		
3	Ambient	530.4	-295.1		
4	Heating 1-cooling	47.0	-463.2	-118.8	127.0
5	Heating 2-cooling	47.0	-115.0	-137.9	14.7
6	Heating 1-cooling	47.0	-470.3	-93.9	145.4
7	Heating 1-cooling	47.0	-358.6	-128.0	155.7

[1] Total applied load; [2] Maximum beam deflection at mid-span; [3] Maximum beam axial force – compresssion; [4] Maximum beam axial force – tension

3.2 Behaviour at Ambient Temperature

3.2.1 Failure modes

Sub-frames from Test 1 and Test 2 failed due to the lateral-torsional buckling of the beams, as illustrated in Figure 10(a) and Figure 11(a), respectively. There was no failure of the joints although the reverse channels showed slight deformation that was mainly concentrated around the bolts holes in the tension zone. The bolts remained almost straight, and the endplates was almost undeformed after both tests (Figure 10(b) and Figure 11(b)). Besides that, the columns did not present any signs of damage.

(a)  (b) 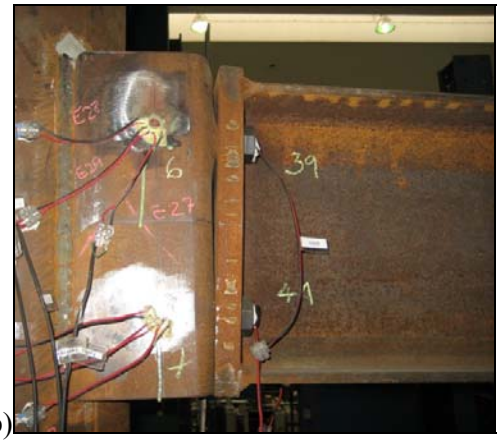

Figure 10. Deformed Shape in the Test 1: (a) Beam; (b) Connection

(a) 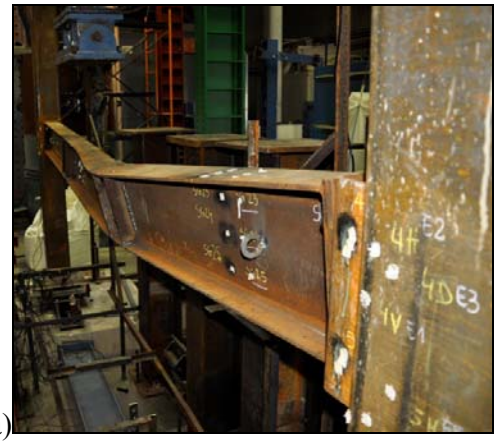 (b) 

Figure 11. Deformed Shape in the Test 2: (a) Beam; (b) Connection

After Tests 1 and 2, the restraint system was reinforced to avoid the lateral-torsional buckling, and consequently increase the maximum applied load during Test 3 (Figure 12(a)). The connections experienced large deformation in both tension and compression zones, although the endplate did not show any deformation after the test, as observed in Figure 12(b).

(a)  (b) 

Figure 12. Deformed Shape in the Test 3: (a) Beam; (b) Connection

3.2.2 Global behaviour

The behaviour of the sub-frame in all ambient temperature tests presented four phases: (1) elastic deflection of the beam, increasing linearly with the mechanical loading, (2) reduction in the rate of increase in the applied load with a continuum increase in beam deflection, (3) decrease in the load carrying capacity of the beam due to failure, and (4) unloading.

In Test 1, the maximum load reached was 356.3 kN and the beam mid-span deflection was 68.1 mm at the same time. After that, the beam lost its load carrying capacity gradually and the joints could not transmit the bending moment to the columns. Similarly, in Test 2, the maximum applied load was 379.5 kN and the corresponding beam mid-span deflection was 94.3 mm (Figure 13). In test 3, the maximum beam deflection was almost 300 mm at the mid-span, which corresponded to the maximum displacement of the piston of the actuator. Consequently, the test was finished with the maximum applied load of 530.4 kN (Figure 12(a) and Figure 13). No failure was observed in the sub-frame and the third phase was not developed; the unloading procedure started after reaching

the maximum piston stroke of the actuator.

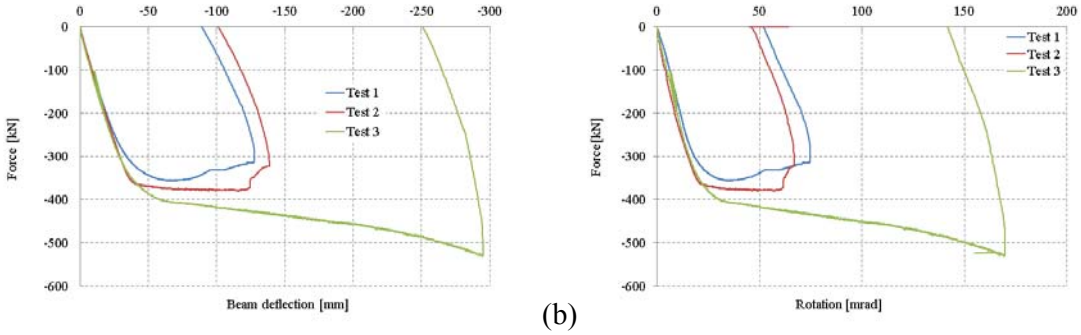

Figure 13. (a) Total Applied Load *versus* Beam Mid-span Deflection; (b). Total Applied Load *versus* Rotation of the Joint (left side)

The initial stiffness of the sub-frame was similar in the three tests at ambient temperature. The beam strength controlled the global behaviour of the structure. Due to the efficient lateral restraints, Test 3 presented the largest spread between plastic strength and maximum load applied on the beam, which is a typical behaviour of sub-assemblies with this type of joints, as observed in previous studies ([8], [11]).

The rotation of the joints could be calculated with the horizontal displacement obtained from the displacement transducer at each edge of the reverse channels, or using the vertical displacement of the beam near to the connection zones, as illustrated in Figure 6. Figure 13(b) presents the force-rotation relationship of the joints. The large deformation of the connections in Test 3 showed the high rotational capacity of the joints despite the thicker reverse channel's web.

3.3 Behaviour at Elevated Temperature

3.3.1 Thermal response

Figure 14 illustrates the evolution of the temperature in the tests. The beam bottom flange at mid-span reached a maximum temperature between 626ºC and 763ºC, although the beam web reached higher temperatures at the same section for all tests.

The temperatures along the beam were not uniform neither constant, as a result of the heating method and the efficiency of the thermal insulation around the beam and the connections. The zones of the beam near to the connections (sections 1 and 5) had occasionally higher temperatures during the heating. As illustrated in Figure 14(b), the temperature was distributed more uniformly in the connection elements (i.e. reverse channel sections, beam endplates, and bolts). For each tested joint, the temperature curve in the endplate is similar to the one in the bolts; the reverse channel legs follow the heating of previous ones, but it reached lower maximum temperatures.

During Test 4 (Heating 1 + Cooling), the heating process lasted about 83 minutes. After that, the heating machines were turned off. The beam reached the maximum temperature (763.4ºC) in the bottom flange after approximately 65 minutes. The cooling phase took about 10 hours until the temperature of the structure was about 50ºC. By safety conditions for workers, the thermal insulation of the beam and of the connections was kept until the total cooling of the structure in all tests. Unfortunately, this increased the duration of the cooling when compared to a natural fire.

In Test 5 (Heating 2 + Cooling), the heating was slower than in Test 4 and it lasted about

108 minutes. The maximum temperature in the beam bottom flange at the mid-span was 626.4ºC after approximately 110 minutes of the start of the heating. The cooling phase lasted approximately 10 hours.

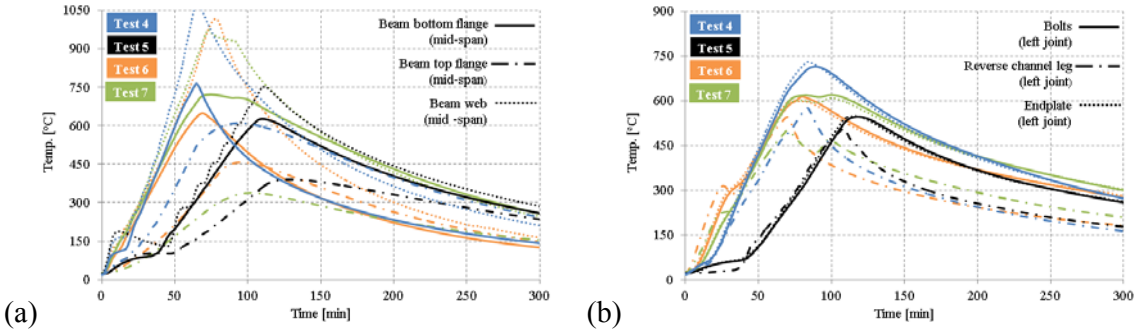

Figure 14. Temperature Evolution Curves: (a) Beam Mid-span (Section 3), (b) Left Joint

The heating profile of Test 6 was similar to Test 4. The heating phase lasted about 83 minutes while the duration of the cooling phase was about 10 hours. The beam bottom flange reached a maximum temperature (648.5ºC) in the beam mid-span after approximately 69 minutes. After 61 minutes of the heating, the beam deflection started to increase quickly, when the temperature in the beam bottom flange at the mid-span was 607.1ºC. The heating process and temperatures distribution in Test 7 was similar to Test 6.

3.3.2 Mechanical response

Figure 15 presents the evolution of the beam deflection at mid-span and the beam axial force during the entire duration of the fire. The beam deflection increased slowly durign the early stage of heating. The rate of increase of the deflection increased rapidly when the beam bottom flange reached temperatures between 587ºC and 730ºC at the mid-span. The lower temperatures in the beam mid-span and connection elements during Test 5 led to little deformation in the beam and connection, as well as the lowest deflection of the beam. The temperatures in the Test 7 were similar to the Test 6, however, the ductility of the thinnest reverse channel in the Test 6 allowed the beam to undergo large deflection and plastic deformation without failure of the structure (Figure 15(a)). However, although the thickness of the reverse channel used in Test 6 was less than the used in Test 4, the maximum temperatures recorded in the connection of Test 4 were higher (the plate and bolts reached maximum values near 750ºC, as depicted in Figure 14(b)); these high temperatures caused higher ductility of the steel (according to the results presented in Section §2.4, the strain at rupture decreases until 600ºC but it increases again for higher temperatures), and thus the maximum deflection of the beam in Test 4 has reached maximum values near the ones observed in Test 6.

Concerning the axial force development represented in Figure 15(b), the axial restraint of the cold columns induced compression forces in the beam due to the thermal expansion during the heating phase. Since the beam reached its limit of axial resistance, it started to move downwards and the axial force, initially compressive, became in tensile forces. The beam experienced the inversion of forces during the heating in almost all tests. The maximum tensile forces reached at the end of the tests were higher than compressive force developed during the heating phase. Unlike the other tests, the speed deflection of the beam remained very low during the Test 5. When the beam increased its deflection, this reduced the axial compressive force in the beam; nevertheless, it did not turn to tension. The axial force in the beam became almost zero at the end of the test. It should be recalled,

that the difference between Test 5 and other tests is the heating-cooling profile only: the heating rate is lower 100 ºC/h than the others tests and the maximum applied temperature was 100ºC lower, however the mechanical response of the frame is completely different.

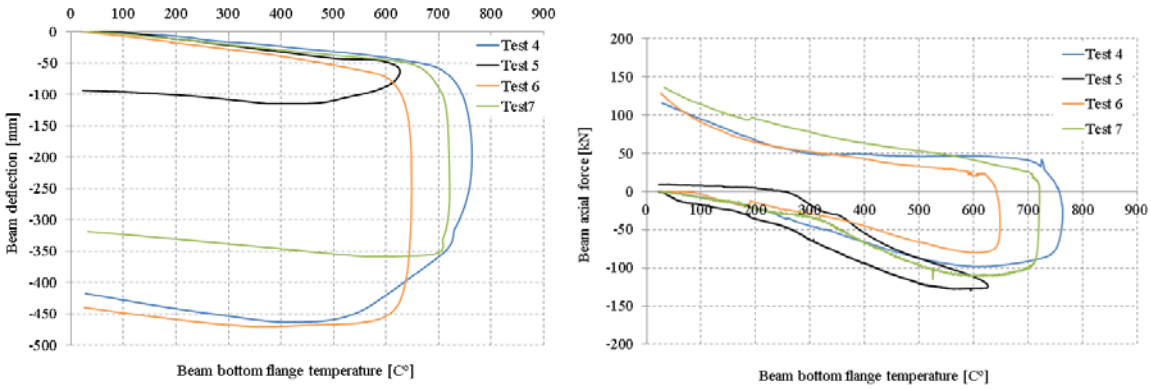

a) b)

Figure 15. a) Beam Vertical Deflection at the Mid-span; b) Beam Axial Force *versus* Temperature in the Beam Bottom Flange

3.3.3 Failure modes

Concerning the failure modes, the beam from Test 4 exhibited local buckling in the bottom flange and web shear buckling near to the connections (Figure 16). The endplate presented a large deformation; meanwhile, the reverse channel presented small deformations, which were specially concentrated around the bolts holes in the top row. This difference of deformation between end plate and reverse channel could be justified by the differences of maximum temperature reached in these components: the maximum end-plate temperature was above 700ºC while in reverse channel it did not reach 600ºC. No failure was observed in the bolts. This behaviour was also responsible for the deflection of the beam, as explained in Section §3.3.2.

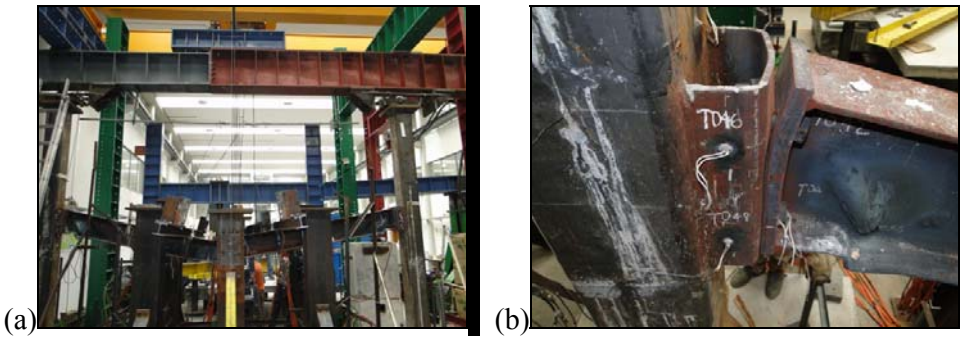

(a) (b)

Figure 16. Deformed Shape in the Test 4: (a) Beam; (b) Connection

The beam from Test 5 presented the lowest deflection and the reverse channel and endplate did not have a noticeable deformation (Figure 17). The permanent deformations could only be observed in the beam bottom flange close to the connections. Again, these results show that even with small differences in the heating-cooling profile, the effect on the behaviour and failure modes is significantly different from the other tests.

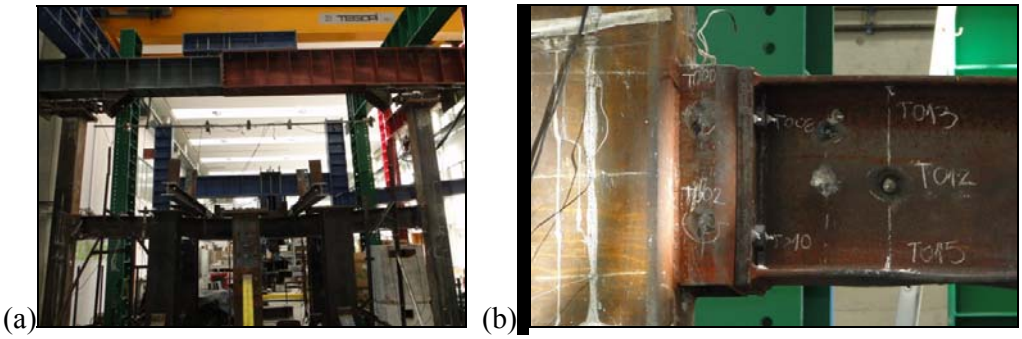

Figure 17. Deformed Shape in the Test 5: (a) Beam; (b) Connection

The highest deflection of the beam at the mid-span occurred in the Test 6. Instead of Test 4, which had similar beam deflection, there is no local buckling in the beam near to the connections. The reverse channel presented large deformation at both the top and bottom zones, as illustrated in Figure 18(b). In this case, this behaviour is justified not by the differences on the temperature, but due to the reduced thickness of the reverse channel (only 8 mm): a thinner reverse channel shows a lower rotational restraint and behaves similar to a pinned joint, inducing larger joint rotations and consequently, larger beam deflections; moreover, the axial restraint to the thermal expansion is also lower and local buckling didn't developed in the beam during the first stage of heating.

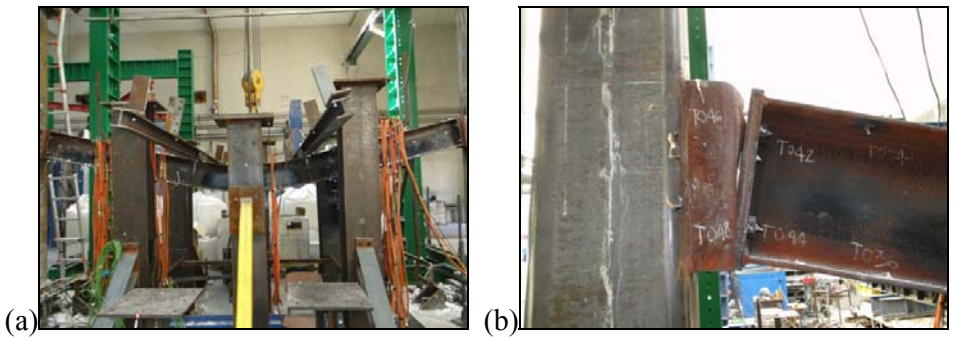

Figure 18. Deformed Shape in the Test 6: (a) Beam; (b) Connection

The beam experienced large deflection in the Test 7 although it was lower than Tests 4 and 6 (Figure 19). The endplates at both ends of the beam showed deformation at the top flange and local buckling of the beam web and bottom flange near to the connection was also noticed. Due to its high thickness (12 mm), the reverse channel showed almost no sign of damage after the test.

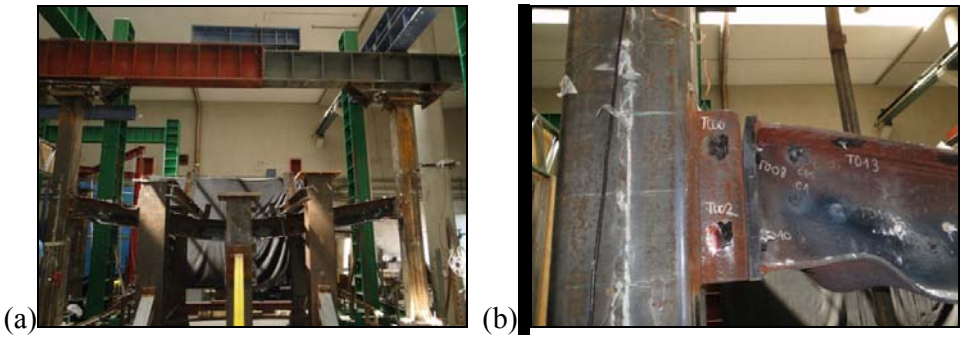

Figure 19. Deformed Shape in the Test 7: (a) Beam; (b) Connection

4. CONCLUSIONS

This paper reports on the experimental results of the investigation on the coupled joint-structure behaviour of the composite sub-frame, using the reverse channel connections between an I-beam and the concrete filled tube (CFT) columns. Seven full-scale tests were performed: three tests at ambient temperature and four tests under two different heating curves, including cooling phase. The main objective of the tests was to provide information on the interaction between joint and the connected structural elements. The study aimed to understand the behaviour of the reverse channel connections during the development of bending, compression, local yielding and buckling and catenary action within the joint and its components.

In the ambient temperature tests, the first failure mode occurred due to the lateral instability of the beam. However, after efficiently restrained the beam, the results showed the large rotation capacity of the joint without global failure of the beam, despite the thicker reverse channel connection than those used in the tests with failure by lateral-torsional buckling.

During the heating-cooling tests, it was concluded that the development of the fire is also a key aspect on the global behaviour of the sub-frame; small differences in the heating – cooling profile could produce completely different results.

Moreover, as mentioned in the introduction of this paper, the demand for connection performance to prevent fracture is very high in fire design for structural robustness, and a way to prevent fracture is to enhance the connection's ductility rather than its strength. The tests showed that even with large deflection at the mid-span of the beam, no global collapse of the sub-frames was observed during the heating-cooling phases. The ductility of the thinnest reverse channel allowed the beam to undergo large deflection and plastic deformation without failure of the structure. The local failure was concentrated in the beam in those tests with thicker reverse channel; the thinnest reverse channel allowed the beam to deform without local buckling.

ACKNOWLEDGEMENTS

The research that produced these results was supported by funding from the European Community's Research Fund for Coal and Steel (RFCS) under grant agreement n° RFSR-CT-2009-00021 and also by the Portuguese Foundation for Science and Technology (FCT) under research projects PTDC/ECM/110807/2009

REFERENCES

[1] Schleich, J.B. and Cajot, L.G., "Natural Fire Safety Concept – Full Scale Tests, Implementation in the Eurocodes and Development of User-friendly Design Tools", Final Report, ECSC Research 7210-060, 1997-2000 – EUR 20580 EN, 2003, pp. 200.

[2] Lawson, R.M., "Behaviour of Steel-beam-to-column Connections in Fire", The Structural Engineer, 1990, Vol. 68, No. 14, pp. 263-271.

[3] Schleich, J.B. and Cajot, L.G., "Valorisation Project: Natural Fire Safety Concept", ECSC Research, 2001, 7215-PA/PB/PC-042/057, Belgium, pp. 80.

[4] Simões da Silva, L., Santiago, A., Vila Real, P. e and Moore, D., "Behaviour of Steel Joints and Fire Loading", International Journal of Steel and Composite Structures, 2005, Vol. 5, No. 6, pp. 485-513.

[5] Santiago, A., Simões da Silva, L., Vaz, G., Vila Real, P. and Lopes, A.G., "Experimental Investigation of the Behaviour of a Steel Sub-frame under Natural Fire", Steel and Composite Structures, 2008, Vol. 8, No. 3, pp. 243-264.

[6] Neves, L.C., Simões da Silva, L. and Vellasco, P.C.G.S., "Experimental Behaviour of End Plate I-beam to Concrete-filled Rectangular Hollow Section Column Joints", International Journal of Applied Mechanics and Engineering, 2004, Vol. 9, No. 1, pp. 63-80.

[7] Silva, L.A.P., Neves, L.F.N. and Gomes, F.C.T., "Rotational Stiffness of Rectangular Hollow Sections Composite Joints", Journal of Structural Engineering, ASCE, 2003, Vol. 129, No. 4, pp. 487-494.

[8] Ding J. and Wang Y.C., "Experimental Study of Structural Fire Behaviour of Steel Beam to Concrete Filled Tubular Column Assemblies with Different Types of Joints", Engineering Structures, 2007, Vol. 12, No. 29, pp. 3485-3502.

[9] Simões da Silva, L., Santiago, A., Lopes, F., Veljkovic, M., Heistermann, T., Iqbal, N., Wald, F., Janá, T., Davison, B., Burgess, I., Huang, S-S., Dong, G., Wang, Y., Mandal, P., Hu, Y., Jafarian, M. and Koutlas, G., "COMPFIRE: Design of Composite Joints for Improved Fire Robustness", Final Report No. 4, 2013, Research Fund for Coal and Steel, Grant agreement n.º RFSR-CT-2009-00021, European Commission, Brussels.

[10] Lopes F.C., Santiago A., Simões da Silva L., Heistermann T., Veljkovic M. and da Silva J.G.S., "Experimental Behaviour of the Reverse Channel Joint Component at Elevated and Ambient Temperatures", International Journal of Steel Structures, 2013, Vol. 13, No. 3, pp. 459-472.

[11] Huang, S-S., Davison, B. and Burgess, I., "Experiments on Reverse-channel Connections at Elevated Temperature", Engineering Structures, 2013, Vol. 49, pp. 973-982.

[12] Elsawaf, S., Wang, Y.C. and Mandal, P., "Numerical Modelling of Restrained Structural Subassemblies of Steel Beam and CFT Columns Connected Using Reverse Channels in Fire", Engineering Structures, 2011, Vol. 33, pp. 1217-1231.

[13] EN 1993-1-8, Eurocode 3: Design of Steel Structures Part 1-8: Design of Joints, Brussels: European Committee for Standardization, 2005.

[14] Jaspart, J-P., Pietrapertosa, C., Weynand, K., Busse, E., and Klinkhammer, R., "Development of a Full Consistent Design Approach for Bolted and Welded Joints in Building Frames and Trusses between Steel Members Made of Hollow and/or Open Sections", Application of the component method. Draft final report – Volume 1: Practical design guide, Research Project 5BP, CIDECT, 2005.

[15] ISO. ISO 6892-1. Metallic Materials - Tensile Testing - Part 1: Method of Test at Room Temperature, International Organization for Standardization, 2009.

[16] CEN. EN 10002-5. Metallic Materials - Tensile Testing - Part 2: Method of Test at Elevated Temperature, European Committee for Standardization, 1991.

[17] CEN. EN 206-1. Concrete - Part 1: Specification, Performance, Production and Conformity, European Committee for Standardization, 2000.